MECHANICAL PROPERTIES OF SHEET METAL UNDER FORMING CONDITIONS

MECHANICAL PROPERTIES OF SHEET METAL UNDER FORMING CONDITIONS

A thesis presented for the degree of
DOCTOR OF PHILOSOPHY
of the
UNIVERSITY OF ASTON IN BIRMINGHAM, ENGLAND

by

Huai-Min SHANG

April, 1974

CONTENTS

SYNOPSIS

In the bulge test, a sheet metal specimen is clamped over a circular hole in a die and formed into a bulge by the hydraulic pressure on one side of the specimen. As the unsupported part of the specimen is deformed in this way, its area is increased, in other words, the material is generally stretched and its thickness generally decreased. The stresses causing this stretching action are the membrane stresses in the shell generated by the hydraulic pressure, in the same way as the rubber in a toy balloon is stretched by the membrane stresses caused by the air pressure inside it.

The bulge test is a widely used sheet metal test, to determine the 'formability' of sheet materials. Research on this forming process (2)-(15)* has hitherto been almost exclusively confined to predicting the behaviour of the bulged specimen through the constitutive equations (stresses and strains in relation to displacements and shapes) and empirical work hardening characteristics of the material as determined in the tension test. In the present study the approach is reversed; the stresses and strains in the specimen are measured and determined from the geometry of the deformed shell. Thus, the bulge test can be used for determining the stress-strain relationship in the material under actual conditions in sheet metal forming processes.

When sheet materials are formed by fluid pressure, the workpiece assumes an approximately spherical shape. The exact nature and magnitude of the deviation from the perfect sphere can be defined and measured by an index called prolateness.

*Numbers in brackets designate references at the end of thesis.

The distribution of prolateness throughout the workpiece at any particular stage of the forming process is of fundamental significance, because it determines the variation of the stress ratio on which the mode of deformation depends. It is found that, before the process becomes unstable in sheet metal, the workpiece is exactly spherical only at the pole and at an annular ring. Between the pole and this annular ring the workpiece is more pointed than a sphere, and outside this ring, it is flatter than a sphere.

In the forming of sheet materials, the stresses, and hence the incremental strains, are closely related to the curvatures of the workpiece. This relationship between geometry and state of stress can be formulated quantitatively through prolateness. The determination of the magnitudes of prolateness, however, requires special techniques. The success of the experimental work is due to the technique of measuring the profile inclination of the meridional section very accurately. A travelling microscope, workshop protractor and surface plate are used for measurements of circumferential and meridional tangential strains. The curvatures can be calculated from geometry. If, however, the shape of the workpiece is expressed in terms of the current radial (r) and axial (l) coordinates, it is very difficult to calculate the curvatures within an adequate degree of accuracy, owing to the double differentiation involved. In this project, a first differentiation is, in effect, by-passed by measuring the profile inclination directly and the second differentiation is performed in a round-about way, as explained in later chapters. The variations of the stresses in the workpiece thus observed have not, to the knowledge of the author, been reported experimentally.

The static strength of shells to withstand fluid pressure and their buckling strength under concentrated loads, both depend on the distribution of the thickness. Thickness distribution can be controlled to a limited extent by changing the work hardening characteristics of the work material and by imposing constraints. A technique is provided in this thesis for determining accurately the stress distribution, on which the strains associated with thinning depend. Whether a problem of controlled thickness distribution is tackled by theory, or by experiments, or by both combined, the analysis in this thesis supplies the theoretical framework and some useful experimental techniques for the research applied to particular problems. The improvement of formability by allowing draw-in can also be analysed with the same theoretical and experimental techniques.

Results on stress-strain relationships are usually represented by single stress-strain curves plotted either between one stress and one strain (as in the tension or compression tests) or between the effective stress and effective strain, as in tests on tubular specimens under combined tension, torsion and internal pressure. In this study, the triaxial stresses and strains are plotted simultaneously in triangular coordinates. Thus, both stress and strain are represented by vectors and the relationship between them by the relationship between two vector functions.

From the results so obtained, conclusions are drawn on both the behaviour and the properties of the material in the bulge test. The stress ratios are generally equal to the strain-rate ratios (stress vectors collinear with incremental strain vectors) and the work-hardening characteristics, which apply only to the particular strain paths are deduced.

Plastic instability of the material is generally considered to have been reached when the oil pressure has attained its maximum value so that further deformation occurs under a constant or lower pressure. It is found that the instability regime of deformation has already occurred long before the maximum pressure is attained. Thus, a new concept of instability is proposed, and for this criterion, instability can occur for any type of pressure growth curves.

NOTATION

Every chapter in this thesis is divided into various major sections represented by an alphabet. Thus, for the purpose of indicating a section at any place in the thesis, each section is designated as Chapter (integer . alphabet) - where the alphabet stands for the appropriate section and the integer represents the chapter number in which this section is belonged. For example, Chapter (2.A) refers to section A in Chapter 2.

The system used for identifying equations is similar to that described above except that all alphabets are replaced by integers. Thus, Eq. (2.1) indicates the first equation in Chapter 2. Figures and Tables throughout the thesis are represented exactly in the same way as equations.

Each intermediate stage of deformation in the bulge test is denoted by an alphabet from A to M. The following table is the meaning of such alphabets.

Stage	Pressure, psi	Polar height, in
A	145	0.509
B	350	0.759
C	440	0.848
D	500	0.905
E	570	0.990
F	600	1.021
G	720	1.149
H	810	1.260
I	920	1.411
J	1000	1.544
K	1050	1.754
L	1050	2.005
M (fractured)	1000	2.150

The following table is a glossary of all important symbols consistently used throughout the thesis. Certain notations which are of less significance and used only to assist discussion, such as dF_j and dA_i in Chapter (5.A), will not be included. Except for the suffices, the listing in the table follows the order of first appearance of each symbol used.

A <u>dot</u> above any parameter	refers to time rate of that parameter
Suffix 0	refers to original dimension
Suffix θ, s, t	refers to circumferential, meridional tangential and through-thickness directions respectively
Suffix I, II, III	triangular coordinate axes for general consideration
ε	logarithmic principal strain
ℓ	axial (or longitudinal) displacement of specimen
r	radial distance during deformation
T	time
s	arc length of the meridian section
t	through-thickness of specimen
ϕ	profile inclination of the meridian section
ρ	principal radius of curvature
σ	principal flow stress
P	oil pressure
a	radius of die hole
θ	angle subtended by ρ_s through the pole and die edge for a spherical bulge
N	index of sphericality
$\bar{P}$	prolateness of a surface of revolution
$\bar{\sigma}$	effective stress
$\bar{\varepsilon}$	effective strain
A, n	work-hardening coefficients of material
Y	yield stress in the tension test
H	polar height of bulge
$\int d\bar{\varepsilon}$	length of strain paths

σ_o	hydrostatic (or spherical) stress
σ'	deviatoric (or reduced) stress
κ	yield stress in the pure shear test
$\lambda, d\lambda$	scalar factor of proportionality in flow rules
μ, ν	Lode's variables
α	angle of any position vector in the triangular coordinate system
η	characteristic index for strain
ζ	characteristic index for stress
δ	vertical deviation of the meridional slope curve from the radial tangent line
Ω	slope of the radial tangent line to the meridional slope curve
ε_o	polar effective strain
Req	radius of an equivalent sphere
d	vertical displacement of workpiece from the pole
ψ	angle between current stress and strain vectors
$d\bar{\sigma}^*$	effective stress increment component parallel to incremental strain vector
ξ	true work-hardening coefficient
γ	angle between stress and strain increments
$\int d\bar{\sigma}$	length of stress paths

Chapter 1

INTRODUCTION

Sheet metal products of non-developable surfaces are formed to their required shapes by processes either asymmetrical or axisymmetrical. In asymmetrical process, such as forming of square and elliptical products, the principal axes of the product vary with deformation and consequently the strain paths are non-coaxial. For axisymmetrical processes, such as forming through a circular die, the principal axes remain fixed with respect to the material throughout the process and coaxial strain paths are obtained.

In coaxial and non-coaxial sheet metal forming, the required shapes are usually formed by means of a die and punch, either solid or liquid. The size of the solid punch is always less than the die hole; and the shape of the punch and die determines the product shape. For a liquid punch, the liquid fills completely under the blank so that the product shape is influenced by the die shape, the work hardening and resistance to hardening of the test material.

Tests to assess sheet metal behaviour and performance are usually limited to axisymmetrical processes (1). Of the tests commonly used in industries and laboratories, the simple tension and plunger tests are well known. The simple tension test (BS:18:Part 1:1970) which requires a sheet metal strip to be loaded uniaxially is useful only for deformations whose principal strain ratios are -1 :-1 : +2. In the plunger test, a die with a circular hole in it and a solid cylindrical punch of various profile radius are used. By altering the test conditions such as the punch profile radius and holding load, the material formability changes. Fig. (1.1) is an attempt to elucidate the effect of test conditions on the formability of sheet metal in bi-axial stretching systems as occurred in the plunger test. The triangular coordinate axes in Fig. (1.1) represent the (natural) through-thickness strain (ε_t), (natural) circumferential strain (ε_θ) and (natural) meridional tangential strain (ε_s) in a plane. Any point in this plane is characterised by a certain mode of deformation having strain ratios $\varepsilon_\theta : \varepsilon_s : \varepsilon_t$. Thus, the formability curve in the plunger test varies from nearly balanced bi-axial stretching ($\varepsilon_\theta : \varepsilon_s : \varepsilon_t = 1 : 1 : -2$) to a simple tension test ($\varepsilon_\theta : \varepsilon_s : \varepsilon_t = -1 : +2 : -1$) via pure shear ($\varepsilon_\theta : \varepsilon_s : \varepsilon_t = 0 : 1 : -1$). Therefore, the plunger test as a formability test is suitable only for a process whose strain path at the failed section coincides with that in the test. Since the plunger test does not provide a unique indication of the material performance, a set of test conditions is arbitrarily specified in the British Standards as the Erichsen test (BS: 3855 : 1965) in order that some comparison for different materials may be made.

Though not among the British Standards, the axisymmetrical bulge test is also widely used, especially for situations where a metal membrane is exposed to hydrostatic pressures. In the test, a sheet metal specimen is clamped over a circular die hole and formed into a bulge by introducing hydraulic pressure on one side of the specimen until a crack appears in it (1)-(15). The forming process is stopped when the hydraulic pressure reaches a maximum value (considered to correspond to the beginning of a crack). As the crack usually occurs at the pole where balanced bi-axial stretching occurs throughout the test, the bulge test as a formability test is applicable only to processes whose strain ratios are $\varepsilon_\theta : \varepsilon_s : \varepsilon_t = 1 : 1 : -2$.

By marking suitable grids onto the face of the specimen and measuring their geometrical transformations, the mechanical behaviour of the work material in the bulge test can be determined. Thus, this test can also be viewed as a test for material behaviour instead of the restricted use for formability test.

It can readily be seen that the bulge and plunger tests can be compared in two ways: (i) test conditions, and (ii) the process.

(i) Test conditions

The 'liquid punch' in the bulge test transmits a uniform pressure over the entire bulge during the test because it is filled completely with pressurised oil, Fig. (2.1).

In the plunger test, the effective zone for pressure transmission by the 'solid punch' is restricted only to the contact region of the punch and specimen, and is governed by the size and shape of the punch. Theoretically, maximum punch size is used in cup drawing where the punch diameter approximately equals the die hole less twice the specimen nominal thickness. When the punch size is smaller than the die hole, some part of the specimen is unsupported either by the punch or die and the boundary of the contact zone moves with the punch penetration.

(ii) Process

As the space under the deformed shell in the bulge test is filled entirely by pressurised oil, the process is in a frictionless state. In the plunger test, friction exists between the punch and specimen in the contact region, however small. Thus, in terms of formability test, failure usually occurs at the pole in the bulge test, where balanced bi-axial stretching occurs. However, the location of failure in the plunger test is essentially controlled by the friction within the contact zone, apart from the vital importance of draw-in of the flange. In general, the higher the friction, the further the location of failure would be from the pole; and when friction is eliminated by perfect lubrication within the contact region, failure can be made to occur at the pole. Therefore, the plunger test can be made to approximate the bulge test, Fig. (1.1).

Inspite of the equivalence of the plunger to the bulge test, the analysis of the two processes are different owing to the presence of friction and the moving boundary separating the contact and unsupported zones. For a frictionless condition, the mechanical behaviour (stresses and strains) of the work material can be readily determined (Chapter 2), by measuring geometrical transformations of grids marked onto the face of the specimen. In the plunger test, the friction complicates this analysis because the method used for the bulge test cannot be applied (Chapter 14). The material in the contact zone flows along the punch profile and gradually takes its shape as deformation proceeds. The profile of the unsupported region, however, depends on various factors such as the existence of draw-in of the flange.

From the above discussion, it is seen to be simpler to analyse for the mechanical behaviour of sheet metal in axisymmetrical forming by the bulge test than by the plunger test. This project is confined to the bulge test in order to provide a framework for the analysis of the plunger test.

Chapter 2

BEHAVIOUR OF THE WORK MATERIAL IN THE BULGE TEST - BASIC RELATIONS

This Chapter is focussed on two aspects of the bulge test: (i) the basic knowledge on the deformed shell through geometrical and kinematical considerations and this forms the experimental aspects of this project, (ii) the basic knowledge is further extended towards an attempt to generalise the prediction of the work material performance which many research workers have been doing (2), (4), (6)-(15).

Sheet metal forming processes may be idealised into geometrical transformation of a plane into non-developable curved surfaces so that it can be analysed mathematically. It is easy to imagine the plane midway between the two surfaces of the flat blank being transformed into a curved surface midway between the inner and outer surfaces of the formed shell; and it is assumed throughout this project that such a geometrical transformation adequately represents the sheet metal forming process. In this assumption, the variation of the stresses within the thickness of the sheet - in particular, the bending stresses - are ignored.

(A) Relation between strains and shape of the bulge

The circular bulge test is illustrated in Fig. (2.1) in the cylindrical coordinate axes OL and OR, and the mutually orthogonal θ-, s- and t-axis at a typical element A. In such an axisymmetrical case, the geometrical transformation is completely determined by the two parametric equations as follows,

$$\begin{aligned} \ell &= \ell(r_o, T) \\ r &= r\,(r_o, T) \end{aligned} \qquad (2.1)$$

where ℓ and r are, respectively, the current longitudinal and radial coordinates; and r_o and T are, respectively, the initial radial distance and time. The elimination of the parameter r_o for a particular value of T in Eq. (2.1) yields a relationship between ℓ and r which represents a meridian contour of the partly formed shell; and the elimination of the parameter T for a particular value of r_o yields the path of a particle in the work piece.

In order to derive the mechanical behaviour of the work material from the bulge test, it is necessary to determine the strains and stresses from the hydraulic pressure and basic equation in Eq. (2.1). By symmetry, the principal strains are the meridional tangential (ε_s), the circumferential (ε_θ) and the through-thickness (ε_t) strains and they are, by definition,

$$\begin{aligned} \varepsilon_s &\equiv \log_e \left(\frac{ds}{dr_o}\right) \\ \varepsilon_\theta &\equiv \log_e \left(\frac{r}{r_o}\right) \\ \varepsilon_t &\equiv \log_e \left(\frac{t}{t_o}\right) \end{aligned} \qquad (2.2)$$

where s is the arc length of the meridian section in Fig. (2.1), and t and t_o are the current and original through-thickness respectively.

The arc length, s, in general is difficult to measure, so that modification of the ε_s term in Eq. (2.2) is necessary. Suppose ϕ is the inclination of element A with the OR axis, then,

$$\sec\phi = \frac{ds}{dr} \tag{2.3}$$

so that ε_s in Eq. (2.2) becomes

$$\varepsilon_s = \log_e \left(\frac{dr}{dr_o} \quad \frac{1}{\cos\phi}\right) \tag{2.4}$$

The two principal radii of curvature of an axisymmetrical curved surface lie in two mutually perpendicular planes through the normal (t-axis in Fig. (2.1)), one in the meridian plane (the plane of the paper in Fig. (2.1)) and one in a plane perpendicular to it. By definition, the former (ρ_s) is,

$$\rho_s = \frac{dr}{d\phi} \quad \frac{1}{\cos\phi} \tag{2.5}$$

and the latter radius (ρ_θ) is the sub-normal, thus,

$$\rho_\theta = \frac{r}{\sin\phi} \tag{2.6}$$

These radii of curvature are important to this study because, as shown in the following section, they are related to the principal stresses in the deformed shell.

(B) Relation between principal stresses and curvatures

The thickness of the workpiece is small relative to the radii of curvature of the shell, hence the bending stresses are relatively small. Since the bending stresses are relatively small, and since the thickness is small in comparison with the other dimensions of the bulge, the shear stresses are small and negligible. If, together with the shear and bending stresses, the small through-thickness is also ignored, then the workpiece may be considered to be under plane stress shown by the inset in Fig. (2.1). The meridional tangential stress (σ_s) is always tensile, but the circumferential stress (σ_θ) can be compressive near the edge of the bulge; and both these stresses are assumed to be uniformly distributed through the thickness. In general, the work material is stretched bi-axially and the deformation involves progressive thinning. The principal stresses are related to the curvatures of the shell by the well-known formula for membrane stresses, namely,

$$\frac{\sigma_s}{\rho_s} + \frac{\sigma_\theta}{\rho_\theta} = \frac{P}{t} \tag{2.7}$$

where P is the oil pressure.

Since the meridional tangential stress (σ_s) is always tensile, considering the equilibrium of a cap of radius r and using Eq. (2.6), it can be shown that

$$\sigma_s = \frac{P}{2t}\rho_\theta \tag{2.8}$$

where P and ρ_θ are always positive. Combining Eqs. (2.7) and (2.8), we get

$$\begin{aligned}\sigma_\theta &= (\frac{P}{t} - \frac{\sigma_s}{\rho_s})\rho_\theta \\ &= \frac{P}{t}\rho_\theta - \frac{\rho_\theta}{\rho_s}\sigma_s \\ &= (2 - \frac{\rho_\theta}{\rho_s})\sigma_s \end{aligned} \tag{2.9}$$

The equations governing the deformation in the bulge test can now be traced. The formula for the membrane stresses, Eq. (2.7), expresses in fact an equilibrium condition together with the equilibrium equation Eq. (2.8) - it determines the stresses for a particular load (or hydraulic pressure) and a particular geometrical configuration of the workpiece. At any particular stage of the bulge test, these bi-axial stresses at any point of the specimen are, in fact, the flow stresses of the material at that point. As deformation progresses, an incremental load (pressure P) produces incremental stresses throughout the workpiece and these incremental stresses give rise to incremental strains according to the strain-hardening characteristics of the test material. The change in the shape of the bulge is, of course, closely related to these incremental strains and, for a particular material and a particular stage in the bulge test, this change of shape is uniquely determined because the strains must be mutually compatible, as implied in the first two of Eqs. (2.2), where

$$s = \int_{o}^{r} \sqrt{1 + \left(\frac{d\ell}{dr}\right)^{2}}\; dr \qquad (2.10)$$

(C) Principal strain rates in terms of rate of change of r and ℓ

It was suggested in the previous section of this Chapter that the change in bulge shape for subsequent deformation is closely related to the principal strain rates. Since the geometrical transformation of the specimen is completely determined by the parameters r and ℓ for any stage of deformation, Eq. (2.1), the principal strain rates can sufficiently be defined by the rate of change of r and ℓ only. The rates of any variable can be expressed in terms of two monotonically increasing parameters, hydraulic pressure (P) and time (T). In accordance to Eq. (2.1), it is convenient at this stage to have the time rates of the various quantities in terms of time (T) and these are sometimes expressed mathematically by a dot above the parameter considered.

The principal strain rates can easily be derived through the definitions of principal strains, Eq. (2.2) as

$$\dot{\varepsilon}_\theta \equiv \frac{\partial \varepsilon_\theta}{\partial T} = \frac{\partial}{\partial T}\left(\log_e \frac{r}{r_o}\right) = \frac{\dot{r}}{r} \qquad (2.11)$$

$$\dot{\varepsilon}_t \equiv \frac{\partial \varepsilon_t}{\partial T} = \frac{\partial}{\partial T}\left(\log_e \frac{t}{t_o}\right) = \frac{\dot{t}}{t} \qquad (2.12)$$

$$\dot{\varepsilon}_s \equiv \frac{\partial \varepsilon_s}{\partial T} = \frac{\partial}{\partial T}\left(\log_e \frac{ds}{dr_o}\right) = \frac{\partial}{\partial T}\log_e\left(\frac{dr}{dr_o}\sqrt{1+\left(\frac{dr}{d\iota}\right)^2}\right) \qquad (2.13)$$

Metals under normal deformation are incompressible so that the three principal strain rates (and hence the principal strains) have only two degrees of freedom governed by the following relation,

$$\dot{\varepsilon}_\theta + \dot{\varepsilon}_t + \dot{\varepsilon}_s = 0 \qquad (2.14)$$

These equations on strain rates are used to constitute a foundation on the theoretical prediction of the change of state of strain corresponding to a pressure increment together with the relationship between curvatures and stresses. This is elucidated in section E of this chapter.

(D) Principal strain rates in terms of rate of change of r, ι and ϕ

As seen in the last section, $\dot{r}$ and $\dot{\iota}$ are theoretically sufficient to describe the change of state of strain by a pressure increment. However, it is frequently more convenient to include the bulge profile inclination (ϕ) as a variable especially for $\dot{\varepsilon}_s$. The variable ϕ is in fact related to r and ℓ by the function

$$\phi = \tan^{-1}\left(\frac{d\ell}{dr}\right) \tag{2.15}$$

Thus, the meridional tangential strain rate in Eq. (2.13) can be obtained by differentiating Eq. (2.4) with respect to T,

$$\dot{\varepsilon}_s = \frac{\partial}{\partial T}\left(\log_e\left(\frac{dr}{dr_o}\ \frac{1}{\cos\phi}\right)\right) = \frac{d\dot{r}}{dr} + \dot{\phi}\tan\phi \tag{2.16}$$

The rate of change of current radius in the bulge test can be expressed by the time rates of circumferential curvature and profile inclination so that

$$\begin{aligned}\dot{r} &= \frac{d}{dT}\left(\rho_\theta \sin\phi\right)\\ &= \dot{\rho}_\theta \sin\phi + \rho_\theta\dot{\phi}\cos\phi\end{aligned} \tag{2.17}$$

The circumferential strain rate then becomes

$$\dot{\varepsilon}_\theta = \frac{\dot{r}}{r} = \frac{\dot{\rho}_\theta}{\rho_\theta} + \dot{\phi}\cot\phi \tag{2.18}$$

and the corresponding through-thickness strain rate can be calculated through the incompressibility equation, Eq. (2.14)

(E) Theoretical prediction in general

Based on the geometrical and kinematical considerations of a shell discussed in earlier sections of this Chapter, theoretical prediction of the bulge test can be attempted. The approach is based on that by Chakrabarty and Alexander (2) in a more general manner. Perusal of Eqs. (2.16) and (2.18) indicates that a compatibility equation for strain rates can be arrived at by eliminating $\dot{r}$. From Eq. (2.11)

$$\frac{d\dot{\varepsilon}_\theta}{dr} = \frac{d}{dr}\left(\frac{\dot{r}}{r}\right) = \frac{1}{r}\left(\frac{d\dot{r}}{r} - \dot{\varepsilon}_\theta\right)$$

or

$$\frac{d\dot{r}}{dr} = \frac{d(r\dot{\varepsilon}_\theta)}{dr} \qquad (2.19)$$

On substituting Eq. (2.19) into Eq. (2.16),

$$\dot{\varepsilon}_s = \frac{d(r\dot{\varepsilon}_\theta)}{dr} + \dot{\phi}\tan\phi \qquad (2.20)$$

The parameter $\dot{\phi}$ is not an independent variable, but is a function of $\dot{\varepsilon}_\theta$ governed by Eq. (2.18) so that Eq. (2.20) becomes

$$\begin{aligned}\dot{\varepsilon}_s &= \frac{d(r\dot{\varepsilon}_\theta)}{dr} + \left(\dot{\varepsilon}_\theta - \frac{\dot{\rho}_\theta}{\rho_\theta}\right)\tan^2\phi \\ &= r\frac{d\dot{\varepsilon}_\theta}{dr} + \dot{\varepsilon}_\theta(1 + \tan^2\phi) - \frac{\dot{\rho}_\theta}{\rho_\theta}\tan^2\phi \\ &= r\frac{d\dot{\varepsilon}_\theta}{dr} + \dot{\varepsilon}_\theta\sec^2\phi - \frac{\dot{\rho}_\theta}{\rho_\theta}\tan^2\phi \qquad (2.21)\end{aligned}$$

Eq. (2.21) is thus the compatibility equation relating $\dot{\varepsilon}_\theta$ and $\dot{\varepsilon}_s$ satisfying the basic equations in Eq. (2.1).

Sheet metal engineers are often interested in thickness distributions during forming. This can be obtained through the incompressibility equation, Eq. (2.14), and the compatibility equation, Eq. (2.21), Thus,

$$-\dot{\varepsilon}_t = (1 + \sec^2\phi)\dot{\varepsilon}_\theta + r\frac{d\dot{\varepsilon}_\theta}{dr} - \frac{\dot{\rho}_\theta}{\rho_\theta}\tan^2\phi \qquad (2.22)$$

and the through-thickness strain at any point on the bulge profile at any particular stage of deformation is readily given by

$$-\varepsilon_t = \iint(1 + \sec^2\phi)\, d\varepsilon_\theta dr + \iint r\, d\dot{\varepsilon}_\theta dT - \iint \frac{\tan^2\phi}{\rho_\theta} d\rho_\theta dr + \text{constant} \qquad (2.23)$$

Integration, either mathematically or graphically, is extremely difficult. Thus Eq. (2.23) can further be simplified by relating the parameter r to ϕ. Then, from Eq. (2.6),

$$\frac{dr}{d\phi} = \rho_\theta \cos\phi = \rho_\theta \frac{\sin\phi}{\tan\phi} = \frac{r}{\tan\phi}$$

or

$$\frac{dr}{r} = \frac{d\phi}{\tan\phi}$$

or

$$\frac{d\dot{\varepsilon}_\theta}{dr} = \frac{\tan\phi}{r}\,\frac{d\dot{\varepsilon}_\theta}{d\phi} \qquad (2.24)$$

Hence the conversion from $\frac{d\dot{\varepsilon}_\theta}{dr}$ in Eq. (2.22) to $\frac{d\dot{\varepsilon}_\theta}{d\phi}$ is given by Eq. (2.24). Substituting Eq. (2.24) into the compatibility equation, Eq. (2.22), yields

$$-\dot{\varepsilon}_t = (1 + \sec^2\phi)\dot{\varepsilon}_\theta + \tan\phi\,\frac{d\dot{\varepsilon}_\theta}{d\phi} - \frac{\dot{\rho}_\theta}{\rho_\theta}\tan^2\phi$$

or

$$\tan\phi\,\frac{d\dot{\varepsilon}_\theta}{d\phi} + (1 + \sec^2\phi)\dot{\varepsilon}_\theta = \left(\frac{\dot{\rho}_\theta}{\rho_\theta}\tan^2\phi - \dot{\varepsilon}_t\right)$$

Multiplying both sides by sinϕ and simplifying,

$$\frac{d}{d\phi}(\dot{\varepsilon}_\theta \sin\phi \tan\phi) = \left(\frac{\dot{\rho}_\theta}{\rho_\theta}\tan^2\phi - \dot{\varepsilon}_t\right)\sin\phi \qquad (2.25)$$

Eq. (2.25) suggests that any one of the strain (ε_θ or ε_t) as a function of (ϕ, T) together with the function $\rho_\theta = \rho_\theta(\phi, T)$ is sufficient to determine the state of strain at any material particle in the bulge at any time. In practice, the circumferential strain can easily be determined so that the thickness strain rate in Eq. (2.25) is treated as the dependent variable,

$$\dot{\varepsilon}_t = \frac{\dot{\rho}_\theta}{\rho_\theta}\tan^2\phi - \frac{1}{\sin\phi}\frac{d}{d\phi}(\dot{\varepsilon}_\theta \sin\phi \tan\phi) \qquad (2.26)$$

Some reflection will show that the parametric functions

$$\begin{aligned} \varepsilon_\theta &= \varepsilon_\theta(\phi, T) \\ \rho_\theta &= \rho_\theta(\phi, T) \end{aligned} \qquad (2.27)$$

are related to the strain-hardening characteristics of the test material so that the new state of stress under a pressure (or time increment) can be calculated through Eqs. (2.8) and (2.9).

(F) Plastic instability in the bulge test

Plastic instability is usually considered to have been reached when the pressure growth curve reaches its maximum value. This can be done by differentiating the membrane stress equation and equate pressure increment to zero. Starting with Eq. (2.9),

$$\sigma_\theta = \frac{P}{2t_o k_t}\left(2 - \frac{\rho_\theta}{\rho_s}\right)\rho_\theta \quad ; \quad k_t \equiv \exp(\varepsilon_t)$$

On differentiation,

$$\left(2 - \frac{\rho_\theta}{\rho_s}\right)\rho_\theta \, dP = 2t_o(\sigma_\theta dk_t + k_t d\sigma_\theta) - P\left(2 - \frac{\rho_\theta}{\rho_s}\right)d\rho_\theta + P\left(\frac{\rho_s d\rho_\theta - \rho_\theta d\rho_s}{\rho_s^2}\right)\rho_\theta$$

At instability (dP = 0), then everywhere along the bulge at this pressure satisfies the following equation,

$$2t_o d(\sigma_\theta e^{\varepsilon_t}) + 2P\left(\frac{\rho_\theta}{\rho_s} - 1\right)d\rho_\theta - P\left(\frac{\rho_\theta}{\rho_s}\right)^2 d\rho_s = 0 \qquad (2.28)$$

Eq. (2.28) is the general equation for the instability of the bulge test and is extremely difficult to solve. We shall see in Chapter (4.E) how this equation becomes soluble by considering only at the pole as most investigators did.

(i) Special case: spherical bulge

Under such an assumption, equilibrium of the membrane stresses shows that the specimen is everywhere under balanced bi-axial stretching and $\rho_s = \rho_\theta$. Thus, the incompressibility equation, Eq. (2.14) yields

$$\dot{\varepsilon}_t = -2\dot{\varepsilon}_\theta \qquad (2.29)$$

From the definition of ρ_θ and Fig. (2.2) for spherical bulge,

$$\rho_\theta = \frac{r}{\sin\phi} = \frac{a}{\sin\theta}$$

and

$$\frac{\dot{\rho}_\theta}{\rho_\theta} = -\dot{\theta}\cot\theta \qquad (2.30)$$

Thus, the $\frac{\dot{\rho}_\theta}{\rho_\theta}$ term for a spherical bulge is independent of ϕ. Substituting Eqs. (2.29) and (2.30) into the general solution, Eq. (2.25), yields

$$\frac{d}{d\phi}(\dot{\varepsilon}_\theta \sin\phi\tan\phi) = (\dot{\theta}\cot\theta\tan^2\phi + 2\sin\phi\frac{d}{d\phi}(\dot{\varepsilon}_\theta\sec\phi) + \dot{\varepsilon}_\theta)\sin\phi$$

$$\sin^2\phi\frac{d}{d\phi}(\dot{\varepsilon}_\theta\sec\phi) + 2\dot{\varepsilon}_\theta\sec\phi\sin\phi\cos\phi$$

$$= \dot{\theta}\cot\theta\tan^2\phi\sin\phi + 2\sin^2\phi\frac{d}{d\phi}(\dot{\varepsilon}_\theta\sec\phi) +$$

$$2\dot{\varepsilon}_\theta\sin\phi$$

and finally,

$$\frac{d}{d\phi}(\dot{\varepsilon}_\theta\sec\phi) = -\dot{\theta}\cot\theta\sec\phi\tan\phi \qquad (2.31)$$

Thus, Eq. (2.31) is the solution for a spherical bulge and on integration with the boundary condition $\dot{\varepsilon}_\theta = 0$ at $\phi = \theta$ for a rigidly clamped specimen, it becomes

$$\dot{\varepsilon}_\theta = \left(\frac{\cos\phi - \cos\theta}{\sin\theta}\right)\dot{\theta} \qquad (2.32)$$

It then follows that the through-thickness strain rate $\dot{\varepsilon}_t$ is

$$\begin{aligned}
\dot{\varepsilon}_t &= -2\dot{\varepsilon}_\theta = -2\left(\frac{\cos\phi - \cos\theta}{\sin\theta}\right)\dot{\theta} \\
&= -\dot{\theta}\left(\frac{2\cos\phi}{\sin\theta} - 2\cot\theta\right) \\
&= -\dot{\theta}\left(\frac{\sin^2(\frac{\theta}{2}) + \cos^2(\frac{\theta}{2})}{\sin(\frac{\theta}{2})\ \cos(\frac{\theta}{2})}\cos\phi + \frac{\tan^2(\frac{\theta}{2}) - 1}{\tan(\frac{\theta}{2})}\right) \\
&= -\dot{\theta}\left(\frac{\tan^2(\frac{\theta}{2}) + 1}{\tan(\frac{\theta}{2})}\cos\phi + \left(\tan(\tfrac{\theta}{2}) - \cot(\tfrac{\theta}{2})\right)\right) \\
&= -\dot{\theta}\left(\left(\tan(\tfrac{\theta}{2}) + \cot(\tfrac{\theta}{2})\right)\cos\phi + \left(\tan(\tfrac{\theta}{2}) - \cot(\tfrac{\theta}{2})\right)\right) \\
&= -\dot{\theta}\left(\tan(\tfrac{\theta}{2})(1 + \cos\phi) - (1 - \cos\phi)\cot(\tfrac{\theta}{2})\right) \qquad (2.33)
\end{aligned}$$

Both Eqs. (2.32) and (2.33) are solutions by Chakrabarty and Alexander (2) at a particular stage. Behaviour of the specimen for successive stages may also be obtained from the solution derived above if the work-hardening characteristics $\theta = \theta(T)$ are known. States of stress are also determinable from Eqs. (2.8) and (2.9).

Chapter 3

SURFACE OF REVOLUTION OF A SHELL WITH REFERENCE TO MEMBRANE STRESSES

The equilibrium equation for the membrane stresses in a shell, Eq. (2.9), reveals that the principal stress ratios at anywhere along the bulge profile is determined by the ratio of the local principal curvatures of the bulge profile. Since the shape of a surface can be determined from the ratio of the two principal curvatures, it is essential to study in detail the surface of revolution of a shell with reference to membrane stresses. Some reflection will show that the ratio (ρ_θ/ρ_s) in Eq. (2.9) measures the departure of the local surface element from the perfect spherical shape. We shall call the ratio N, the index of sphericality; that is,

$$N = \frac{\rho_\theta}{\rho_s} \tag{3.1}$$

In terms of membrance stress, it is shown in Eq. (2.9) that

$$N = 2 - \frac{\sigma_\theta}{\sigma_s} \tag{3.2}$$

The two cases of stresses in thin shells usually considered in elementary Strength of Materials are for N = 0 (cylinder), where the hoop stress (σ_θ) is twice the longitudinal stress (σ_s), and for N = 1 (spherical), where the two membrane stresses are equal. As can be seen in Eq. (3.2), in surfaces for which N = 2, the hoop stress (σ_θ) vanishes. Such surfaces have, indeed, been used in the design of pressure vessels, like the ends of boiler drums. When N is greater than 2, the hoop stress, contrary to common sense expectation, is compressive for a vessel under internal pressure. When N is negative, the hoop stress is more than twice the longitudinal stress. Fig. (3.1) shows the variation of the stress ratio with respect to N.

(A) Surfaces of constant N - values

Two types of surface of revolution with constant N - value are widely used in engineering, namely, the sphere (N = 1) and the cylinder (N = 0) - especially the latter, which is a developable surface and easy to fabricate. There are, of course, infinitely many surfaces of revolution with constant N - values. For example, when N = 2, the surface is one in which the hoop stress disappears and it can be constructed graphically by Biezeno's method. Thus, in Fig. (3.2) the meridian section of this surface is constructed by starting from an arbitrary point T on the OR - axis. Take $\overline{ST} = \frac{1}{2}\,\overline{OT}$ and draw a small arc TT' with ST as radius. Then take half of the normal at T' (O'T') as radius (S'T') and draw the next small segment of the meridian section T T", and so on till a quarter of the meridian section is completed.

Other surfaces of constant N - value can be constructed graphically with methods similar to that just described. The meridian sections of these surfaces can, however, be expressed in parametric equations. Thus, by definitions of and ,

(3.3)

and therefore (3.4)

On integrating, Eq. (3.4) becomes

(3.5)

where A is a constant of integration.

Eq. (3.5) is the parametric equation relating ϕ, r and N values in the bulge test. For constant N surfaces, Eq. (3.5) is simplified to

$$r^N = k \sin\phi \tag{3.6}$$

where k is the constant of integration. For exploring the shapes of these surfaces, it is convenient to assume

$$(r)_{\phi=\frac{\pi}{2}} = 1 \tag{3.7}$$

so that, Eq. (3.6) takes the following simpler form,

$$\sin\phi = r^N \tag{3.8}$$

The curve relating r and $\sin\phi$ for constant N values given by Eq. (3.8) are non-linear and we can linearise them by using (log-log) scales so that the curves become radial lines emerging from the origin, Fig. (3.3), each having a slope of N.

For the other coordinate, ι, combination of Eq. (3.8) and the definitions of ρ_θ and N gives

$$\rho_s = \frac{(\sin\phi)^{(\frac{1-N}{N})}}{N} \tag{3.9}$$

However,

$$d\iota = -\rho_s \sin\phi \, d\phi \tag{3.10}$$

the negative sign is due to the increase in ι with decrease in ϕ; hence,

$$\iota = -\frac{1}{N}\int_{\pi/2}^{\phi} (\sin\phi)^{\frac{1}{N}} \, d\phi \tag{3.11}$$

Eq. (3.11) cannot be expressed in terms of elementary functions, except for values of N equal to zero, ± 1 and reciprocal of integers. Nevertheless, Eqs. (3.8) and (3.11) constitute the parametric equations of the meridian sections of the surfaces of constant N-value. The integral in Eq. (3.11) can, of course, be easily evaluated by graphical or mechanical means. These meridian sections are as shown in Fig. (3.4). It can be seen there that only when N is positive are the surfaces closed, otherwise they are bollard-shaped and open at the top and the bottom. As positive N becomes infinitely large, the surface becomes like the outside surface of flatter and flatter pancakes; and as N approaches negative infinity, the surface becomes like two flat sheets of paper each with a hole and the two sheets are joined at the edges of the holes.

The variation of the membrane stresses in these surfaces of constant N-value can now be explored. The variation of ρ_θ represents, by Eq. (2.8), that of the meridional tangential membrane tension. Eliminating ϕ from Eqs. (2.6) and (3.8) we get,

$$\rho_\theta = r^{(1-N)} \tag{3.13}$$

and the variations are as shown in Fig. (3.5). Since the variations of ρ_θ with r shown in Fig. (3.5) are for constant values of N, the variation of ρ_s follows the same pattern, but in different scales, of course. The line for constant ρ_θ (N = 1) is self-explanatory; but the linear variation for N = 0 requires some elucidation. When N = 0 the surface may either be a cone or a cylinder. When it is a cylinder, only the point $(\rho_\theta)_{r=1} = 1$ is operative; and when it is a cone, ρ_θ is, of course, proportional to r. For surfaces of constant N-value, at the pole (r = 0), the stress, and the radius of curvature, is either zero $(N < 1)$, or infinity $(N > 1)$, except for the sphere (N = 1). When N is less than unity, the meridional tangential tension rises gradually or rapidly towards $\frac{P}{2t}$ as the equator is approached; and when N is greater than unity, this tension starts at $\frac{P}{2t}$ at the equator and rises gradually or rapidly towards infinity as the pole is approached. If surfaces of constant N-values greater than unity are constructed and subjected to pressure, the material near the pole will yield and the shape will be changed so that finite stresses are generated and sustained.

In surfaces of constant N-value, the circumferential stress is, of course, proportional to the meridional tangential one, hence Fig. (3.6) also represents the variations of the circumferential stress. The ratio between the meridional tangential and the circumferential stress is not, however, simply N, but is related to N as in Eq. (3.2). For exploring the variation of the circumferential, or hoop stress, it is desirable to divide the N-values into four ranges, as in Table (3.1).

Range	N	Shape of surfaces	σ_θ/σ_s
1	> 2	Pancake-shaped	< 0 (σ_θ compressive)
	$= 2$	Tangerine-shaped	$\sigma_\theta = 0$ (uniaxial tension test)
2	$1 < N < 2$	Oblate spheroid	$0 < \frac{\sigma_\theta}{\sigma_s} < 1$ (tensile σ_θ less than σ_s)
	$= 1$	Sphere	$\sigma_\theta = \sigma_s$ (Balanced bi-axial stretch)
3	$0 < N < 1$	Prolate spheroid	$1 < \sigma_\theta/\sigma_s < 2$
	$= 0$	Cone or cylinder	$\sigma_\theta = 2\sigma_s$
4	< 0	Bollard-shaped	$\sigma_\theta > 2\sigma_s$

Table (3.1). Summary of constant N-surfaces

(B) Curvatures and stresses in thin shells of revolution

The local geometrical properties of a surface is completely defined by the principal curvatures, just as the local state of stress in a thin shell is defined by the principal stresses. Furthermore, just as the stresses on sections not along the principal stress can be represented by the Mohr circle (32)-(34) the curvatures of the surface along sections other than those of the principal curvatures can also be represented by Mohr circles. There is, therefore, a more general and complex relationship between the curvatures and the membrane stresses than that represented by Eq. (2.7). Before exploring this relationship, however, it is necessary first to construct the Mohr circle for the curvatures.

At a typical point in a curved surface, suppose three Cartesian axes are set up as follows: η-axis along the normal, and ζ- and ξ-axis in the tangent plane. On each of the two axes in the tangent plane, there are two gradients of slope, for example, along the ζ-axis, the gradient of the longitudinal slope $d^2\eta/d\zeta^2$ (or curvature) and the gradient of the transverse slope $d^2\eta/d\zeta d\xi$. It can easily be shown that if ζ-axis and ξ-axis rotate in the tangent plane, these two gradients may be represented by a Mohr circle, in the same way as the direct and shear stresses in a plane element are represented in the Mohr circle for stresses. The extremum values of the gradient of the longitudinal slope are the principal curvatures and they occur in directions along which the gradient of transverse slope vanishes. Also, the gradient of the transverse slope attains its numerically maximum values along two orthogonal directions in which the gradient of the longitudinal slope (or curvature) are equal.

To show the general relationship between the curvatures and the states of stress, therefore, it is only necessary to show the relationship between the two types of Mohr circles.

Corresponding Mohr circles for stress and curvature are shown in Fig. (3.6), together with the values of N. Three kinds of typical Mohr circle may be distinguished in Fig. (3.6), the point circle, for balanced bi-axial stress or spherical surface; the circle tangent to the vertical axis, for uniaxial stress or cylindrical surface; and the circle with its diameter equal to its nearest distance from the origin, for one principal stress being twice the other, or a surface of N equals 2. Thus, for a spherical surface (N = 1), both the Mohr circles for stresses and for curvatures are point circles; for a surface of N = 2, the Mohr circle for stress corresponds to uniaxial tension; and for a cylindrical surface (N = 0), one principal stress is twice the other. This complex relationship may be visualised by reading Fig. (3.6) in a cinematographic way from left to right and imagining the Mohr circle for stress shrinking and expanding in opposite directions to that for the curvatures; the two Mohr circles becoming identical only once, when they are both point circles for N = 1.

(C) Prolateness of the real shell

Any real specimen of sheet material formed by hydraulic or pneumatic pressure can never be a surface of constant N-value, owing to the constraints on the deformations in the material. Thus, at the pole the strains and stresses are, by symmetry, balanced bi-axial stretching and there N must be equal to unity; but at the edge of the bulge, the circumferential strain is either zero, or slightly compressive (if there is draw-in), hence the meridional tangential stress must be at least twice the circumferential stress, and the N value must therefore, be greater than one but smaller than two (see Fig. 3.6).

In most of the important papers on the bulge test, the workpiece has been assumed to be a spherical surface in the predictive or interpretative theories (2)-(5), (8), (10)-(13), It has just been shown that a real specimen cannot be any surface of constant N value, let alone a sphere, the simplest of constant N surfaces. Even just for describing an actual bulged specimen, therefore, it is necessary first to define accurately the characteristics of an actual surface from point to point.

At any point in a continuous surface of revolution, there is an N-value, which applies to a vanishingly narrow ribbon of surface at the same latitutde. If this (positive) value of N is less than one, then the surface at that latitude may be said to be more pointed than a sphere (prolate); and, if it is greater than one, to be more flattened than a sphere (or oblate), because, if a surface of that constant N value is constructed to pass through that point, that surface will be prolate or oblate, respectively, as compared with a perfect sphere. In fact, (1-N) may be defined as prolateness, $\overline{P}$, and the negative of prolateness, or $N > 1$, is oblateness. Prolateness and curvatures are two distinct concepts, and a surface can have either large curvature and large prolateness, or small curvature and large prolateness. As the bulging action progresses, the curvature generally increases, but, in theory, the prolateness does not necessarily decrease. As has been shown, a sheet metal bulged specimen is always spherical (zero prolateness) at the pole, and theoretically, it is prolate at the edge, because, if there are no bending (only membrane stresses present) and no draw-in, then the circumferential strain disappears at the edge, and both the stress ratio $\frac{\sigma_\theta}{\sigma_s}$ and the prolateness $(1-N)$ are equal to $\frac{1}{2}$ there; though in practice, there are, in metal shells being formed, always bending and friction at the rim so that the theoretical ratios of the curvatures and stresses are obscured. Between the pole and the rim, the surface may be prolate, spherical or oblate, as the plastic properties of the work material dictate. Indeed, it is all three in the metal shell, for which experimental results are shown in Chapter (8.C).

Chapter 4

PAST LITERATURE AND OBJECTIVES

Through the basic considerations of the bulge test in Chapters 1 to 3, past literature can be reviewed in a logical manner. From the vast body of literature on both the practical and theoretical aspects of the bulge test, this Chapter is devoted to summarise the lines of approach on this particular type of forming process. As we shall see later, there have been various difficulties in the previous analyses and it is in relation to these difficulties that the main object of this project is defined.

(A) Experimental investigations

As far as publications are concerned, the bulge test was studied experimentally at least as early as 1948 (3). In the early investigations, 6 to 20 in diameter bulges (4), (3) on 0.020 to 0.1303 in thick (6) specimens were usually formed. The test material used varied over a wide range including various grades of annealed and hardened steel, aluminium, brass and copper. The specimen with grids on its surface was subjected to hydraulic pressures which were subsequently released before geometrical measurements of the grid were taken, (3)-(6), (8), (11).

When a circular die is used, the process is axisymmetrical and the principal stresses and strains are along the through-thickness, meridional tangential and circumferential directions of the bulge. To study the behaviour of sheet metal in the bulge test, obviously, the fundamental objective is to observe how the material flows - that is, states of strain involved in the whole process. Metals in the plastic range can be considered to be incompressible so that the three principal (natural) strains add up to zero, Eq. (2.14). With triaxial strains having only two degrees of freedom, any two of them are sufficient to define the state of strain of the material particle concerned under a given applied stress condition. Investigators have unanimously measured the circumferential strains because they can be obtained easily and accurately with a travelling microscope (3)-(5), (8), (9), (11). For the remaining two strains, there is an alternative choice. Many workers (5), (7), prefer through-thickness strains because they can be read directly from a dial gauge installed on a rig with a fixed anvil at the base and with the specimen placed between the fixed and the measuring anvils of the dial gauge. It is evident that this method requires the anvils to be normal to the specimen. Some authors (3), (4), (8), (9), however, measure the meridional tangential strain instead. As this involves profile measurement of the deformed bulge, Eq. (2.2) a tape provided with squares identical to those on the undeformed grid was used for the arc length (3), (4), (8). Wang and Shammamy (9) tilt the specimen so that the plane through two successive grid lines is nearly horizontal and measure the distance between them. This distance is taken to be the arc length increment (ds).

Having obtained states of strain along the bulge profile for various pressure, it is desirable to determine the stresses induced by the deformation so that the stress-strain relationship of the test material in bi-axial stretching can be deduced. Only a few investigators (4), (5), (8) have attempted to determine the stress-strain relationship of the test material subjected to the bulge test; but they have confined the determination only to balanced bi-axial stretching at the pole. In the work by Brown and Sachs (4), and Brown and Thompson (8), decisive stress (defined as twice the maximum shear stress) and decisive strain (defined as the maximum absolute natural strain) are used. Since the pole has zero prolateness (or N=1), the decisive stress is simply the meridional tangential stress and the decisive strain is the through-thickness strain. Mellor (5), however, uses the root-mean-square shear stress and natural strain analogue proposed by Swift (29) as the representing stress and strain.

As seen in Eqs. (2.8) and (2.9), stress calculation should involve the accurate measurement of the bulge contour. The generally accepted method for contour measurement, proposed by Brown and Sachs (4), is to measure the radial (r) and vertical (d) distances of a point on the bulge and, neglecting any deviation of the arc from a circle (passing through the pole and that point) of centre along the line of symmetry of the bulge, the radius of curvature for the circle can easily be shown to be

$$\rho = \frac{r^2 + d^2}{2d} \qquad (4.1)$$

On repeating for several points along the bulge, the polar curvature is obtained by extrapolation. Results on the computed curvature by Eq. (4.1) reveal that the entire bulge does not have a constant curvature for each stage of deformation (e.g. Fig. 5

of ref. 4). It will be shown in Chapter (8.D) that the true circumferential radius of curvature (ρ_θ) is always greater than the radius of curvature calculated from Eq. (4.1). Furthermore, the use of this method assumes zero prolateness (or N=1) and hence balanced bi-axial stretching at everywhere along the deformed shell. This assumption has been shown in Chapter (3.C) to violate the mechanical constraints in a real specimen. Therefore, the stress-strain relationship based on the bulge contour from Eq. (4.1) can at best represent only the work-hardening characteristics for balanced bi-axial stretching at the pole where the extrapolated curvature is the true curvature. Any data of work-hardening characteristics on positions other than the pole is erroneous because the true curvature of the bulge is not determined accurately.

(B) Theoretical investigations

While experimental investigation on the bulge test are performed, attempts to predict the material behaviour for this process gradually takes place (2), (6), (7), (10)-(15). Two types of theoretical prediction can be classified. The first type belongs to the special solution in which the bulge shape and particle trajectories are assumed before stresses and strains are predicted for successive polar heights (2), (10)-(13). The second type of prediction is referred to as numerical solution in which displacements and shapes of the bulge for various polar heights are predicted by iteration techniques on a computer (6), (7), (14), (15). Whether by special or numerical solution the general line of approach on the prediction is the same. Thus, this section is devoted to summarise the approach of different investigators.

An attempt to generalise the bulge test for material behaviour and instability was made in Chapter 2, but the equations are too complex to solve so that a spherical solution for special bulges is deduced.

(i) Mechanical behaviour

As seen from the analysis in Chapter 2, there are certain relationships and equations which hold true for all bulge tests, and they can be divided into three groups:

(a) the kinematic relationships between displacement and shapes on the one hand, and strains and strain rates on the other, Eqs. (2.1) to (2.6), (2.11) to (2.18).

(b) the equations which relate the specimen shape and the hydraulic pressure with the stresses, Eqs. (2.7) to (2.9).

(c) the stress-strain relationship, or work-hardening characteristics of the material, Eq. (2.27).

All research papers on this topic having a sound theoretical basis start, without exception, from the first two groups of equations, called sometimes 'constitutive equations', and aim at predicting, in various degree, the shapes of the bulge or the strain distributions in it, or both.

The kinematic relationships and the equilibrium equations alone, cannot, however, lead to a unique prediction of the shape and strain distributions. Therefore, between the 'constitutive equations' and the prediction of empirical results, some assumed or empirical data have to be introduced. The research papers on this subject differ from one another mainly in the type and extent of the assumed or empirical data introduced, and also in the type of predicted results obtained.

Moreover, for the 'constitutive equations', two types of approach, total strain theory and incremental strain theory, are used. The former is based on the Hencky-Mises flow rule in that states of plastic strains are proportional to the change of state of deviatoric stress. This theory is later superseded by the incremental strain theory which assumes that the deviatoric stresses affect only plastic strain increments. This incremental strain theory offers an advantage over the total strain theory in that it is more general and also applicable to curved strain paths.

Apart from neglecting bending stress at the die edge and through-thickness stresses, all investigators having special Solutions assume spherical bulges so that at everywhere along the bulge, the material is subjected to balanced bi-axial stretching and the two principal radii of curvature are equal (2), (10)-(13). From then on, Hill (10) assumes the material particles have circular trajectories along the entire bulge at different pressures. Ross and Prager (12) assumes constant wall thickness throughout the bulge for each stage of deformation; Chakrabarty and Alexander (2) and Gleyzal (11) assume parabolic strain distributions.

For numerical solutions (6), (7), (13)-(15), a computer is used to predict the bulge behaviour. All of them arbitrarily assume values of ε_s and ε_θ along the profile for various pressures to initiate the iteration process of the 'constitutive equations'. The iteration is terminated when the calculated (or predicted) solution satisfies the equilibrium equation along the tangential direction of the bulge,

$$\frac{d(t\sigma_s)}{d\phi} = \left(\frac{\sigma_\theta - \sigma_s}{\tan\phi}\right)t \qquad (4.2)$$

For successive increments, it is necessary to know the work-hardening characteristics of the material. Except Ross and Prager (12) and Chakrabarty and Alexander (2) who use the Tresca criterion, and its associated flow rule, all other investigators use the Mises yield criterion. Furthermore, most investigators use the generalised stress-strain relationship in the uniaxial tension test (2), (6)-(15). Hill (10), Ross and Prager (12), and Chakrabarty and Alexander (2) further assume the equivalent strain as the absolute value of the through-thickness strain. The experimental data for stresses and strains in the tension test is fitted by an equation, generally accepted to be of the form

$$\bar{\sigma} = Y + A\bar{\varepsilon}^n$$

or

$$\bar{\sigma} = Y\bar{\varepsilon}^n$$

and

$$\bar{\sigma} = \frac{1}{\sqrt{2}}\sqrt{(\sigma_1-\sigma_2)^2+(\sigma_2-\sigma_3)^2+(\sigma_3-\sigma_1)^2}$$

$$\bar{\varepsilon} = \sqrt{\frac{2}{9}}\sqrt{(\varepsilon_1-\varepsilon_2)^2+(\varepsilon_2-\varepsilon_3)^2+(\varepsilon_3-\varepsilon_1)^2} \qquad (4.3)$$

where, $\bar{\sigma}$ and $\bar{\varepsilon}$ are the equivalent stress and strain; Y is the initial yield stress and A and n are the work-hardening constant and exponent in the uniaxial tension test.

Hill (10) besides using non-hardening materials, also assumes a linearly hardening material. Ross and Prager (12) also use a linear work-hardening equation. Gleyzal (11) and Weil and Newmark (6) use the octahedral shear stress-strain relationship instead of the actual generalised stress-strain relationship although both the octahedral and generalised values are, by definition, different only by a constant.

Except Wang and Shammamy (14) and Kular and The (7) who attempt anisotropic materials, all other research papers deal with isotropic hardening materials. A summary of the procedure of all investigators discussed above is shown in Table (4.1) at the end of this Chapter. The classification is in accordance to the type of strain theory used and to the year as well. The instability section on Table (4.1) includes those authors whose main line of approach is on the instability of the bulge test. Various authors such as Hill (10) and Woo (15) have contributed some information to the instability aspect, but are classified into the predictive sections in Table (4.1) because their main considerations are in the predictive aspect of the bulge test. In Table (4.1), column I indicates the name of authors and the year of publications. Columns II and III refer to the material behaviour. Column IV is added in order to show the polar strain at instability. Column V gives the main assumptions for the theoretical results.

From Table (4.1), some comments on the individual investigator can be made. Gleyzal (11) using engineering strains for the entire analysis, limits his solution only to small strains up to $\frac{H}{a} = 0.3$. Both he and Chakrabarty and Alexander (2), who assume parabolic strain distributions, show scattering results as pressure increases. Weil and Newmark, extending Gleyzal's work and use natural strain and a computer to obtain a numerical solution, show close correlation of theory with experiment (6) in strains. Chakrabarty and Alexander's analysis (2) has a serious draw-back for the general solution - Eqs. (18) and (19) in ref. (2) - and strain distribution near the pole - Eqs. (25), (30) and (31) in ref. (2) -. They have constantly used the geometrical properties of a spherical bulge in which the principal radii of curvature and the two principal stresses must be equal so that $\varepsilon_s = \varepsilon_\theta = -\frac{1}{2}\varepsilon_t$. However, for their solutions, the equations for ε_s and ε_θ are not identical and hence all derivations that lead to the equation for ε_s and ε_θ violate the condition of sphericality. Ross and Prager's spherical and uniform wall thickness bulges (12) are unrealistic, though mathematically convenient, if we consider the membrane stress which becomes, on these assumptions, a uniform stress distribution throughout the bulge profile for a pressure P. If this is true, then fracture must occur at the die edge and also the solution violates the flow rule. In actual case, fracture usually occurs at the vicinity of the pole.

It can readily be seen from Table (4.1) that a fundamental restriction on the theoretical analysis of the bulge test is the assumption of spherical bulges because, as discussed in Chapter (3.C), an actual bulge can never be a surface of constant N ($\equiv \rho_\theta / \rho_s$) value let alone a sphere of N=1 (the simplest of constant N surfaces).

To the view of the present author, it is worthwhile to select a representative work on the predictive theory of the bulge test among those listed in Table (4.1), say by Hill (10), and study the analysis in detail as representative of many of the past papers on predictive theories. Hill's solution can be reviewed in the following sections:

(1) Main assumptions

(2) Constitutive equations

(3) Stress-strain relationship

(4) Instability and

(5) Predicted results

(1) Main assumptions

The test material is assumed to be isotropic and the bulge profile to be spherical for every stage of deformation. Furthermore, all material particles in the test specimen describe circular paths that are orthogonal to the momentary profile.

(2) Constitutive equations

As seen earlier, the constitutive equations comprise of two groups: (a) the kinematic relations between displacement, and shapes on the one hand and strains and strain rates on the other hand, and, (b) the equilibrium equation for stresses. For a spherical bulge, the material at everywhere along the profile is subjected to balanced bi-axial stretching. Therefore, with circular particle trajectories, the displacement equation can easily be shown to be

$$r = r_o\left(1 + \frac{H}{a^2}\iota\right) \qquad (4.4)$$

and

$$\iota = \frac{(a^2 - r_o^2)\,H\,a^2}{a^4 + r_o^2\,H^2}$$

where r and r_o are, respectively, the current and original radii; H and a are the polar height and die hole radius respectively; and ι is the axial displacement of the specimen at r_o. Thus, Eq. (4.4) gives the new coordinate (r, ι) of any material particle after deformation to a polar height of H from an original coordinate $(r_o, 0)$. As for the relationship between displacement and shape for a spherical bulge, it can easily be deduced that the radius of curvature (ρ) is

$$\rho = \frac{a^2 + H^2}{2H} \tag{4.5}$$

The circumferential strain of any material particle having a coordinate $(r_o, 0)$ transformed to (r, ι) can be calculated from the first of Eq. (4.4) so that

$$\varepsilon_\theta = \log_e\left(1 + \frac{H\iota}{a^2}\right) \tag{4.6}$$

For a spherical bulge, the incompressibility condition of metals together with Eq. (4.6) are sufficient to determine the state of strain. Thus,

$$\varepsilon_t = -2\varepsilon_s = -2\varepsilon_\theta = -2\log_e\left(1 + \frac{H\iota}{a^2}\right) \tag{4.7}$$

The balanced bi-axial stresses for Hill's bulge can be calculated through the stress equation shown in Eq. (2.8),

$$\begin{aligned} \sigma &= \frac{P}{2t}\rho \\ &= \frac{P}{2t}\left(\frac{a^2 + H^2}{2H}\right) \end{aligned} \tag{4.8}$$

where P and t are the oil pressure and through-thickness of the bulge respectively.

Under the assumption of spherical bulges and circular particle trajectories, the displacement and hence state of strain of any material particle originally at $(r_o, 0)$ for any value of polar height (H) can be determined from Eqs. (4.4) to (4.7). The magnitude of the stress, however, cannot be calculated because of the pressure term, Eq. (4.8). Therefore, in order that the stresses be soluble, the relationship between pressure and polar height must be known.

(3) Stress-strain relationship

This relationship defines the work-hardening characteristics of the material subjected to the bulge test. In the special solution by Hill for non-hardening materials, the specimen deforms under a constant load (σt). Thus,

$$\sigma t = \text{constant} \tag{4.9}$$

Furthermore, if the material of original thickness (t_o) begins to yield when the stress in the virgin material reaches σ_o in balanced bi-axial stretching, then Eq. (4.9) requires that

$$t\sigma = t_o\sigma_o$$

or

$$\sigma = \sigma_o \exp(-\bar{\varepsilon}) \tag{4.10}$$

where $\bar{\varepsilon}$ is the effective strain which is $\log_e (\frac{t}{to})$ for balanced bi-axial stretching so that the stress becomes determinate.

For linear hardening materials, Hill assumes

$$\sigma = (1 - A\bar{\varepsilon})\ \sigma_o \tag{4.11}$$

where A is a non-dimensional constant of order unity and σ_o is the initial yield stress in balanced bi-axial stretching. Thus, for any given strain, the corresponding flow stress can be calculated from Eq. (4.11). On substituting Eq. (4.11) into Eq. (4.8), and simplifying,

$$P = 4t_o e^{\bar{\varepsilon}} \left(\frac{H}{a^2 + H^2}\right)(1 - A\bar{\varepsilon})\sigma_o \tag{4.12}$$

Eq. (4.12) shows that the pressure required to deform a specimen to a polar height of H can be predicted. To calculate the pressure from Eq. (4.12), it is necessary to know the constants H, to, A and σ_o . In addition, a material particle originated at $(r_o, 0)$ has to be assigned in order to calculate the effective strain in Eq. (4.12) through Eqs. (4.4) to (4.7). The location of the material particle $(r_o, 0)$ is arbitrary except at the pole since the pressure under the specimen is uniform for any stage of deformation and the bulge profile is spherical.

Hill considers Eq. (4.12) as too complicated and assumes further that $(^H/_a)^2$ is negligible and the profile inclination (ϕ) as small so that $\sin\phi = \phi$. In so doing, the bulge profile becomes a paraboloid (P. 1140) on Hill's paper) and therefore contradicts the assumptions and hence the method of analysis. Moreover, his solution is suitable only to small deformations.

Based on the assumptions of spherical bulges and circular particle trajectories during deformation, the location of every material particle, (r, ι), should not be affected by the work-hardening characteristics of the test material. The only parameter that is influenced by the hardening characteristics is the stress term, Eq. (4.11). Thus, Hill's results - Eqs. (21) to (31) in his paper - contradict his original assumptions.

(4) Instability

The maximum pressure criterion is used for analysing the instability aspect. Hill's line of approach for a spherical bulge can be obtained by placing $\rho_\theta / \rho_s = 1$ into the general equation, Eq. (2.28). Thus, on simplifying,

$$\frac{1}{\sigma}\frac{d\sigma}{d\bar{\varepsilon}} - \frac{1}{\rho}\frac{d\rho}{d\bar{\varepsilon}} + 1 = 0 \qquad (4.13)$$

The polar strain at instability can then be solved for by fitting the stress-strain curve to $\sigma = A\,\bar{\varepsilon}^n$. Theoretical values of polar strain at instability for different work-hardening exponents are shown in Fig. (12.1).

(5) Comparison of predicted and actual results

The predicted results of Hill (10) are shown from time to time in Chapters (8) to (12) in order to compare with actual test results. It can be seen that Hill's solution is far from reality.

(C) Stress-strain relationship

It is evident that the stress-strain relationship of the material is required for theoretical analysis of the bulge test. The stress system in the bulge test, unfortunately, is much more complicated than that in the uniaxial tension test because states of stress/strain, rather than a significant stress/strain are used. In order to represent the change of states of strain corresponding to the change of states of stress with a scalar function, the generalised stress-strain relationship is unanimously used by past investigations. The definitions of generalised stress and strains are discussed in Chapter 6.

Of the many existing tests for stress-strain relationships in metals (16)-(26), the uniaxial tension is frequently used. This test to determine the stress-strain relationship is limited only to a stress condition of $\sigma_1 : \sigma_2 : \sigma_3 = 1 : 0 : 0$ (strain ratio $\varepsilon_1 : \varepsilon_2 : \varepsilon_3 = -2 : 1 : 1$). Kaftanoglu and Alexander (30) use a plane compression test after the specimen is prestrained by tension to approximately 40% longitudinal strain. Another method frequently used is Ford's cold rolling technique (25) although his original work is for plane strain problems in cold rolling processes. Watts and Ford (26) then extended this method for the yield stress-strain curves of materials. In this method a strip is cut from a slab rolled to a certain reduction in thickness and then subjected to the tension or compression test till the material just begins to deform plastically. With continual reduction of slab thickness followed by either the tensile or compression test, a mean curve can be drawn to represent the yield stress-strain curve. His assumption is that elongation in the tensile (or compressive) test produces the same work-hardening as the equivalent elongation by rolling. However, experimental results show the invalidity of his assumptions and that a number of small passes give a greater amount of work-hardening than a single pass of the same total amount. The crucial draw-back of this method is different amount of pre-straining gives different stress-strain relationship and consequently it is difficult to know the exact amount of pre-strain to give comparable results in actual sheet metal forming processes.

Table (4.1) shows that, in predictive papers on the bulge test, the uniaxial tension test is unanimously used. Thus, this test is equivalent to a balanced bi-axial tension test and therefore, is valid for a spherical bulge. In actual case, however, the bulge cannot be a sphere (Chapter 3.C) so that the stress-strain relationship of a material in the uniaxial tension test can no longer be applicable to the unbalanced bi-axial stretching case in the bulge test. Therefore, the only condition when the uniaxial tension test result be applicable to the bulge test is at the pole of the shell.

(D) Assumed stress-strain relationship

The difficulty encountered in fitting the stress-strain data obtained from any test mentioned in the previous section to a single equation is that the experimental curve represents at least two different modes of mechanical behaviour, the linear and non-linear functions, representing elastic and in-elastic deformation respectively. Nevertheless, many formulae have been proposed (27) to describe the work-hardening characteristics. The commonest formula used presently is the parabolic equation for generalised stress-strain relation, Eq. (4.3).

As seen in Table (4.1), the work-hardening characteristics of the material in the bulge test is assumed to be equivalent to that in the uniaxial tension test for predictive papers (2), (6), (7)-(15). The basic assumptions of the tension test used are the coaxiality and radiality of the strain paths. Only in axisymmetrical forming are the strain paths coaxial in which the principal axes do not rotate with respect to the material. A strain path is said to be radial when the strain ratio $\varepsilon_t : \varepsilon_\theta : \varepsilon_s$ remains constant during deformation. In an axisymmetrical bulge test, the strain path at the pole of the shell is always radial having a strain ratio $\varepsilon_t : \varepsilon_\theta : \varepsilon_s = -2 : 1 : 1$. When there is no draw-in of the flange, the strain ratio at the die edge is always $\varepsilon_t : \varepsilon_\theta : \varepsilon_s = -1 : 0 : 1$. However, at everywhere between the pole and die edge, the strain paths are not radial (Chapter 10.B). Thus, the stress-strain relationship in the bulge test must be of the form:

$$\bar{\sigma} = F\left(\int d\bar{\varepsilon}\right) \tag{4.14}$$

where $\int d\bar{\varepsilon}$ represents the length of the strain path. For radial strain paths, Eq. (4.14) becomes

$$\bar{\sigma} = F(\bar{\varepsilon}) \tag{4.15}$$

where $\bar{\varepsilon}$ is the effective strain defined in Eq. (4.3). It may then be seen that only in radial strain paths for an axisymmetrical process are the length of the strain paths be equal to effective strains. In this case, either the total or incremental strains theory can be used. As a result, none of the stress-strain relationships used in the predictive theory of the bulge test can be truely representative of the work-hardening characteristics in the actual forming process. A clear account on the effective strain and length of strain paths is given in Chapter (6.A).

(E) Instability

The approach, based on Sachs and Lubahn (28) shown in Chapter (2.F) for any axisymmetrical bulge shape, is to obtain the stress and strain condition for maximum pressure from membrane stress equation, Eq. (2.9). For the special case of spherical bulge, Eq. (2.9) is reduced to Eq. (4.13) as

$$\frac{d(\log_e \sigma)}{d\bar{\varepsilon}} = \frac{d(\log_e \rho)}{d\bar{\varepsilon}} - 1 \tag{4.16}$$

This equation for instability for spherical bulge, Eq. (4.16) is easily soluble by graphical technique in which the point of intersection of the two functions:

$$\frac{d(\log_e \sigma)}{d\bar{\varepsilon}} \quad \text{and} \quad \frac{d(\log_e \rho)}{d\bar{\varepsilon}} - 1$$

plotted against the absolute thickness strain at the pole gives the instability polar strain, Fig. (4.1). As seen from Table (4.1), those with special solutions assume spherical bulge formation so that Eq. (4.16) is obtained automatically. Whereas those papers with numerical solutions (6), (13), (14) have all regarded instability to occur at the pole where balanced bi-axial stretching exists so that Eq. (4.16) still applies. From then on, minor variations of prediction occur. Weil and Newmark (6) use the octahedral shear stress and strain at the pole; Hill (10) and others make use of the work-hardening exponent, n , into the instability equation so that the polar strain at instability is expressed as a function of n ; Wang and Shammamy (14) further introduce the anisotropic factor R into consideration; Ross and Prager (12) obtain their instability solution through constant wall thickness for each stage of deformation and find the polar height at instability to be $1/\sqrt{3}$ of die hole radius. Instability on Hill's (10) non work-hardening material occurs when the bulge becomes a hemisphere. Theoretical results of various authors are replotted in Fig. (12.1), to compare with the theoretical uniaxial tension test results.

Kaftanoglu and Alexander (30) have proposed another criterion of instability - strain propagation criterion and Kaftanoglu (31) applies this criterion onto the bulge test. Instability is said to occur when the strains cannot transmit to neighbouring position of the material so that localised necking occurs. In order to find the onset of instability by this criterion, a computer program in a step-by-step manner is used until the stress equilibrium equation cannot be satisfed. The theoretical instability strain by the strain propagation criterion is close to, or even identical to, that by the maximum pressure criterion in the bulge test - Table (1) of ref. (31).

(F) Concluding remarks and objectives

From the above brief review of the vast work on the subject of bulge test over the past two decades, it can easily be observed that studies on this particular type of process has hitherto been almost exclusively confined to predicting the behaviour of the bulged specimen through assumed or empirical work-hardening characteristics of the material as determined in the tension test, as well as through assumed spherical bulge shape and strain distribution. Even on measuring the contour of the bulge, the shape of the bulge is assumed to be close to a sphere. The use of generalised stress-strain relationship is restricted only to radial strain paths in axisymmetrical bulge test. In the actual case, there are no theoretical grounds to say that the strain ratios are constant throughout the process.

In the present study the approach is reversed; the stresses and strains in the specimen are measured and determined through the geometry of the bulge (Chapters 8 to 10). Thus, the bulge test can be used for determining the stress-strain relationship in the material under actual conditions in sheet metal forming processes (Chapter 11).

The test material has been considered to become unstable when the oil pressure reaches a maximum value. Under this criterion, mild steel will not have an instability point before fracture since a turning point does not exist in the pressure growth curve. Chapter 12 is an attempt to identify when the test material just becomes unstable before fracture takes place. This new concept of instability, to the opinion of the author, will be applicable to pressure growth curves without turning points.

Table (3.1). A summary of some important work on the bulge test

(I) Author	(II) Yield Criterion	(III) Stress/strain relation	(IV) Polar strain at instability	(V) Main assumptions
1. TOTAL STRAINS THEORY				
Gleyzal (11) 1948	Mises	$\tau = \tau(\gamma)$ in the uniaxial tension. τ, γ = shear stress and strain	–	1. Isotropic materials 2. Spherical bulge 3. Parabolic strain distribution 4. Engineering strains used 5. Absence of draw-in
Weil and Newmark (6) 1955	Hencky-Mises	$\tau = \tau(\gamma)$ in the uniaxial tension	$\frac{d\tau_o}{\tau_o d\gamma_o} - \frac{dR_o}{R_o d\gamma_o} = \frac{1}{\sqrt{2}}$	1. Extension of Gleyzal (11) 2. Maximum pressure for instability 3. Natural strains used 4. Numerical solution by a computer 5. Absence of draw-in
Storakers (13) 1966	Hencky-Mises	$\bar{\sigma} = Y \bar{\varepsilon}^n$ in uniaxial tension	$\frac{n}{\varepsilon_\theta} = \frac{1}{\rho} \frac{d\rho}{d\varepsilon_\theta} + 2$	1. Isotropic materials 2. Spherical bulge 3. Superposition of strains indicated by Hill(10) 4. Numerical solution by a computer 5. Maximum pressure for instability 6. Absence of draw-in
2. INCREMENTAL STRAIN THEORY				
Hill (10) 1950	Mises	(i) $\bar{\sigma} = Y \exp(-\bar{\varepsilon})$ (ii) $\frac{\bar{\sigma}}{Y} = 1 - A\bar{\varepsilon}$ in uniaxial tension	$\varepsilon_t = -\frac{4}{11}(1+2n)$	1. Isotropic materials 2. Spherical bulge 3. Trajectory of material particle is circular and momentarily perpendicular to specimen 4. Maximum pressure for instability 5. Absence of draw-in

Author	Yield Criterion	Stress/strain relation	Polar strain at instability	Main assumptions
Ross & Prager (12) 1954	Tresca	(i) $\bar{\sigma} = Y$ = const. (ii) $\bar{\sigma} = Y(1 - A\bar{\varepsilon})$ in uniaxial tension	$P\ max = \frac{3\sqrt{3}Yt}{4a}$ when $\theta = 60^\circ$ $\varepsilon_t = -0.3$	1. Isotropic material 2. Spherical bulge 3. Uniform wall thickness 4. Maximum pressure for instability 5. Absence of draw-in
Woo (15) 1964	Mises	$\bar{\sigma} = Y + A\bar{\varepsilon}^n$ in hydrostatic bulging (due to Mellor) and cold rolling	–	1. Isotropic material 2. Numerical solution by a computer 3. Stress-strain relationship by cold rolling is used for theoretical results 4. Total strains are used for calculation 5. Absence of draw-in
Wang & Shammamy (14) 1969	Mises	$\bar{\sigma} = Y\bar{\varepsilon}^n$ in uniaxial tension	$\left(\frac{2}{1+R}\right)^{\frac{1}{2}} - \frac{n}{\varepsilon_t} = \frac{1}{\rho}\frac{d\rho}{d\varepsilon_t}$	1. Anisotropic material 2. Compared incremental and total strain theory 3. Numerical solution by a computer 4. Maximum pressure for instability 5. Absence of draw-in
Chakrabarty & Alexander (2) 1970	Tresca and Mises	(i) $\bar{\sigma} = Y e^{\bar{\varepsilon}}$ $(\bar{\varepsilon} \equiv -\varepsilon_t)$ (ii) $\bar{\sigma} = Y\bar{\varepsilon}^n$ in uniaxial tension	$\varepsilon_t = -\frac{2(2-n)(1+2n)}{11-4n}$	1. Isotropic material 2. Spherical bulge 3. Parabolic strain distributions 4. Introduce a parameter λ to generalise sdns.of Ross & Prager and Hill 5. Absence of draw-in
Kular & The (7) 1972	Mises	$\bar{\sigma} = Y\bar{\varepsilon}^n$ in uniaxial tension test	–	1. Anisotropic material 2. Absence of draw-in of flange 3. Spherical arc for contour measurement
3. Instability				
Sachs & Lubahn (28) 1946			$\frac{1}{\sigma_s}\frac{d\sigma_s}{d\varepsilon_t} - \frac{d\rho}{\rho d\varepsilon_t} + 1 = 0$	1. Isotropic material 2. Maximum pressure criterion

Author	Yield Criterion	Stress/strain relation	Polar strain at instability	Main assumptions
Brown & Sachs (4) 1948 Brown & Thompson (8) 1949	Modified maximum shear	$\sigma_s = \sigma_s(\varepsilon_t)$ in uniaxial tension test	$\frac{d\sigma_s}{\sigma_s d\varepsilon_t} - \frac{d\rho}{\rho d\varepsilon_t} + 1 = 0$	1. Isotropic material 2. Maximum pressure criterion 3. Spherical arc for contour measurement
Swift (29) 1952	Mises	(i) $q = c(a+\psi)^n$ $q \equiv$ representative rms shear stress $\psi \equiv$ rep. rms angular strain (ii) $\bar{\sigma} = Y\bar{\varepsilon}^n$ in uniaxial tension	$\varepsilon_t = -\frac{1}{2}(\frac{33}{10} + n - (\frac{729}{100} - \frac{3}{5}n + n^2)^{1/2})$ based on (ii)	1. Isotropic material 2. Maximum pressure criterion 3. Radial stress and strain paths
Mellor (5) 1956	Mises	$q = c\ (a+\psi)^n$ in cold rolling	$\frac{d\sigma_s}{\sigma_s d\varepsilon_t} - \frac{d\rho}{\rho d\varepsilon_t} + 1 = 0$	1. Isotropic material 2. Maximum pressure criterion 3. Spherical arc for contour measurement
Kaftanoglu (31) 1972	Mises	$\bar{\sigma} = (\frac{3(R+1)}{2(R+2)})^{1/2} A \cdot$ $(B + (\frac{3(R+1)}{2(R+2)})^{1/2} \bar{\varepsilon})^n$		1. Anisotropic material 2. Strain propagation criterion 3. Numerical solution by a computer

Chapter 5

DEFINITIONS

Some of the concepts involving both the bulge test and plasticity theory have already been introduced in earlier chapters. Since an important portion of this project is to deal with the theory of plastic bulging of sheet metal under fluid pressure in depth, it is considered necessary to devote this chapter to discussing some fundamental concepts used in this project.

(A) Hydrostatic and deviatoric stresses

Stress has frequently been defined as force per unit area as put forward by the Cauchy stress principal. A more rigid definition, however, is that stress is an operator transforming a surface area into force by the following equation:

$$\begin{vmatrix} dF_1 \\ dF_2 \\ dF_3 \end{vmatrix} = \begin{vmatrix} \sigma_{11} & \sigma_{12} & \sigma_{13} \\ \sigma_{21} & \sigma_{22} & \sigma_{23} \\ \sigma_{31} & \sigma_{32} & \sigma_{33} \end{vmatrix} \cdot \begin{vmatrix} dA_1 \\ dA_2 \\ dA_3 \end{vmatrix} \qquad (5.1)$$

where the column matrices dF_i and dA_i are respectively the force and area vectors. Thus, the 3 x 3 matrix σ_{ij} is the stress matrix connecting force to area. The diagonal elements in this stress matrix are the normal stresses and the non-diagonal represents shear stresses. Since the resultant force and moment acting on an arbitrary volume of a continuum subjected to a system of forces dF_i and body forces (including inertia forces, if present) is zero for equilibrium, it can easily be shown that the stress matrix σ_{ij} is symmetrical and is

$$\begin{vmatrix} \sigma_{11} & \sigma_{12} & \sigma_{13} \\ \sigma_{12} & \sigma_{22} & \sigma_{23} \\ \sigma_{13} & \sigma_{23} & \sigma_{33} \end{vmatrix} \qquad (5.2)$$

If the triaxial coordinate axes for the stress matrix in Eq. (5.2) are chosen so that the shear stresses vanish, then these three orthogonal axes represent the principal directions of the triaxial stress. Simultaneously, any triaxial state of stress can readily be denoted by a point in this stress space with $\sigma_1 \underset{\sim}{i}$, $\sigma_2 \underset{\sim}{j}$, $\sigma_3 \underset{\sim}{k}$ as three mutually perpendicular axes representing the scalar principal stresses. Thus, the stress matrix in Eq. (5.2) becomes

$$\begin{vmatrix} \sigma_1 & 0 & 0 \\ 0 & \sigma_2 & 0 \\ 0 & 0 & \sigma_3 \end{vmatrix} \qquad (5.3)$$

and any position vector in this space is the stress vector written mathematically as

$$\underset{\sim}{\sigma} = \sigma_1 \underset{\sim}{i} + \sigma_2 \underset{\sim}{j} + \sigma_3 \underset{\sim}{k}$$

or in matrix form,

$$\begin{vmatrix} \underset{\sim}{\sigma}_1 \\ \underset{\sim}{\sigma}_2 \\ \underset{\sim}{\sigma}_3 \end{vmatrix} = \begin{vmatrix} \sigma_1 & 0 & 0 \\ 0 & \sigma_2 & 0 \\ 0 & 0 & \sigma_3 \end{vmatrix} \cdot \begin{vmatrix} \underset{\sim}{i} \\ \underset{\sim}{j} \\ \underset{\sim}{k} \end{vmatrix} \qquad (5.4)$$

It is often convenient to resolve the stress vector into two components of which one is the mean stress, that is,

$$\begin{vmatrix} \underset{\sim}{\sigma}_1 \\ \underset{\sim}{\sigma}_2 \\ \underset{\sim}{\sigma}_3 \end{vmatrix} \equiv \left[\begin{vmatrix} \frac{\sigma_1+\sigma_2+\sigma_3}{3} & 0 & 0 \\ 0 & \frac{\sigma_1+\sigma_2+\sigma_3}{3} & 0 \\ 0 & 0 & \frac{\sigma_1+\sigma_2+\sigma_3}{3} \end{vmatrix} + \begin{vmatrix} \frac{2\sigma_1-\sigma_2-\sigma_3}{3} & 0 & 0 \\ 0 & \frac{-\sigma_1+2\sigma_2-\sigma_3}{3} & 0 \\ 0 & 0 & \frac{-\sigma_1-\sigma_2+2\sigma_3}{3} \end{vmatrix} \right] \begin{vmatrix} \underset{\sim}{i} \\ \underset{\sim}{j} \\ \underset{\sim}{k} \end{vmatrix} \qquad (5.5)$$

$$\equiv \left[\begin{vmatrix} \sigma_0 & 0 & 0 \\ 0 & \sigma_0 & 0 \\ 0 & 0 & \sigma_0 \end{vmatrix} + \begin{vmatrix} \sigma_1' & 0 & 0 \\ 0 & \sigma_2' & 0 \\ 0 & 0 & \sigma_3' \end{vmatrix} \right] \cdot \begin{vmatrix} \underset{\sim}{i} \\ \underset{\sim}{j} \\ \underset{\sim}{k} \end{vmatrix} \qquad (5.6)$$

The mean stress, σ_0, is also termed the hydrostatic stress and σ_1', σ_2', σ_3' are the deviatoric or reduced stresses. It is well known that a moderate hydrostatic pressure or tension, either applied alone or superposed on some state of combined stress does not affect yielding of the material to the first approximation (35). This means that hydrostatic stresses produce only elastic dilation and is recoverable on removal of the stress. It follows, therefore, plastic deformation can only occur by the action of deviatoric stresses. The Mohr circles for stress (σ_1, σ_2, σ_3) can also be used to find the deviatoric stresses. In Fig. (5.1), the vertical axis is displaced by σ_0 to be the new axis.

The hydrostatic stress in Eq. (5.6) is readily seen to have direction cosines $\left(\frac{1}{\sqrt{3}}, \frac{1}{\sqrt{3}}, \frac{1}{\sqrt{3}}\right)$ with the principal axes and, can be viewed geometrically as along an axis passing through the origin of the vector space and making equal angles with the axes $\sigma_1\underset{\sim}{i}$, $\sigma_2\underset{\sim}{j}$, $\sigma_3\underset{\sim}{k}$. This axis is the hydrostatic axis. The deviatoric stress component can also be shown to lie in the π-plane of equation $\sigma_1 + \sigma_2 + \sigma_3 = 0$. Fig. (5.2) shows the deviatoric and hydrostatic components of a space vector.

It will be shown in Chapter 6 that a triangular coordinate system could be deviced to represent states of deviatoric stresses with three axes, 120° apart in the π-plane. This property will be used in the experimental stress analysis in this project

(B) Postyield behaviour of work materials

In the study of mechanical behaviour of material in their plastic region, two sectors in the theory of plasticity are considered. One is associated with the strength of the material, or how plastic strains correspond to stress increments. The other is the law relating the flow of the material at any instant under any given set of stress. Both these aspects have long been discussed in numerous texts and research papers (16)-(23), and, therefore, only the basic concepts are discussed in this section.

A test material is said to have reached its yield condition under a given set of loading function when an infinitesimal increment of the loading function produces a plastic deformation, which, unlike elastic deformation, is unrecoverable on removal of the applied load. The strength of the material in the plastic zone then requires studies on yield criteria as well as their subsequent changes. Of the various yield criteria proposed, the Tresca and Mises criteria are reasonably simple mathematically and at the same time widely accepted by investigators.

(i) The Tresca yield criterion

This criterion states that yielding occurs when the maximum shear stress of an applied stress function reaches a certain value C. Mathematically, this criterion is

$$\frac{\sigma_1 - \sigma_3}{2} = C \qquad (5.7)$$

where $\sigma_1 > \sigma_2 > \sigma_3$ are the principal stresses.

If the yield stress, Y, in the simple tension test is related to the yield value C, then the maximum shear stress in simple tension test can be shown by Mohr stress circles, Fig. (5.3) to be $\frac{Y}{2}$. Therefore, Tresca's yield criterion becomes

$$\sigma_1 - \sigma_3 = Y \qquad (5.8)$$

or

$$\sigma_1' - \sigma_3' = Y$$

where σ_1' and σ_3' represent the deviatoric stresses.

It is also permissible to relate the yield stress, K, by a pure shear ($\sigma_i = -\sigma_j$, $\sigma_k = 0$) to the yield constant C in Eq. (5.7). Then the Mohr stress circles in Fig. (5.3) show that C equals K so that Eq. (5.7) becomes

$$\sigma_1 - \sigma_3 = 2K \qquad (5.9)$$

or

$$\sigma_1' - \sigma_3' = 2K$$

Thus, the Tresca yield locus, whether by the simple tension, Eq. (5.8), or pure shear test, Eq. (5.9), constitutes a hexagon in Cartesian coordinates. In the π-plane as described in section A of this chapter, the locus becomes a regular hexagon with the principal axes as the six corners, Fig. (5.4).

(ii) The Mises yield criterion

This criterion states that yielding occurs when the second deviatoric stress invariant reaches a specific value; and mathematically,

$$I_2' = C \qquad (5.10)$$

which, in terms of the principal stresses $\sigma_1, \sigma_2, \sigma_3$ takes the form

$$(\sigma_1 - \sigma_2)^2 + (\sigma_2 - \sigma_3)^2 + (\sigma_3 - \sigma_1)^2 = 6C \qquad (5.11)$$

Using yield stress, Y, in the simple tension test ($\sigma_1 = Y$, $\sigma_2 = \sigma_3 = 0$), the value of C in Eq. (5.11) is $\frac{1}{3}Y^2$ so that the

Mises yield criterion becomes

$$(\sigma_1 - \sigma_2)^2 + (\sigma_2 - \sigma_3)^2 + (\sigma_3 - \sigma_1)^2 = 2Y^2 \qquad (5.12)$$

or $$(\sigma_1' - \sigma_2')^2 + (\sigma_2' - \sigma_3')^2 + (\sigma_3' - \sigma_1')^2 = 2Y^2$$

and is an ellipse in Cartesian coordinates; or a circle in the π-plane of radius $\sqrt{\frac{2}{3}}\,Y$. With respect to the yield stress, K, in pure shear and by similar operation as the simple tension test, Eq. (5.11) takes the form

$$(\sigma_1 - \sigma_2)^2 + (\sigma_2 - \sigma_3)^2 + (\sigma_3 - \sigma_1)^2 = 6K^2 \qquad (5.13)$$

or $$(\sigma_1' - \sigma_2')^2 + (\sigma_2' - \sigma_3')^2 + (\sigma_3' - \sigma_1')^2 = 6K^2$$

so that the yield locus is a circle of radius $\sqrt{2}\,K$ in the π-plane. The Mises yield loci by two tests are shown in Fig. (5.5).

It is then permissible to compare the relative values of both the Tresca and Mises yield loci based either on the simple tension or pure shear test. It can readily be seen that, with reference to the simple tension test, the Mises circle of radius $\sqrt{\frac{2}{3}}\,Y$ circumscribes the regular Tresca hexagon; whilst, based on the yield stress K in pure shear, the Mises circle of radius $\sqrt{2}\,K$ is inscribed in the Tresca hexagon, Fig. (5.6).

Having discussed briefly the Tresca and Mises yield criteria, it may be possible to pursue the postyield behaviour of materials. Continual loading beyond the initial yield of the material leads to plastic deformation. Therefore the loading function can be generalised through the introduction of plastic strains, ε_{ij}, and work-hardening characteristics of the material, n, so that

$$F(\sigma_{ij}, \varepsilon_{ij}, n) = 0 \qquad (5.14)$$

Eq. (5.14) defines a loading surface that $F = 0$ is the yield surface; $F < 0$ is a surface in the elastic region (inside the yield surface) and $F > 0$ is outside the yield locus. On differentiating Eq. (5.14)

$$dF = \frac{\partial F}{\partial \sigma_{ij}} d\sigma_{ij} + \frac{\partial F}{\partial \varepsilon_{ij}} d\varepsilon_{ij} + \frac{\partial F}{\partial n} dn \qquad (5.15)$$

Thus, with $F = 0$ and $(\frac{\partial F}{\partial \sigma_{ij}})\, d\sigma_{ij} > 0$, loading occurs; $\frac{\partial F}{\partial \sigma_{ij}}\, d\sigma_{ij} < 0$ means unloading; and neutral loading occurs when $\frac{\partial F}{\partial \sigma_{ij}}\, d\sigma_{ij} = 0$. Also, for a non-hardening material, $dF = 0$ so that the yield surface remains unchanged during plastic deformation and the initial yield condition holds. In general, for hardening materials, $dF \neq 0$ and the size of the yield surfaces $F = 0$ is increased. For isotropic hardening, the material remains isotropic after deformation so that the yield surface simply increases its size and maintains its original shape. Thus, the Mises circles and Tresca hexagons for isotropic hardening are shown in Fig. (5.7).

The manner in which the plastic strains enter into Fig. (5.14) when loading occurs is governed by the hardening characteristics, n, of the material. Osgood (27) has reviewed 17 ways of expressing the stress-strain formulae of materials in the plastic range. All these equations involved the relationship of one significant stress with one significant strain. This offers no difficulty in simple loading functions, that is, uniaxial tension or compression test, because the significant stress is the magnitude of the applied stress, and the significant strain is along the applied stress. In complex stress systems, loading is done by the change of state of stress which produces change of state of plastic strain; and it becomes impossible to define the significant stress and strain magnitudes. Thus, the equations reviewed by Osgood (27) can no longer be valid in complex stress systems. Under such a system, the change of states can, physically and mathematically, be understood by introducing the terms generalised (or equivalent or effective) stress and strain. These terms can be viewed as the severity of the applied stresses and produced strains analogous to the significant stress and strain in the simple tension test. Mathematically, they are defined as,

$$\text{Effective stress, } \bar{\sigma} = \frac{1}{\sqrt{2}}((\sigma_1 - \sigma_2)^2+(\sigma_2 - \sigma_3)^2+(\sigma_3 - \sigma_1)^2)^{1/2}$$

$$= \sqrt{\frac{3}{2}}(\sigma_1^2 + \sigma_2^2 + \sigma_3^2)^{1/2} \qquad (5.16)$$

$$\text{Effective strain, } \bar{\varepsilon} = \sqrt{\frac{2}{3}}(\varepsilon_1^2 + \varepsilon_2^2 + \varepsilon_3^2)^{1/2} \qquad (5.17)$$

$$\sqrt{\frac{2}{9}}((\varepsilon_1 - \varepsilon_2)^2 + (\varepsilon_2 - \varepsilon_3)^2 + (\varepsilon_3 - \varepsilon_1)^2)^{1/2}$$

It will be shown in Chapter 6 that both the effective stress and strain are proportional to the radius of the Mises circle in the π-plane and hence proportional to the yield stress.

Using these terms, Hill (35) postulates that, for isotropic strain hardening materials, the change of yield surfaces conforms to either the work hardening or strain hardening hypothesis. The work hardening hypothesis postulates that the current yield surface depends only on the total plastic work, and for Mises yield criterion, the radius of the circle is a function of plastic work. Thus,

$$\bar{\sigma} = F(W_p) = F(\int \sigma_{ij}\, d\varepsilon_{ij}) \qquad (5.18)$$

The strain hardening hypothesis states that the hardening of material in the plastic range is a function of the amount of plastic strain, (ie), for Mises yield criterion,

$$\bar{\sigma} = F\left(\int d\bar{\varepsilon}\right)$$

where $$d\bar{\varepsilon} = \sqrt{\frac{2}{9}}\left((d\varepsilon_1 - d\varepsilon_2)^2 + (d\varepsilon_2 - d\varepsilon_3)^2 + (d\varepsilon_3 - d\varepsilon_1)^2\right)^{1/2} \tag{5.19}$$

= equivalent plastic strain increments

For coaxial and radial (constant strain ratios) strain paths,

$$\int d\bar{\varepsilon} = \bar{\varepsilon} = \sqrt{\frac{2}{3}}\left(\varepsilon_1^2 + \varepsilon_2^2 + \varepsilon_3^2\right)^{1/2} \tag{5.20}$$

and hence $$\bar{\sigma} = F(\bar{\varepsilon})$$

Eq. (5.20) is called the generalised stress-strain relationship of the material during plastic deformation and is widely used to represent the strength of the material. This also requires that only in radial and coaxial strain paths do the generalised relationship holds.

(iii) Flow rules

Having established the strength of the material in the plastic range, the flow of the material under any given state of stress is yet to be found. There are many proposed flow rules, of which, the commonest are due to Hencky and Levy - Mises (and Prandtl-Reuss).

Hencky, assuming small strains, states that the components of the total plastic strain is proportional to the corresponding deviatoric stress component through a scalar quantity λ, that is

$$\varepsilon_{ij} = \lambda \sigma'_{ij} \tag{5.21}$$

Drucker (36) has shown that this relationship is unsuitable on the complete plastic properties of materials. Although he comments on the inconsistencies of the flow rule being twofold, actually it could be summarised into a statement that plastic strains could occur during natural loading for Hencky flow rule. Moreover, this flow rule is applicable only to radial strain paths.

Hencky's flow rule can also be written in terms of principal shear stresses and strains,

$$\frac{\varepsilon_1 - \varepsilon_2}{\sigma_1 - \sigma_2} = \frac{\varepsilon_2 - \varepsilon_3}{\sigma_2 - \sigma_3} = \frac{\varepsilon_3 - \varepsilon_1}{\sigma_3 - \sigma_1} \qquad (5.22)$$

This relationship has been used by Lode who introduces the parameter

$$\mu = \frac{2\sigma_2 - \sigma_3 - \sigma_1}{\sigma_1 - \sigma_3} \qquad (5.23)$$

$$V = \frac{2\varepsilon_2 - \varepsilon_3 - \varepsilon_1}{\varepsilon_1 - \varepsilon_3}$$

It is evident that Eq. (5.23) leads to the conclusion that $\mu = V$ and that the Mohr circles for stresses and strains must be geometrically similar at any point and instant. Lode's results on combined tension and internal pressure; and Taylor and Quinney's combined tension-torsion tests all show that the two parameters are not equal and the degree of departure varies from material to material (22).

Eq. (5.21) can be expanded into the following equations,

$$(\varepsilon_1 - \varepsilon_2)^2 + (\varepsilon_2 - \varepsilon_3)^2 + (\varepsilon_3 - \varepsilon_1)^2$$

$$= \lambda((\sigma_1' - \sigma_2')^2 + (\sigma_2' - \sigma_3')^2 + (\sigma_3' - \sigma_1')^2)$$

$$\text{or,} \quad \lambda = \left(\frac{(\varepsilon_1 - \varepsilon_2)^2 + (\varepsilon_2 - \varepsilon_3)^2 + (\varepsilon_3 - \varepsilon_1)^2}{(\sigma_1' - \sigma_2')^2 + (\sigma_2' - \sigma_3')^2 + (\sigma_3' - \sigma_1')^2} \right)^{1/2} \qquad (5.24)$$

By using the definitions of effective stress and strain , we have

$$\lambda = \frac{3}{2} \cdot \frac{\bar{\varepsilon}}{\bar{\sigma}} \qquad (5.25)$$

so that Eq. (5.21) becomes

$$\frac{\varepsilon_{ij}}{\sigma'_{ij}} = \frac{3\,\bar{\varepsilon}}{2\,\bar{\sigma}} \qquad (5.26)$$

A more general approach to the postulation of flow rules in the plastic range is the incremental strain theory which takes into account of the strain history of the deforming material. Based on St. Venant's proposal of the principal axes of the strain-increment being coincident with the principal stress axes, Levy and Mises independently postulate that the total strain increment is related to the deviatoric stress components through the equation,

$$d\varepsilon_{ij} = \sigma'_{ij}\; d\lambda$$

$$(5.27)$$

or
$$\frac{d\varepsilon_1}{\sigma'_1} = \frac{d\varepsilon_2}{\sigma'_2} = \frac{d\varepsilon_3}{\sigma'_3} = d\lambda$$

in terms of principal values, and $d\lambda$ is a scalar factor of proportionality which is a function of the yield stress (hence effective stress) and the rate of hardening, that is

$$d\lambda = \frac{3}{2}\,\frac{d\bar{\varepsilon}}{\bar{\sigma}} \qquad (5.28)$$

and the Levy-Mises flow rule becomes

$$d\varepsilon_{ij} = \frac{3}{2}\,\frac{d\bar{\varepsilon}}{\bar{\sigma}}\,\sigma'_{ij} \qquad (5.29)$$

with plastic work done equals

$$W_p = \int \sigma_{ij}\; d\varepsilon = \int \bar{\sigma}\; d\bar{\varepsilon} \qquad (5.30)$$

The Levy-Mises flow rule is restricted to deformation where plastic strains are large compared to elastic strains such as those in sheet metal deformation. For processes like thick tubes under internal pressures, however, elastic strains have the same order of magnitude as plastic strains and the Levy-Mises flow rule no longer holds. Prandtl and Reuss then modify the flow rule to the form,

$$d\varepsilon_{ij} = \sigma'_{ij}\, d\lambda$$

or

$$\frac{d\varepsilon_1}{\sigma'_1} = \frac{d\varepsilon_2}{\sigma'_2} = \frac{d\varepsilon_3}{\sigma'_3} \qquad (5.31)$$

by considering the elastic strain tension following Hooke's law. In this equation, plastic strain tensor is used instead of total strain tensor in the Levy-Mises equation. Eq. (5.31) also requires that the Lode's variables for incremental strains must be equal, that is,

$$\mu = \nu$$

where

$$\mu = \frac{2\sigma_1 - \sigma_2 - \sigma_3}{\sigma_2 - \sigma_3} \qquad (5.32)$$

$$\nu = \frac{2d\varepsilon_1 - d\varepsilon_2 - d\varepsilon_3}{d\varepsilon_2 - d\varepsilon_3}$$

Chapter 6

GRAPHICAL REPRESENTATION OF MECHANICAL BEHAVIOUR OF METALS DURING PLASTIC DEFORMATIONS

In the tension or compression test, only one stress and one strain are normally considered significant and they are determined and plotted against each other in the stress-strain curve which is usually considered to represent the mechanical behaviour of the material. In more complex deformations, like those in sheet metal forming, states of stress rather than single stresses and states of strain rather than single strains are involved, and, when measured, they can no longer be plotted against each other in a single curve. Past investigators have frequently used the generalised stresses and strains in order to show metal behaviours by a single curve. This generalised stress-strain relationship is expressed in Chapter (4.D) as

$$\bar{\sigma} = F(\bar{\varepsilon}) \qquad (4.15)$$

where $\bar{\sigma} = \frac{1}{\sqrt{2}}\left((\sigma_1 - \sigma_2)^2 + (\sigma_2 - \sigma_3)^2 + (\sigma_3 - \sigma_1)^2\right)^{1/2}$

and $\bar{\varepsilon} = \sqrt{\frac{2}{9}}\left((\varepsilon_1 - \varepsilon_2)^2 + (\varepsilon_2 - \varepsilon_3)^2 + (\varepsilon_3 - \varepsilon_1)^2\right)^{1/2}$

In sheet metal forming, neither of the two assumptions (coaxiality and radiality of strain paths) for generalised stress -strain relationships is true. Therefore, the use of generalised stress-strain relationship is at best an approximation only. Only in axisymmetrical sheet metal forming are the strains coaxial, but not necessarily radial. Thus, in order to represent graphically the states of stress and strain for curved strain paths in axisymmetrical forming, a totally different type of graphical method must be used.

The graphical method which facilitates the exploration of triaxial stress-strain relationship is the triangular coordinate system. This system has been proposed independently by Marciniak (37) and Hsü (38), (39). Hsü has extensively applied this system to sheet metal forming processes with a rigid punch (40), (41). Therefore, only the fundamentals will be discussed in this section.

(A) Triangular coodinate system for strains

Three axes OI, OII and OIII are used in the triangular coordinate system and they are spaced at 120° to each other in a plane, Fig. (6.1). Thus, any position vector OP making an angle α (clockwise) with the OI-axis will have projections onto the three axes given by

$$\begin{aligned} (OI)p &= (OP)\cos\alpha \\ (OII)p &= (OP)\cos(240^\circ-\alpha) \\ (OIII)p &= (OP)\cos(120^\circ-\alpha) \end{aligned} \qquad (6.1)$$

The addition of the component vectors in Eq. (6.1) can easily be shown to have a zero value.

Metals under large deformations may be considered to be incompressible. By equating the volume of a unit cube before and after deformation, and using natural strains, the three principal strains add up to zero; that is,

$$\varepsilon_1 + \varepsilon_2 + \varepsilon_3 = 0 \qquad (6.2)$$

or

$$\varepsilon_t + \varepsilon_s + \varepsilon_\theta = 0$$

where ε_t, ε_s and ε_θ are the principal strains involved in the bulge test and represent the through-thickness, meridional tangential and circumferential strains respectively. By comparing Eqs. (6.1) and (6.2), it is obvious that these three axes in the coordinate system can adequately be used to represent the three principal (natural) strains so that a point in the coordinate system shows the state of strain at some stage of deformation.

Assignment of each axis to a particular principal strain is arbitrary so that it becomes advantageous to adopt a standard choice of coordinates. Of the six different ways of assigning them, Hsü (38), (39) suggests the vertical axis to denote the through-thickness strain since sheet metal engineers are often interested in the through-thickness of materials during deformation; and psychologically, the vertical axis is the most prominant of the three. In most axisymmetrical sheet metal forming, the meridional tangential strain is always tensile whilst the circumferential strain falls on both the positive and negative region of the ε_θ-axis depending on the condition of draw-in of the flange. Thus, in order to suit right-handed people by having most of the strain paths falling on the right-hand side of the ε_t-axis, Hsü further suggests the ε_θ- and ε_s-axis to be on the left- and right-hand side of the ε_t-axis respectively. The choice of the coordinate axis in this thesis will follow that proposed by Hsü and is shown in Fig. (6.2).

Using the sign conventions shown in Fig. (6.2), it is obvious that points on the three axes, together with their backward extensions, represent states of strain given by

$$\varepsilon_i = \varepsilon_j = -\frac{\varepsilon_k}{2} \qquad (i, j, k = t, \theta, s) \qquad (6.3)$$

These are the states of strain involved in both uniaxial tension and compression tests for isotropic materials. Thus, the strain paths for uniaxial tension tests will follow the positive axes and those for compression tests will follow the negative axes. By introducing 6 more lines through the origin and perpendicular to the axes, these lines then represent pure shears whose states of strain are given by

$$\varepsilon_i = -\varepsilon_j \quad , \quad \varepsilon_k = 0 \qquad (i,j,k = t,\theta,s) \tag{6.4}$$

By numbering these 12 lines from 0 to 12 clockwise, like the face of a clock, each number has a specific physical meaning. Hsü (38) further defines the characteristic index for strain (η) giving the strain ratio $\varepsilon_t : \varepsilon_\theta : \varepsilon_s$. These strain ratios implicitly are related to a particular line of the 12 which in turn is a function of the angle α in Fig. (6.1) through the equation

$$\eta = \frac{6}{\pi}\alpha \tag{6.5}$$

Thus, odd values of η indicate pure shear and even η's show uniaxial tension and compression test. All the typical modes of deformation are shown in Fig. (6.3). It has been shown (40) that under usual axisymmetrical sheet metal forming processes, the strain paths fall between 2 to 8 o'clock, and process corresponding to strain paths beyond this range, though possible, rarely exist. In connection with the bulge test, geometrical and mechanical constraints require that the state of strain at the pole of the bulge is along 6 o'clock where balanced bi-axial stretching occurs. The state of strain at the die edge, for the case of no draw-in, is along 5 o'clock. Therefore, the work material everywhere along the bulge is expanded circumferentially with tensile meridional tangential strain, with strain paths between 5 to 6 o'clock.

A strain path of constant strain ratio is called a radial (or proportional) strain path. This particular type of strain path occurs at the pole of the bulge for obvious reasons. In general, the strain ratio at any position (r_o) in the specimen is not constant for every stage of deformation. Therefore, the strain paths plotted in the triangular coordinate system becomes curved and they are known as curved strain paths.

When strain paths are plotted on the triangular coordinate system, it is obvious that they do not fall exactly along the 12 lines representing typical modes of deformation; that is, the values of η are not integers. It is then necessary to discover more about the interpretation of the triangular coordinate system. For coaxial strain paths with nil transverse displacement gradient, the resultant of two successive deformations,

$$\begin{vmatrix} e^{\varepsilon_t'} & 0 & 0 \\ 0 & e^{\varepsilon_\theta'} & 0 \\ 0 & 0 & e^{\varepsilon_s'} \end{vmatrix} \quad \text{and} \quad \begin{vmatrix} e^{\varepsilon_t''} & 0 & 0 \\ 0 & e^{\varepsilon_\theta''} & 0 \\ 0 & 0 & e^{\varepsilon_s''} \end{vmatrix}$$

is equal to

$$\begin{vmatrix} e^{\varepsilon_t'+\varepsilon_t''} & 0 & 0 \\ 0 & e^{\varepsilon_\theta'+\varepsilon_\theta''} & 0 \\ 0 & 0 & e^{\varepsilon_s'+\varepsilon_s''} \end{vmatrix} \qquad (6.6)$$

The resulting Eq. (6.6) indicates that the final state of strain is independent of the order of transformation and the resultant is merely obtained by vector addition. Since any point in the coordinate system shows a state of strain, it is possible to perform vector addition and resolution on the triangular coordinate diagram into a combination of plane strains; or cylindrical strains; or a cylindrical and a plane strain depending on the convenience at the time of analysis. For example, Fig. (6.4) shows a strain path in the area between $\eta = 12$ and $\eta = 1$. It is possible to resolve the vector OP into two components - one along $\eta = 12$ and the other along $\eta = 1$; thus,

$$\underset{\sim}{OP} = \underset{\sim}{OM} + \underset{\sim}{ON} \tag{6.7}$$

Eq. (6.7) can also be regarded that the resultant strain is $\underset{\sim}{OP}$ when $\underset{\sim}{OM}$ and $\underset{\sim}{ON}$ are vectorially added.

The magnitude of any position vector in the triangular coordinate system can be found from the following analysis. Let vector $\underset{\sim}{OP}$ be resolved into two perpendicular components along $\eta = 12$ and $\eta = 3$, Fig. (6.5) then

$$x = \varepsilon_t$$

$$Y = \frac{\varepsilon_s}{\cos 30^\circ} + \frac{\varepsilon_t}{\tan 60^\circ}$$

$$= \frac{1}{\sqrt{3}}\,(2\varepsilon_s + \varepsilon_t)$$

then, $$|\underset{\sim}{OP}|^2 = X^2 + Y^2 = \varepsilon_t^2 + \frac{1}{3}(2\varepsilon_s + \varepsilon_t)^2 \tag{6.8}$$

Using the incompressibility equation, Eq. (6.2), Eq. (6.8) becomes

$$3|\underset{\sim}{OP}|^2 = 2\varepsilon_t^2 + 2\varepsilon_s^2 + 4\varepsilon_s\varepsilon_t + 2(-\varepsilon_s - \varepsilon_\theta)^2 + 2(-\varepsilon_t - \varepsilon_\theta)^2$$

$$= 4(\varepsilon_t^2 + \varepsilon_s^2 + \varepsilon_\theta^2) + 4(\varepsilon_s\varepsilon_t + \varepsilon_\theta\varepsilon_t + \varepsilon_\theta\varepsilon_s) \tag{6.9}$$

This incompressibility equation can also be expressed as

$$\varepsilon_s^2 + \varepsilon_t^2 + \varepsilon_\theta^2 = -2(\varepsilon_s\varepsilon_t + \varepsilon_t\varepsilon_\theta + \varepsilon_s\varepsilon_\theta) \qquad (6.10)$$

So that Eq. (5.9) is further reduced to

$$3\,|\underset{\sim}{OP}|^2 = 2(\varepsilon_t^2 + \varepsilon_s^2 + \varepsilon_\theta^2)$$

which gives the magnitude of vector $\underset{\sim}{OP}$ as

$$|\underset{\sim}{OP}| = \sqrt{\frac{2}{3}}(\varepsilon_t^2 + \varepsilon_s^2 + \varepsilon_\theta^2)^{1/2} \qquad (6.11)$$

and inclination

$$\alpha = \tan^{-1}\left(\frac{Y}{X}\right) = (\varepsilon_\theta - \varepsilon_s)/(\sqrt{3}\,(\varepsilon_\theta + \varepsilon_s))$$

which is also the effective strain defined in Eq. (5.33). This is also the length of any radial strain path emerging from the origin of the coordinate system. For curved strain paths, the incremental equivalent strain rate must be used so that the integral over the entire strain path is the length of the path. Thus, only in radial strain paths does the length of the path equal the magnitude of the position vector shown in Eq. (6.11).

(B) Triangular coordinates for deviatoric stresses

Unlike strains, states of stress ($\sigma_1, \sigma_2, \sigma_3$) cannot be plotted directly in the triangular coordinates system because the principal stresses, in general, do not add up to zero. However, some modifications may be made to enable the use of this system.

Any stress vector $\underset{\sim}{OP}$ in the Haigh-Westergaard Space may be expressed as

$$\underset{\sim}{OP} = \sigma_1 \underset{\sim}{i} + \sigma_2 \underset{\sim}{j} + \sigma_3 \underset{\sim}{k} \qquad (6.12)$$

Any stress vector consists of two components; hydrostatic component, σ_o, given by the first invariant I_1 ; and the combination of the second and third invariants, I_2 and I_3 to form the deviatoric component, σ'_{ij} . Thus, Eq. (6.12) is rewritten via

$$\begin{vmatrix} \sigma_1 \\ \sigma_2 \\ \sigma_3 \end{vmatrix} = \begin{vmatrix} \frac{\sigma_1+\sigma_2+\sigma_3}{3} \\ \frac{\sigma_1+\sigma_2+\sigma_3}{3} \\ \frac{\sigma_1+\sigma_2+\sigma_3}{3} \end{vmatrix} + \begin{vmatrix} \frac{2\sigma_1-\sigma_2-\sigma_3}{3} \\ \frac{-\sigma_1+2\sigma_2-\sigma_3}{3} \\ \frac{-\sigma_1-\sigma_2+2\sigma_3}{3} \end{vmatrix} = \begin{vmatrix} \sigma_o \\ \sigma_o \\ \sigma_o \end{vmatrix} + \begin{vmatrix} \sigma'_1 \\ \sigma'_2 \\ \sigma'_3 \end{vmatrix} \qquad (6.13)$$

as $$\underset{\sim}{OP} = \sigma_o(\underset{\sim}{i} + \underset{\sim}{j} + \underset{\sim}{k}) + (\sigma'_1\underset{\sim}{i} + \sigma'_2\underset{\sim}{j} + \sigma'_3\underset{\sim}{k}) \qquad (6.14)$$

$$\sigma'_1 + \sigma'_2 + \sigma'_3 = 0 \qquad (6.15)$$

It has already been shown in section A of Chapter 5 that the hydrostatic component of vector $\underset{\sim}{OP}$ lies along the hydrostatic axis which makes equal angles with the principal axes in space, and the deviatoric stress component lies in the π-plane of equation

$$\sigma_1 + \sigma_2 + \sigma_3 = 0$$

By the theory of plasticity, the component of the triaxial stress which is related to deformation is the deviatoric component consisting of three deviatoric stress σ'_s , σ'_θ and σ'_t. Since the sum of the three deviatoric stresses is zero identically, as seen in Eq. (6.15), the triangular coordinate system for strain can also be used to represent states of deviatoric stresses. These deviatoric stress states can also be obtained by the projection of the space vector onto the π-plane if we look along the hydrostatic axis. Thus, there are two methods of expressing graphically states of deviatoric stress for any stress system.

(1) <u>The direct method</u>

This technique employs the property given by Eq. (6.15) that the sum of the three deviatoric stress components in any stress state is zero. Like states of strain, states of deviatoric stress components are readily shown as points in the triangular coordinate system described earlier on knowing any two of the three deviatoric components. The axes in Fig. (6.2) now represent the deviatoric stresses. In order that the stress-strain relationship can be obtained, it is essential that the assignment for the axes for deviatoric stress correspond to that for strain. Thus, the vertical axis in the triangular coordinate system represents σ'_t and the axis down to the right represents σ'_s and the remaining down to the left denotes σ'_θ. The grid pattern for this technique is the same as that for strains shown in Fig. (6.2). It can be seen that, with this system of plotting, recovery of states of stress (in space) is not unique as the magnitude of the hydrostatic components has no effect on the representation. Referring to Fig. (6.5), in which the axes are altered to represent deviatoric stresses, the position vector $\underset{\sim}{OP}$ is readily shown to be

$$|\underset{\sim}{OP}| = \sqrt{\frac{2}{9}}\left((\sigma_t - \sigma_\theta)^2 + (\sigma_\theta - \sigma_s)^2 + (\sigma_s - \sigma_t)^2 \right)^{1/2} \qquad (6.16)$$

The method of arriving at this equation is similar to that for strains, in Eq. (6.11), together with the property that

$$\begin{aligned} \sigma_t' - \sigma_\theta' &= \sigma_t - \sigma_\theta \\ \sigma_\theta' - \sigma_s' &= \sigma_\theta - \sigma_s \\ \sigma_s' - \sigma_t' &= \sigma_s - \sigma_t \end{aligned} \tag{6.17}$$

The deviatoric component $\underset{\sim}{\sigma}'$ given by part of Eq. (6.14) can be shown to have a magnitude

$$\begin{aligned} \sigma' &= \sigma_t'^2 + \sigma_s'^2 + \sigma_\theta'^2 \\ &= \frac{1}{\sqrt{3}}\left((\sigma_t - \sigma_s)^2 + (\sigma_s - \sigma_\theta)^2 + (\sigma_\theta - \sigma_t)^2 \right)^{1/2} \end{aligned} \tag{6.18}$$

by using Eqs. (6.15) and (6.17). Therefore, any position vector in such a coordinate system has a magnitude proportional to the deviatoric stress component through the equation

$$|\underset{\sim}{OP}| = \sqrt{\frac{2}{3}}\,\sigma' \tag{6.19}$$

and furthermore, it is proportional to the effective stress of that stress state $(\sigma_1, \sigma_2, \sigma_3)$ shown by the following equation,

$$|\underset{\sim}{OP}| = \frac{2}{3}\bar{\sigma} \tag{6.20}$$

The direction of $\underset{\sim}{OP}$ in the triangular coordinate system is given by the deviatoric stress ratio $\sigma_t' : \sigma_s' : \sigma_\theta'$. Similar to the triangular coordinate for strains, a characteristic index for deviatoric stress (ζ) defines the mode of the deviatoric stress system. For the twelve radial lines emerging from the origin of the axes, it can easily be shown that the three positive branches of the axes (ζ = 12, 4, 8) and negative branches of the axes (ζ = 2, 6, 10) represent uniaxial tension and compression, respectively, because

$$\sigma_i = \sigma_i \quad , \quad \sigma_j = \sigma_k = 0 \qquad (i, j, k = t, s, \theta)$$

generates

$$\sigma'_j = \sigma'_k = -\frac{\sigma'_i}{2} \tag{6.21}$$

Similarly, odd values of ζ are characterised by

$$\sigma'_i = 0 \qquad \sigma'_j = -\sigma'_k \qquad (i, j, k = t, s, \theta)$$

showing pure shear systems of (6.22)

$$\sigma_i = 0 \qquad \sigma_j = -\sigma_k$$

A complete diagram for all typical stress system by Mohr stress circle is shown in Fig. (6.6)

(2) The projection method

This method is based on the fact that the deviatoric component of a stress system $(\sigma_1, \sigma_2, \sigma_3)$ lies in the π-plane and can be obtained by the projection of this space vector onto the π-plane by looking along the hydrostatic axis. The three principal axes then appear to be 120 degrees apart each with a unit length, $\sqrt{\frac{2}{3}}$ of the original axes in space. Mathematically, this technique is based on the following analysis: From Eq. (6.12), the components $\sigma_1 \underset{\sim}{i}$, $\sigma_2 \underset{\sim}{j}$ and $\sigma_3 \underset{\sim}{k}$ in space can be resolved into their respective deviatoric and hydrostatic components as

$$\begin{aligned} \sigma_1 \underset{\sim}{i} &= \sqrt{\frac{1}{3}}\sigma_1 \underset{\sim}{h} + \sqrt{\frac{2}{3}}\sigma_1 \underset{\sim}{t}_1 \\ \sigma_2 \underset{\sim}{j} &= \sqrt{\frac{1}{3}}\sigma_2 \underset{\sim}{h} + \sqrt{\frac{2}{3}}\sigma_2 \underset{\sim}{t}_2 \\ \sigma_3 \underset{\sim}{k} &= \sqrt{\frac{1}{3}}\sigma_3 \underset{\sim}{h} + \sqrt{\frac{2}{3}}\sigma_3 \underset{\sim}{t}_3 \end{aligned} \tag{6.23}$$

where $\underset{\sim}{h}$ is the unit vector of the hydrostatic axis and $\underset{\sim}{t}_1$, $\underset{\sim}{t}_2$ and $\underset{\sim}{t}_3$ are unit vectors of the projected principal axes (of unit vectors $\underset{\sim}{i}$, $\underset{\sim}{j}$, $\underset{\sim}{k}$) respectively. Note that the unit vectors $\underset{\sim}{t}_1$, $\underset{\sim}{t}_2$

and $\underset{\sim}{t}_3$ all lie in the π-plane and have only two degrees of freedom. By substituting Eq. (6.23) into Eq. (6.12), we have the space vector represented in terms of the hydrostatic and deviatoric components as

$$\underset{\sim}{\sigma} = \sqrt{\frac{1}{3}}(\sigma_1 + \sigma_2 + \sigma_3)\underset{\sim}{h} + \sqrt{\frac{2}{3}}(\sigma_1\underset{\sim}{t}_1 + \sigma_2\underset{\sim}{t}_2 + \sigma_3\underset{\sim}{t}_3) \qquad (6.24)$$

where $\sqrt{\frac{1}{3}}(\sigma_1 + \sigma_2 + \sigma_3)\underset{\sim}{h}$ is the hydrostatic stress along the hydrostatic stress axis and $\sqrt{\frac{2}{3}}(\sigma_1\underset{\sim}{t}_1 + \sigma_2\underset{\sim}{t}_2 + \sigma_3\underset{\sim}{t}_3)$ is the deviator stress in the π-plane. The deviator stress given in this form

$$\underset{\sim}{\sigma} = \sqrt{\frac{2}{3}}(\sigma_1\underset{\sim}{t}_1 + \sigma_2\underset{\sim}{t}_2 + \sigma_3\underset{\sim}{t}_3) \qquad (6.25)$$

is necessarily identical to that expressed in the right hand term of Eq. (5.14) which is

$$\frac{2\sigma_1 - \sigma_2 - \sigma_3}{3}\underset{\sim}{i} + \frac{-\sigma_1 + 2\sigma_2 - \sigma_3}{3}\underset{\sim}{j} + \frac{-\sigma_1 - \sigma_2 + 2\sigma_3}{3}\underset{\sim}{k}$$

because the unit vectors $\underset{\sim}{t}_1$, $\underset{\sim}{t}_2$ and $\underset{\sim}{t}_3$ in the π-plane are related to $\underset{\sim}{i}$, $\underset{\sim}{j}$, $\underset{\sim}{k}$, mutually perpendicular to each other, by the transformation equation for coordinates as

$$\begin{vmatrix} \underset{\sim}{t}_1 \\ \underset{\sim}{t}_2 \\ \underset{\sim}{t}_3 \end{vmatrix} = \begin{vmatrix} \sqrt{\frac{2}{3}} & -\sqrt{\frac{1}{6}} & -\sqrt{\frac{1}{6}} \\ -\sqrt{\frac{1}{6}} & \sqrt{\frac{2}{3}} & -\sqrt{\frac{1}{6}} \\ -\sqrt{\frac{1}{6}} & -\sqrt{\frac{1}{6}} & \sqrt{\frac{2}{3}} \end{vmatrix} \cdot \begin{vmatrix} \underset{\sim}{i} \\ \underset{\sim}{j} \\ \underset{\sim}{k} \end{vmatrix} \qquad (6.26)$$

Perusal of Eq. (6.25) shows that the vectorial resultant of $\underset{\sim}{\sigma}'$ with $\sqrt{\frac{2}{3}}\sigma_1$, $\sqrt{\frac{2}{3}}\sigma_2$ and $\sqrt{\frac{2}{3}}\sigma_3$ as axes 120 degrees apart is no longer identical to that shown in the direct method. Instead this method is shown in Fig. (6.7). By resolving any position vector OD along $\sqrt{\frac{2}{3}}\sigma_2$ and the line perpendicular to it,

$$X = \sqrt{\tfrac{2}{3}}\sigma_2 - \sqrt{\tfrac{2}{3}}\sigma_3 \sin 30° - \sqrt{\tfrac{2}{3}}\sigma_1 \cos 60°$$

$$= \sqrt{\tfrac{1}{6}}(2\sigma_2 - \sigma_3 - \sigma_1)$$

$$Y = -\sqrt{\tfrac{2}{3}}\sigma_3 \cos 30° + \sqrt{\tfrac{2}{3}}\sigma_1 \sin 60°$$

$$= \frac{1}{\sqrt{2}}(\sigma_1 - \sigma_3)$$

So that

$$OD = \left(\tfrac{1}{6}(2\sigma_2 - \sigma_3 - \sigma_1)^2 + \tfrac{1}{2}(\sigma_3 - \sigma_1)^2\right)^{1/2}$$

$$= \frac{1}{\sqrt{3}}\left((\sigma_1 - \sigma_2)^2 + (\sigma_2 - \sigma_3)^2 + (\sigma_3 - \sigma_1)^2\right)^{1/2} \qquad (6.27)$$

Thus, when the stresses involved are $(\sigma_t, \sigma_s, \sigma_\theta)$ and using the vertical axis as $\sqrt{\frac{2}{3}}\sigma_t$, down to the right as $\sqrt{\frac{2}{3}}\sigma_s$ and down to the left as $\sqrt{\frac{2}{3}}\sigma_\theta$,

$$OD = \frac{1}{\sqrt{3}}\left((\sigma_t - \sigma_\theta)^2 + (\sigma_\theta - \sigma_s)^2 + (\sigma_s - \sigma_t)^2\right)^{1/2} \qquad (6.28)$$

With this method, the length of any position vector reads the deviatoric component of a stress state $(\sigma_t, \sigma_\theta, \sigma_s)$ and consequently proportional to the effective stress given by the following equation,

$$OD = \sigma' = \sqrt{\tfrac{2}{3}}\,\bar{\sigma} \qquad (6.29)$$

The two methods of representing states of deviatoric stresses graphically on the triangular coordinate system, although seem to be totally different, are in fact interchangeable. That is to say, together with the grid pattern for each method, we can switch from one method to another on the same graph and at the same time preserving the conclusion obtained by each method. This offers an advantage that more information can be obtained from only one diagram and the method is shown in the following.

In order to combine the two methods into one diagram for a given state of stress (σ_t, σ_θ, σ_s), it is necessary to find the relative direction and magnitude of the two position vectors, that is, OP and OD in the respective diagram, Fig. (6.2) for the direct method and Fig. (6.7) for the projection method. The directions of these position vectors can be shown to be equal under a given state of stress (σ_t, σ_θ, σ_s) from the equation

$$\alpha = \tan^{-1}\left(\frac{\sqrt{3}(\sigma'_s - \sigma'_\theta)}{2\sigma'_t - \sigma'_s - \sigma'_\theta} \right)$$

$$= \tan^{-1}\left(\frac{\sqrt{3}(\sigma_s - \sigma_\theta)}{2\sigma_t - \sigma_s - \sigma_\theta} \right) \qquad (6.30)$$

Eqs. (6.19) and (6.29) shows that their relative lengths are related by the equation

$$\text{OP} = \sqrt{\frac{2}{3}}\ \text{OD} \qquad (6.31)$$

that is, the position vector in the projection technique has a magnitude greater than the magnitude of the position vector in the direct technique under the same state of stress (σ_t, σ_θ, σ_s).

Having known the relative magnitude and positions of the two position vectors $\underset{\sim}{OP}$ and $\underset{\sim}{OD}$, superposition of the two diagrams is then possible. Theoretically speaking, the sequence of superposition is not vital; but it appears to be convenient to use the projection method first and then convert to the direct method to find the deviatoric stresses. By this sequence, the deviatoric stresses need not necessarily be calculated and the principal stresses are used. It may be possible to expand the scale of the axes by $\sqrt{\frac{3}{2}}$ so that Eq. (6.31) becomes

$$OP = \frac{2}{3} OD \qquad (6.32)$$

which may be easier in the subsequent method. However, as the scaling factor may lead to confusion for later uses, it is considered best to stick to Eq. (6.31). The technique is shown in Fig. (6.8). In the method shown in Fig. (6.8), at any given state of stress (σ_t, σ_θ, σ_s), the individual principal stress values are multiplied by $\sqrt{\frac{2}{3}}$ and then plotted on the triangular coordinate system by the projection technique, shown as solid lines. The position vector OD then represents the deviatoric stress component of stress (σ_t, σ_θ, σ_s). Divide the line OD internally at P so that OP : OD = $\sqrt{\frac{2}{3}}$: 1. From P, drop perpendiculars to the axes, shown dotted. Thus, taking signs into consideration, the lengths along the axes give the corresponding deviatoric strain, and consequently point P shows the state of deviatoric stress (σ'_t , σ'_θ, σ'_s) corresponding to the given state of stress (σ_t, σ_θ, σ_s). The length OD is the deviatoric component of the applied stress state, Eq. (5.29). The effective stress $\bar{\sigma}$ can be obtained by extending the line OD to point E so that PE is half the length of OP, or $\frac{3}{2}$ times the length of OP.

If the deviatoric stresses are first calculated and plotted as P on the coordinate system by the direct method, shown dotted, then the magnitude of OD (= $\sqrt{\frac{3}{2}}$ OP) is the deviatoric component of the applied stress system. Unfortunately, the values shown by the solid lines cannot be recovered graphically. The effective stress $\overline{\sigma}$ can also be determined by the length of OE ($= \frac{3}{2}$ OP) as before. This sequence seems simpler than the first, because one operation (vectorial addition shown in solid lines) is unnecessary; but it requires the calculation of deviatoric stress which may be tedious. In the first sequence, practically no calculation is required and all information is obtained graphically.

A concluding statement has to be made that any position vector in the triangular coordinate system, whether for the direct or projection method, is sufficient to determine the characteristic index for deviatoric stresses (ζ), deviatoric component (σ') of the applied stress state ($\sigma_t, \sigma_\Theta, \sigma_s$) as well as the effective stress ($\overline{\sigma}$) for this state of stress. Unfortunately the principal stresses, or the applied stress state cannot be recovered because the hydrostatic component is not unique.

(C) Stress-strain relationships in the triangular coordinate System

The stress-strain relationship of metals during deformation can be derived by superposing the triangular coordinate systems for strains and deviatoric stresses one onto the other. There are two ways of establishing this relationship. One way is to plot the experimental states of strain and deviatoric stress on the triangular coordinate system for the whole process. The corresponding strain and deviatoric stress paths then represent the stress-strain relationship of the metal under a particular type of deformation defined by the characteristic indices. Thus, in the bulge test in which the strain distribution curve at the active zone is approximately spaced between 5 to 7 o'clock, there are infinite numbers of such relationships along the entire bulge profile. This method of representation can be seen to be an attempt to treat stresses and strains as vectors and their relationships expressed in vectorial form.

The second method of graphical representation of the relationship, also plotted on the triangular coordinate system, is to use effective stresses and strains. In this case, apart from the necessity of knowing the hardening function H ($= \frac{\bar{\sigma}}{\int d\bar{\varepsilon}}$) the general accepted flow rule has to be used. Hill (35) has successfully attempted to construct the stress-strain paths based on Reuss's equations for coaxial deformations. Alexander (45) then extends the construction to Hencky's equations. Both these equations are involved with elastic and plastic strains during deformation. Since, in sheet metal forming, the elastic strains are negligible compared to the plastic strains, the plastic strains involved are considered to be total so that the Levy-Mises flow rule can be used.

Chapter 7

EXPERIMENTAL TECHNIQUES

(A) Data on specimens

The main part of the results in this thesis are obtained from commercially pure copper sheets (soft) 0.048 in. thick (British Standards specification BS 899). The material is tested in the as-received condition without further annealing.

Before specimens are blanked, scribed lines indicating the rolling direction are made on one side of the sheet. Circular blanks of 8.125 in diameter are sheared and machined down to 7.992 in diameter by sandwiching the blanks between backing plates pressed firmly together between the head and tail stock of a lathe. This is to get rid of burrs and irregularities so as to ensure smooth square edges. The specimens are checked for thickness uniformity and those with maximum thickness variations exceeding 0.0004 in within a specimen are rejected. Similarly, specimens with scratchy surfaces are also rejected. On the side which becomes the outside surface of the bulge (the scribed face), fine lines of approximately 0.1 in pitch are scribed along the rolling direction. For checking the axisymmetry of the deformed bulge, similar grid lines are also scribed along the direction perpendicular to the rolling direction.

(B) Design of the bulge tester

The bulge tester, specially designed and built for this project, consists essentially of two parts: the die set and the hydraulic circuit. The die set consists of two separate plates 0.750 in thick sandwiching the specimen by 8 - 0.750 in BSF bolts spaced uniformly along a pitch circle of 10 in diameter, Fig. (7.1). The die hole is 5.000 in diameter, rounded at its inner edge to a radius of 0.500 in to avoid tearing the specimens. The circular rim on the base plate in Fig. (7.1) provides the centering of the specimens with respect to the die hole. The concentricity of the specimen located is better than 0.0003 in. Where the die is in contact with the blank, it is serrated with circular grooves of 0.020 in pitch, 0.012 in deep (inset of Fig. (7.1)) in an annular area from 6 in to 6.7 in in diameter. These grooves prevent all movement of the flange during the forming process.

The hydraulic system designed and installed for the experimental work, shown schematically in Fig. (7.2), is designed to give a maximum hydraulic pressure of 3000 psi with oil delivered by a variable displacement pump. Pressures lower than this value can be adjusted by the globe valve VI. The solenoid valves used are normally closed while the pressure switches incorporated to control the solenoid valves are bourdon type giving a normally closed electrical circuit. It can be seen in Fig. (7.2) that several solenoid valves, pressure switches and pressure gauges of different range up to 3000 psi are used in order to reduce errors due to inertial effects of instruments. The oil pressure in this project is accurate to 25 psi.

Basically, oil at a controlled flow rate is supplied to the specimen via the control valve. The remaining oil delivered by the pump is returned to the tank passed valve VI. The pressure switches coupled with the corresponding solenoid valves are incorporated at the die inlet so that a particular solenoid valve in action remains open until the bulge pressure has attained a pre-set value.

(C) The forming process

Preliminary tests show that the copper specimens fracture at 1000 psi via 1050 psi. The globe valve VI is then preadjusted to yield maximum pressures of 1500 psi. The control valve is set at A6 indication giving approximately 0.5 in polar height per minute. The recessed hole of the die set shown in Fig. (7.1) is first filled with oil and then the specimen is inserted to the die with air expelled under it. The specimen is then clamped by tightening the eight bolts.

Intermediate test pressures can be pre-selected by setting the appropriate vernier marking on the pressure switch. After the pressure is relieved, apart from the hydraulic pressure, the current radius and the profile slope of the bulge are measured; the former with a two dimensional travelling microscope reading to 0.001 in, and the latter with a tool room protractor reading to 5 min and the measurement is repeatable to ± 5 min. A magnetic stand placed on the surface plate is used to guide the movement of the protractor so that accurate meridional slope is ensured. Measurements of slope and radial coordinates are made in the direction of rolling. The polar height is also measured as an index for the extent of the forming process.

For the range of polar heights covered in the experiments (0.509 in to 2.150 in), the spring-back at the pole is nearly uniformly 0.009 in. It can be estimated that such a springback introduces a maximum error of 0.6 percent in ρ_θ and 2 percent in ρ_s. The maximum 2 percent error in ρ_s occurs near the pole and the rim only in the extreme values of the polar height, and for the major part of the results shown in this thesis it is less than one percent, Appendix A. These errors in no way invalidate the conclusions drawn from the results.

Measurements of the slopes in the direction perpendicular to that of rolling are less than 10 min below that along the direction of rolling. The small deviation from the axial symmetry which these measurements represent is ignored.

As the forming progresses, more and more of the work at the rim comes into contact with the rounded profile of the die, so that the material in this region is formed not only by the membrane stresses but by bending as well. The membrane stresses in the material in this region must, of course, also confirm to Eq. (2.7), but the uncertainty of the frictional and normal stress on the die surface makes it unrewarding to analyse them. Therefore, in the experimental results, the annular region between $r = 2.5$ in and $r = 3.0$ in is neglected.

(D) Analysis of data

It is obvious from Chapter 2 that the mechanical property of the material in the bulge test can be determined through the geometry of the shell. It is convenient to summarise the technique of analysis from the basic measurements - r and ϕ - in this section.

(i) Determination of states of strain

Through the incompressibility condition of metals in plastic deformations, only two principal strains of the three are sufficient to define the state of strain corresponding to any pressure. The circumferential and through-thickness strains are calculated from the following procedures in the project.

The circumferential strain is simply calculated from Eq. (2.2) having measured accurately both the original and current radii. The error is estimated to be less than one percent, except near the pole (to within 0.6 in).

Though the through-thickness strain can readily be calculated from Eq. (2.2) by measuring the current through-thickness a new way based on the measured angle ϕ and $\frac{d\varepsilon_\theta}{dr_o}$ derived from ε_θ to calculate ε_t is proposed and used in this project. By differentiating $\varepsilon_\theta (\equiv \log_e {}^{r}/r_o)$ with respect to r_o and substituting the term ${}^{dr}/dr_o$ into that term in the definition of $\varepsilon_s \ (\equiv \log_e (\frac{dr}{dr_o} \ \frac{1}{\cos\phi}))$, the following compatibility equation is obtained,

$$\varepsilon_s - \varepsilon_\theta = \log_e \left(\frac{1 + r_o \frac{d\varepsilon_\theta}{dr_o}}{\cos \phi} \right) \qquad (7.1)$$

using the incompressibility condition, the through-thickness strain is

$$\varepsilon_t = -2\varepsilon_\theta - \log_e \left(\frac{1 + r_o \frac{d\varepsilon_\theta}{dr_o}}{\cos \phi} \right) \qquad (7.2)$$

In the measurements and calculations to determine the thickness t, the source of the largest error (about one percent) is in ϕ . The overall maximum error in t is estimated to be less than 2 percent - except for the region very near to the pole.

(ii) Determination of index of sphericality (N)

The primary results are plotted in terms of r and sin ϕ, as shown in Fig. (8.2). The coordinates in this figure are so chosen because the curvature $\frac{1}{\rho_\theta}$ can be directly read from it with an adjustable protractor, since

$$\frac{1}{\rho_\theta} = \frac{\sin \phi}{r} \qquad (2.6)$$

As Eq. (2.5) implies, the slope of the curves in Fig. (8.2) is the radius of curvature ρ_s. In practice, however, it is difficult to determine accurately the slope in Fig. (8.2) for any particular value of r, because the curves are all nearly straight lines passing through the origin. It is more practicable to derive the value of N from Fig. (8.4). Thus, differentiating Eq. (2.6) and combining the results of the differentiation with Eq. (2.5), we get

$$N = 1 - \frac{r\, d\rho_\theta}{\rho_\theta\, dr} = 1 - \sin\phi \frac{d\rho_\theta}{dr} \qquad (7.3)$$

The prolateness $(\bar{P})$ at any position on the bulge is thus,

$$\bar{P} = \frac{r\, d\rho_\theta}{\rho_\theta\, dr} = \sin\phi \frac{d\rho_\theta}{dr} \qquad (7.4)$$

(iii) Determination of states of deviatoric stress

States of flow stress can readily be obtained from known values of prolateness, through-thickness and Eqs. (2.8) and (2.9). States of deviatoric stress can be deduced from Eq. (5.5) thus,

hydrostatic stress, $\sigma_0 = \frac{\sigma_s + \sigma_\theta}{3}$

deviatoric circumferential stress, $\sigma'_\theta = \sigma_\theta - \sigma_0$

deviatoric meridional tangential stress, $\sigma'_s = \sigma_s - \sigma_0$

and deviatoric through-thickness stress, $\sigma'_t = -\sigma_0$

$$= -(\sigma'_\theta + \sigma'_s) \qquad (7.5)$$

Chapter 8

SPHERICALITY OF A DIAPHRAM IN THE BULGE TEST

It is shown in Chapter (3.C) that the prolateness of the surface in the bulge test is never constant. Therefore, this Chapter is aimed at studying in detail the local sphericality of copper specimens in the bulge test. Moreover, since the sphericality of a shell is defined as the ratio of the principal curvatures, it becomes necessary to discuss the variation of the principal curvatures first.

(A) Distribution of the ρ_θ- curve in the bulge test

The distribution of the ρ_θ-curve in the bulge test can be analysed through the shape of the (r against sin ϕ) curve. It can easily be shown that the ρ_θ -distribtuion curve depends on how the (r against sin ϕ) curve crosses the radial lines emerging from the origin of the (r against sin ϕ) curve. We begin from the definition of N, index of sphericality,

$$N \equiv \frac{\rho_\theta}{\rho_s} = \frac{\cot\phi \, d\phi}{dr/r}$$

so that

$$N \frac{dr}{d(\sin\phi)} = \frac{r}{\sin\phi} \qquad (8.1)$$

The index N is always positive in order to have a close surface in the meridional section of the deformed bulge, (Chapter 3.A). The ratio $\left(\frac{r}{\sin\phi}\right)$ in Eq. (8.1) is simply the average slope of the (r against sin ϕ) curve at any point; the term $\left(\frac{dr}{d\,(\sin\phi)}\right)$, however, yields the slope of the tangent of the (r against sin ϕ) curve. Thus, from Eq. (8.1), the following observations may be made:

(a) if $\frac{dr}{d(\sin\phi)} > \frac{r}{\sin\phi}$, then $N < 1$

(b) if $\frac{dr}{d(\sin\phi)} < \frac{r}{\sin\phi}$, then $N > 1$

(c) if $\frac{dr}{d(\sin\phi)} = \frac{r}{\sin\phi}$, then $N = 1$ (18.2)

The relative magnitudes of the slopes in Eq. (8.1) distinguishes the prolateness ($\overline{P} \equiv 1-N$) or oblateness (negative prolateness of the deformed shell according to Eq. (8.2).

In order that Eq. (8.2) may lead to the distribution of the ρ_θ -curve, it is necessary to approach from the definition of ρ_θ and its differential coefficient with respect to the current radius. Thus, Eq. (7.3) is rewritten as

$$\frac{d\rho_\theta}{dr} = \frac{\rho_\theta}{r}(1-N) \qquad (8.3)$$

Comparison of Eqs. (8.2) and (8.3) then yields,

$$\begin{array}{llll}
(a) & \frac{d\rho_\theta}{dr} > 0 & \text{if} & \frac{dr}{d(\sin\phi)} > \frac{r}{\sin\phi} \\
(b) & \frac{d\rho_\theta}{dr} < 0 & \text{if} & \frac{dr}{d(\sin\phi)} < \frac{r}{\sin\phi} \\
(c) & \frac{d\rho_\theta}{dr} = 0 & \text{if} & \frac{dr}{d(\sin\phi)} = \frac{r}{\sin\phi}
\end{array} \qquad (8.4)$$

The ρ_θ-distribution curve as a result of the (r against sin ϕ) curve can now be observed. If the (r against sin ϕ) curve is sagging, then ρ_θ is always monotonic increasing. When the curve becomes hogging, ρ_θ is monotonic decreasing. However, for a radial (r against sin ϕ) curve, then the (ρ_θ against r) curve becomes a horizontal line, Fig. (8.1).

It has been shown in Chapter (3.C) that a real specimen cannot be any surface of constant N-value, let alone a sphere, the simplest of constant N-surfaces. Therefore, from Eqs. (8.3) and (8.4), the spherical condition (C) in Fig. (8.1) is invalid in the case of the bulge test and the circumferential radius of curvature for each stage must have a variation along the bulge. To identify the circumferential curvature variations with ease, the following technique is proposed based on the basic curve - (r against sin ϕ) curve - shown in Fig. (8.2).

Around any curve from Fig. (8.2), say an intermediate stage J of polar height 1.544 in, draw radial lines from the origin of the coordinate axes, Fig. (8.3), to show the direction which the curve intersects the radial lines. The initial segment (oa) of curve J is seen to intersect the radial lines in an anticlockwise direction as shown by the arrowhead in Fig. (8.3). Thus, at any point along the segment oa, condition (a) of Eq. (8.4) is valid and the circumferential radius of curvature is monotonically increasing. Since the whole segment ab of curve J in Fig. (8.3) crosses the radial lines in a clockwise direction as shown by the arrowhead, condition (b) of Eq. (8.4) holds and consequently, the radius of curvature is monotonic decreasing. The point a in Fig. (8.3) is the point of tangency between a radial line and the curve J, and therefore it corresponds to a maximum ρ_θ .

Similar analysis of all other stages in Fig. (8.2) reveals that the meridional slopes of the shell vary in a similar manner as curve J. Thus, in the bulge test, the (ρ_θ against r) curve is monotonic increasing up to a certain region containing the pole of the bulge. Beyond this region, the (ρ_θ against r) curve becomes monotonic decreasing until the die edge is reached, Fig. (8.4).

The point of tangency defined in Fig. (8.3) for each stage shifts towards the die edge as the specimen deforms further in general, showing that the ring of maximum ρ_θ expands with deformation. For the fractured specimen (M), the point of tangency does not occur at all, indicating a monotonic increasing function of ρ_θ over the entire meridional section. The maximum ρ_θ locus is shown dotted in Fig. (8.4). This maximum ρ_θ loci in Fig. (8.4) suggest at least two different modes of deformation in the bulge test. At small deformation (stage A to D), the location for maximum ρ_θ at the bulge appears to remain stationary. For larger deformation (stage F to L), the maximum ρ_θ locus then shifts towards the die edge and its movement becomes very rapid after stage K. Stage E seems to be the transition region from one mode of deformation to another. These two different modes of deformation are later described as the initial and stable regimes of deformation.

In the variation of the curvature $\frac{1}{\rho_\theta}$ shown in Fig. (8.5) it can be seen that from curve A to curve K, the specimen is formed into a shell of higher curvature along a discernible pattern. In curves L and M (the latter for fractured shell) however, the deformation is increasingly concentrated near the pole. Examination of the oil pressure for curves K and L will show that the forming process is then unstable. The deformation represented in the highest two curves in Fig. (8.5) is, therefore, similar to the bulge in a boiler tube just before bursting, even though the bulge is indiscernible in the specimen, because the general shape of the shell is a bulge anyway.

A striking feature of all the meridional slope curves in the bulge test is the existence of a loop between segment oa and the tangential line at a, Fig. (8.3). The magnitude of this loop is very small at low pressures, but increases with severity of deformation. It is then essential to discuss the significance of the size of this loop, with particular reference to the vertical deviation (δ) of the meridional slope curve from the tangential line. Let X be the meridional slope curve in the bulge test. The radial line tangent to this curve (slope tan Ω) is first drawn, Fig. (8.6). Then at any position on the bulge, the vertical deviation (δ) is obtained by geometry and definition of ρ_θ . By the property of similar triangles,

$$\frac{r + \delta}{R} = \frac{\sin \phi}{\sin \phi_R} \qquad (8.5)$$

where
$$\frac{R}{\sin \phi_R} = \tan \Omega \quad \text{and}$$
$$\sin \phi = \frac{r}{\rho_\theta}$$

Then Eq. (8.5) becomes

$$\delta = r\left(\frac{\tan \Omega}{\rho_\theta} - 1 \right) \qquad (8.6)$$

There are three important ways of interpreting Eq. (8.6) :- (i) variation of δ along the bulge at any stage of deformation; (ii) relative magnitudes of δ at fixed r for successive stages and (iii) physical meaning of δ .

(i) δ along the specimen

Under this condition, the slope of the tangential line (tan Ω) is constant with varying r. The variation of δ at any two positions r_1 and r_2 is thus

$$\frac{\delta_2 - \delta_1}{\tan\Omega} = \frac{r_2}{(\rho_\theta)_2} - \frac{r_1}{(\rho_\theta)_1}$$

$$\text{where } r_2 > r_1 \tag{8.7}$$

Eq. (8.7) implies that the relative magnitude of δ indicates the distribution of ρ_θ curve for any stage of deformation. In the case of the bulge test in which the typical meridional slope is shown in Fig. (8.3), δ_2 is less than δ_1 so that $(\rho_\theta)_2$ becomes greater than $(\rho_\theta)_1$. After the curve in Fig. (8.3) has passed point a, δ_2 becomes greater than δ_1, so that $(\rho_\theta)_2 < (\rho_\theta)_1$. Thus, the trend of the (ρ_θ against r) curves in Fig. (8.4) is further verified.

(ii) Relative magnitudes of δ for successive stages

It is meaningless to compare the relative magnitudes of δ for successive stages, unless a constant r for all stages is considered. Thus, referring to Eq. (8.6) the slope tan Ω becomes a varying parameter. The relative magnitude of δ for two stages is

$$\frac{\delta_2 - \delta_1}{r} = \frac{\tan\Omega_2}{(\rho_\theta)_2} - \frac{\tan\Omega_1}{(\rho_\theta)_1} \tag{8.8}$$

where suffix 2 denotes a more severely deformed stage and $\Omega_1 > \Omega_2$. Thus, the relative length δ refers to the change of the circumferential curvatures of a point in the specimen for various severity of deformation. From Fig. (8.3), it is observed that $\delta_2 > \delta_1$ for all stages along the entire specimen so that $(\rho_\theta)_2$ is always less than $(\rho_\theta)_1$. In other words, as deformation proceeds, the curvature of the entire bulge increases, Fig. (8.5).

(iii) Physical meaning of δ

It has been shown that any radial line from the origin of the axes in Fig. (8.1) represents a sphere of radius given by the slope of the radial line. Therefore, by its definition δ is a measure of the deviation of circumferential curvature for the deformed bulge from a sphere of radius $\tan\Omega$.

Eq. (8.6) suggests that the circumferential curvatures of the actual surface differs more severely from the curvature of the sphere for increasing δ. However, this does not necessarily mean that the actual bulge becomes more and more distorted from a reference sphere because we have yet another curvature (in the meridional tangential plane) to be defined. This has been discussed in Chapter (3.C).

(B) Distribution of the ρ_s-curve in the bulge test

The trend of the ρ_s-distribution curve may be obtained by considering its definition in conjunction with the definition of ρ_θ. Thus from

$$\rho_s = \frac{dr}{d\phi}\frac{1}{\cos\phi} \qquad \text{and} \qquad \rho_\theta = \frac{r}{\sin\phi}$$

we have

$$\rho_s = \rho_\theta + \tan\phi\,\frac{d\rho_\theta}{d\phi} \tag{8.9}$$

since ρ_s, ρ_θ and ϕ are always positive quantities, the sign of the term $\frac{d\rho_\theta}{d\phi}$ is the sole factor determining the relative magnitude of ρ_s and ρ_θ. When $\frac{d\rho_\theta}{d\phi} > 0$ over a region ϕ, Eq. (8.9) suggests that $\rho_s > \rho_\theta$; and by similar argument $\rho_s < \rho_\theta$; over the region ϕ where $\frac{d\rho_\theta}{d\phi} < 0$. For the special case of a local sphere, Eq. (8.9) shows that the ρ_s- and ρ_θ-curves intersect at the position where $\frac{d\rho_\theta}{d\phi} = 0$.

The variation of ρ_s over the bulge can be visualised in the following manner. On differentiating ρ_s and ρ_θ with respect to ϕ

$$\frac{d\rho_s}{d\phi} = \frac{dr}{d\phi}\,\frac{\sin\phi}{\cos^2\phi} + \frac{1}{\cos\phi}\,\frac{d^2r}{d\phi^2} \tag{8.10}$$

$$\begin{aligned}\frac{dr}{d\phi} &= \sin\phi\,\frac{d\rho_\theta}{d\phi} + \rho_\theta\cos\phi \\ \frac{d^2r}{d\phi^2} &= \sin\phi\,\frac{d^2\rho_\theta}{d\phi^2} + 2\cos\phi\,\frac{d\rho_\theta}{d\phi} - \rho_\theta\sin\phi\end{aligned} \tag{8.11}$$

Substituting Eq. (8.11) into Eq. (8.10)

$$\frac{d\rho_s}{d\phi} = \tan\phi\,\frac{d^2\rho_\theta}{d\phi^2} + (2+\tan^2\phi)\frac{d\rho_\theta}{d\phi} \tag{8.12}$$

Eq. (8.12) then defines the relationship between the trends of ρ_s and ρ_θ curves.

In the actual bulge test, by referring to Fig. (8.4), it is observed that $\frac{d\rho_\theta}{d\phi}$ and $\frac{d^2\rho_\theta}{d\phi^2}$ are negative at the die edge region so that $\frac{d\rho_s}{d\phi} < 0$ meaning a decreasing function of ρ_s curve. For the region where $\frac{d\rho_\theta}{d\phi} > 0$, $\frac{d^2\rho_\theta}{d\phi^2}$ is still negative and the relative magnitude of the right hand terms of Eq. (8.12) cannot be decided.

Thus, over the region ϕ where $\frac{d\rho_\theta}{d\phi} > 0$ we have $\frac{d\rho_s}{d\phi} \gtrless 0$ The function of ρ_s with ϕ for the entire profile is monotonic increasing initially and becomes monotonic decreasing before the position $\frac{d\rho_\theta}{d\phi} = 0$. After this position, ρ_s is still a decreasing function, Fig. (8.7).

(C) Prolateness of the deformed shell

Definition of a surface merely by its principal radii of curvature is insufficient because their numerical values are not indicative of the shape of the surface. This point was suggested in Chapter (3.C) and therefore an index of sphericality (N) and hence prolateness ($\overline{p} \equiv 1-N$) attempting to describe the shape of any surface is defined. For this definition of N, the surface can no longer be specified by the numerical values of the principle curvatures; but by the ratio of them. For example, N=1 always refers to a sphere ($\rho_\theta = \rho_s$) regardless of the numerical values of the curvatures. Thus, prolateness and curvatures are two distinct concepts, and a surface can have either large curvatures and large prolateness, or small curvature and large prolateness. As the bulging action progresses, the curvature generally increases, but, in theory, the prolateness does not necessarily decrease.

Eqs. (8.1) to (8.4) have already suggested the variation of N with respect to the curvature $\frac{1}{\rho_\theta}$. To provide a clearer picture of the N distribution in the actual test specimen, the following is a theoretical analysis on the N curve in general based on the curvature $\frac{1}{\rho_\theta}$. At the pole of the bulged specimen, the material is subjected to balanced bi-axial stretching and N is obviously unity. Then $\frac{d\rho_\theta}{dr}$ can take any value including zero, and the shape of the ρ_θ-curve within the neighbourhood of the pole can be anything continuous. At the edge of the bulge, the circumferential strain is either zero, or slightly compressive (if there is draw-in), hence the meridional tangential stress must be at least twice the circumferential stress, and the N value must therefore, be greater than one but smaller than two.

For the general case that ρ_θ is a non-linear function of r, ρ_θ can either have or not have a turning point. When a turning point does not exist and with $\phi > 0$ always, Eq. (8.3) suggests that the entire surface is always oblate for monotonic decreasing ρ_θ and prolate for monotonic increasing ρ_θ function, conditions (i), (ii) in Fig. (8.8). By virtue of Eq. (8.3), the N value corresponds to the condition $\frac{d\rho_\theta}{dr} = 0$ is

$$N = 1 , \qquad \phi > 0 \tag{8.13}$$

The turning point of N can be obtained by the differential coefficients of Eq. (8.3),

$$\frac{dN}{d\phi} = -\frac{d\rho_\theta}{dr} \cos\phi \quad - \quad \sin\phi \ \frac{d}{d\phi}\left(\frac{d\rho_\theta}{dr}\right) \tag{8.14}$$

and on equating Eq. (8.14) to zero yields the condition

$$\frac{d\rho_\theta}{dr} = -\tan\phi \ \frac{d}{d\phi}\left(\frac{d\rho_\theta}{dr}\right) \tag{8.15}$$

so that the magnitude of N (= N_T) at the turning point ϕ (= ϕ_T) is

$$N_T = 1 + \sin\phi_T \tan\phi_T \ \frac{d}{d\phi}\left(\frac{d\rho_\theta}{dr}\right)_T \tag{8.16}$$

The shape of the N-distribution curve can now be predicted for a given ρ_θ distribution curve in conjunction to the mechanical constraints at the pole and die edge. The case for a monotonic increasing (or decreasing) function of ρ_θ has already been discussed in a previous paragraph in this Chapter. Since N=1 at $\phi > 0$ corresponds to a turning point of the ρ_θ curve, the N curve must cross the N=1 line for a non-linear ρ_θ curve. If the N curve crosses only once, then it must have a minima with $N_T < 1$. On the other hand, for two crossings, the simplest N curve is maximum N_T ($N_T > 1$) initially and becomes a minima ($N_T < 1$) towards the die edge. Similar deductions may be made for multiple intersections of N with the N=1 line. Conversely, for one intersection of the N curve on the N=1 line, the ρ_θ curve has a maximum value; and for two intersections, ρ_θ is a minimum initially followed by a maximum value towards the die edge. Fig. (8.8) is an attempt to summarise the possible N and ρ_θ curves in their simplest forms. It is seen that the bulge along the entire meridian section can either be oblate or a combination of prolate, oblate and spherical shapes.

The prolateness of a deformed bulge can also be visualised from the basic curves shown in Fig. (8.2). The method of analysis is similar to that for circumferential curvature variations shown in Fig. (8.3). By virtue of Eqs. (8.2) and (8.4), the surface is oblate over the region where the basic curve intersects the radial lines in the clockwise direction. A prolate surface will be revealed over the region where the basic curve crosses the radial lines in the anticlockwise direction. Similarly, it can easily be shown that the point of tangency represents spherical shape. This method of analysis shows that the deformed bulge consists of a sphere at the pole and a ring of sphere whose diameter keeps expanding with deformation between the pole and die edge. Between the pole and ring of sphere, the bulge is everywhere prolate ; and becomes oblate in the region between the ring of sphere and die edge, Fig. (8.9).

It is seen in Fig. (8.9) that the deformations in the workpiece follow a clear cut pattern between curves F to K. In the curves L and M, however, unstable deformation results in large prolateness near the rim (the amount N falls below unity). Curves A to E shows that at the beginning of the forming process the deformations pass through an initial regime before the typical mode of stable deformation is established.

The N curves from stage A to D are very nearly equal to each other although the polar height varies from 0.509 in to 0.905 in. Part of the N curve for stage E belongs to the initial regime and part of it to the stable regime. Thus, strictly speaking, stage E belongs to transition zone, relating the initial and stable regimes. Since only near the die edge does the N curve belong to the stable regime, stage E is deliberately classified into the initial regime for the analysis in this project. A study of the polar heights for the initial regime suggests that as soon as the specimen is deformed, the bulge has only one particular shape regardless of further deformation until the stable regime is reached. In the transition zone, a minute change in polar height (0.031 in between stages E and F) will then result in a large variation of shape.

The complex variations of prolateness and stress conditions within a specimen and throughout the forming process can be seen in Fig. (8.9). Thus, between curves A and F, near the rim, the oblateness actually increases (shell becomes more flattened) with the general increase in curvature (Fig. 8.5), showing that curvature and prolateness are two distinct geometrical properties. In the main part of stable deformation (curves F to K), however, the general trend is increasing prolateness (N decreases). The shell is divided into two zones by an annular ring of perfect spherical surface ($N=1$), prolate inside and oblate outside it. As the forming progresses, the prolate expands outwards and this prolate region, except near the pole, becomes more pointed; and the oblate region diminishes in size till near the end of the forming process when unstable deformation leads quickly to fracture (at 2.150 in polar height), the whole shell is prolate.

The same general variation of prolateness with respect to r is also found in aluminium specimens, Fig. (8.10), even at small deformations ($0.92 < N < 1.04$) and the existence of draw-in.

With one exception, it is impossible to compare the results in Fig. (8.9) with those of other research workers, because in their results either the surface is assumed to be a spherical one, or the experimental measurements are unsuitable for the determination of N. In Wang and Shammamy's (14) excellent theoretical results, however, some data on the predicted stress ratios (in Fig. 2(b), ref (14)), can be converted into N and these are replotted in Fig. (8.11), together with some curves from Fig. (8.9), for various values of the effective strain at the pole (ε_o). The similarity in the general shapes of the curves between the two sets is remarkable, in view of the completely different techniques used - one by theoretical calculations with a computer and the other by experimental measurements. The fact that the lowest points in Wang and Shammamy's curves are nearer to the rim is obviously due to their assumption of a sharp die without bending effects. There is, however, one notable difference between theirs and the present results, namely at the initial stages, they predicted entirely oblate bulges (for example, for $\varepsilon_o = 0.1$) whereas it is found presently that the bulge is partly prolate ($N < 1$) even at the very beginning. It is, however, unwarranted to expect coincidance between the two sets of results because, apart from the different boundary conditions, the coefficient of work-hardening they used is 0.2, whereas in the present case, there are two ranges of this coefficient (n) before instability occurs as shown in Fig. (11.14), one at $n = 0.72$ up to $\varepsilon_o = 0.14$, and another at $n = 0.45$ for $0.14 < \varepsilon_o < 0.40$. The work-hardening coefficients of aluminium are $n = 0.13$ up to $\varepsilon_o = 0.142$ and $n = 0.138$ for $0.142 < \varepsilon_o < 0.3$. The difference between the theoretical and experimental results can also be due to the use of the Levy-Mises flow rule by Wang and Shammamy. It is shown in Chapter (11.D) that the deviatoric stress vector and incremental strain vector are inclined at 6 degrees when plotted in the π-planes.

(D) Sphericality from the meridional slope

The use of r and $\sin\phi$ as coordinate axes shown in Fig. (8.2) offers an additional advantage that a radial line on it represents a sphere ($N=1$) and the slope of this straight line is the radius of the sphere. In the actual forming process, the (r against $\sin\phi$) curve is non-linear so that an equivalent sphere can be fitted.

To fit a theoretical sphere to the actual specimen, two sets of boundary conditions generally have to be known - one at the pole and the other at the die edge. The boundary condition at the pole can simply be measured from the test specimen and it is characterised by the polar height. The boundary condition at the die edge is characterised by the deformation at $r = a$. The value $r = a$, however, cannot be easily obtained owing to the presence of the die radius. Of the various possible definitions of $r = a$, three important ones are discussed and from which, an arbitrary definition is selected for the analysis in this project.

(i) <u>Position where specimen touches the die profile</u>

For this criterion, $r = a$ is considered to be at the point of contact of the specimen and the die profile and the material beyond $r = a$ is idealised as the flange. The advantages of this criterion are:

(a) N is maintained positive for $a > r > 0$;

(b) the adjusted polar height (OR-axis is brought up to pass through the point of contact) is easily found by integrating $\int_0^a \tan\phi \, dr$.

The disadvantages are:

(a) the value of a is not constant for each stage and has to be determined from the real specimen;

(b) the adjusted polar height, though easily integrable, cannot be calculated easily directly from the real specimen because the value of ϕ at $r = a$ is not easily available.

(c) though the polar height is adjusted, N does not equal to 1.5

at r = a because draw-in will occur at the theoretical flange. This makes the theory of the bulge test more complicated.

(ii) Position where the profile is extrapolated to $\iota = 0$

This criterion is merely an extended version of the previous one in that the profile is extrapolated to $\iota = 0$ instead of following the die profile. Thus, the advantages are:

(a) N is maintained positive for $a > r > 0$;

(b) polar height is easily measured because it is the true height of the actual specimen.

(c) N can be 1.5 at r = a.

The disadvantages are:

(a) the value of a is not constant for each stage and has to be determined from the real specimen;

(b) the fitted sphere may intersect the die profile.

(iii) Position where the die profile begins from the flange

The advantages of this criterion are:

(a) constant r = a throughout the entire process and, therefore, it can be pre-determined;

(b) N is positive throughout the range $a > r > 0$ and is 1.5 at r = a.

(c) polar height of the fitted sphere is the true height of the actual specimen. Therefore no readjustment is necessary.

The disadvantages are:

(a) the surface of revolution at the die profile has a negative N value. Therefore, the equivalent sphere will cut through the die profile.

(b) the point of intersection of the equivalent sphere with the die throat will not coincide with the point of contact in the actual case.

It is necessary to select an arbitrary definition of a from the various criteria suggested above in order to fit to the deformed shell an equivalent sphere. Criterion (i) gives the best satisfaction of the boundary conditions but is laborious in the fitting procedure. Moreover, it is difficult to locate the position on the bulge where N=0. Criteria (ii) and (iii) are equally good and simple in operation. Since criterion (iii) offers an extra advantage that the value r = a can easily be pre-determined, it is proposed that the definition of the boundary condition r = a be the position in the flange when the die profile commences; and in this particular project, a = 3 in.

Having the boundary conditions found, the equivalent sphere can obviously be obtained by several different ways. Only three ways are discussed in this section.

(i) <u>The polar tangent sphere</u>

This equivalent sphere has a radius of curvature obtained by the tangent at r = 0 of the (r against sin ϕ) curve, that is,

$$R_{eq} = (\rho_\theta)_{r=0} = (\rho_s)_{r=0} \qquad (8.19)$$

where R_{eq} is the radius of curvature of the equivalent sphere. When this sphere is compared to the actual meridional surface, its curvature is larger up to r = 1.8 ~ 2.2 for the initial and stable regimes. Beyond this value of r, its curvature is smaller than the actual surface. After unstable deformation has begun, its curvature is larger throughout the entire specimen because of the excessive deformation at the pole where fracture eventually takes place, Fig. (8.12).

Comparison of the meridional sections of this equivalent sphere with the actual bulge can then be made. Fig. (10.3) shows the meridional sections in the actual bulge test. It can easily be found that the equivalent sphere is always smaller than the actual bulge although the deviation is small for both the initial and stable regimes. In general, the meridional section of the actual bulge departs more severely towards the die bulge.

(ii) <u>the tangent sphere at the rim</u>

The radius of curvature of this equivalent sphere is the average slope of the (r against sin ϕ) curve. This is obtained by calculating the slope of the chord passing through r = 0 and r = a (= 3 in in this project).

$$R_{eq} = (\rho_\theta)_{r=3} \tag{8.20}$$

It is obvious that this equivalent sphere cannot be obtained because of the condition $\phi = 0$ at $r = a = 3$ chosen for this project.

(iii) <u>Spherical segment of the same rim and polar height</u>

This equivalent sphere has its meridional section passing through the polar height and r = a, Fig. (2.2). Thus, by geometry, the radius of the sphere

$$R_{eq} = \frac{a^2 + H^2}{2H} \tag{8.21}$$

Past literature (2)-(8), (10)-(13) shows that equivalent spheres of this type are often assumed in the analysis of the bulge test. However, comparison with the actual specimen indicates that meridional section of the equivalent sphere at any value of r is always higher than the true bulge at the corresponding r, Fig. (10.3).

On discussing Brown and Sachs' method (4), for contour measurement in Chapter 4, it is indicated that an analytical comparison between the actual and estimated curvatures may be made. Let ρ_θ and ρ be the actual circumferential radius of curvature and the estimated value by Brown and Sachs' method respectively. Then,

$$\rho_\theta = \frac{r}{\sin\phi}$$

and

$$\rho = \frac{r^2 + d^2}{2d}$$

so that

$$\rho_\theta : \rho = 2 : \sqrt{1 + (\frac{d}{r})^2} \tag{8.22}$$

In order that Brown and Sachs' radius be equal to the actual radius of curvature, the following condition must hold at any position on the bulge concerned:

$$\frac{d}{r} = \sqrt{3}$$

and

$$\phi = 60^\circ \tag{8.23}$$

In general, the profile angle does not exceed this value of 60° so that from Eq. (8.22), the actual circumferential radius of curvature is always greater than Brown and Sachs' radius, Fig. (8.13).

Chapter 9

FLOW STRESS IN SHEET MATERIAL FORMED BY HYDRAULIC PRESSURES

From the variations of the N-values shown in Fig. (8.9), it is possible to deduce the variations of the stresses in the shell. For the sake of clarity, the forces per unit length of section will be considered first, namely ($\sigma_\theta t$) the force per unit length of the meridian section, and ($\sigma_s t$) the force per unit length of the circumferential section. The approach of the present analysis is valid for any sort of N distribution curves.

The basic equations necessary for the analysis have all been introduced in earlier chapters and are summarised in the following section.

(A) Basic equations

(i) Sphericality

$$N = 1 - \frac{r}{\rho_\theta}\frac{d\rho_\theta}{dr} = 1 - \sin\phi \frac{d\rho_\theta}{dr} \qquad (7.3)$$

Thus, when $\frac{d\rho_\theta}{dr} > 0, \quad N < 1$

$$\frac{d\rho_\theta}{dr} = 0, \quad N = 0$$

$$\frac{d\rho_\theta}{dr} < 0, \quad N > 1$$

(ii) Meridional tension

$$\sigma_s t = \frac{p}{2}\rho_\theta \qquad (2.8)$$

and hence
$$\frac{d(\sigma_s t)}{dr} = \frac{P}{2}\,\frac{d\rho_\theta}{dr} \qquad (9.1)$$

along the profile for every stage of deformation.

Thus, when
$$\begin{array}{llll}
\dfrac{d\rho_\theta}{dr} > 0 \, , & \dfrac{d(\sigma_s t)}{dr} > 0 & \text{and} & N < 1 \\[2ex]
\dfrac{d\rho_\theta}{dr} = 0 \, , & \dfrac{d(\sigma_s t)}{dr} = 0 & & N = 1 \\[2ex]
\dfrac{d\rho_\theta}{dr} < 0 \, , & \dfrac{d(\sigma_s t)}{dr} < 0 & & N > 1
\end{array}$$

(iii) Circumferential tension

From Eq. (3.2),

$$\sigma_\theta t = (2-N)\sigma_s t \qquad (9.2)$$

and
$$\frac{d(\sigma_\theta t)}{dr} = (2-N)\frac{d(\sigma_s t)}{dr} - (\sigma_s t)\frac{dN}{dr} \qquad (9.3)$$

If $\dfrac{d(\sigma_\theta t)}{dr} = 0$, then

$$(\sigma_s t)\frac{dN}{dr} = (2-N)\frac{d(\sigma_s t)}{dr} \qquad (9.4)$$

Eq. (9.4) means that

when
$$\left.\begin{array}{llll}
\dfrac{dN}{dr} > 0 \text{, then} & \dfrac{d(\sigma_s t)}{dr} > 0 & \text{and} & \dfrac{d\rho_\theta}{dr} > 0 \\[2ex]
\dfrac{dN}{dr} = 0 \, , & \dfrac{d(\sigma_s t)}{dr} = 0 & & \dfrac{d\rho_\theta}{dr} = 0 \\[2ex]
\dfrac{dN}{dr} < 0 \, , & \dfrac{d(\sigma_s t)}{dr} < 0 & & \dfrac{d\rho_\theta}{dr} < 0
\end{array}\right\} \quad \text{for} \quad \frac{d(\sigma_\theta t)}{dr} = 0$$

(B) Forces involved in the bulge test

It hasbeen clearly shown in Chapter (8.C) that the surface of a diaphram under hydraulic pressure is locally a sphere only at the pole and at an annular ring whose position shifts towards the die edge as deformation progresses. At everywhere before this annular ring is reached from the pole, the curvature is prolate and becomes oblate after this ring is passed, Fig. (8.9). The stable regime, representing typical deformation of the bulge test, is chosen for the present analysis because it represents the typical deformation in the bulge test. Also this approach of analysis is applicable to both the initial and unstable regimes.

By virtue of the equations in Section A of this Chapter, $\frac{d\rho_\theta}{dr}$ is always positive and the meridional tension is monotonic increasing in the region of prolateness (path abc in Fig. (9.1)). When the annular region of unity N is reached, $\frac{d(\sigma_s t)}{dr} = 0$ and this corresponds to maximum meridional force (point C). Therefore, for successive deformations, a locus for $\frac{d(\sigma_s t)}{dr} = 0$ representing maximum meridional force ($\sigma_s t$) can be drawn. The region of r to the right of the maximum ($\sigma_s t$) locus in Fig. (9.1) is always denoted by $\frac{dN}{dr} > 0$ with $N > 1$ and this results in having ($\sigma_\theta t$) a decreasing function over this range of r. From the N-distribution curve in Fig. (9.1), it is easy to visualise two separate features in the region to the left of $N=1$ at $r \neq 0$, or the maximum ($\sigma_s t$) locus. These features are characterised by the minima of N. Thus, in spite of the property of $N < 1$ in this region, $\frac{dN}{dr}$ is negative initially and becomes positive towards the maximum ($\sigma_s t$) locus. A locus passing through point b in Fig. (9.1) can thus be drawn to indicate minimum N ($\frac{dN}{dr} = 0$) for successive stages. The portion ab represents $\frac{dN}{dr} < 0$. Everywhere between the loci $\frac{dN}{dr} = 0$, and $\frac{d(\sigma_s t)}{dr} = 0$ (region bc) defines $\frac{dN}{dr} > 0$. After the maximum $(\sigma_s t)$ locus is passed, $\frac{dN}{dr} > 0$ and this is shown as path cd in Fig. (9.1).

Such properties are of vital importance to the circumferential force $(\sigma_\theta t)$ distribution in the bulge test. At the portion near to the pole (path ab), since $\frac{d(\sigma_s t)}{dr} > 0$ and $\frac{dN}{dr} < 0$, Eq. (9.3) requires that $\frac{d(\sigma_\theta t)}{dr} > 0$ and the circumferential force must be monotonic increasing. At everywhere of the specimen after the maximum $(\sigma_s t)$ locus is passed (path cd) both meridional and circumferential forces are decreasing functions since $\frac{d(\sigma_s t)}{dr} < 0$ and $\frac{dN}{dr} > 0$. In the area between the two loci $\frac{d(\sigma_s t)}{dr} = 0$ and $\frac{dN}{dr} = 0$ (path bc), the circumferential force becomes monotonic decreasing although the meridional tension is still increasing.

These three distinctive properties of ab, bc and cd in Fig. (9.1) requires the force distribution curve in the cartesian coordinates to be spiral in the clockwise direction towards the die edge, Fig. (9.2). This figure is obtained by plotting $(\sigma_\theta t)$ against $(\sigma_s t)$ and the 45 degrees line represents equal forces with unity N. The four boundary conditions a, b', c and d in Fig. (9.2) will then have some physical importance in the analysis of the bulge test. Point a represents the state of force at the pole and is at some point on the line N=1. Point b' is the position r in the specimen where the resultant force is maximum and this corresponds to a point having passed the minimum N value with N still less than unity but its gradient

$\frac{dN}{dr}$ becomes positive. Point d is the condition at the die edge.

When the force distribution curve in Fig. (9.2) intersects the N=1 line again at c, the local surface is temporarily a sphere and it can easily be shown that ρ_θ is a maximum and the tangent at c in Fig. (9.2) then becomes vertical, giving $\frac{d(\sigma_s t)}{dr} = 0$. The locus of this point c for successive stages is then represented by a horizontal line N=1 and the $\frac{d(\sigma_s t)}{dr} = 0$ locus in Fig. (9.1).

It is seen that the position vector at point b' in Fig. (9.2) has always a maximum value, meaning greatest resultant force occurs at that part in the specimen. The locus of b' for successive stages then represents the locus of maximum resultant force which, from Figs. (9.3) to (9.5), occurs at $r = 1$ in in the initial regime (since the bulge takes only approximately one shape); $1.0 < r < 1.45$ in in the stable regime and finally $1.70 < r < 1.80$ in in the unstable regime. That maximum resultant force does not occur at the pole can be explained by the following analysis.

Let $\bar{F}$ be the resultant force. By vector algebra,

$$\bar{F}^2 = (\sigma_\theta t)^2 + (\sigma_s t)^2 \tag{9.5}$$

By substituting Eq. (9.2) into Eq. (9.5),

$$\begin{aligned} \bar{F}^2 &= (\sigma_s t)^2(1 + (2-N)^2) \\ &= (\sigma_s t)^2(N^2 - 4N + 5) \end{aligned} \tag{9.6}$$

Thus,

$$\begin{aligned} \bar{F} &= (\sigma_s t)\,(N^2 - 4N + 5)^{1/2} \\ &= F_1\,F_2 \end{aligned} \tag{9.7}$$

where,

$$F_1 \equiv \sigma_s t \qquad (9.8)$$
$$F_2 \equiv (N^2 - 4N + 5)^{1/2}$$

In Eq. (9.8), F_1 is maximum along the maximum ($\sigma_s t$) locus and F_2 is maximum along the minimum N locus. Some reflection will show that the maximum resultant force must occur at some position or r ($\neq 0$) between the $\frac{d(\sigma_s t)}{dr} = 0$ and $\frac{dN}{dr} = 0$ loci, that is, between points b and c in Fig. (9.1).

The coordinate axes in Figs. (9.3) to (9.5) represent non-dimensional forces per unit sectional length which are given by

$$\frac{\sigma_s t}{R_{eq} P} = \frac{\rho_\theta}{2R_{eq}} \qquad (9.9)$$

$$\frac{\sigma_\theta t}{R_{eq} P} = (2 - N)\frac{\rho_\theta}{2R_{eq}} \qquad (9.10)$$

where Req is the radius of curvature at the pole taken from Fig. (8.4). Thus, the non-dimensional forces per unit sectional length are equal to $\frac{1}{2}$ in a spherical shell, for obvious reasons. When the shell deviates from a sphere, ρ_θ and N in Eqs. (9.9) and (9.10) deviate from R_{eq} and 1 respectively. The set of curves in Figs. (9.3) to (9.5) represent the initial, stable and unstable regimes and are plotted on different scales for clarity, but the figures overlap in order that the relative magnitude can be seen. If the surface is a sphere, the non-dimensional forces are represented by a vector drawn from the region (0,0) to the point ($\frac{1}{2}$,$\frac{1}{2}$) in Figs. (9.3) to (9.5). Thus, the curves show purely the effect of the shape on the forces in the shell, the effects of oil pressure and thickness variations having been eliminated by the grouping of the variables into non-dimensional quantities.

In Figs. (9.3) to (9.5), the vector from the origin (0,0) to the point $(\frac{1}{2},\frac{1}{2})$ serves as the norm for both the magnitude and the direction of the other non-dimensional force vectors drawn from the origin (0,0) to a point on the curves. The direction of such vectors has a definite meaning. Along the line through the origin making 45 degrees angles with the coordinate axes in Figs. (9.3) to (9.5), N is equal to one and the forces are balanced biaxial stretching forces. Above this line, N is less than unity, the shape of the shell is prolate, and the circumferential force exceeds the meridional tangential; and below this line, N is greater than unity, the shape of the shell is oblate, and the relative magnitudes of the forces are reversed. The curves for a metal shell lie between two lines through the origin (0,0) and making angles of $\tan^{-1}\frac{1}{2}$ and $\tan^{-1}2$ with the horizontal on which N is, respectively, $1\frac{1}{2}$ and 0, and the stress conditions are $\sigma_s = 2\sigma_\theta$ and $\sigma_\theta = 2\sigma_s$, respectively.

Some features of the forces per unit sectional length are noticeable in Fig. (9.3) to (9.5). Deviations from a sphere generally increase the forces (or the length of the force vectors). For the deviations from the theoretical forces in a sphere, the curves divided into three groups show that in the initial regime, Fig. (9.3), variations of the length of the force vectors are 4.9% and -5.1% (curve A as typical); in the stable regime where the variations are +7% and −5% (curve H); and for curves L and M, the variations are always increasing, being 28% and 48% respectively. The change of shape near the rim ($r = 2.4$ in) from relative prolateness ($N \doteq 1.125$ in curve A) in the initial regime via the stable regime ($N \doteq 1.20$ in curve H) to nearly spherical shape ($N \doteq 1.01$ in curves L and M) in the unstable regime is also noticeable (see also Fig. (8.9)). The explanation for all these differences between the stable and unstable regime is obviously the unstable character of the deformation of which curve K represents the beginning. Indeed, instability can occur under constant oil pressure by the very fact that even though the oil pressure is constant (as between curves K and L), the change in shape can cause relatively large increases in the forces in the shell.

(C) Flow stresses in the deformed shell

By taking into account the oil pressure P and the thickness t in Figs. (9.3) to (9.5) and Eqs. (9.9), and (9.10), the stress distribution curves can be plotted as in Figs. (9.6) to (9.8). If the shell were always a perfect sphere, each stress distribution curve would collapse into a single point on the line for $N=1$. For actual shells, only the material particle at the pole is represented by a point on this line ($N=1$) throughout the whole process, hence, in Figs. (9.6) to (9.8) the movement of the point for $r = 0$ along the line labelled $N=1$ represents the work-hardening of the material at the pole. Elsewhere, the work-hardening of the material is more complicated, because with increasing deformation, not only the magnitude of the stresses σ_θ

and σ_s increases, but the ratio between them changes also. The effect of unstable deformation on the stress distribution, already visible in Fig. (9.5) becomes conspicuous in Fig. (9.8), where curves K, L and M differ in shape even more from curves A to J than Fig. (9.5).

Comparison between Figs. (9.3) to (9.8) shows that whereas in the former the loops in the curves above the line for N=1 are all in one direction;in the latter the loops in curves I to M are in the reverse directions of those in curves A to H. This reversal is due to the effect of the variation of thickness, Figs. (10.4). The shell being always thinnest at the pole, the stress there would be greater than elsewhere even if the force per unit length were constant throughout the shell. Thus, from Figs. (9.3) to (9.8), the points near $r = 0$ are moved relative to the rest of the curve, radially outwards from the origin, and each movement is greater, the greater the variation of thickness. Owing to this distortion, it can be surmised from Fig. (9.7) that, if a curve had been plotted for $H \doteq 1.35$ in the loop would collapse into a single line and, if the stresses were then measured from the pole outwards, they would repeat themselves exactly but in the reverse order, over a certain range of radial distances.

The intensity of tri-axial stresses is measured by the effective stress in this case is that for the von Mises ellipses, as follows,

$$\sigma_\theta^2 - \sigma_\theta \sigma_s + \sigma_s^2 = \text{(a constant)} \qquad (9.11)$$

A series of von Mises ellipses are shown in Figs. (9.6) to (9.8). With these ellipses as guides, it can be seen that the greatest effective stress is not at the pole, except after some unstable deformation has taken place (curve L) and the workpiece is nearly cracking (fracture occurs at H = 2.150 in). The point of maximum effective stress remains near r = 1.0 in. until unstable deformation sets in. This particular phenomenon is very different from the uniaxial tension test in which the stress is inversely proportional to the cross-sectional area of the specimen at any particular stage so that maximum stress always occur at the thinnest section. In the bulge test, because of the antagonising effects of ρ_θ and t, only when the curvature of the bulge does not affect the stress function will maximum stress occurs at the thinnest section. This condition is valid only for a spherical bulge in which the curvature is constant over the entire specimen at a certain stage. Such a profile can never occur experimentally in the usual test method.

The fact that maximum stress does not occur at the pole where through-thickness is thinnest for both the initial and stable regimes can be explained by considering the force diagram, Figs. (9.3) to (9.5). It can easily be shown that the magnitude of the resultant stress(σ) in Figs. (9.6) to (9.8) is

$$\begin{aligned} \sigma^2 &= \sigma_s^2 + \sigma_\theta^2 \\ &= \left(\frac{\sigma_s t}{t}\right)^2 \left(1 + (2 - N)^2\right) \end{aligned} \qquad (9.12)$$

By combining with Eq. (9.6), Eq. (9.12) becomes

$$\sigma = \frac{\bar{F}}{t} \qquad (9.13)$$

Thus, if the current through-thickness strain of each specimen had been constant, then the magnitude resultant stress follows that of the resultant force vector and the position of maximum resultant stress is between the $\frac{dN}{dr} = 0$ and $\frac{d(\sigma_s t)}{dr} = 0$ loci. Similarly, for a constant resultant force vector along the bulge, maximum stress occurs at the pole where the thickness is thinnest.

In the actual specimen, neither the force ($\bar{F}$) nor thickness (t) is constant. However, Fig. (11.3) shows that before the maximum through-thickness variation of 64% (curve H) is reached the resultant stress distribution follows closely to that of the force distribution. At higher pressures, deformation begins to localise around the pole so that the position of maximum stress is shifted towards the pole until shortly before fracture, the pole has the maximum stress.

In forming processes without draw-in and neglecting the effect of the die profile, the value of N varies between 0 and 1.5, Fig. (8.9). Thus, the stress condition varies from the mean condition of balanced bi-axial stretching ($\sigma_\theta = \sigma_s$) to those of plane strain ($\sigma_\theta = 2\sigma_s$ and $\sigma_s = 2\sigma_\theta$). In the two conditions of plane strain at the extremes, at one extreme when $\sigma_\theta = 2\sigma_s$, the meridional tangential incremental strain tends to be zero, the circumferential expansion being compensated by thinning; and at the other extreme when $\sigma_s = 2\sigma_\theta$, the circumferential incremental strain tends to be zero, the stretch in the meridional tangential direction being also compensated by thinning. All the stress conditions in between these extremes may, in fact, be resolved into two components, a balanced bi-axial stretching, and a stress for plane strain (or pure shear, as it is sometimes called); thus,

$$\begin{aligned} \sigma_\theta &= \frac{\sigma_\theta + \sigma_s}{2} + \frac{\sigma_\theta - \sigma_s}{2} \\ \sigma_s &= \frac{\sigma_\theta + \sigma_s}{2} - \frac{\sigma_\theta - \sigma_s}{2} \end{aligned} \qquad (9.14)$$

where the first terms on the right-hand sides of Eq. (9.14) constitute a balanced bi-axial stretching, and the second terms constitute the stress producing plane strain, or pure shear. The ratio between these two components is, of course, a function of N, or prolateness ($\bar{P}$), thus,

$$\frac{\text{Balanced bi-axial stretching stress } \left(\frac{\sigma_\theta + \sigma_s}{2}\right)}{\text{Pure shear component } \left(\frac{\sigma_\theta - \sigma_s}{2}\right)}$$

$$= \frac{\bar{P} + 2}{\bar{P}} = \frac{3 - N}{1 - N} \qquad (9.15)$$

The balanced bi-axial stretching stress is also positive (tensile), but the pure shear component in Eq. (9.15) is positive or negative according to whether the local surface is prolate or oblate.

In Fig. (9.9), the pure shear stress is plotted against balanced bi-axial stress for the initial, stable and unstable regimes in the bulge test. The radial lines in Fig. (9.9) indicate the prolateness of the local surface obtained from Eq. (9.15); thus, the $\left(\frac{\sigma_\theta + \sigma_s}{2}\right)$ axis denotes a sphere and the negative $\left(\frac{\sigma_\theta - \sigma_s}{2}\right)$ - axis shows an oblate spheroid of N=1.5.

If the surface of a deformed shell had been a sphere for all stages, everywhere the shell would be subjected to balanced bi-axial stretching and the curves in Fig. (9.9) would collapse into a horizontal straight line. Some features of the curves in Fig. (9.9) can be observed. The loops in Fig. (9.9) are all in the same direction for stages A to H (initial and most of stable regimes) and reverse their directions after stage I (not shown), like those shown in Figs. (9.6) to Fig. (9.8). The maximum variation of the balance bi-axial stresses along the bulge increases with deformation,being 1.2 ksi for stage A and 16.2 ksi for stage L. The difference of the balanced bi-axial stresses at the pole and annular ring of spherical surface, however, does not follow this pattern. In fact, at the initial regime,the difference does increase but the amount decreases with deformation when the stable regime sets in because of the tendency to reverse the loop. As soon as the loop is reversed, the difference increases again with severity of deformation until fracture takes place. All the curves in Fig. (9.9) show that the balanced bi-axial stress at the pole is not greatest except when the workpiece is near to fracture.

The maximum variation of pure shear stresses in the sheet between the pole and die edge tends to increase in the initial regime of the bulge test but decreases in the stable regime. Curve L in Fig. (9.9) suggests that when the bulge is near to fracture, this maximum pure shear stress variation increases again tremendously. This maximum variation in terms of length along the $(\frac{\sigma_\theta - \sigma_s}{2})$ - axis consists of two parts separated by the line N=1. Thus, the length above the line N=1 represents pure shear stress variation in the prolate portion of the shell; and the length beneath the line N=1 shows the shear stress variation in the oblate region of the bulge. The shear stress in the bulged material can now be visualised clearly. In general, the shear stress variation in the prolate portion increases with deformation throughout the bulging action owing to the general increase of prolateness. However, the shear stress variation in the oblate portion increases only in the initial regime. Beyond this regime, this variation of shear stress in the oblate portion reduces its magnitude rapidly with further deformation.

Like the case of non-dimensional force per unit length, the effective stresses in the bulge test can become non-dimensional by comparing it with the effective stresses in the equivalent sphere. The equivalent sphere chosen, as seen by Eqs. (9.9) and (9.10), is the polar tangent sphere whose radius of curvature is that at the pole taken from Fig. (8.4). Thus, the ratio between the real and the equivalent effective stress (effective stress in the equivalent sphere) is given by

$$\mu \equiv \sqrt{\frac{\sigma_s^2 - \sigma_s \sigma_\theta + \sigma_\theta^2}{\left(\frac{PR_{eq}}{2t_{r=0}}\right)^2 - \left(\frac{PR_{eq}}{2t_{r=0}}\right)^2 + \left(\frac{PR_{eq}}{2t_{r=0}}\right)^2}} = \frac{\rho_\theta \, t_{r=0}}{t \, R_{eq}} \sqrt{N^2 - 3N + 3} \tag{9.16}$$

where $t_{r=o}$ and t are the thickness at the pole and some distance r respectively. Two special cases (N=1 and μ =1) for Eq. (9.16) are considered. When N=1, Eq. (9.16) is reduced to

$$\mu = \frac{\rho_\theta}{R_{eq}} \frac{t_{r=0}}{t} \qquad (9.17)$$

and for $\mu = 1$, Eq. (9.16) becomes

$$\frac{\rho_\theta}{R_{eq}} \frac{t_{r=0}}{t} \sqrt{N^2 - 3N + 3} = 1 \qquad (9.18)$$

Thus, owing to the different concepts of curvature and prolateness the effective stress ratio (μ) will not be unity even though the local surface is a sphere (N=1). Only at the pole (whose conditions are used for the fitted sphere in the present analysis) will $\mu = N = 1$. The variation of μ shown in Fig. (9.10) reveals that before instability sets in the effective stress in the real bulge is always greater and becomes smaller than that in the equivalent sphere towards the die edge. The region of larger effective stress keeps contracting with severity of deformation until at some stage in the unstable regime (2 in polar height), the effective stress in the real bulge becomes smaller than that in the equivalent sphere. This general trend of the non-dimensional stress curves can also be visualised by the stress distribution curves, Figs. (9.6) to (9.8) in that the resultant polar stress is largest in the specimen after 2 in polar height is reached, and before this height is attained, the resultant stress is always smaller than the resultant stress in most part of the specimen.

Chapter 10

DISPLACEMENTS AND STRAINS IN THE BULGE TEST

A detail study of the geometry of a real bulged specimen based on Chapters (2.A) and (7.D) is given in this Chapter. States of strain thus derived are plotted in the triangular coordinate system instead of the usual cartesian coordinate system. To serve as a basis for stress-strain relationship determination, states of strain rate are calculated and plotted in the triangular coordinate system. Whenever it is convenient, the experimental results are compared with some important theoretical results of past investigations.

(A) Displacements - longitudinal and radial

In the typical axisymmetrical forming process as shown in Fig. (2.1), a point in the blank at an initial distance r_o from the axis of symmetry moves to a new coordinate (r, ℓ) at some deformation stage T. The displacements are determined by the parametric equations given by Eq. (2.1). It is easier to show the displacements by tracing out the profile of the product at successive stages than to express Eq. (2.1) analytically. Thus, this section is aimed at considering the longitudinal and vertical displacements in a real bulge specimen.

The radial movements of each material particle can adequately be elucidated by plotting the original radius against the current radius as shown in Fig. (10.5). Owing to its almost linear relationship between the current and original radii, it is more convenient to plot $(r - r_o)$ against r_o as shown in Fig. (10.1).

The radial lines in Fig. (10.1) represent constant natural circumferential strains and the slope of these lines reads the corresponding engineering circumferential strains simultaneously.

Theoretical results of Hill (10) and Gleyzal (11) are generated and plotted on Fig. (10.1). It is seen that Hill's assumption on circular trajectory yields a smaller radial displacement than Gleyzal's parabolic strain distribution up to about 2/3 of the bulge radius (between the pole and die edge). Beyond this distance, Hill's results show a larger displacement than Gleyzal's. Curves for present experimental results on copper specimens are much lower than the theoretical curves by Hill and Gleyzal, thus indicating that the actual circumferential strain is always less severe than the predicted values. The particle trajectories in Fig. (10.3) clearly illustrates this point.

Apart from their relative magnitudes, the theoretical and experimental curves have all the same shape in that the radial displacement is non-uniform along the specimen at every stage of deformation. Gleyzal's results show that maximum displacement occur at approximately 7/12 of the bulge radius and it shifts gradually to about 1/3 of the bulge radius. Hills's theoretical results and the experimental results reveal that the position for maximum displacement, inspite of its gradual shift, occurs at almost 7/12 of the bulge radius.

Ignoring the results based on unrealistic assumptions by Hill and Gleyzal, a fallacy of theoretical results occurs at the die edge. In Fig. (10.1), all predicted curves, based on the absence of draw-in of the flange, meet at the point $r_0 = a = 3$ in. Although a serrated die set is used to prevent draw-in in experiments, the actual curves do not meet at $r_0 = a = 3$ in. In fact, the curves intersect the r_0-axis at various positions owing to the presence of the die profile to prevent tearing of specimens. To the author's knowledge, not a single investigator on theoretical prediction, including Wang and Shammamy (14), has taken the effect of die profile into consideration.

Based on the assumptions made in predictive investigations, the theoretical extent of forming of a 6 in diameter bulge can be studied by plotting the polar effective strain against the corresponding polar height as shown in the inset of Fig. (10.3). These predicted curves are used to compare with the present experimental results on copper specimens. Some conclusions on the limiting polar height can also be deduced from this inset. In the actual specimen, fracture takes place at the pole when its through-thickness strain is (-0.93) corresponding to a polar height of 2.15 in. Therefore, using this magnitude of strain as a criterion for material formability, Gleyzal's theoretical results (11), on extrapolation, would predict fracture to occur at a lower polar height of 2.05 in. Hill's solution (10) would yield a limiting polar height of 2.29 in which is well before the presence of instability (which occurs when the bulge is a hemisphere of 3 in radius for non-workhardening materials). Wang and Shammamy's theoretical solution (14) would show that fracture occurs at 2.19 in polar height.

The actual longitudinal displacements of the bulge at each stage of deformation are obtained through the measured inclination of the profile (ϕ) as

$$\iota = H - \int_0^r \tan\phi \, dr \tag{10.1}$$

where H is the polar height of the bulge and the integral in Eq. (10.1) is obtained by a planimeter. The meridional section of the deformed bulge for different severity of deformation is shown in Fig. (10.2) in which the dotted lines are the particle trajectories.

Fig. (10.3) gives an indication on how the theoretical results deviate from the actual results. As mentioned in Chapter (8.D), the actual displacements do not vary much from that of the fitted polar tangent sphere except near the die edge and in the unstable regime. For an equivalent sphere whose meridional section passes through the polar height and die edge, as used by Hill (10) and Gleyzal (11) and others (2)-(5), the vertical displacement of the equivalent sphere is always greater than that of the actual specimen. Moreover, the particle trajectories are more curved in Hill's and Gleyzal's solution except at high pressures. Wang and Shammamy's results (14) show that the bulge shape is larger with trajectories very close to the actual meridional section.

(B) General disposition of strain paths and strain distributions

As shown in Chapter (2.A), geometrical transformations of any element particle in the bulge test are sufficient to determine the triaxial strains of that element particle, Eq. (2.2). The magnitude of these triaxial strains define the state of strain and their ratios represent the mode of deformation. Metals are incompressible under normal loading conditions so that the triaxial (natural) strains have only two degrees of freedom, Eq. (2.14). Thus, as shown in Chapter (6.A), states of strain in the bulge test can graphically be represented as points in the triangular coordinate system. Not only these points can be located from experimental results for every stage in the deformation, but also along the entire specimen. These, as expressed in Eq. (2.1), constitute the strain path and strain distribution curves respectively. The material at the pole at any stage of deformation is subjected to balanced bi-axial stretching because of equal local curvatures; and the circumferential strain, for material particles at the edge of the die, is zero or nearly zero (depending on whether or not there is draw-in). Thus, the modes of deformation along the bulge profile at every stage generally cluster within the region 5 to 6 o'clock in the clock diagram for strains.

It is obvious that a strain distribution curve can only have three movements with a pressure change, relative to its original position in the triangular coordinate system. Some reflection will show that moving towards the origin from its original location indicates reversal of loading function in addition to stress relief. This reversal of loading function means the three deviatoric stresses are so adjusted that the effective stress is reduced. On the contrary, movement of the strain distribution curve away from the origin indicates an increment of effective stress. If this distribution curve remains stationary, then the loading function permissible is that the effective stress at every point in the specimen produced by this loading function should not exceed the corresponding radius of the Mises yield locus; this means no deformation at all. Thus, in the case of a continous bulge test with pressure increasing monotonically, the strain distribution curve can only move away from the origin indicating increasing effective strain in response to the increasing effective stress.

The strain paths and distribution curves for copper specimens in the bulge test are shown in Fig. (10.4) in which the solid and dotted lines represent strain paths and strain distributions respectively. The strain paths and distribution curves in the unstable regime (stage K to M) are not shown in Fig. (10.4). The strain paths for both the initial and stable regimes are seen to spread from 6 o'clock to 5 o'clock at the pole to the die edge respectively. This was explained from the mechanical constraints of the bulge test in a previous paragraph. The strain paths in the initial regime (stage A to E) are nearly radial along the specimen towards the die edge, indicating an almost constant strain ratio for any particular element particle during successive deformations. The strain paths in the stable regime (stage F to J) are not radial so that every particle element is subjected to a different strain ratio at a different stage of deformation. It is seen in Fig. (10.4) that, up to 1.4 in from the pole, smooth strain paths can be drawn linking the two regimes of deformation. Whereas for element particles beyond 1.4 in from the pole, such smooth strain paths cannot be drawn.

The characteristic index (η) of any state of strain can be decided by Eq. (7.1), or simply by the definitions of ε_θ and ε_s. Thus,

$$\begin{aligned} \varepsilon_s - \varepsilon_\theta &= \log_e \left(\frac{dr}{dr_o} \, \frac{r_o}{r} \, \frac{1}{\cos\phi} \right) \\ &= \log_e \left(\frac{d(\log_e r)}{\cos\phi \; d(\log_e r_o)} \right) \end{aligned} \tag{10.5}$$

Obviously, for any stage of deformation, the bracketed term in Eq. (10.5) must have some positive values, that is,

$$\frac{dr}{dr_o} \, \frac{r_o}{r} \, \frac{1}{\cos\phi} > 0 \tag{10.6}$$

since r_o and r are positive quantities and $\phi < \frac{\pi}{2}$, Eq. (10.6) can be simplified to

$$\frac{dr}{dr_o} > 0 \tag{10.7}$$

meaning r must increase with r_o. This condition is shown in Fig. (10.5). It is clearly shown in Eq. (10.5) that the characteristic index (η) in the bulge test is greater or less than 6 o'clock depending on whether $\left(\frac{dr}{dr_o} \, \frac{r_o}{r} \, \frac{1}{\cos\phi}\right)$ is less or greater than unity respectively. For the curves plotted in Fig. (10.4), all the strain distribution curves lie in the region $5 < \eta \leqslant 6$ regardless of the N variation in the shell, unlike the stress distribution curve that vary according to the local prolateness of the shell. This condition of strain distribution curves requires that

$$\frac{dr}{dr_o}\,\frac{r_o}{r}\,\frac{1}{\cos\phi} > 1$$

or (10.8)

$$\frac{d(\log_e r)}{d(\log_e r_o)} > \cos\phi$$

Therefore, by knowing the function $r = r\,(r_o)$ of any element particle in the shell, the minimum value of ϕ satisfying Eq. (10.8) can be obtained. Conversely, for any given function of $r = r\,(r_o)$ and $\phi = \phi\,(r_o)$, the characteristic index is known. The following is an example to illustrate this point. The (r against r_o) curves shown in Fig. (10.5) may be fitted by an equation

$$r^{\alpha} = k r_o \qquad \text{and} \qquad \alpha\,,\, k > 0 \tag{10.9}$$

so that

$$\frac{d(\log_e r)}{d(\log_e r_o)} = \frac{1}{\alpha} \tag{10.10}$$

Thus, in order to have $\varepsilon_s > \varepsilon_\theta$ always, Eqs. (10.8) and (10.10) require always

$$\cos\phi < \frac{1}{\alpha} \tag{10.11}$$

The magnitude of α will then decide the minimum angle ϕ that gives the condition $\varepsilon_s > \varepsilon_\theta$. When $\alpha < 1$, then the state of strain at everywhere along the bulge profile lies in the region $5 < \eta \leq 6$ because $\cos\phi$ is always less than unity as soon as deformation begins. For $\alpha > 1$, then there is a minimum value of angle for which Eq. (10.11) holds.

Some reflection will show that when the angle ϕ measured in experiments is less than $\cos^{-1}(\frac{1}{\alpha})$, then the state of strain will lie in the region $6 < \eta < 7$. This is clearly shown in the unstable regime of deformation in Fig. (10.6) in which stage L is typical. Therefore, the implication of Eq. (10.5) is significant to the predictive theory of the bulge test. It is noticed also that Wang and Shammamy's theoretical results show the presence of a loop at low pressures ($\varepsilon_o = 0.3$, Fig. 4 of ref. (14)).

(C) Strain rates in the bulge test

Having obtained states of strain involved in the bulge test, it is permissible to pursue towards the strain rates. Strain rates expressed in terms of time (T) though mathematically required, are difficult to acquire because of the experimental difficulty in time measurements. Thus, it is convenient to express strain rates in terms of polar height (H).

Just like strains, the principal strain rates have only two degrees of freedom as shown in Eq. (2.14) so that the triangular coordinate system may be used in the analysis of strain rates. In order to comply with the use of this coordinate system for strains, the vertical axis denotes the through-thickness strain rate; and the left- and right-hand axis represent the circumferential and meridional tangential strain rates respectively. Some reflection will show that, when such a coordinate system is used, the state of strain rate $(\dot{\varepsilon}_t, \dot{\varepsilon}_\theta, \dot{\varepsilon}_s)$ is shown as a point in the coordinate system and is obtained by differentiating the strain path at the point $(\varepsilon_t, \varepsilon_\theta, \varepsilon_s)$ also in the triangular coordinate system. The direction of the radial line passing through the origin and ($\dot{\varepsilon}_t$, $\dot{\varepsilon}_\theta$, $\dot{\varepsilon}_s$) is also that of the tangent at that point (ε_t, ε_θ, ε_s) on the strain path.

States of strain rates in the bulge test for initial and stable regimes of deformation are shown in Figs. (10.7) and (10.8) respectively. It is easily seen in these figures that the instantaneous mode of deformation at any instant in the bulge test is confined only to half-past five and six o'clock. The strain rate paths are broader in the initial regime as compared to the reversed phenomenon in the case of strain paths (Fig. (10.4)). This is because the strain paths in the stable regime tend to curve towards 6 o'clock whereas those in the initial regime emerge almost radially towards 5 o'clock. The strain rate paths will be used in the following chapter to study the stress-strain relationship of the test material in the bulge test.

Chapter 11

STRESS-STRAIN RELATIONSHIP IN THE PLASTIC RANGE, WITH SPECIAL REFERENCE TO THE BULGE TEST

Having obtained the flow stresses and the corresponding strains involved in the bulge test, the stress-strain relationship or the work-hardening characteristics of the test material subjected to hydrostatic pressures can be studied. Unlike from past investigations (19)-(27) using only scalar quantities of stress and strain vectors, it is proposed in this project to study the work-hardening characteristics in the vectorial form.

As discussed in Chapter (5.A), any flow stress consists of its hydrostatic and deviatoric component, Eq. (5.5), responsible for elastic and plastic deformation respectively. In the present analysis, the hydrostatic component is ignored since only large plastic strains are considered. The deviatoric stress components (σ'_t , σ'_θ , σ'_s) of the bi-axial principal stresses (σ_s, σ_θ) in the bulge test can be seen to have only two degrees of freedom, Eq. (6.15), and that both the direct and projection methods may be used to express graphically states of deviatoric stress for any stress system in the triangular coordinate system Chapter (6.B). Therefore, before proceeding to the study of stress-strain relationship of the test material in the bulge test, the deviatoric stresses in the test specimens are discussed.

(A) Relation between deviatoric stresses and prolateness

Chapter (6.B) shows that the direct and projection methods for representing states of deviatoric stresses in the triangular coordinate system are interchangeable merely by rotating the coordinate axes by 30 degrees. In order that the coordinate axes for deviatoric stresses be superposable onto the coordinate axes for strains, states of deviatoric stresses for the present project are obtained by the direct method. Thus, the vertical axis denotes the through-thickness deviatoric stress and the left and right hand axes represent the circumferential and meridional-tangential deviatoric stresses respectively. Just like the case for strains, a characteristic index for deviatoric stress (ζ) defining the deviatoric stress ratios is defined. Thus, 6 o'clock represents balanced bi-axial stretching ($\sigma_\theta = \sigma_s$) and the three coordinate axes represent uniaxial tension.

It is possible to relate any state of deviatoric stress to the local sphericality of the deformed shell by including the index of sphericality (N) into the clock diagram. By the definitions of σ_s and σ_θ given by Eqs. (2.8) and (2.9) the hydrostatic and deviatoric stresses are

$$\begin{aligned} \sigma_o &= \frac{3-N}{3}\sigma_s \\ \sigma'_s &= \frac{N}{3}\sigma_s \\ \sigma'_\theta &= \frac{3-2N}{3}\sigma_s \end{aligned} \qquad (11.1)$$

and hence $\sigma'_t = \frac{N-3}{3}\sigma_s = -\sigma_o$

The expressions in Eq. (11.1) can become dimensionless by dividing the stresses on the left hand side of the equality sign by the meridional-tangential stress. Thus,

$$\frac{\sigma_o}{\sigma_s} = \frac{3 - N}{3} = -\frac{\sigma'_t}{\sigma_s}$$

$$\frac{\sigma'_s}{\sigma_s} = \frac{N}{3} \qquad (11.2)$$

$$\frac{\sigma'_\theta}{\sigma_s} = \frac{3 - 2N}{3}$$

These non-dimensional stresses in Eq. (11.2) are only functions of the index of sphericality (N) so that when they are plotted against N, $\frac{\sigma'_s}{\sigma_s}$ is a radial straight line (OB) of slope 1/3, Fig. (11.1); $\frac{\sigma'_\theta}{\sigma_s}$ is also a straight line (AB) of slope $(-\frac{2}{3})$ passing through the coordinate (0,1). Similarly, the dimensionless deviatoric through-thickness stress curve is also a straight line (CD) of slope (1/3) passing through the point (0,-1) in Fig. (11.1). The two straight lines AB and OB intersect at N=1, thus forming a triangle having vertices of coordinates O(0,0), A(0,1) and $B(1,\frac{1}{3})$. Moreover, for any given value of N, it can easily be shown that the prolateness of the shell corresponding to this N value is given by the vertical distance between the two sides (AB and OB) of the shaded triangle OBA in Fig. (11.1). The dimensionless hydrostatic stress, from Eq. (11.2) is equal to the absolute value of the dimensionless deviatoric thickness stress or to the distance between OB and the horizontal line passing through point A in Fig.(11.1).

The above analysis suggests the possible use of N value onto the clock diagram for deviatoric stress so that prolateness

($\overline{P} \equiv 1-N$) can be related to the characteristic indices (ζ) as shown in Fig. (11.2). The insets in Fig. (11.2) for $2 < \zeta < 8$ show the meridional section of constant N surfaces which are discussed in Fig. (3.4). Thus, it is seen that within this region of $2 < \zeta < 8$, the surface is prolate only when $6 < \zeta \leq 7$ and at everywhere of $2 < \zeta < 6$, the surface is always oblate. For the special case of $\zeta = 6$, the surface is spherical. Some reflection will show that the surface of shell is always closed for $2 < \zeta < 7$ and becomes open in the region $7 < \zeta < 9$.

(B) Deviatoric stresses in the bulge test

States of deviatoric stress for copper specimens, obtained by the direct method, are shown in Fig. (11.3). It can be deduced from Fig. (11.3) that the deviatoric stress paths have three different families representing the initial, stable and unstable (not shown) regimes. These paths for the initial regime of deformation are nearly radial, especially for $0 < r_o < 1.6$ in. For the stable regime, however, the deviatoric stress paths are more curved when $r_o > 0$ in. and broader than the curves in the initial regime. The direction of widening of the range of ζ, however, does not occur in the region near to the pole of the bulge so that the deviatoric stress paths have a maximum shift towards 5 o'clock at the die edge. The reason for this phenomenon can be explained by the N distribution curves, Fig. (8.9), and their effects on the clock diagram which are shown in Fig. (11.2).

The initial deformation characterised by curve A in Fig. (8.9) reveals that the local sphericality is less prolate before and less oblate after the annular ring of perfect sphere is reached on comparing with the sphericality at the beginning of the stable deformation (stage F) so that widening of the ζ-range is resulted from the initial to the stable regimes of deformation. Since the change of N values at any particular element particle through successive stages in the initial regime is minute, Fig. (8.10), the deviatoric stress paths in the clock diagram are therefore necessarily nearly radial.

In the main part of the stable deformation (curves F to J), the general trend is increasing prolateness so that the deviatoric stress paths have to curve towards the left of $\zeta = 6$ line as shown in Fig. (11.3). As forming progresses, the prolate region expands outwards when unstable deformation leads quickly to fracture, the whole shell is prolate. Thus, although not shown in Fig. (11.3), it is possible to visualise the deviatoric stress paths, especially near the die edge, to be more drastically curved towards the prolate region of the clock diagram ($6 < \zeta < 7$) so that the entire stress distribution curve lies within this region.

As discussed in Chapter (8.C), the deformed shell is divided into two zones by an annular ring of perfect spherical surface ($N = 1$), prolate inside the oblate outside it. Moreover, the local sphericality at the pole of the bulge is always a perfect sphere. It may be concluded that, in the clock diagram for deviatoric stresses, the strain distribution curve at any severity of bulging must intersect the $\zeta = 6$ line twice; thus forming a loop in the region of prolateness $(6 < \zeta < 7)$.

The direction of the loops in the clock diagram in Fig. (11.3) can easily be seen by considering the meridional-tangential stress condition at the pole and annular ring of perfect sphere. At these two positions in the bulge, N is unity and from Figs. (9.6) and (9.8), it can easily be deduced from Eq. (11.1) that the loops emerge in the counter-clockwise direction for stages A to F and then reverse their directions to clockwise from stage G onwards to fracture.

(C) Work-hardening characteristics - general considerations

It has been indicated in Chapter 6 that in the uniaxial tension test, one significant stress and strain are sufficient to determine the stress-strain relationship. Thus,

$$\sigma = \sigma(\varepsilon)$$

or $\qquad\qquad\qquad\qquad\qquad\qquad\qquad\qquad\qquad\qquad$ (11.3)

$$\sigma = \left(\frac{\sigma}{\varepsilon}\right)\varepsilon$$

where σ and ε are the significant stress and strain respectively; and $\left(\frac{\sigma}{\varepsilon}\right)$ is the tangent of the angle as shown in Fig. (11.4). This stress-strain relationship is restricted by the condition of monotonic increments, otherwise, the stress-strain is not valid, because the curve in unloading and reloading is a-b-c.

In unbalanced bi-axial stretching, the stresses and strains involved are in two dimensions. Then treating the problem as a graphical problem only, the effective stress $(\bar{\sigma})$ and effective strain $(\bar{\varepsilon})$ vectors are related by

$$\bar{\sigma} = \begin{vmatrix} a_{11} & a_{12} \\ a_{21} & a_{22} \end{vmatrix} \cdot \bar{\varepsilon} \qquad (11.4)$$

where the matrix corresponds to ($\frac{\sigma}{\varepsilon}$) in the unidirectional case, Eq. (11.3). The form which the matrix $|a_{ij}|$ takes is

$$\begin{aligned} \sigma_1 &= a_{11}\varepsilon_1 + a_{12}\varepsilon_2 \\ \sigma_2 &= a_{21}\varepsilon_1 + a_{22}\varepsilon_2 \end{aligned} \qquad (11.5)$$

There are four unknowns in Eq. (11.5), hence the problem is underdetermined and there are an infinite number of solutions. Among all the possible solutions it is desirable to take one which contains the most significant element. Thus, it is proposed to use

$$\bar{\sigma} = m \begin{vmatrix} \cos\psi & -\sin\psi \\ \sin\psi & \cos\psi \end{vmatrix} \cdot \bar{\varepsilon} \qquad (11.6)$$

where m has the dimensions of stress and ψ is an angle shown in Fig. (11.5). The initial value of m is infinity (at the yield point of the initial material) - as in the case of ($\frac{\sigma}{\varepsilon}$) in the tension test, when ε represents the plastic strain only.

Both m and ψ are functions of time T, and the functions are understood to be restricted to:

(i) monotonic increasing T

(ii) the particular strain (or stress) path.

The forms of the functions m(T) and ψ(T) are constrained by the laws of plasticity. These constraints can be explored as follows.

By geometry, $d\bar{\varepsilon}$ in the triangular coordinate system is tangent to the strain path (assumed continuous). This tangent is normal to the current yield locus. By the normality rule, the direction of the incremental stress has no effect on the direction of the incremental strain - the tangent of the strain path is fixed in direction. In other words, under any continuously loading stress path, the strain path is always a smooth curve, or a curve of which the slope is continuous in T.

Suppose the incremental stress can vary in direction. For a smooth yield locus, if the stress is a loading one, its increment can only vary by 180 degrees. In such a variable incremental stress, it is reasonable to believe that the neutral component is ineffective with regard to plastic deformation, Fig. (11.6). Thus,

$$d\bar{\sigma} \cdot d\bar{\varepsilon} = \text{constant (with respect to the direction of } d\bar{\sigma}\text{)} \qquad (11.7)$$

In other words, the most effective incremental stress is along the tangent of the strain path. It is therefore only necessary to define the strain hardening for the incremental stress along the tangent of the corresponding point in the strain path, called $d\bar{\sigma}^*$, say. Once this is defined, then

$$\left|\frac{d\bar{\sigma}}{d\bar{\varepsilon}}\right| = \frac{\dfrac{|d\bar{\sigma}^*|}{|d\bar{\varepsilon}|}}{\dfrac{d\bar{\sigma} \cdot d\bar{\varepsilon}}{|d\bar{\sigma}|\,|d\bar{\varepsilon}|}} \qquad (11.8)$$

At neutral loading, the numerical value of this strain hardening coefficient becomes infinity.

Assuming loading incrementally along the tangent to the strain path; and further $d\bar{\sigma}^*$ is parallel to $d\bar{\varepsilon}$, then the properties of the prestrained material is defined by ξ,

$$\xi \equiv \frac{|d\bar{\sigma}^*|}{|d\bar{\varepsilon}|} \tag{11.9}$$

where $d\bar{\sigma}^* \times d\bar{\varepsilon} = 0$ (in vector form)

This equation is formally similar to the Levy-Mises flow rule, which is

$$\bar{\sigma} \times d\bar{\varepsilon} = 0 \tag{11.10}$$

The properties of the pre-strained material (ξ) may be called the true work-hardening coefficient.

In actual forming, $d\bar{\sigma}$ is along the tangent of the stress path. Then

$$\cos\gamma = \frac{\frac{d\bar{\sigma}}{dT} \cdot \frac{d\bar{\varepsilon}}{dT}}{\left|\frac{d\bar{\sigma}}{dT}\right| \left|\frac{d\bar{\varepsilon}}{dT}\right|} \tag{11.11}$$

where γ is the angle between $d\bar{\sigma}$ and $d\bar{\varepsilon}$. Combination of Eqs. (11.8) and (11.9) yields

$$\left|\frac{d\bar{\sigma}}{d\bar{\varepsilon}}\right| = \xi \cos\gamma \tag{11.12}$$

This is the operative strain-hardening coefficient (scalar). Further, from Eq. (11.11), we have

$$d\bar{\sigma} = \frac{\xi}{\cos\gamma} \begin{vmatrix} \cos\gamma & \mp\sin\gamma \\ \pm\sin\gamma & \cos\gamma \end{vmatrix} \cdot d\bar{\varepsilon} \qquad (11.13)$$

The matrix in Eq. (11.13) is the operative strain hardening coefficient (vector).

(D) Validity of Levy-Mises flow rule in the bulge test

For the special case in which the Levy-Mises flow rule is obeyed in the plastic range, then the relationship of the current stress and incremental strain is given by Eq. (11.10) In other words, with suitable selection of the scales, the deviatoric stress and incremental stress paths can be made to be identical in the triangular coordinate system. Therefore, $d\bar{\varepsilon}$ and hence $d\bar{\sigma}^*$ is parallel to the current stress vector and Eq. (11.11) becomes the cosine of the angle between the current and incremental stress vectors.

Test for the validity of this flow rule on the unstable regime of deformation in the bulge test is not made. Fig. (11.7) shows how the Levy-Mises flow rule is violated in the initial regime. It is seen that the strain rate vector always leads the current stress vector by less than 8 degrees. Except near to the die edge, the degree of violation appears to reduce with increasing polar height. Similarly, the maximum variation of τ (angle between $\bar{\sigma}$ and $d\bar{\varepsilon}$) seems to increase towards the die edge, being 20% at $r_o = 0.6$ in to 34.5% at $r_o = 2.0$ in.

In the stable regime of deformation, a main portion of the bulge has strain rate vectors leading the current stress vector ($0 < r_o < 2.2$ in), Fig.(11.8). At $r_o = 2.4$ in, the strain rate vector lags behind the current stress vector, (not shown). The pattern of violating the flow rule is different from that in the initial regime. Between $0.6 < r_o < 1.0$ in, violation tends to ease off with further deformation; whereas the reverse effect occurs in the region $1.0 < r_o < 1.8$ in. Results at positions greater than $r_o = 2.0$ in are neglected because the effect of bending may be appreciable. The maximum variation of angular difference (τ) is 59% at $r_o = 0.6$ in and 35% at $r_o = 1.6$ in. Therefore, it may be seen that although the angular difference (τ) is generally smaller in the stable regime, the value τ is more susceptable to change with deformation.

From Figs. (11.7) and (11.8), it is conveneient to regard the Levy-Mises flow rule is violated by an average value of 5 degrees with strain rate vector leading in order to visualise the significance of this magnitude of angular difference. Let $|d\bar{\sigma}'|$ be the projection of the stress increment $|d\bar{\sigma}|$ onto the current stress vector $\bar{\sigma}$ produced. Then,

$$\frac{|d\bar{\sigma}^*| - |d\bar{\sigma}'|}{|d\bar{\sigma}^*|} = 1 - \frac{\cos(5^\circ + \gamma)}{\cos\gamma}$$

$$= 0.0038 + 0.0872 \tan\gamma \qquad (11.14)$$

In the actual bulge test, the angle γ does not exceed 20 degrees up to 2.2 in as shown in Fig. (11.9) so that Eq. (11.14) becomes

$$\frac{|d\bar{\sigma}^*| - |d\bar{\sigma}'|}{|d\bar{\sigma}^*|} = 0.0038 + 0.0872 \tan 20^\circ$$

$$\doteq 3.6\% \qquad (11.15)$$

Therefore, from the practical point of view, commercially soft copper can be considered to obey the Levy-Mises flow rule in the bulge test.

(E) Work-hardening characteristics in the bulge test

In spite of the minute error (maximum 3.6%) caused by regarding the test material to obey the Levy-Mises flow rule, it is of academic interest to study the work-hardening characteristics in the general case in which the flow rule is invalid.

The vectorial operative work-hardening coefficient given in Eq. (11.13) is shown in Fig. (11.9) in terms of the angle γ defined in Fig. (11.6). It is seen in Fig. (11.9) that at the region near to the pole ($r_o < 1.0$ in), the angle between $d\bar{\varepsilon}$ and $d\bar{\sigma}$ remains unchanged, being 3.5 degrees at $r_o = 0.6$ in and 4.4 degrees at $r_o = 1.0$ in. This means that up to 1/3 of the bulge radius, a change in the incremental strain direction will lead to an equal change of direction in the incremental stress vector. Beyond 1/3 of bulge radius, however, the response of $d\bar{\sigma}$ is retarded so that the angle γ increases exponentially with original radius for every stage of deformation. The reason for this is that near to the pole, the stress paths are very linear whilst at the die edge region, the stress paths become very curved.

The scalar operative work-hardening coefficient for the initial and stable regimes of deformation are shown in Figs. (11.10) and (11.11) respectively. These coefficients are obtained by differentiating the length of the stress path ($\int d\bar{\sigma}$)

with respect to the length of the strain path ($\int d\bar{\varepsilon}$). It is seen that the work-hardening coefficients decrease with deformation and they exist in two ranges - one at $\int d\bar{\varepsilon} < 0.15$ and the other at $0.15 < \int d\bar{\varepsilon} < 0.4$. With reference to the stress paths shown in Fig. (11.3), it can be seen that the stress ratios (σ_θ/σ_s) are very nearly constant for each stress path. Thus, the curves in Figs. (11.10) and (11.11) can be viewed as the operative work-hardening characteristics at various stress ratios between $0.75 < \sigma_\theta/\sigma_s < 1.16$.

By taking in account the vectorial operative work-hardening coefficient, the true work-hardening characteristics (ξ) can be obtained and are plotted in Fig. (11.12) for various stress ratios. The shape of the curves are similar to those in Figs. (11.10) and (11.11) and for obvious reasons, the operative and true work-hardening coefficients are identical for unity stress ratio. The stress ratio of 0.75 at r_o = 2 in is only approximate because at this position in the bulge, the stress path is already very curved.

Generalised stress-strain relationship of the form given in Eq. (4.15) is frequently used to determine the work-hardening property of the test material. The stress-strain relationship of copper specimens in the bulge test is plotted in natural logarithmic scales as shown in Fig. (11.13). It is seen that the work-hardening exponent (n) in terms of the gradient of the straight lines varies with the original radii in the specimen. This variation is due to the different strain ratios along the workpiece. The relationship between the work-hardening exponent (n) is shown in Fig. (11.14). Since the bulge is subjected to unbalanced bi-axial stretching, the work-hardening exponent (n) is plotted against stress ratio, Fig. (11.14). It is seen that there are two ranges of n-values for the same stress or strain ratio - one at $\varepsilon_o < 0.14$ and the other at $0.14 < \varepsilon_o < 0.40$. Thus, the stress-strain relationship of metals in the bulge test is a complicated function of time (and hence polar effective strain) and stress ratio.

Chapter 12

INSTABILITY IN THE BULGE TEST

It has been observed in Chapters 8 to 11 that the bulge test consists of three regimes of deformation - initial, stable and unstable regimes. Both the initial and stable regimes have already been discussed in depth in these chapters. Instability has arbitrarily been chosen to commence at stage K . The chapter is then aimed at a detail study of the instability phenomenon of commercially soft copper sheets undergoing the bulge test.

As seen in Chapter (4.E), all analyses of instability are based on the maximum pressure criterion proposed by Sachs and Lubahn (28), who considered instability to occur at the pole of the bulge. Having obtained the condition of instability, Eq. (4.16), minor variations exist among different investigators so that different theoretical results are arrived at, Fig. (12.1). It appears in Fig. (12.1) that the theoretical results by Swift (29) and Wang and Shammamy (14) tend to envelop all theoretical investigators. Mellor's experimental results (5) for various materials plotted in Fig. (12.1) show that none of the investigators has accurately predicted the instability polar strain. This may be due to the difficulty in fitting the stress-strain curve.

To by-pass the difficulty of fitting the stress-strain curve, a graph of polar strain at instability against polar height for isotropic material is plotted in Fig. (12.2) for various authors. In the present project on soft copper specimens, based on the maximum pressure criterion, instability should occur at a polar height of 1.86 in from the pressure against polar height curve, Fig. (12.3). Thus, instability of copper specimens occurs when the polar height is approximately $\frac{5}{8}$ of the die hole radius compared to $(\frac{H}{a} = 1)$ by Hill (10) for non-workhardening materials and $\frac{H}{a} = \frac{1}{\sqrt{3}}$ by Ross and Prager (12). It is found in Fig. (12.3) that Wang and Shammamy's prediction (14) agrees with the present result on soft copper specimens.

Instability of the bulge material can occur under constant oil pressure by the very fact that even though the oil pressure is constant, the change in shape can cause relatively large increases in the forces in the shell. Thus, excessive thinning occurs in the material until fracture eventually takes place. On referring to the flow stress curves in Fig. (9.8), instability occurs after the loop of the stress curve has already reversed its direction and the maximum effective stress at the pole begins to be the greatest, as compared to those along the profile at that polar height. The effective stress at the pole then continues to be the greatest until fracture takes place. This phenomenon is readily observed in Fig. (11.3).

Some metals, such as medium steels, do not possess an instability point so that theoretically they do not become unstable. It is convenient to select a suitable criterion in order that all metals in the bulge test pass through the instability point before fracture occurs. The following is an attempt to propose a new criterion for instability.

It is convenient at this stage to fit the actual meridional profile by a sphere passing through the die edge (a = 3 in) and the polar height (H). Thus, the equivalent sphere has a radius (Req) calculated by Eq. (8.21). When Req is plotted against the oil pressure (P) shown on the left side of Fig. (12.4), a smooth curve can be drawn through the initial regime of deformation and a large portion of the stable regime. It has been arbitrarily defined in previous chapters that the stable regime includes stages F to J. After some stage of deformation (887 psi), the (Req against P) locus begins to curl downwards, passing through the point of maximum pressure and then towards the Req-axis until fracture occurs(stage M). At this fractured stage, the magnitude of Req is minimum. The dotted line in the (Req against P) graph - Fig. (12.4) - shows the theoretical locus if the mechanism of deformation had been like those in the initial and stable regimes. Thus, it is obvious that the deviation of actual from theoretical curve indicates deformation at a different regime.

Having obtained the theoretical (Req against P) curve, it is possible to construct a theoretical curve for the relationship between Req and polar height (H). The right side of Fig. (12.4) shows the comparison between the actual and theoretical (Req. against H) locii. However, deviation of one curve from another is negligible so that the unstable regime of deformation cannot be easily detected, even by the maximum pressure criterion.

On multiplying the radius (Req) of the equivalent sphere by the oil pressure, the product becomes the membrane force per unit length in the sphere. Thus, when this force (P Req) is plotted against pressure (P) and Req individually as shown in Fig. (12.5), it is observed that the actual results again deviate from the theoretical results.

It is then feasible to propose that instability occurs when the actual curve in Figs. (12.4) and (12.5) begins to deviate from the trend of early stages of deformation. This point of instability is seen to correspond to a pressure of 887 psi and polar height of 1.35 in.

The pressure growth curve, Fig. (12.3), will show that the test material will become unstable much earlier under this new criterion of instability than under the maximum pressure criterion. However, under this new criterion for instability, the actual pressure in Fig. (12.3) is seen to remain increasing even though the point of instability has already been reached. Therefore, this criterion is not influenced by the absence or presence of maximum pressure in the pressure growth curve.

Referring to the flow stress curves, Figs.(9.6) to (9.8) it is seen that the point of instability (887 psi and 1.35 in polar height) corresponds to a stress distribution curve when its loop just disappears. After this point is passed, the loop begins to appear again and grows continuously until fracture takes place. The direction of the loop is reversed so that fracture can occur at the pole with maximum effective stress.

Chapter 13

CONCLUSIONS

The relationship between the shape of an axisymmetrical thin shell under internal pressure and the stress in it, is usually expressed in equations for the membrane stresses like Eqs. (2.7) to (2.9). These equations, however, conceal certain experimental difficulties. To explain these difficulties, take the cylindrical coordinates L and r of the formed shell, considered as a geometrical surface, Fig. (2.1). The coordinates L and r, which have often been measured in past experimental investigations (2), (3) do not enter directly into the equations for the membrane stresses, rather, it is the first and second derivations ($\frac{dL}{dr}$ and $\frac{d^2L}{dr^2}$) which enter these equations in terms of curvatures. If only the coordinates L and r are measured, the determination of the stresses requires a graphical or numerical double differentiation. Accurate results of such differentiations are practically impossible to obtain with the mechanical and mathematical instruments available in ordinary engineering laboratories. This is probably why the complex variations of curvatures and stresses in these shells have, to the author's knowledge, never been observed experimentally before. In this project, the first differentiation for $\frac{dL}{dr}$ is, in effect, by-passed by measuring the meridional inclination ϕ directly, hence the possibility of the present results. Even then, the complexity of the stress distributions and modes of deformation cannot be fully revealed without plotting the results in different ways, as a careful examination of Figs. (8.2), (8.9), (9.4) to (9.9) will show.

In the past literature on this subject, the surface is usually assumed to be spherical. It is shown here that such an assumption is far from being adequate in either predictive or interpretative theories. That such an assumption is inadequate is not only because the surface deviates from a sphere (which is a well-known fact), but also because the exact deviation is of fundamental significance in the forming process. This deviation is now quantitatively defined and the complexity of the geometry is now revealed and measured.

The stresses and strains measured and calculated enable the work-hardening characteristics of sheet metal in the bulge test to be studied. In the uni-dimensional case such as in the tension test, if the stress-strain relationship is expressed as Eq. (11.3), then the strain hardening coefficient $\frac{d\sigma}{d\varepsilon}$ can be easily derived. In the two-dimensional case,

$$\bar{\sigma} = m \begin{vmatrix} \cos\psi & -\sin\psi \\ \sin\psi & \cos\psi \end{vmatrix} \cdot \bar{\varepsilon} \qquad (11.6)$$

the strain hardening coefficients, variously defined, cannot be easily derived from m and ψ , though they are related to these quantities. Even when the normally accepted generalised stress-strain relationship is used in the present project, the work-hardening coefficient (n) is a complicated function of time and stress ratio. Thus, the present results are suggestions of further stress-strain predictive theories incorporating experimental relationships between stress and strain rate vectors.

Chapter 14

SUGGESTED FUTURE WORK

(A) Draw-in of the flange

Draw-in can be defined as the phenomenon of material at the die edge being fed into the unsupported region during deformation. It has been reviewed in Chapter 4 that all predictive theories of the bulge test (2), (6), (7), (10)-(15) have invariably assume zero circumferential strain at the die edge, meaning no draw-in of the flange. For experimental investigation, only Sachs et al (3), Brown and Sachs (4) and Brown and Thompson (8) have attempted to eliminate draw-in by using serrated die sets. Unfortunately, these experimental results have not been used to compare with the predicted results (2), (5), (6), (11), (13), (14) - most investigators have used Mellor's experimental results from plain die sets (5) as a standard of comparison. Lee et al (45) has shown that draw-in exists even though the holding load is as high as 20000 lb in the plunger test on a plain die set.

Weil and Newmark (6) are the first to observe the effect of draw-in but they fail to pursue this aspect to depth. Since then, it occurs to the author that no one else has investigated the effect of draw-in. With the special technique used in this project, improvement of sheet metal formability in the bulge test can be investigated.

(B) Extension towards the plunger test

The main part of the test results are for either stress-free surfaces or the workpiece in the bulge test. Conditions on these surfaces are such that the formula for membrane stresses can be used to produce accurate results. With surfaces in contact with the plunger or die, neither the friction nor the pressure is accurately known. For such surfaces it is customary to make assumptions either on the friction or on the material properties in order that some theoretical analysis can be made at all (42)-(44). In this chapter, it is proposed to reverse this usual procedure. The accurate properties will first be determined from the measurement on the stress-free surface and in the bulge test. The data on the mechanical properties of the work material so obtained are then used to analyse the normal pressure and the friction on surfaces in contact with the die and plunger. The theoretical technique for such analysis can be derived by reversing the theoretical analyses based on assumptions of friction.

(i) Experiments

The method of test is identical to the bulge test in which the current radius and slope of the meridional section are measured. Instead of reading the hydraulic pressure in the bulge test, the plunger load is read.

(ii) Analysis

The main results in this proposed investigation are the strains involved in the plunger test. It is hardly necessary to explain the measurement of the strains in the axisymmetrical forming process such as the plunger test.

After states of strain along the specimen are determined for various stages, they are plotted in the triangular coordinate system as for the bulge test. The strain paths of the plunger test within 5/6 o'clock region would be identical or nearly identical to those in the bulge test so that the principal stresses can be read from the stress curves in the bulge test. On determining the pressure and friction between the specimen and punch, two types of plungers may be used: (i) hemispherical and (ii) flat bottom plungers.

(a) Hemispherical punch

Theoretically, in the contact zone, the profile of the deformed shell, ignoring bending, conforms to a spherical cap of radius equal to the punch (Rp). It may be worthwhile to note that although the profile at this region is spherical, it does not mean that every part of the material in this region is subjected to balanced bi-axial stretching and this is due to the presence of friction.

Since states of stress can be read from known strain paths, the pressure at any point in the contact zone is readily calculated through Eq. (2.8) as

$$P = \frac{2\,t\,\sigma_s}{\rho_\theta} \tag{14.1}$$

At positions beyond the contact zone, however, the pressure is zero for obvious reasons.

The coefficient of friction (μ) at any position in the contact region can be calculated through the equilibrium equation of forces along the tangential direction. This can easily be shown to be

$$\frac{d(t\,\sigma_s)}{d\phi} = \left(\frac{(\sigma_\theta - \sigma_s)}{\tan\phi} + \mu(\sigma_\theta + \sigma_s) \right) t$$

of which

$$\mu = \frac{1}{e^{\varepsilon_t}(\sigma_s+\sigma_\theta)} \frac{d(e^{\varepsilon_t}\sigma_s)}{d\phi} - \frac{t_0 e^{\varepsilon_t}(\sigma_\theta - \sigma_s)}{\tan\phi(\sigma_\theta + \sigma_s)} \tag{14.2}$$

As the process of forming is slow, the friction involved can be regarded essentially as static rather than dynamic or a mixture of both. The frictional forces at any position may be computed having obtained the coefficient of friction (μ) and pressure (P) so that

$$f = \mu P \tag{14.3}$$

(b) Flat-bottom punch

The analysis for a flat-bottom punch of profile radius r_p is similar to that of a hemispherical punch. The strains at the flat region are practically zero except near the punch profile. Therefore, the stresses, and hence pressure, at this flat base are zero and near the punch profile region, we assume them to be zero. In this case of a flat-bottom punch, it is only necessary to consider the punch profile region where the material flows. It can easily be shown that the equilibrium equation is given by:

$$\frac{d(t\sigma_s)}{d\phi} = (t\sigma_\theta(\cos\phi + \mu\sin\phi) - t\sigma_s\cos\phi)\frac{r_p\, d\phi}{(R_p - r_p) + r_p\sin\phi} + t\mu\sigma_s \tag{14.4}$$

Hence the coefficient of friction (μ) is obtainable. The pressure and frictional force at any particular point in this region is determined by Eqs. (14.1) and (14.3) respectively.

Appendix A

ESTIMATION OF ERRORS

(A) Experimental details

Specification of the work material: commercially pure copper (soft), British Standards Specification BS 899.

Thickness of the work material: 0.048 in

Diameter of the blank: 7.992 in

Rate of forming: 0.5 in polar height per minute

Die opening: 5.000 in

Die surface serrated in an annular area from 6.0 in to 6.7 in diameter to prevent draw-in.

Concentricity of specimen location: accurate to 0.0003 in

Accuracy of protractor reading (for ϕ): ± 5 min

Accuracy of readings for the radial distance r: 0.0005 in

Accuracy of pressure readings: ± 25 psi

Springback of bulge at the pole: 0.009 in

(B) Inaccuracies due to springback

Suppose the springback at the pole is Y and die hole radius is a. Then, from the definition of polar height (H) being $\int_0^a \tan\phi \, dr$,

$$Y = \int_0^a (\tan\phi - \tan\phi_m)\, dr \qquad (A.1)$$

where suffix m refers to the measured angle after springback has occurred. It is reasonable to assume that the bracketed term in Eq. (A.1) increases linearly with r so that Eq. (A.1) becomes

$$Y = \frac{a(\Delta\phi)}{2} \qquad (A.2)$$

where $\Delta\phi$ is the difference of the true and measured angle of the bulge at the die edge. Since the springback by relieving the oil pressure is 0.009 in, Eq. (A.2) becomes

$$\Delta\phi = \frac{2 \times 9}{3 \times 1000} = 6 \times 10^{-3} \text{ rad}$$

$$= 20.6' \text{ (at the die edge)} \qquad (A.3)$$

The range of the meridional slope at the die edge can be estimated by approximating a spherical bulge. By geometry,

$$\frac{H}{a} = \frac{1 - \cos\theta}{\sin\theta} \qquad (A.4)$$

where θ is the meridional inclination at the die edge defined in Fig. (2.2). Thus, from the initial stage A (H = 0.509 in) to the fractured stage M (H = 2.150 in), θ varies from approximately 20 degrees to 70 degrees.

Since it is assumed that the change of profile inclination due to springback varies linearly with r, this change at any position, r, in the bulge is thus

$$\delta\phi = \frac{\Delta\phi}{a} r = 6 \times 10^{-3} \frac{r}{a} \qquad (A.5)$$

The errors in ρ_θ and ρ_s can then be estimated by the effect of springback. By definition of ρ_θ, its error owing to a change in ϕ is

$$\frac{\delta\rho_\theta}{\rho_\theta} = -\cot\phi \, \delta\phi \qquad (A.6)$$

By Eq. (A.5), Eq. (A.6) becomes

$$\frac{\delta\rho_\theta}{\rho_\theta} = -\cot\phi \, \frac{r}{a} \times 6 \times 10^{-3}$$

$$= -6 \times 10^{-3} \cos\phi \tag{A.7}$$

Thus, the error of ρ_θ owing to springback varies from 0.6% at the pole (maximum for all stages) to 0.2% at the die edge when H = 2.150 in.

The error in ρ_s caused by springback can be estimated from the definition of ρ_s. Thus, using the subscript m as the measured quantities, at any position r,

$$ds_m = \frac{dr}{\cos\phi_m} = \frac{dr}{\cos(\phi - (\phi - \phi_m))}$$

$$= \frac{dr}{\cos\phi\cos(\phi - \phi_m) + \sin\phi\sin(\phi - \phi_m)}$$

$$\simeq \frac{dr}{\cos\phi + (\phi - \phi_m)\sin\phi}$$

$$= \frac{dr}{\cos\phi + 6 \times 10^{-3}\,\frac{r}{a}\,\sin\phi} \tag{A.8}$$

since, $$\frac{d\phi_m}{d\phi} = \frac{\frac{d\phi_m}{dr}}{\frac{d\phi}{dr}} = \frac{\theta - 6 \times 10^{-3}}{\theta}$$

we have the measured ρ_s as

$$(\rho_s)_m = \frac{ds_m}{d\phi_m} = \frac{\dfrac{dr}{\cos\phi + 6 \times 10^{-3} \frac{r}{a} \sin\phi}}{\dfrac{\theta - 6 \times 10^{-3}}{\theta} \quad d\phi}$$

$$= \frac{\rho_s}{(1+6 \times 10^{-3} \frac{r}{a} \sin\phi)(1 - \frac{6 \times 10^{-3}}{\theta})}$$

so that

$$\rho_s = (\rho_s)_m \, (1 + 6 \times 10^{-3} \frac{r}{a} \tan\phi - \frac{6 \times 10^{-3}}{\theta})$$

$$= (\rho_s)_m \, (1 + (\frac{r}{a} \tan\phi - \frac{1}{\theta}) \, 6 \times 10^{-3}) \qquad (A.9)$$

Based on a spherical bulge, Eq. (A.9) becomes

$$\rho_s = (\rho_s)_m \, (1 + (\tan\theta - \frac{1}{\theta}) \, 6 \times 10^{-3}) \qquad (A.10)$$

when θ is 20 degrees for stage A (H = 0.509 in), the error in ρ_s owing to springback is 1.52%. The magnitude of error is reduced to 1.2% for the fractured stage M (H = 2.150 in and $\theta = 70^\circ$).

(C) Error in strains

The error in circumferential strain given by

$$\frac{d\varepsilon_\theta}{\varepsilon_\theta} = \frac{dr}{r\varepsilon_\theta} \qquad (A.11)$$

is amplified when r and ε_θ are small. For the initial regime of deformation (H < 0.990 in), the average circumferential strain at the pole is 0.05 so that the error is less than one percent to within one inch from the pole. At the early stages in the stable regime of deformation, an error of less than one percent can be obtained to within 0.6 in from the pole (stage F as typical).

The through-thickness strain shown in this project is calculated from Eq. (7.2). Within 0.6 in from the pole for the stable regime (stage F as typical), the largest error is in ϕ and is about one percent so that the overall maximum error is less than two percent.

(D) Error in prolateness and stresses

The error in prolateness can be estimated from the following equation,

$$\frac{dN}{N} = \frac{-\cos\phi \; d\phi \; \frac{d\rho_\theta}{dr} - \sin\phi \; d\left(\frac{d\rho_\theta}{dr}\right)}{1 - \sin\phi \frac{d\rho_\theta}{dr}} \qquad (A.12)$$

Based on stage F for r = 0.6 in (hence ϕ is approximately 10°) and that the adjustable protractor to determine the slope graphically being accurate to 0.01, the maximum error in N is 1.6%.

The error in the meridional tangential stress is given by the following equation,

$$\frac{d\sigma_s}{\sigma_s} = \frac{dP}{P} + \frac{d\rho_\theta}{\rho_\theta} - \frac{dt}{t} \qquad (A.13)$$

Using stage F (P = 600 psi) as a typical case, the maximum error in σ_s is 6%.

By taking into account of the prolateness of the shell, the maximum error in the circumferential stress is less than eight percent.

ACKNOWLEDGEMENTS

The author gratefully acknowledges all who have offered their assistance towards the project, especially to his Supervisor, Professor T.C. Hsü, for the valuable guidance and advice received. Thanks are also due to Messrs. S.Y. Lee and T.C. Lee for helping to carry out part of the experimental work and frequent discussions. The author is also grateful to Professor R.H. Thornley, Head of the Department of Production Engineering, for permitting the use of all equipment in the Department as well as the assistance of all technicians within the Department. Special attributes are also due to Mrs. S.D. Barratt for typing the manuscript and Miss K.C. Lee for proof reading. Finally, but not of least importance, the author is indebted to the Republic of Singapore for their support to embark on this project; and the Association of Commonwealth Universities and British Council in the United Kingdom for their financial support over the years of research.

BIBLIOGRAPHY

1. G.S.A. Shawki, "Assessing deep-drawing qualities of sheet", Sheet Metal Industries, 1695, 42, 363-368; 417-424; 524-532.

2. J. Chakrabarty and J.M. Alexander, "Hydrostatic bulging of circular diaphrams", J. Strain Analysis, 1970, 5 (3), 155-161.

3. G. Sachs, G. Espey and G.B. Kasik, "Circular bulging of Al-alloy sheet at room and elevated temperatures", Trans. ASME, 1946, 68, 161-173.

4. W.F. Brown, Jr, and G. Sachs, "Strength and failure characteristics of thin circular membranes", Trans. ASME, 1948, 70, 241-149.

5. P.B. Mellor, "Stretch forming under fluid pressure", J. Mech. Phys. Solids, 1956, 5, 41-56.

6. N.A. Weil and N.M. Newmark, "Large plastic deformations of circular membranes", J. Applied Mech., 1955, 22, 533-538.

7. G.S. Kular and J.H.L. The, "The bulging of anisotropic aluminium

sheets - A comparison of theory and experiments",
Int. J. Machine Tool Design and Research, 1972, 12, 281-296.

8. W.F. Brown and F.C. Thompson,
"Strength and failure characteristics of metal membranes in circular bulging",
Trans. ASME, 1949, 71, 575-585.

9. N.M. Wang and M.M. Shammamy,
"Comparison of experimental and theoretical results for the hydrostatic bulging of circular sheets",
Experimental Mechanics, 1971, 11, 71-75.

10. R. Hill,
"A theory of the bulging of a metal diaphram by lateral pressure",
Philosophical Magazine, 1950, 41, 1133-1142.

11. A. Gleyzal,
"Plastic deformation of a circular diaphram under pressure",
J. Applied Mech., 1948, 15, 288-296.

12. E.W. Ross and W. Prager,
"On the theory of the bulge test,
Q. Appl. Math., 1954, 12, 86-91.

13. B. Storakers, "Finite plastic deformation of a circular membrane under hydrostatic pressure", Int. J. Mech. Sci., 1966, 8, 619-628.

14. N.M. Wang and M.M. Shammamy, "On the plastic bulging of a circular diaphram by hydrostatic pressure", J. Mech. Phys. Solids, 1969, 17, 43-61.

15. D.M. Woo, "The analysis of axisymmetrical forming of sheet metal and the hydrostatic bulging process", Int. J. Mech. Sci., 1964, 6, 303-317.

16. T.C. Hsü and A.S. Williamson, "Plastic deformation of an aluminium alloy in the tension test", Proc. ASTM, 1965, 65, 575-596.

17. T.C. Hsü, G.S. Littlejohn and B.M. Marchbank, "Elongation in the tension test as a measure of ductility", Proc.ASTM, 1965, 65, 874-898.

18. T.C. Hsü and A.J. Young, "Plastic deformation in the compression test of pure copper", J. Strain Analysis, 1967, 2(2), 159-170.

19. H.J. Ivey, "Plastic stress-strain relations and yield surfaces for aluminium alloys", J. Mech. Eng. Sci., 1961, 3, 15-30.

20. W.M. Mair and H. Ll.D. Pugh, "The effects of pre-strain on yield surfaces in copper", J. Mech. Eng. Sci., 1964, 6, 150-163.

21. G.I. Taylor and H. Quinney, "The plastic distortion of metals", Phil. Trans. Roy. Soc., Lond., Series A, 1931, 230, 323-362.

22. E.A. Davis, "Increase of stress with permanent strain and stress-strain relationships in the plastic state for copper under combined stresses", J. Appl. Mech. 1943, 65, 187-196.

23. W. Szczepinski, "On the effect of plastic deformation on yield criterion", Archiwum Mechaniki Stosowanej, 1963, 2(15), 275-296.

24. Y. Sato and S. Shiguma, "Yielding of mild steel under bi-axial

state of uniform stress",
Bulletin JSME, 1971, 72(14), 517-524.

25. H. Ford, "Researches into the deformation of metals by cold rolling",
Proc. I. Mech. E., 1948, 159, 115-143.

26. A.B. Watts and H. Ford,
"An experimental investigation of the yielding of strip between smooth dies",
Proc. I. Mech. E., 1952-53, (B), 1B, 448-453.

27. W.R. Osgood, "Stress-strain formulas",
J. Aero. Sci., 1946, 13, 45-48.

28. G. Sachs and J.D. Lubahn,
"Failure of ductile metals in tension",
Trans. ASME, 1946, 68, 271-276.

29. H.W. Swift, "Plastic instability under plane stress",
J. Mech. Phy. Solids, 1952, 1, 1-18.

30. B. Kaftanoglu and J.M. Alexander,
"On quasistatic axisymmetrical stretch forming",
Int. J. Mech. Sci., 1970, 12, 1065-1084.

31. B. Kaftanoglu, "Plastic instability of thin shells deformed by rigid punches and by hydraulic pressure", ASME Winter Annual Meeting, New York, 1972. Paper Number 72-WA/Mat-4.

32. O. Hoffman and G. Sachs, "Introduction to the theory of plasticity for engineers", McGraw-Hill, N.Y., 1953.

33. A. Nadai, "Theory of flow and fracture of solids", 2nd edition, McGraw-Hill, N.Y., Vol. 1, 1950.

34. W. Johnson and P.B. Mellor, "Plasticity for mechanical engineers", van Nostrand, 1962.

35. R. Hill, "The mathematical theory of plasticity", Oxford Clarendon Press, 1950

36. D.C. Drucker, "A reconsideration of deformation theories", Trans. ASME, 1949, 71, 587-592.

37. Z. Marciniak, "Graphical representation of states of stress and strain", Nadbitka Z Archiwum Mechaniki stosowanej, 1957, 261-273.

38. T.C. Hsü, "The characteristics of coaxial and non-coaxial strain paths",
J. Strain Analysis, 1966, 1(3), 216-222.

39. T.C. Hsü, "The effect of the rotation of the stress axes on the yield criterion of prestrained materials",
ASME Winter Annual Meeting, Chicago, 1965.
Paper Number 65-WA/Met-4.

40. T.C. Hsü, W.R. Dowle, C.Y. Choi and P.K. Lee,
"Strain histories and strain distributions in a cup drawing operation",
ASME Winter Annual Meeting, New York, 1970.
Paper Number 70-WA/Prod-6.

41. P.K. Lee, C.Y. Choi and T.C. Hsü,
"Effect of draw-in on formability in axisymmetrical sheet metal forming",
ASME, Winter Annual Meeting, New York, 1972.
Paper Number 72-WA/Prod-1.

42. D.M. Woo, "On the complete solution of the deep-drawing problem",
Int. J. Mech. Sci., 1968, 10, 83-94.

43. J. Chakrabarty, " A theory of stretch forming over hemispherical punch heads", Int. J. Mech. Sci., 1970, 12, 315-325.

44. K. Nakagawa and S. Okazaki, " The coefficient of friction on the round headed punch", Proc. ICSTIS, Suppl. Trans. ISIJ, 1971, 11, 908-910.

45. H. Ford and J.M. Alexander, " Advanced Mechanics of Materials", Longmans, 1963.

LIST OF FIGURES

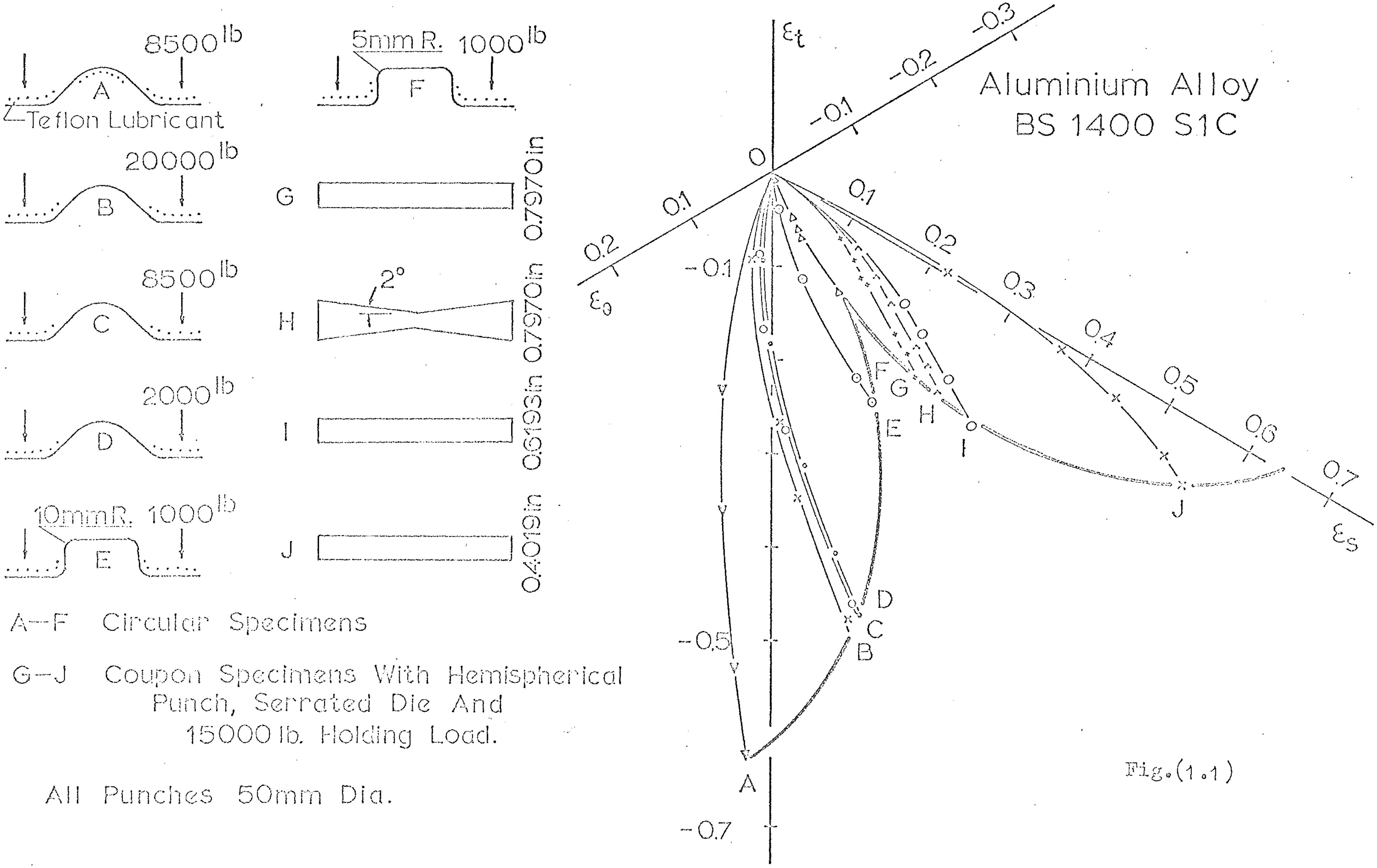

Aluminium Alloy
BS 1400 S1C

A—F Circular Specimens

G—J Coupon Specimens With Hemispherical Punch, Serrated Die And 15000 lb. Holding Load.

All Punches 50mm Dia.

Fig.(1.1)

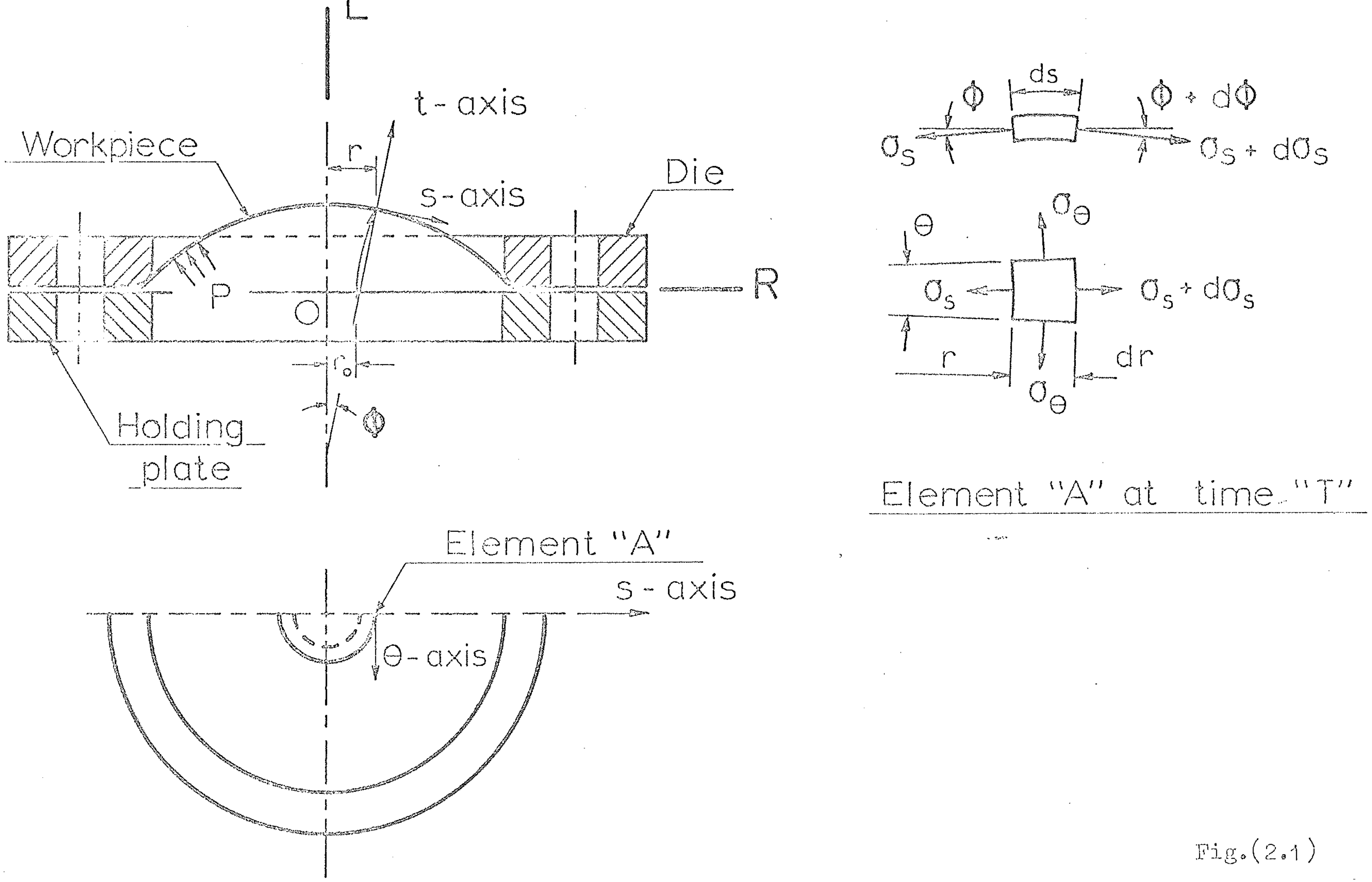
L
t - axis
Workpiece
r
s - axis
Die
P
O
R
r_o
Φ
Holding plate
Element "A"
s - axis
θ - axis
ds
Φ
$\Phi + d\Phi$
σ_s
$\sigma_s + d\sigma_s$
σ_θ
θ
σ_s
$\sigma_s + d\sigma_s$
r
dr
σ_θ
Element "A" at time "T"

Fig.(2.1)

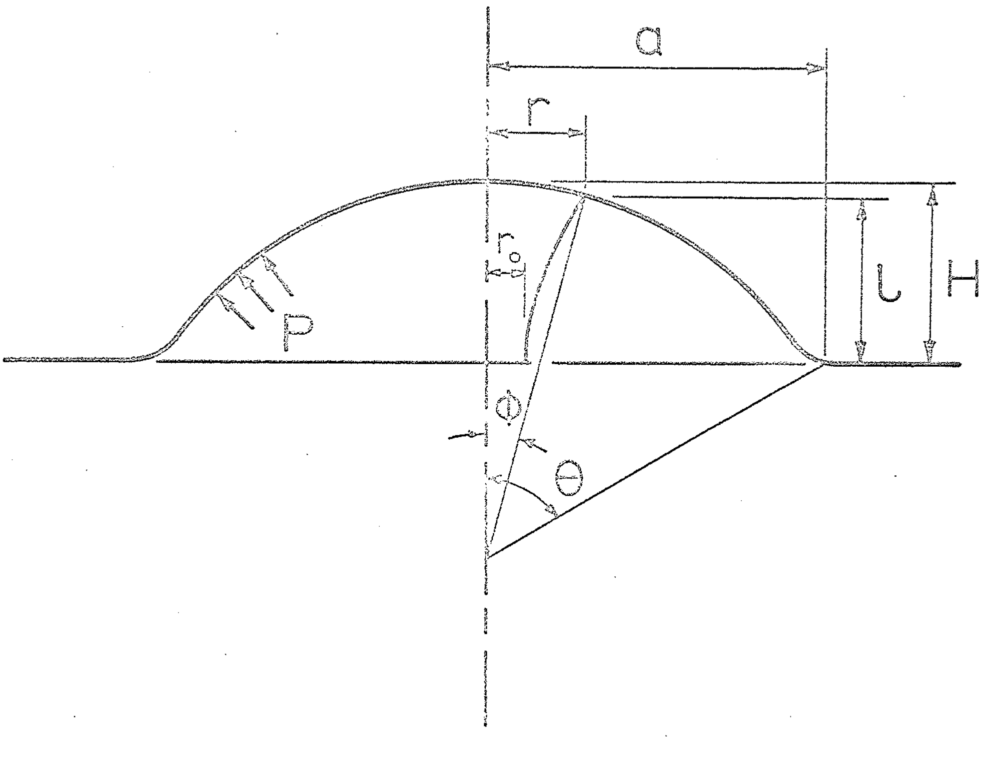

Fig.(2.2)

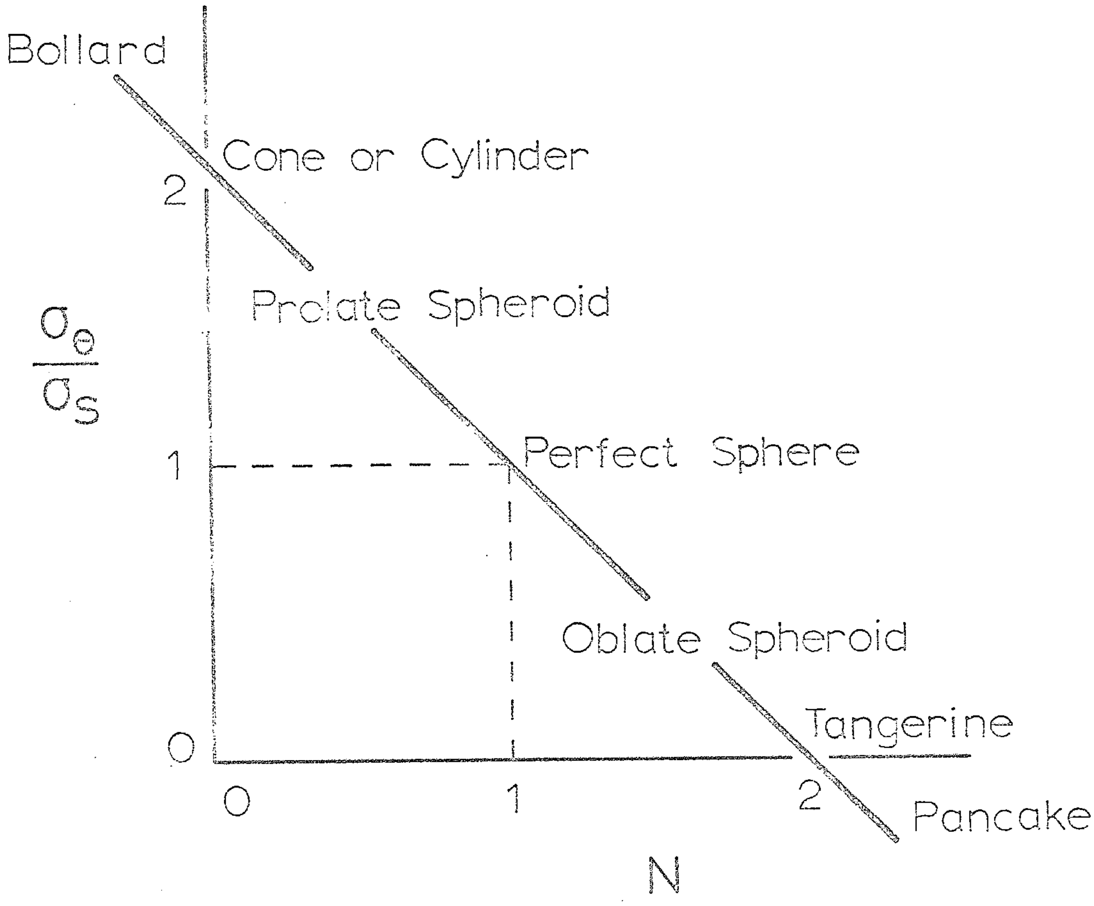
Bollard
Cone or Cylinder
Prolate Spheroid
Perfect Sphere
Oblate Spheroid
Tangerine
Pancake
$\frac{\sigma_\theta}{\sigma_s}$
2
1
0
0
1
2
N

Fig.(3.1)

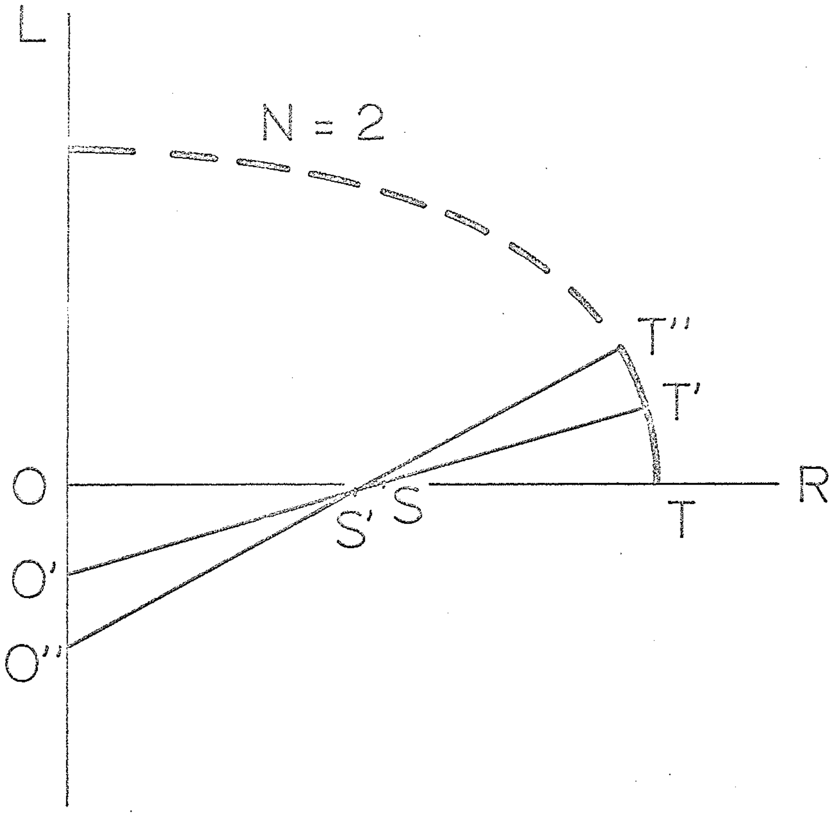

Fig.(3.2)

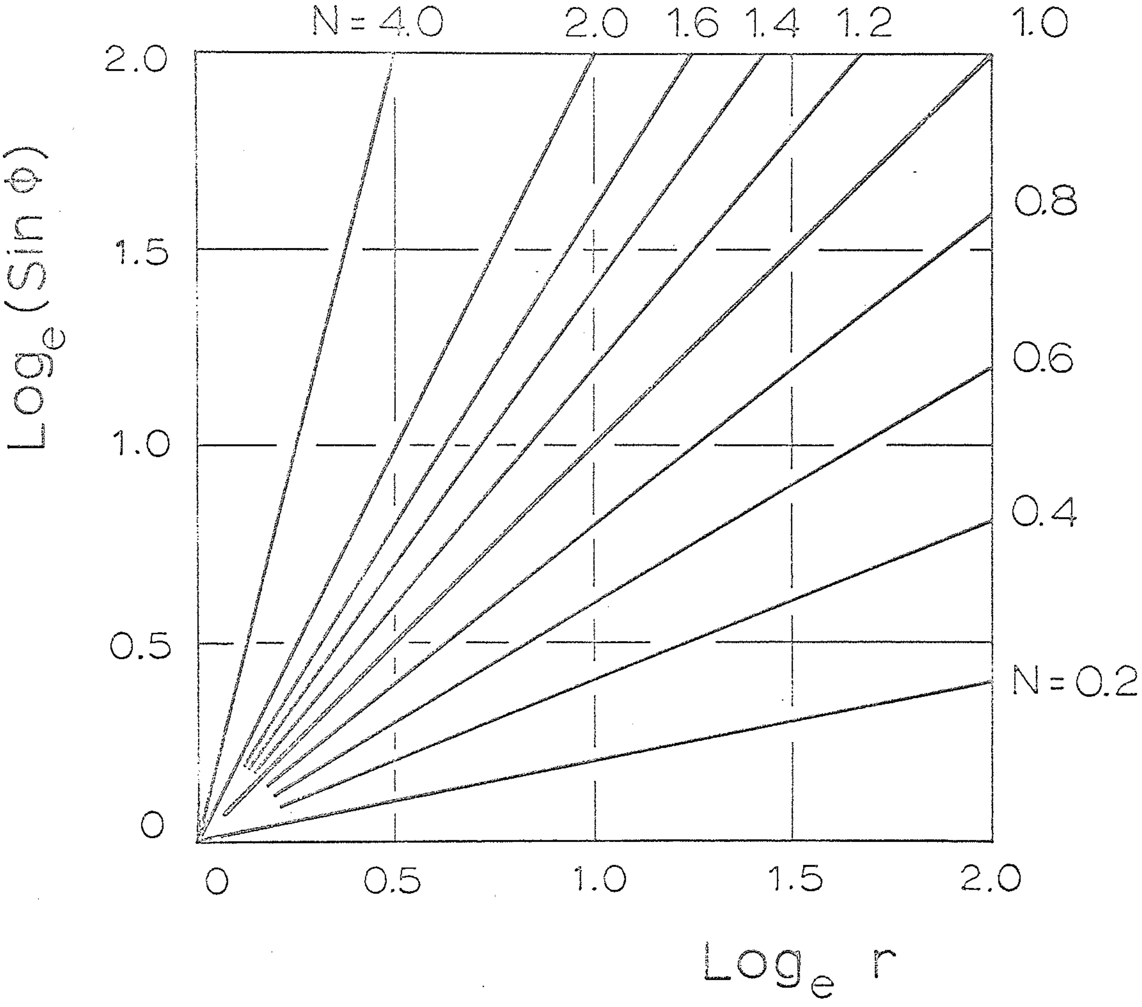
N=4.0
2.0
1.6
1.4
1.2
1.0
0.8
0.6
0.4
N=0.2
2.0
1.5
1.0
0.5
0
0
0.5
1.0
1.5
2.0
Log$_e$ (Sin ϕ)
Log$_e$ r

Fig.(3.3)

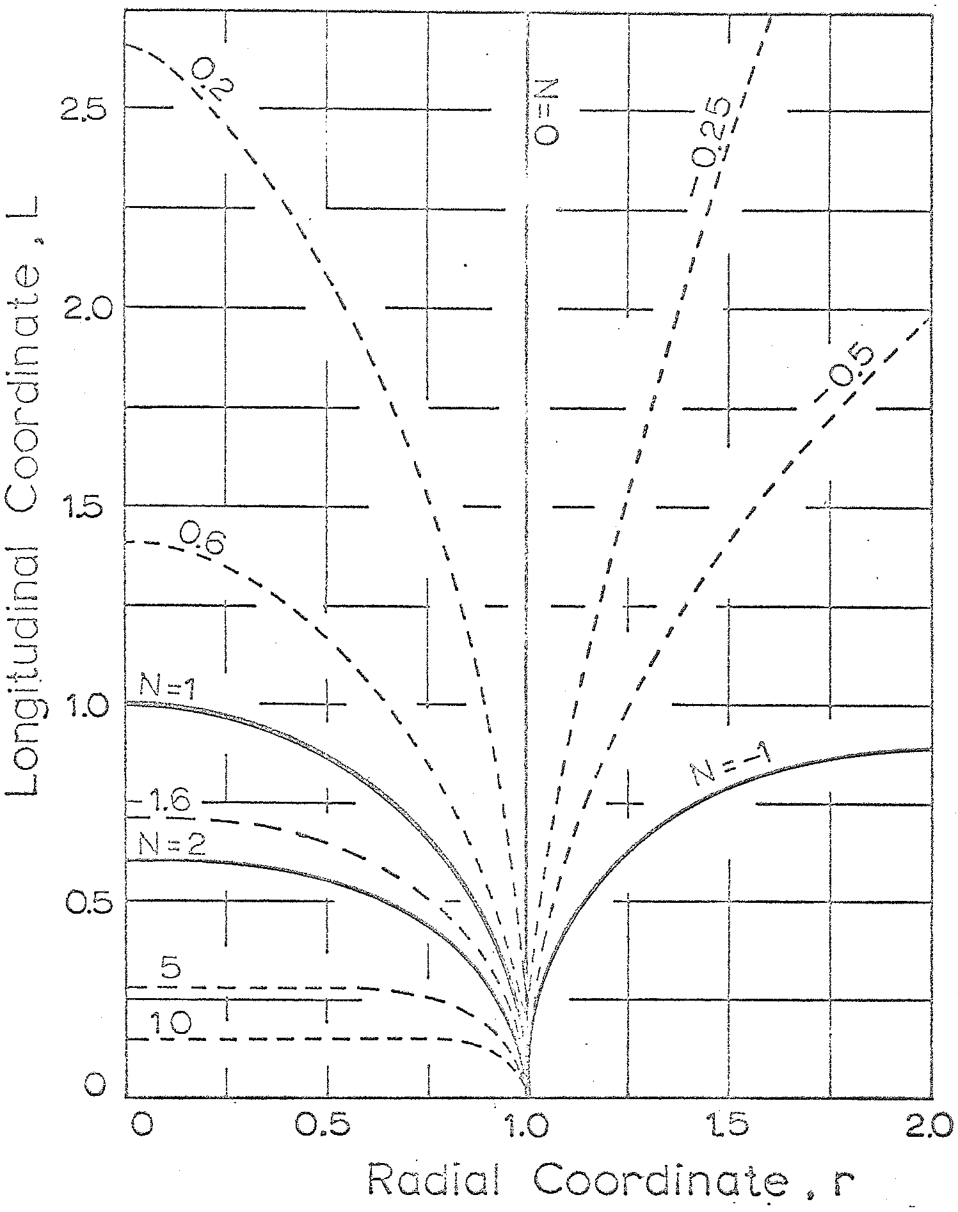

Longitudinal Coordinate, L
Radial Coordinate, r
0
0.5
1.0
1.5
2.0
2.5
0
0.5
1.0
1.5
2.0
0.2
N=0
0.25
0.5
0.6
N=1
N=-1
1.6
N=2
5
10

Fig.(3.4)

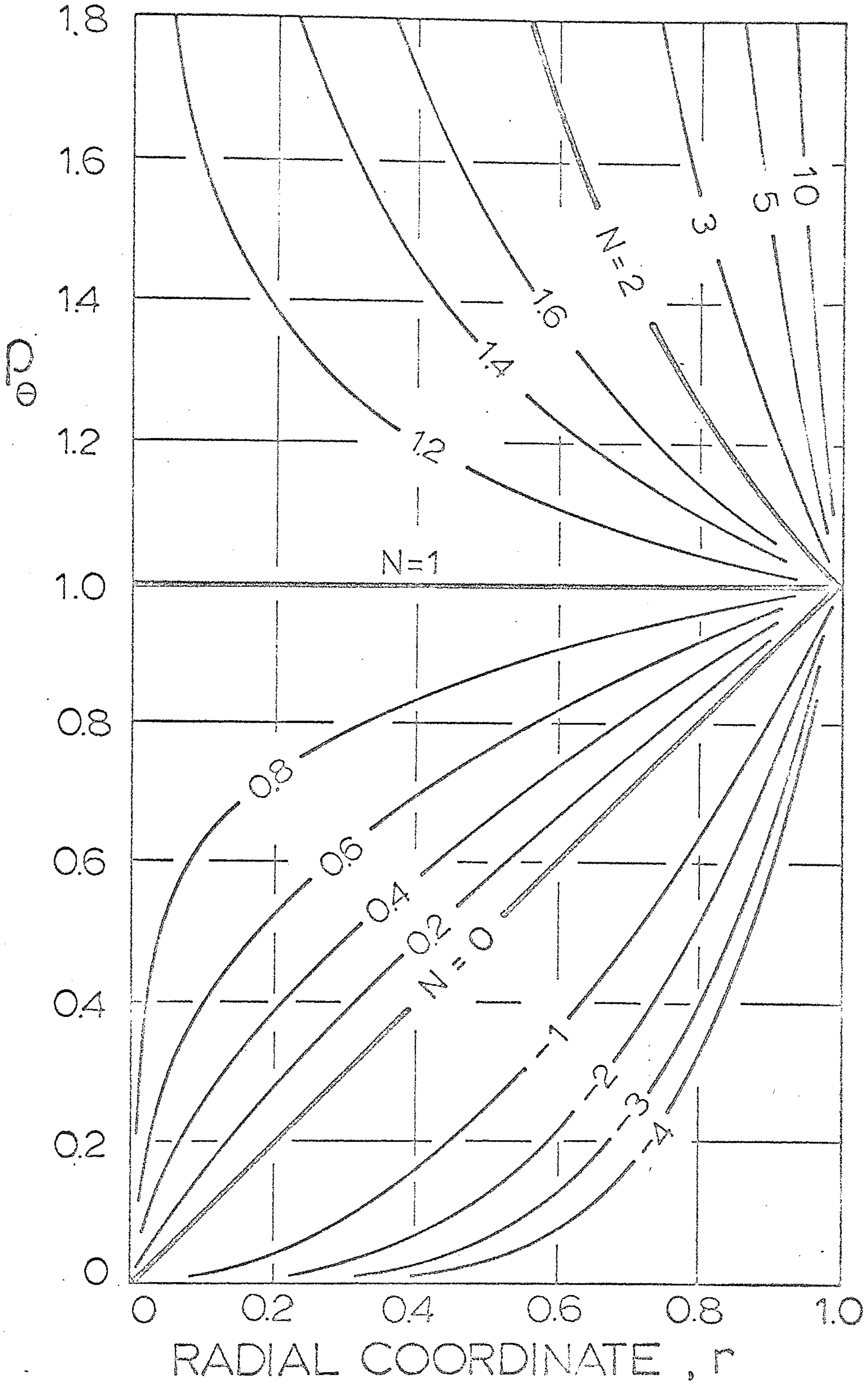
1.8
1.6
1.4
1.2
1.0
0.8
0.6
0.4
0.2
0
ρ_θ
0
0.2
0.4
0.6
0.8
1.0
RADIAL COORDINATE , r
10
5
3
N=2
1.6
1.4
1.2
N=1
0.8
0.6
0.4
0.2
N=0
-1
-2
-3
-4

Fig.(3.5)

	Solid Circle For N=0	Solid Circle For N=0 Point Circle For N=1	Solid Circle For N=2 Point Circle For N=1	Solid Circle For N=2
Mohr Circles For Stresses	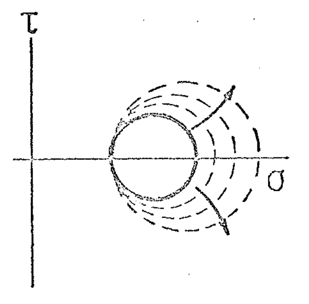	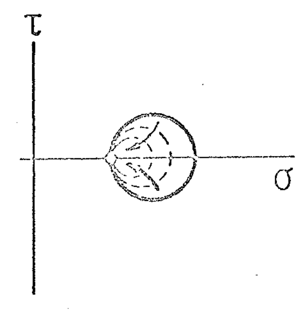	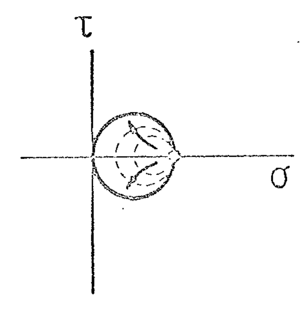	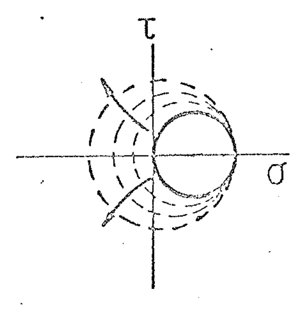
	Dotted Circles For N<0	Dotted Circles For 0<N<1	Dotted Circles For 1<N<2	Dotted Circles For N>2
Mohr Circles For Curvatures	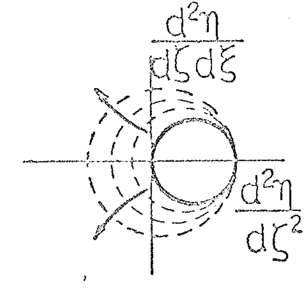	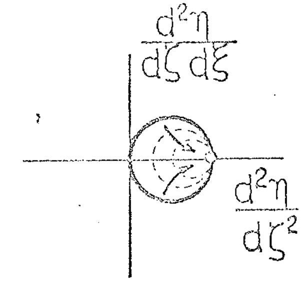	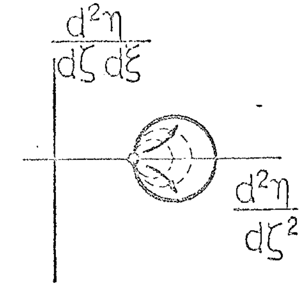	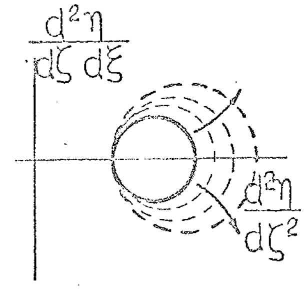
	Dotted Circles For N<0	Dotted Circles For 0<N<1	Dotted Circles For 1<N<2	Dotted Circles For N>2

Fig.(3.6)

Fig.(4.1)

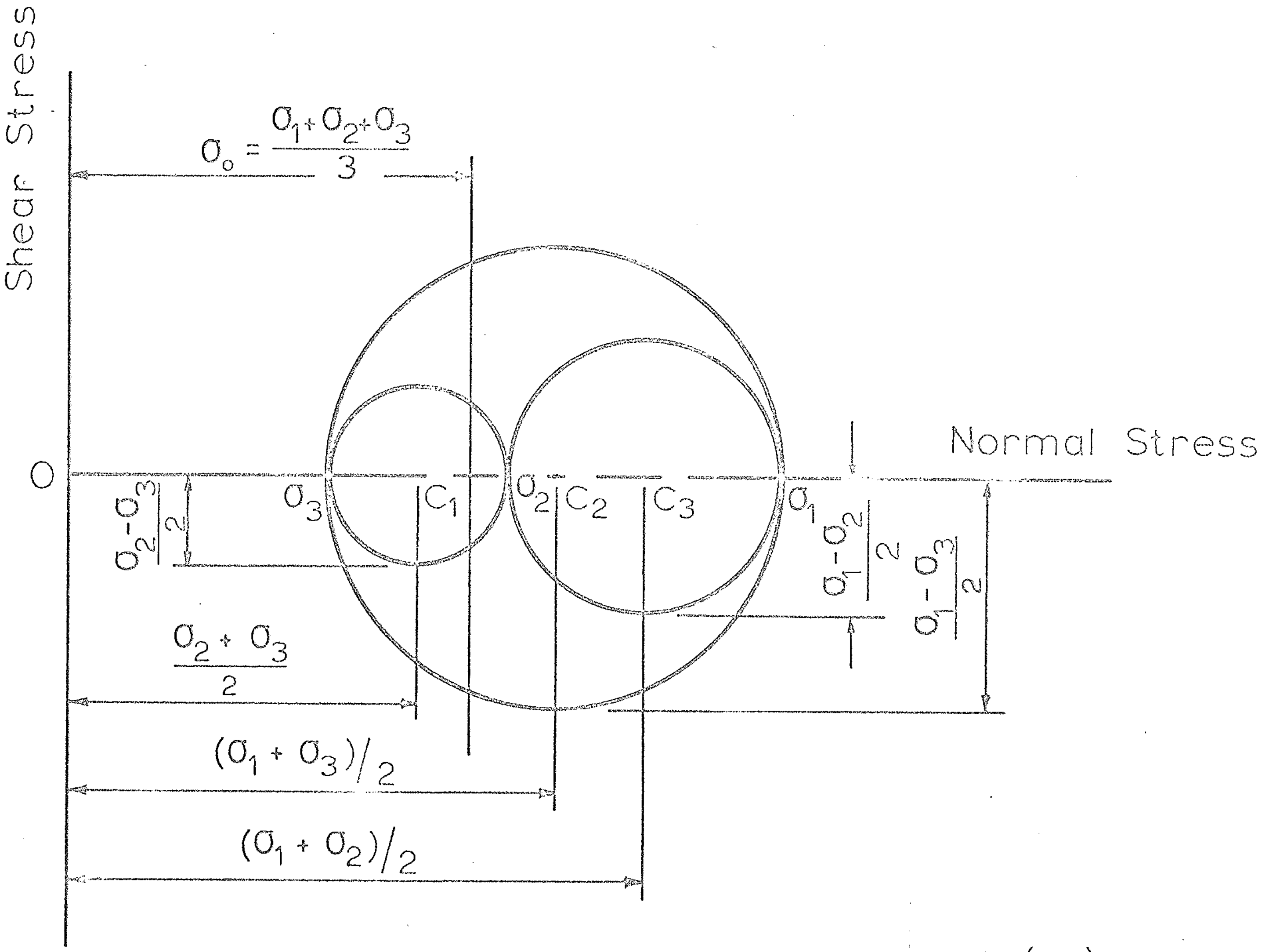
Shear Stress
Normal Stress
O
$\sigma_o = \frac{\sigma_1+\sigma_2+\sigma_3}{3}$
σ_3
C_1
σ_2
C_2
C_3
σ_1
$\frac{\sigma_2-\sigma_3}{2}$
$\frac{\sigma_1-\sigma_2}{2}$
$\frac{\sigma_1-\sigma_3}{2}$
$\frac{\sigma_2+\sigma_3}{2}$
$(\sigma_1+\sigma_3)/_2$
$(\sigma_1+\sigma_2)/_2$

Fig.(5.1)

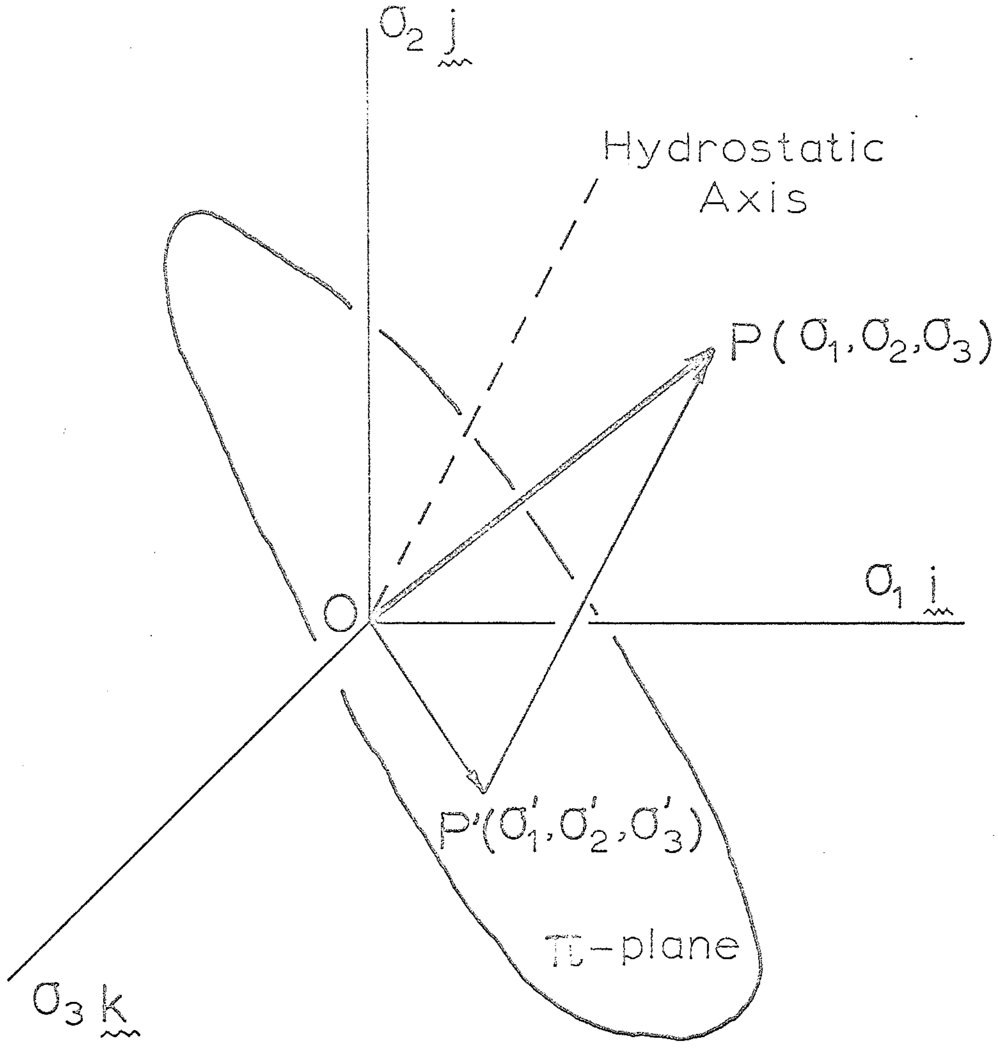

OP' — Deviatoric Stress Component

PP' — Hydrostatic Stress Component

Fig.(5.2)

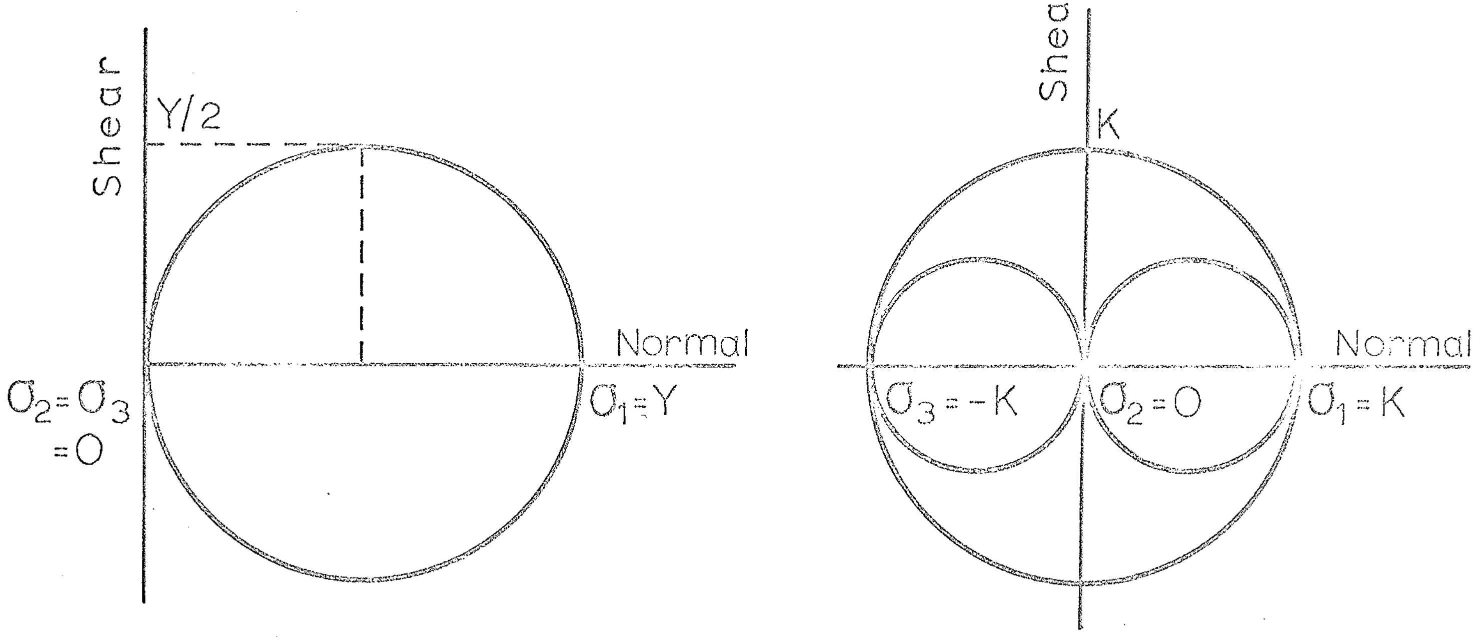

Simple Tension

Pure Shear

Fig.(5.3)

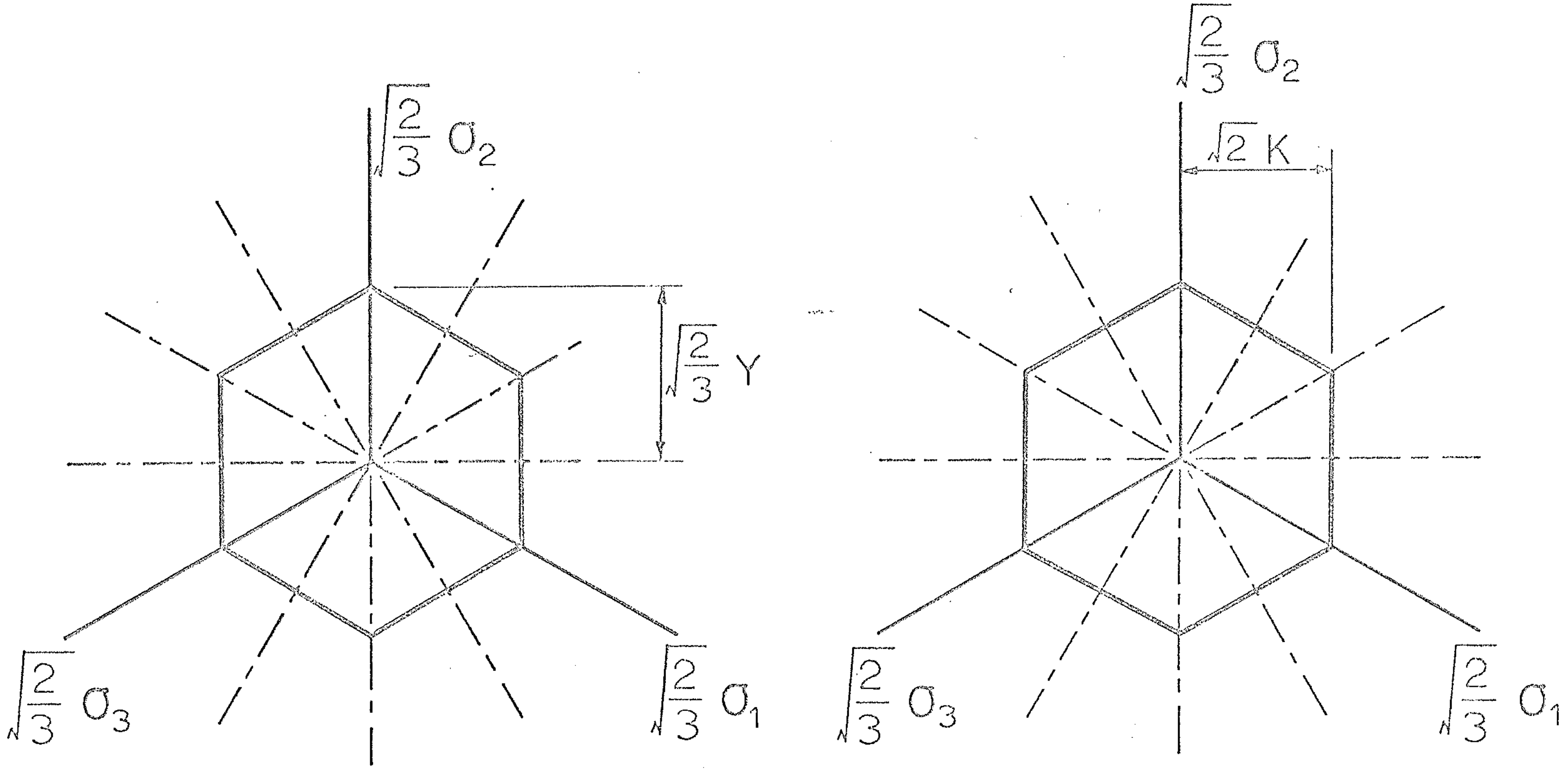

Simple Tension Test

Pure Shear Test

Fig.(5.4)

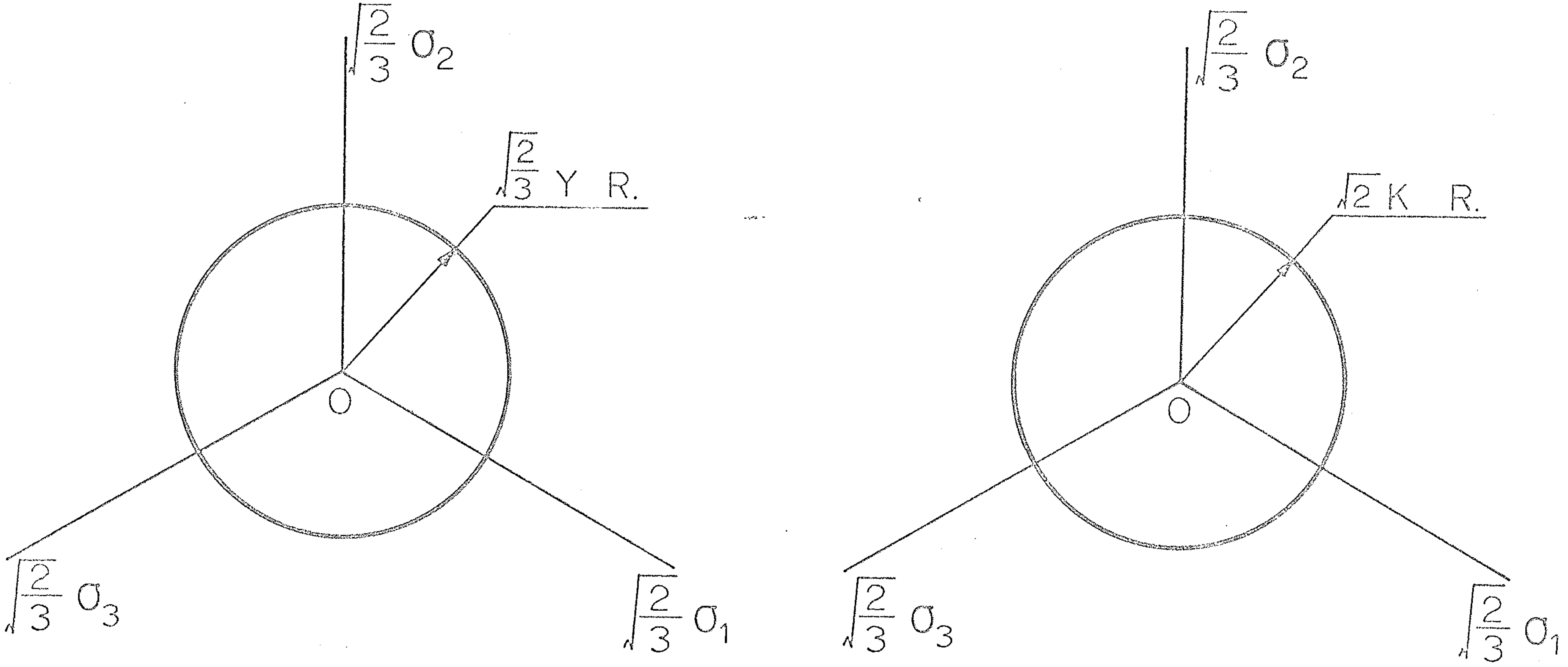

Simple Tension Test

Pure Shear Test

Fig.(5.5)

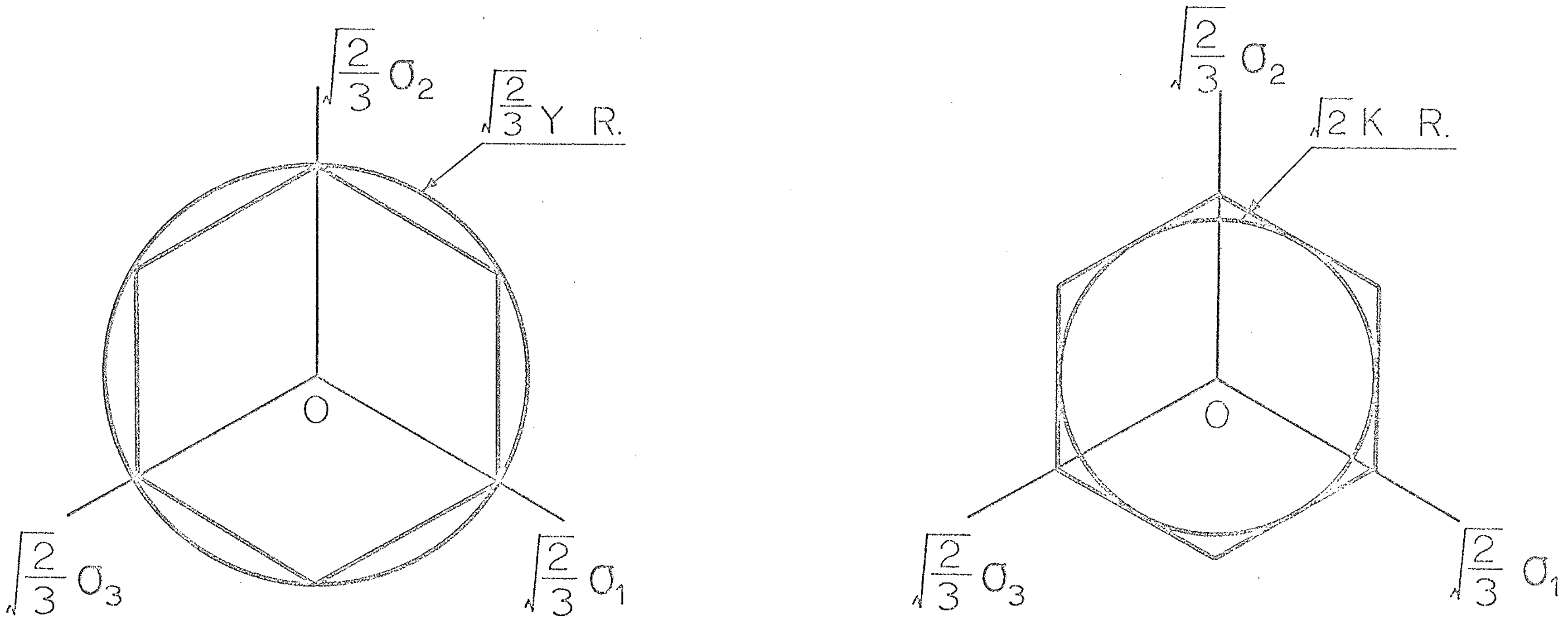

Simple Tension Test

Pure Shear Test

Fig.(5.6)

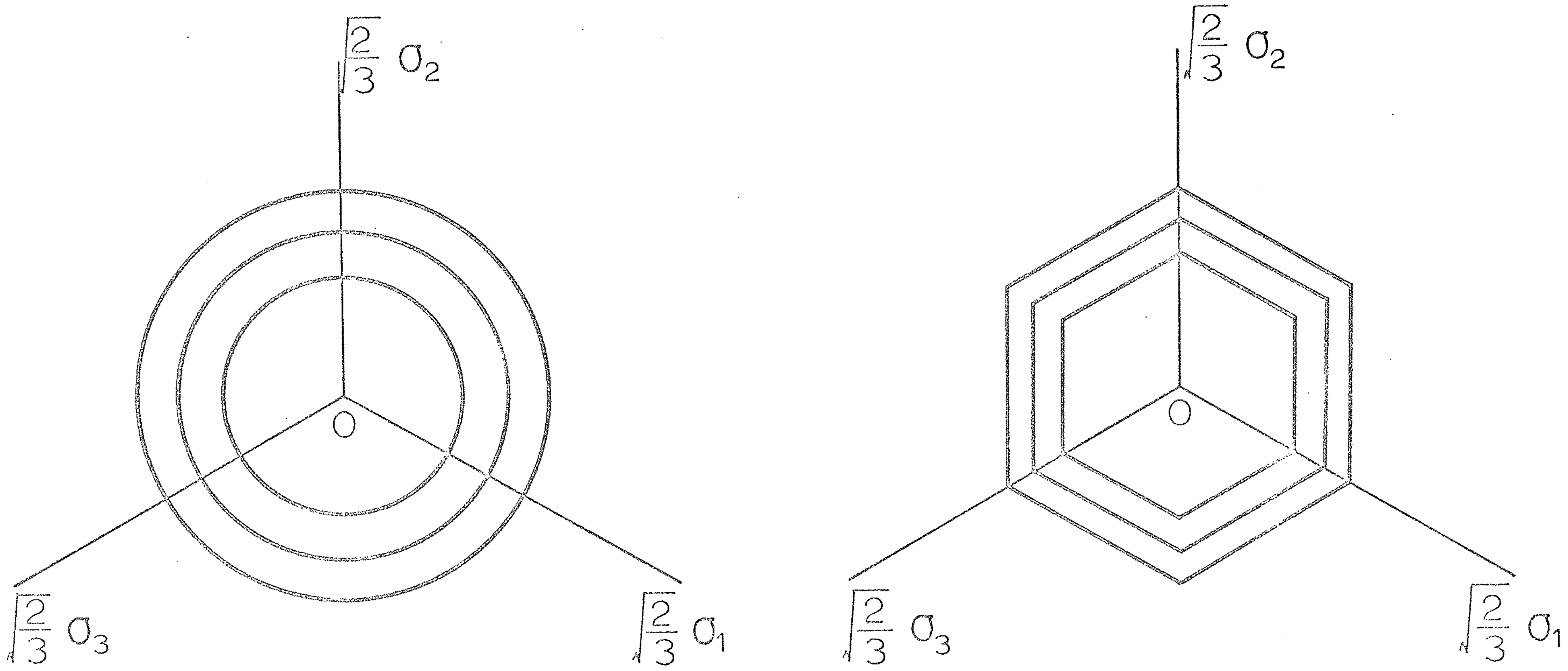

Mises Yield Loci

Tresca Yield Loci

Fig.(5.7)

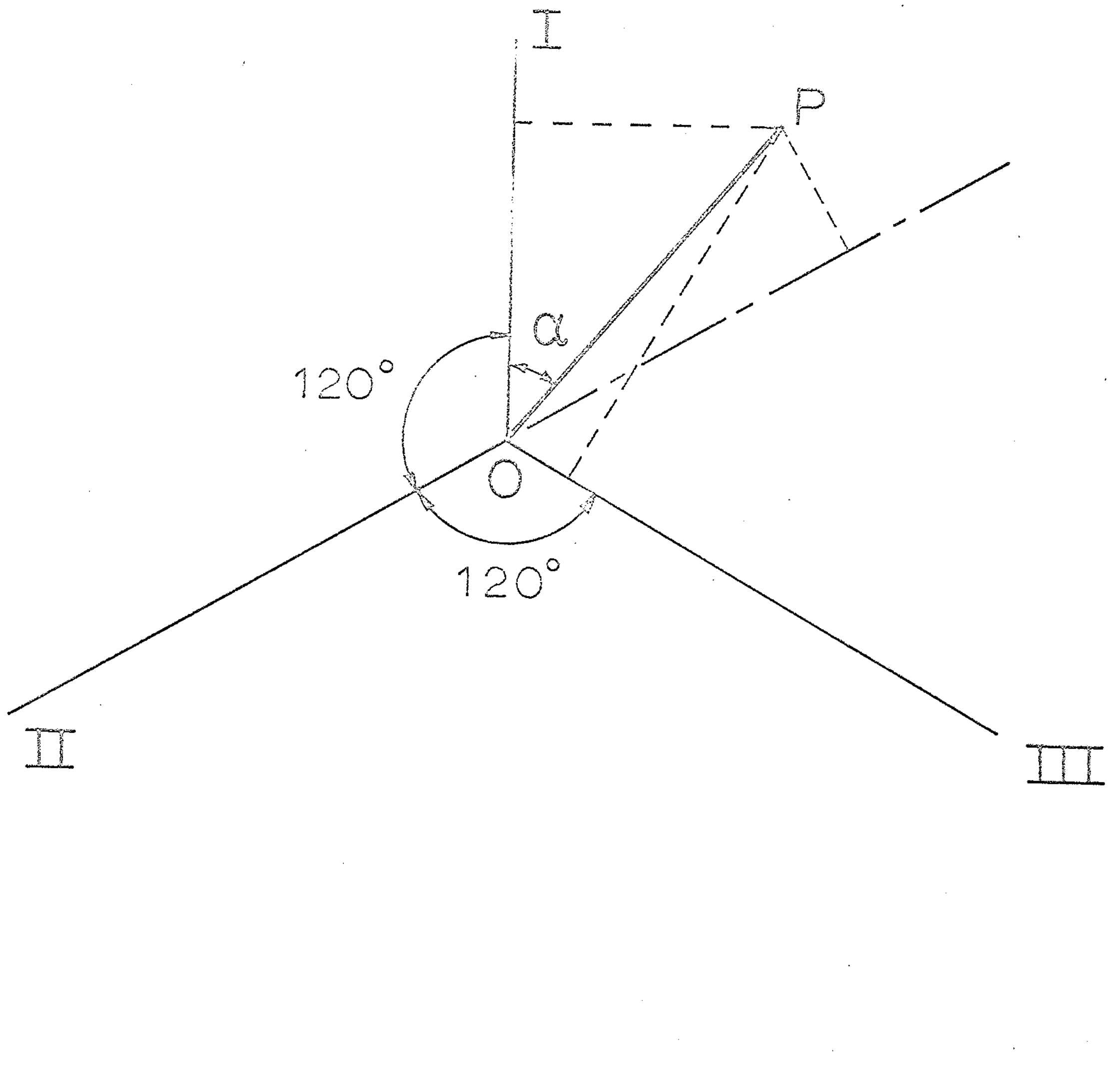

Fig.(6.1)

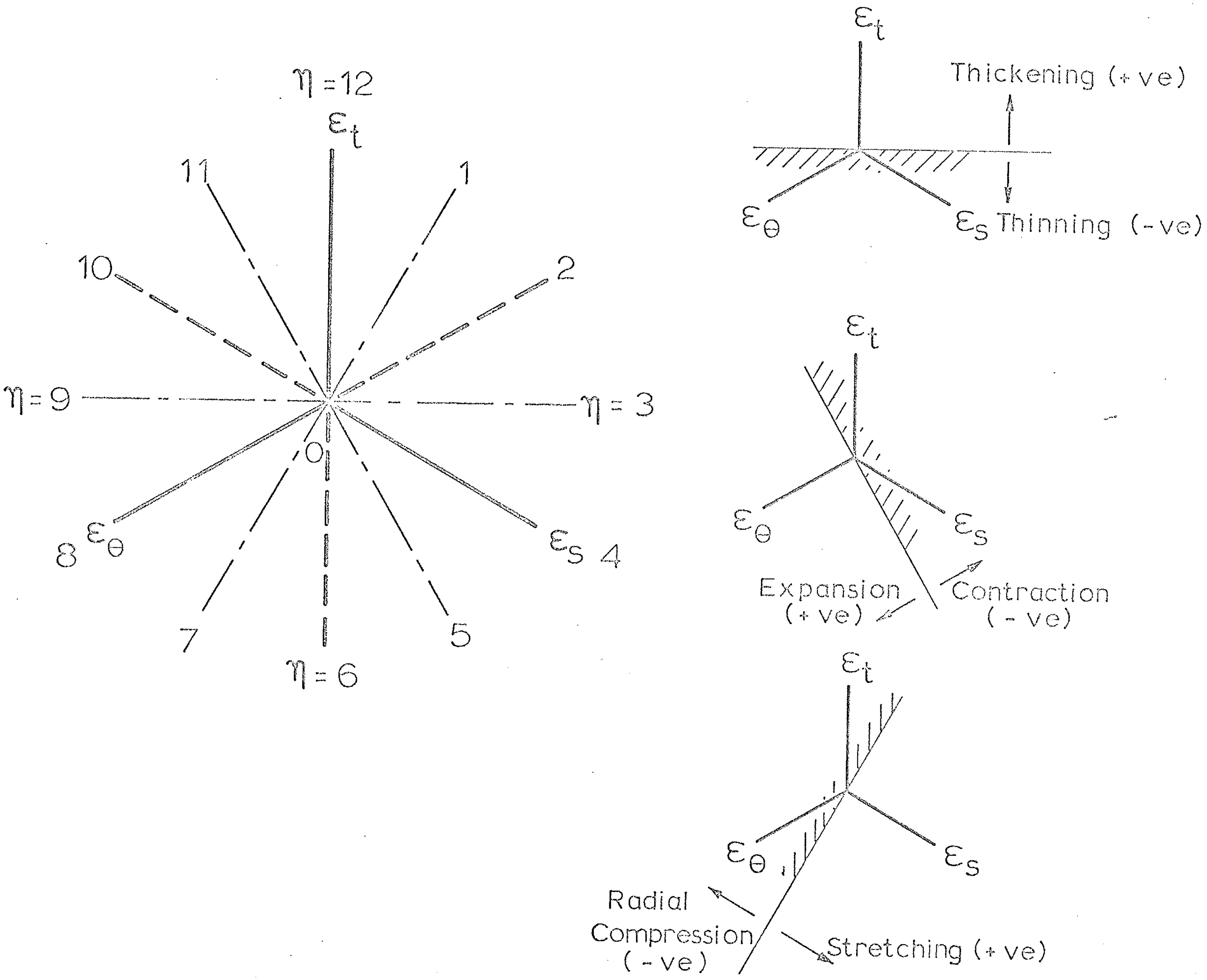
$\eta=12$
ε_t
11
1
10
2
$\eta=9$
$\eta=3$
0
8
ε_θ
ε_s
4
7
5
$\eta=6$
ε_t
Thickening (+ve)
ε_θ
ε_s
Thinning (-ve)
ε_t
ε_θ
ε_s
Expansion (+ve)
Contraction (-ve)
ε_t
ε_θ
ε_s
Radial Compression (-ve)
Stretching (+ve)

Fig.(6.2)

After T.C. Hsu, 'The Characteristics of Coaxial and Non-coaxial Strain Paths,' Journal of Strain Analysis, 1966,1(3),219

Fig.(6.3)

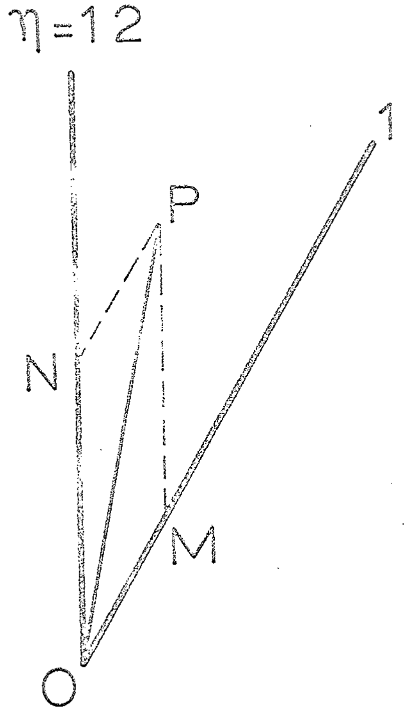

Fig.(6.4)

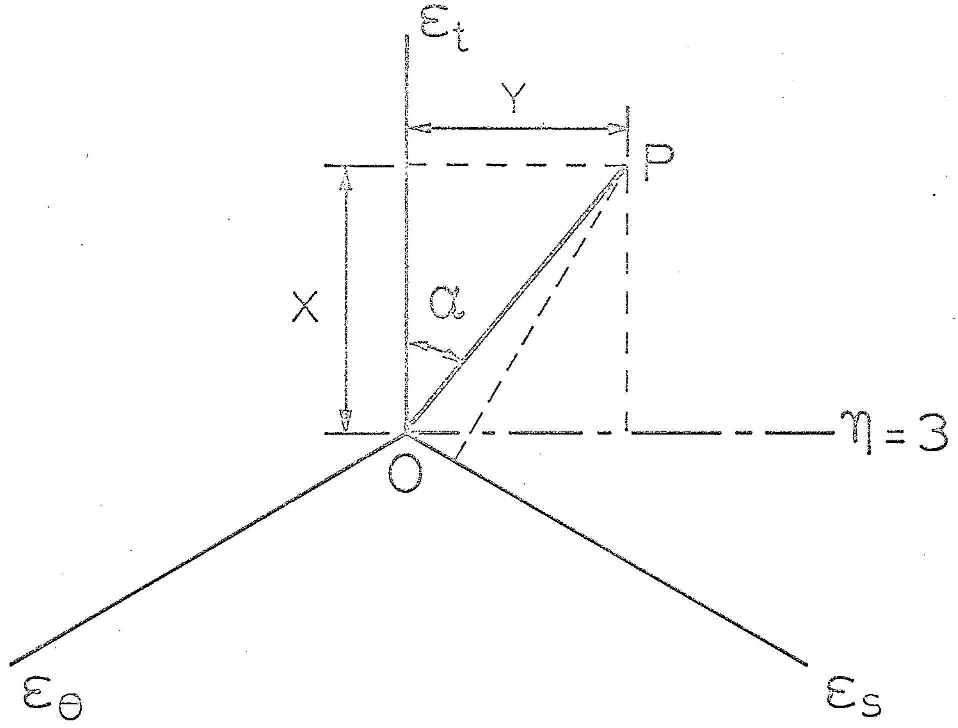
ε_t
Y
P
X
α
$\eta = 3$
O
ε_θ
ε_s

Fig.(6.5)

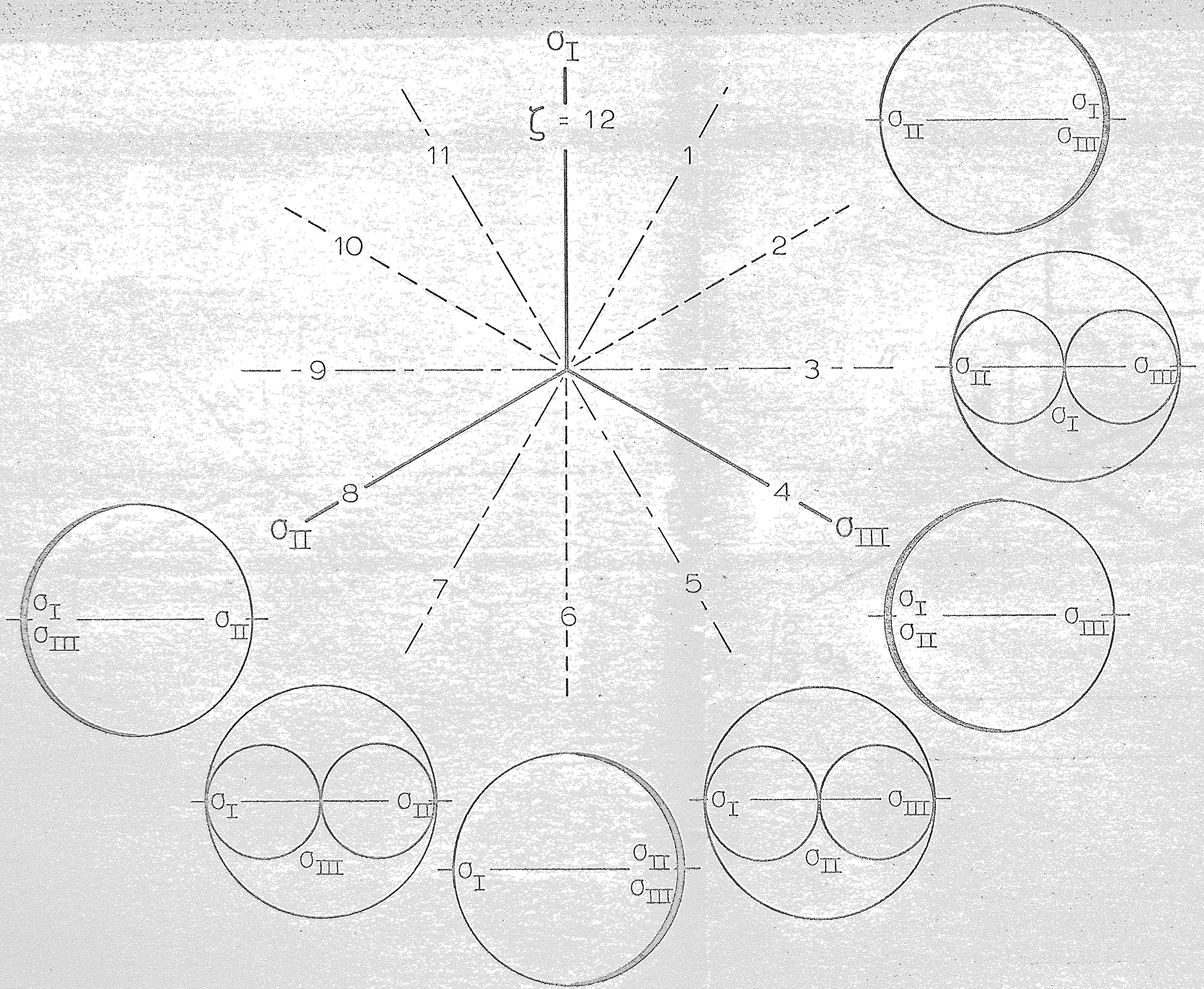

σ_I
ζ = 12
1
2
3
4
5
6
7
8
9
10
11
σ_{II}
σ_{III}
σ_I
σ_{II}
σ_{III}

Fig.(6.6)

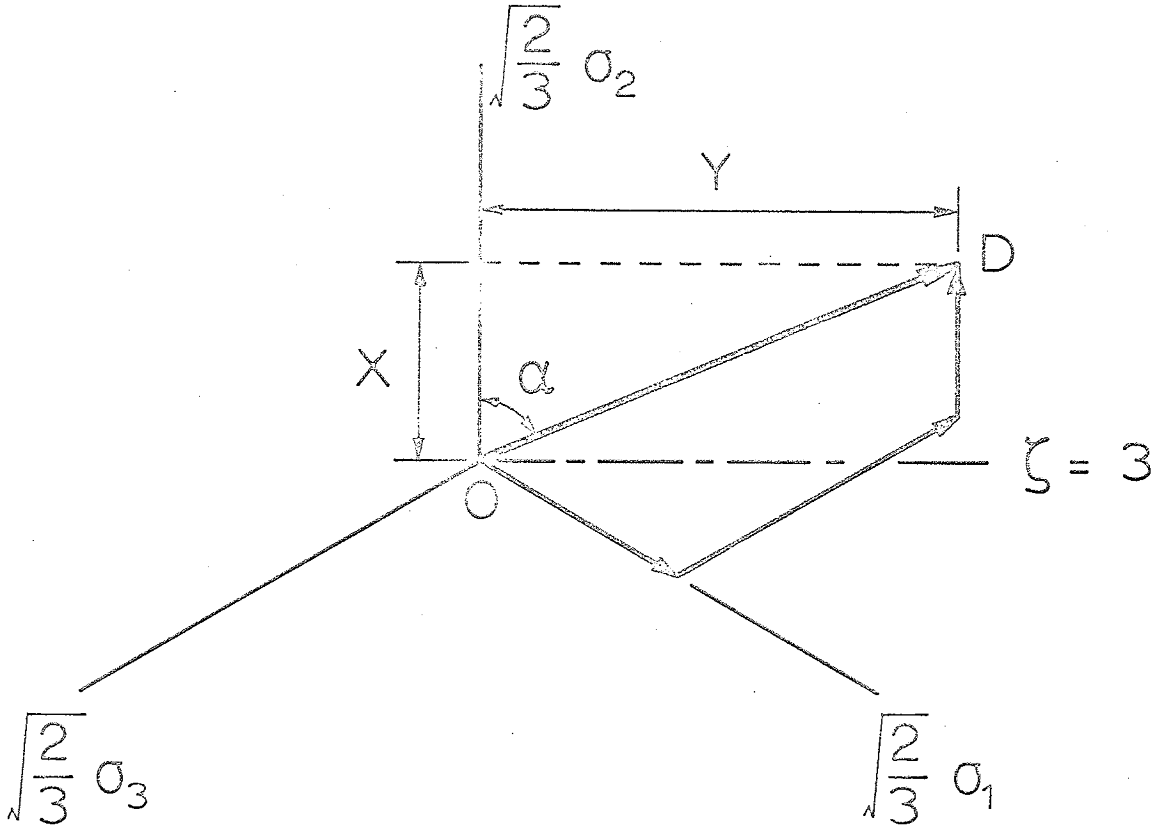
$\sqrt{\frac{2}{3}}\sigma_2$
Y
D
X
α
O
ζ = 3
$\sqrt{\frac{2}{3}}\sigma_3$
$\sqrt{\frac{2}{3}}\sigma_1$

Fig.(6.7)

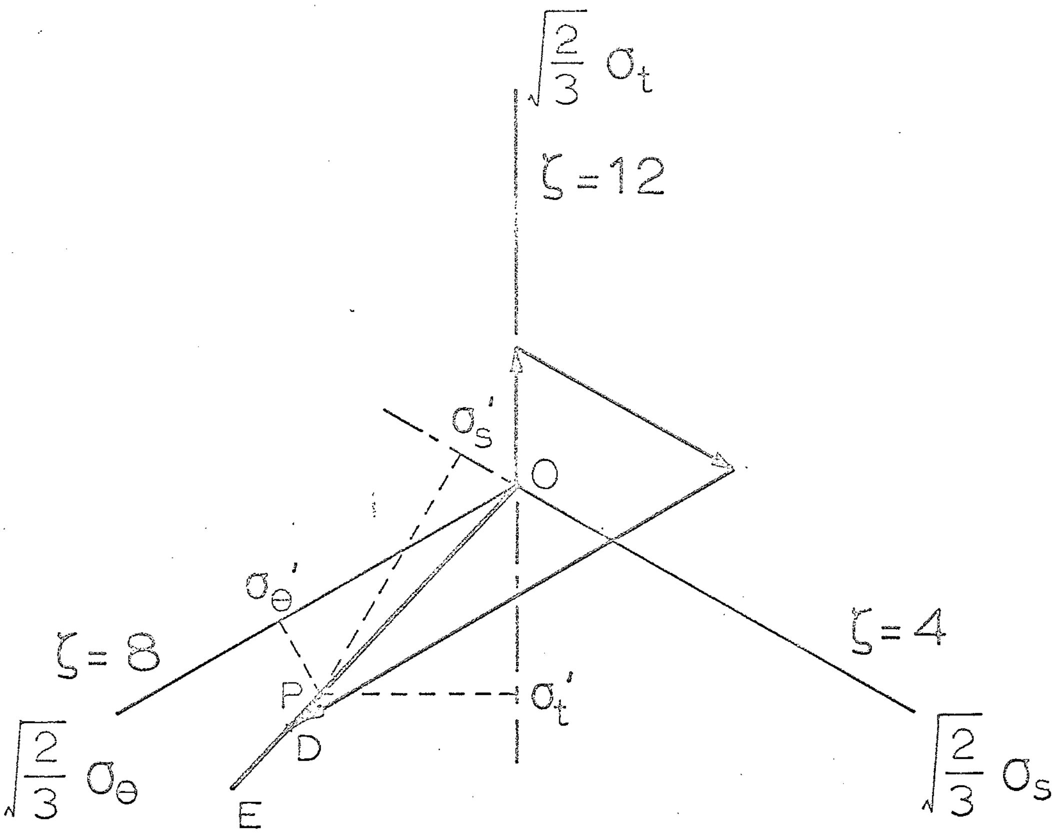

$$OP = \sqrt{\frac{2}{3}}\,OD = \sqrt{\frac{2}{3}}\,\sigma'$$

$$OE = \sqrt{\frac{3}{2}}\,OD = \frac{3}{2}\,OP = \bar{\sigma}$$

Fig.(6.8)

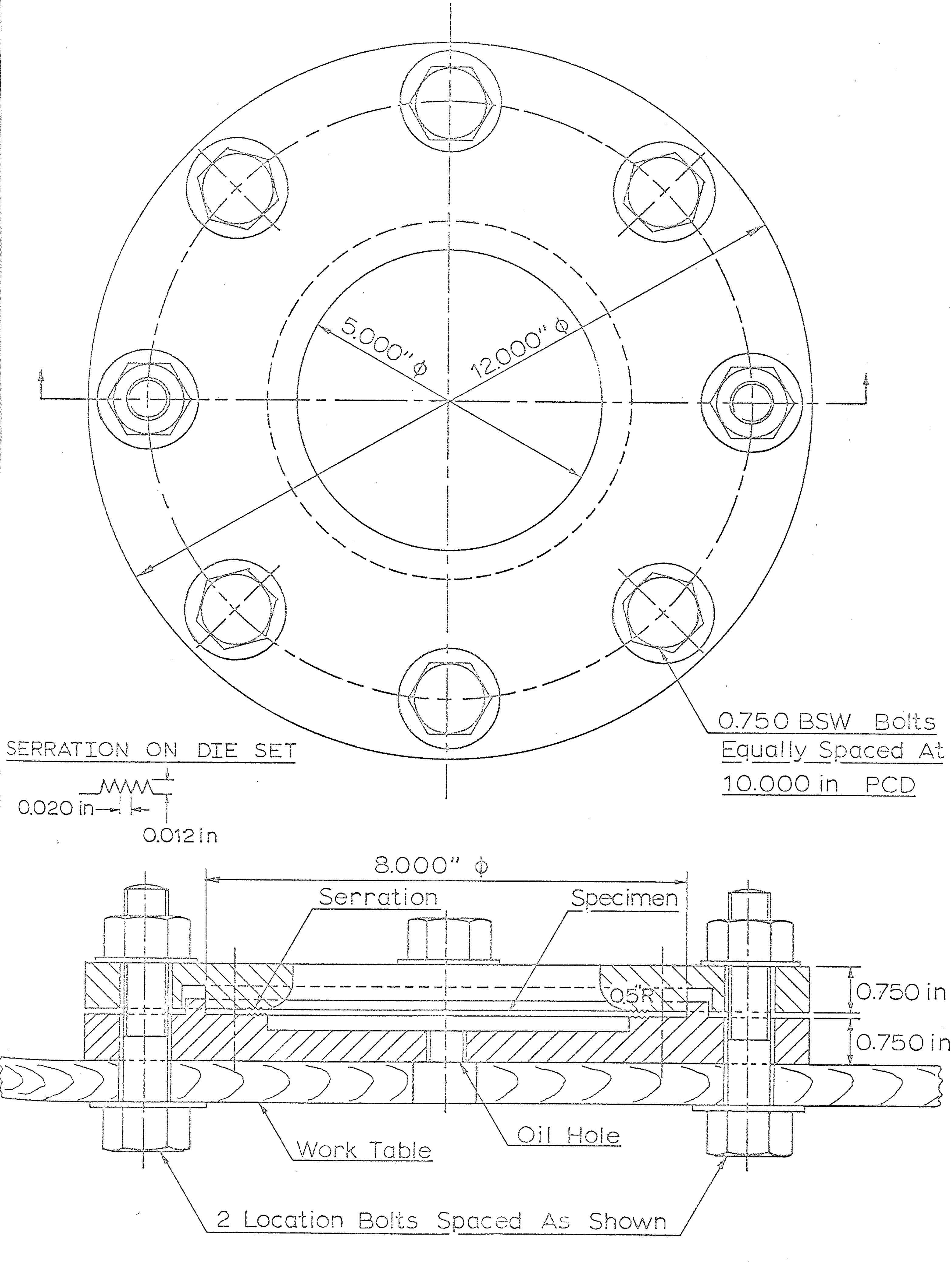
5.000" φ
12.000" φ
0.750 BSW Bolts
Equally Spaced At
10.000 in PCD
SERRATION ON DIE SET
0.020 in
0.012 in
8.000" φ
Serration
Specimen
0.5"R
0.750 in
0.750 in
Work Table
Oil Hole
2 Location Bolts Spaced As Shown

Fig.(7.1)

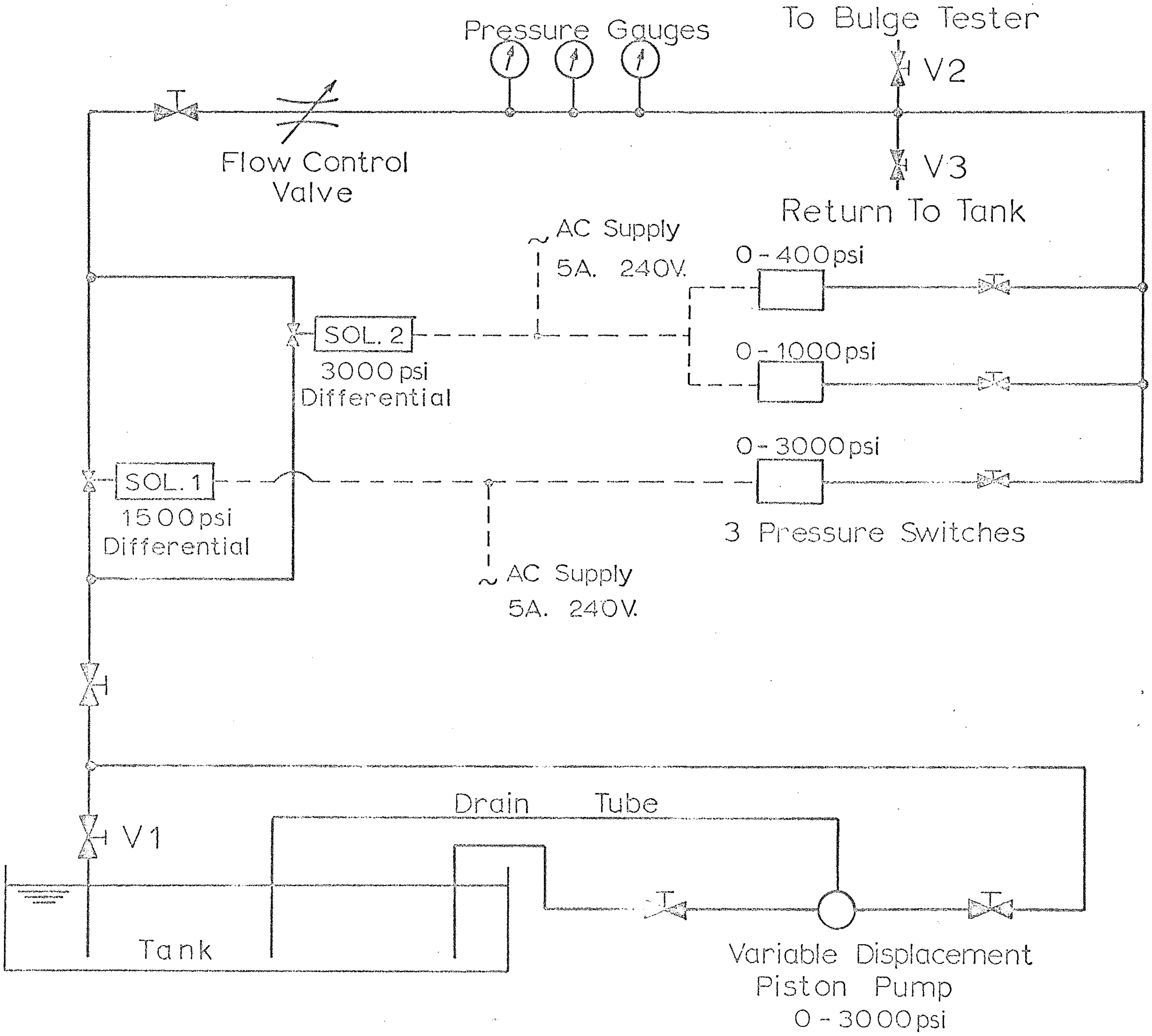

Pressure Gauges
To Bulge Tester
V2
V3
Flow Control Valve
Return To Tank
AC Supply
5A. 240V.
0-400psi
SOL. 2
3000 psi Differential
0-1000psi
0-3000psi
SOL. 1
1500psi Differential
3 Pressure Switches
AC Supply
5A. 240V.
Drain Tube
V1
Tank
Variable Displacement Piston Pump
0-3000psi

Fig.(7.2)

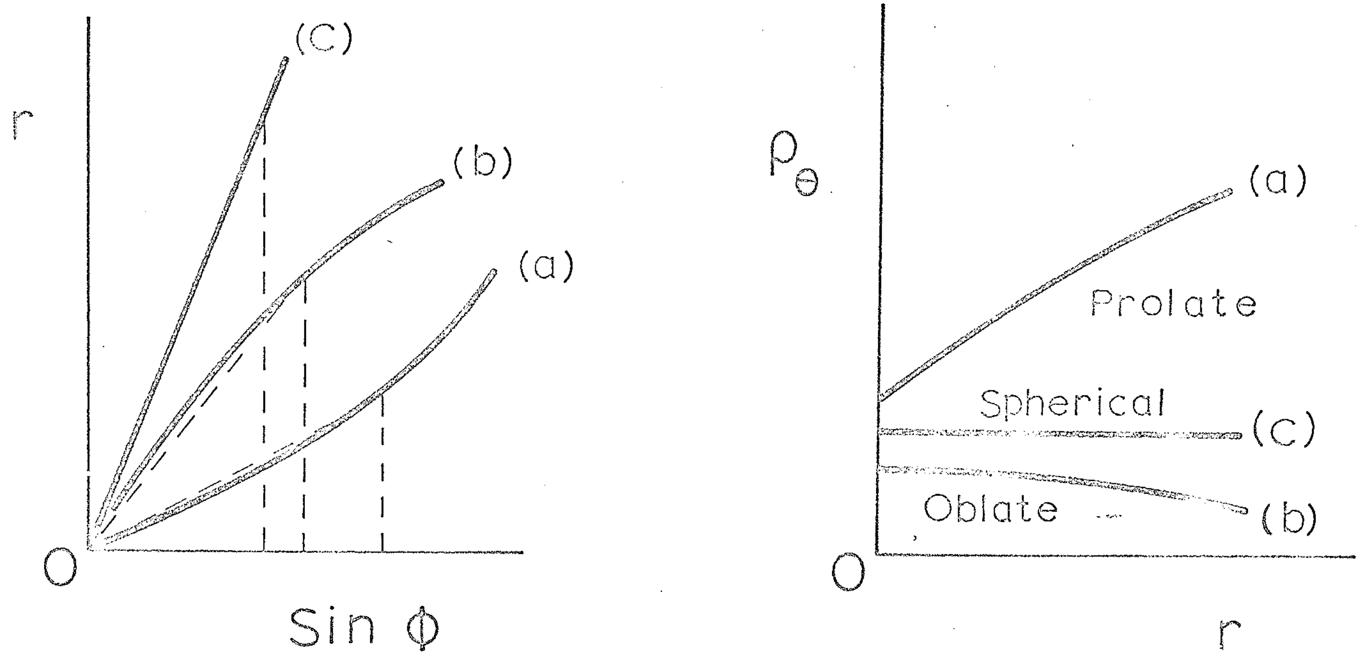

Fig.(8.1)

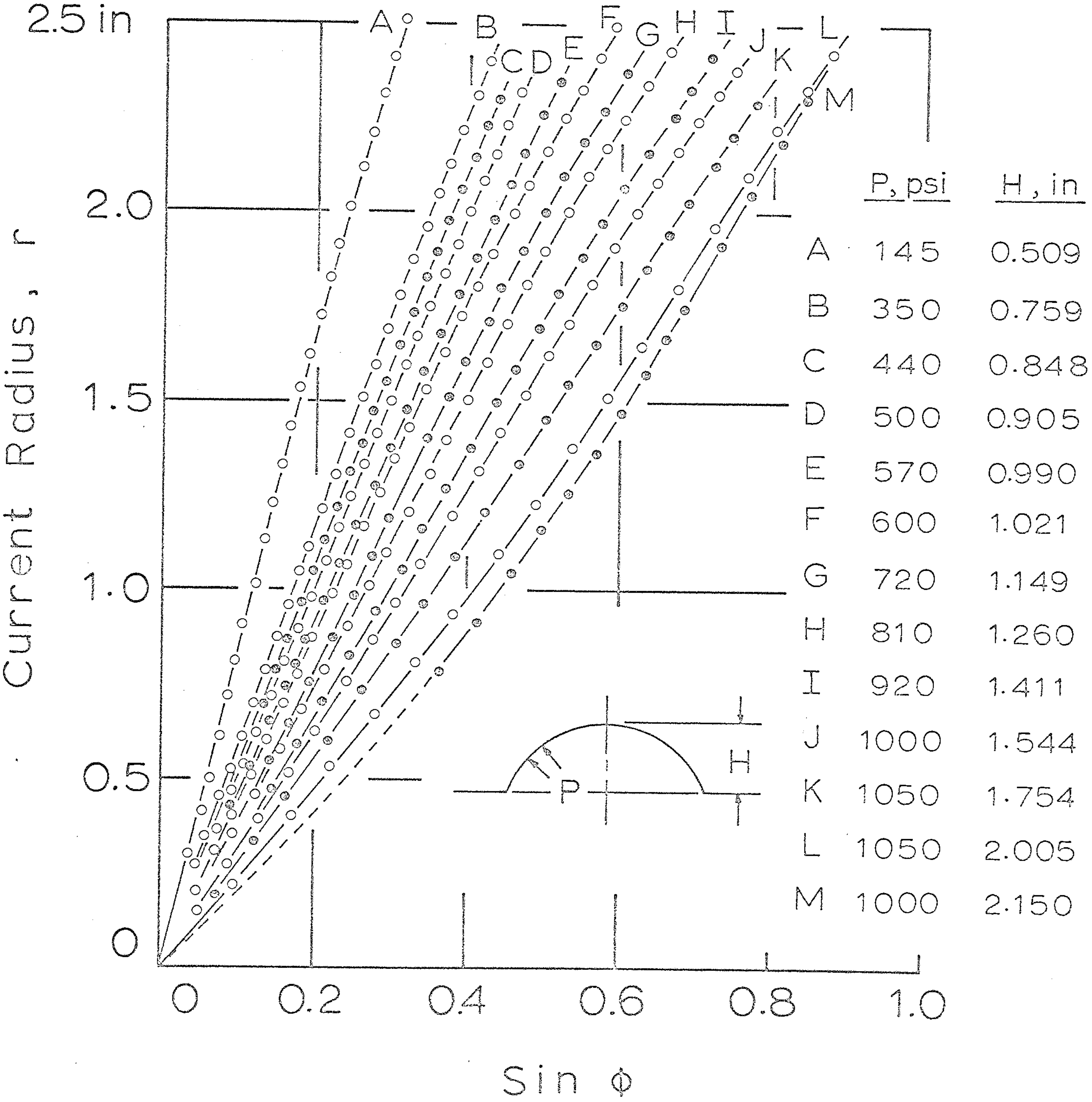

	P, psi	H, in
A	145	0.509
B	350	0.759
C	440	0.848
D	500	0.905
E	570	0.990
F	600	1.021
G	720	1.149
H	810	1.260
I	920	1.411
J	1000	1.544
K	1050	1.754
L	1050	2.005
M	1000	2.150

Fig.(8.2)

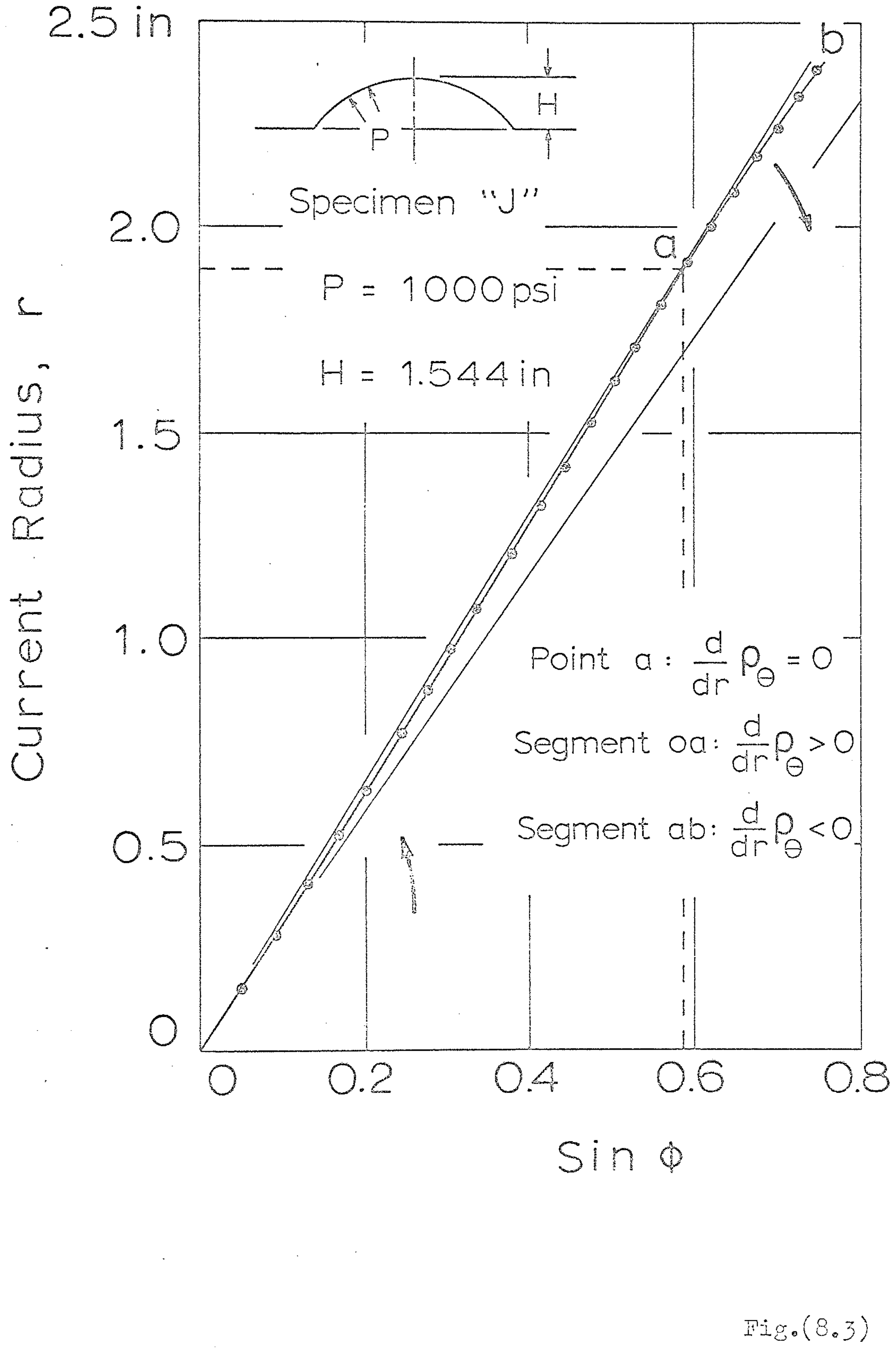
2.5 in
2.0
1.5
1.0
0.5
0
0.2
0.4
0.6
0.8
Current Radius, r
Sin φ
H
P
Specimen "J"
P = 1000 psi
H = 1.544 in
a
b
Point a : $\frac{d}{dr}\rho_\theta = 0$
Segment oa: $\frac{d}{dr}\rho_\theta > 0$
Segment ab: $\frac{d}{dr}\rho_\theta < 0$

Fig.(8.3)

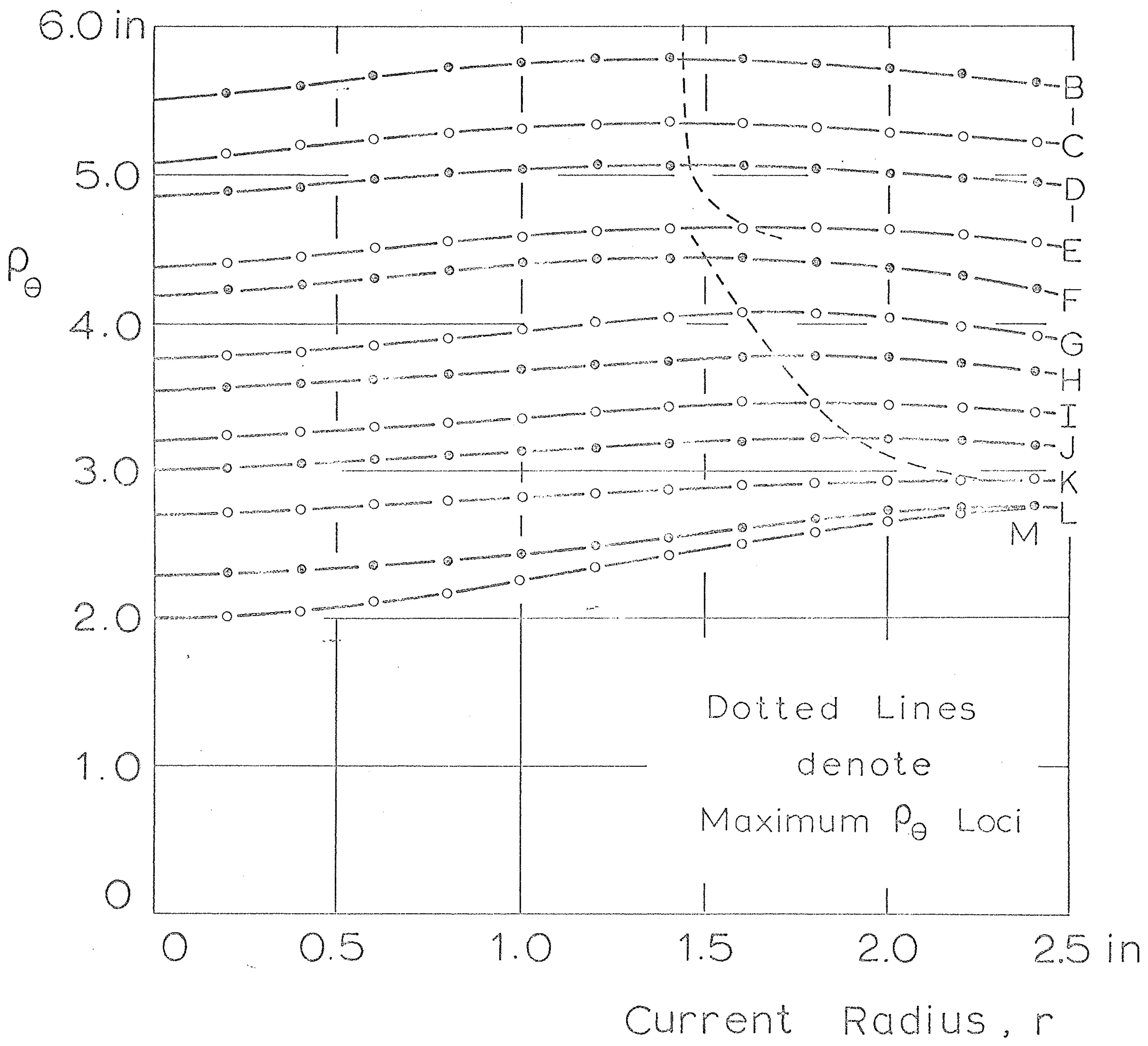
6.0 in
5.0
4.0
3.0
2.0
1.0
0
ρ_θ
0
0.5
1.0
1.5
2.0
2.5 in
Current Radius , r
B
C
D
E
F
G
H
I
J
K
L
M
Dotted Lines
denote
Maximum ρ_θ Loci

Fig.(8.4)

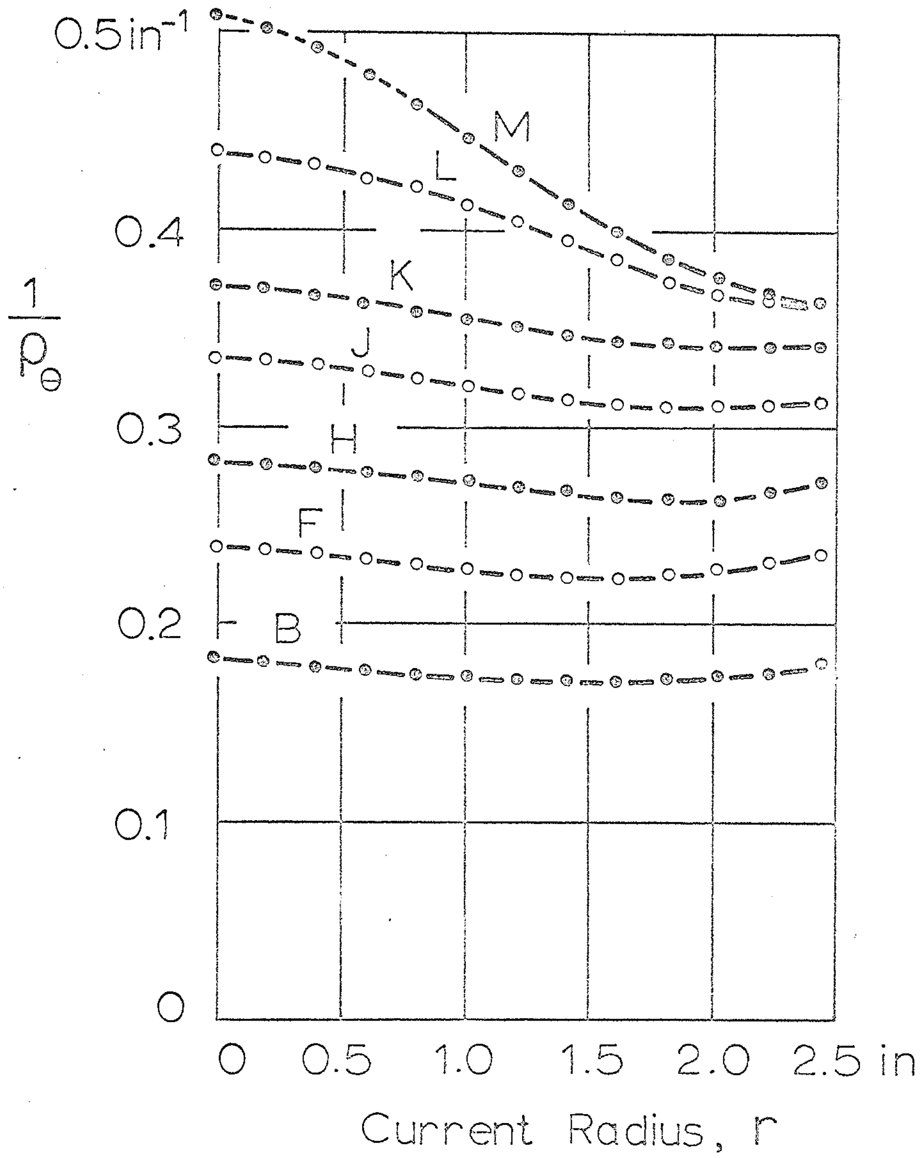
0.5 in⁻¹
0.4
0.3
0.2
0.1
0
1/ρθ
M
L
K
J
H
F
B
0
0.5
1.0
1.5
2.0
2.5 in
Current Radius, r

Fig.(8.5)

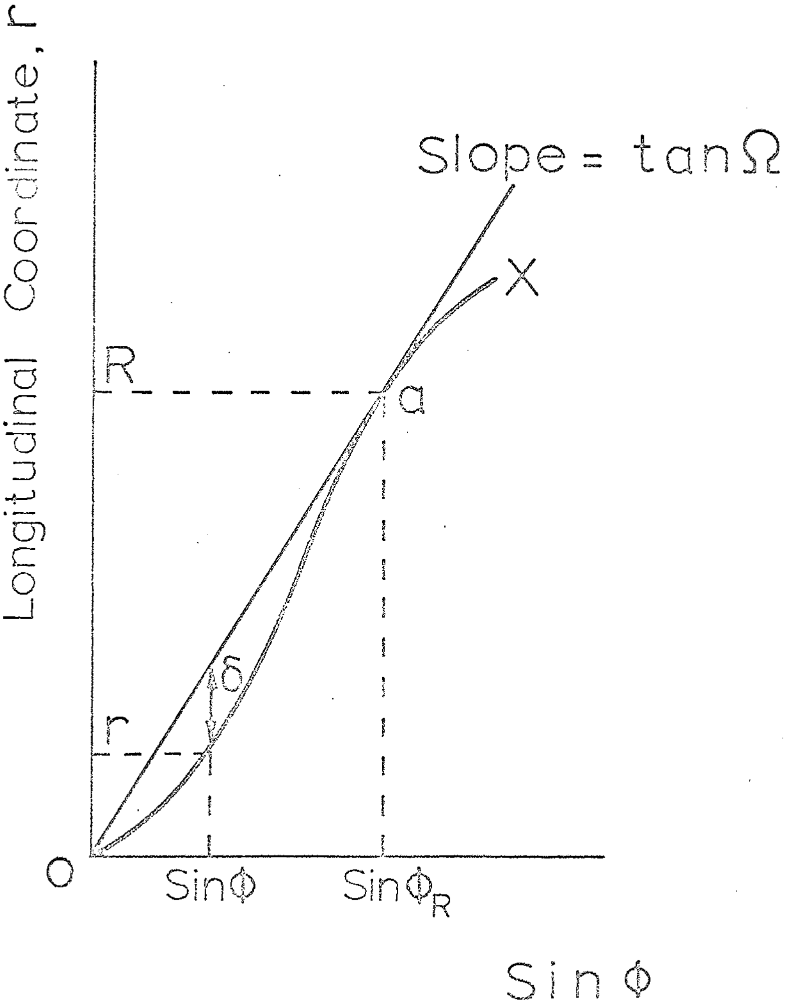
Longitudinal Coordinate, r
Slope = tanΩ
X
R
a
δ
r
O
Sinϕ
Sinϕ_R
Sin ϕ

Fig.(8.6)

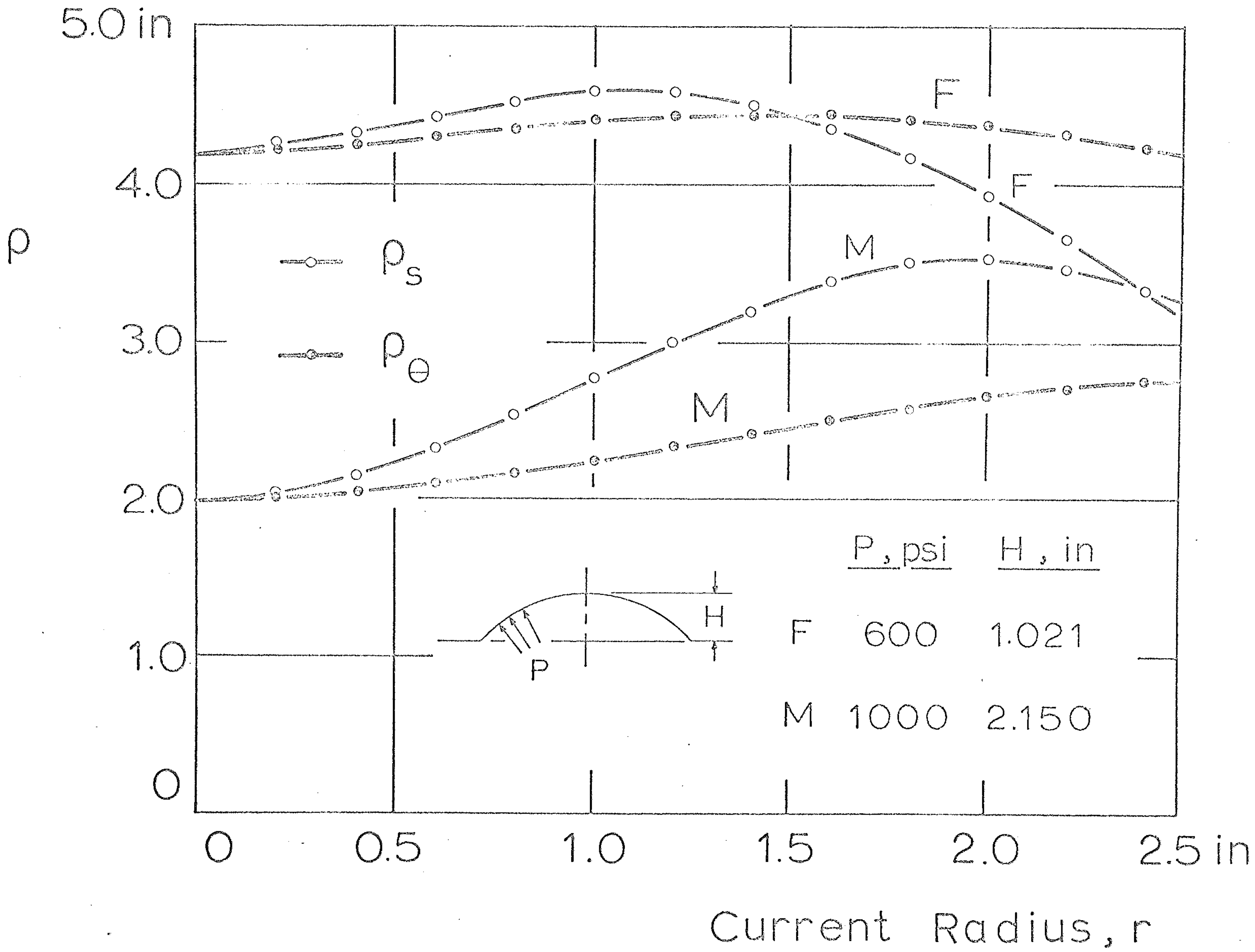
5.0 in
4.0
3.0
2.0
1.0
0
ρ
ρ_s
ρ_θ
F
F
M
M
P
H
P, psi
H, in
F 600 1.021
M 1000 2.150
0
0.5
1.0
1.5
2.0
2.5 in
Current Radius, r

Fig.(8.7)

(i) Monotonic Increasing ρ_θ

Impossible - Violates Mech. Constraint Of $2>N>1$ At The Die Edge

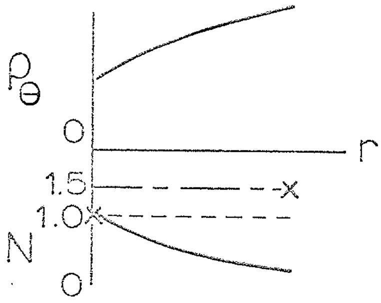

(ii) Monotonic Decreasing ρ_θ

Mathematically Possible

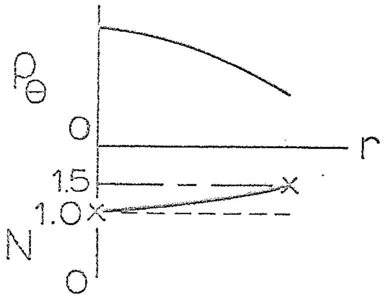

(iii) Maximum ρ_θ Curve

Mathematically Possible With Only One Crossing Of N With The N = 1 Line

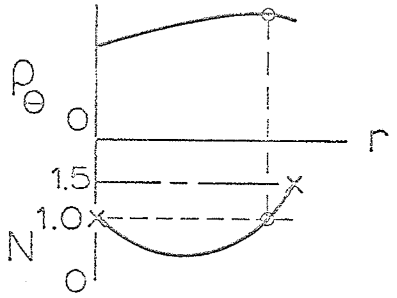

(iv) Minimum ρ_θ Curve

Impossible - Violates Mech. Constraint Of $2>N>1$ At The Die Edge

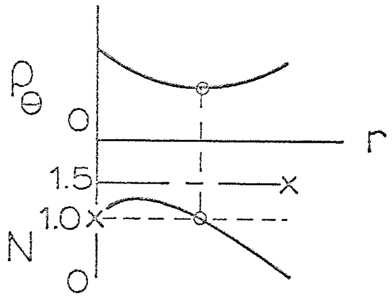

(v) Maximum & Minimum ρ_θ

Impossible - Violates The $2>N>1$ Constraint At The Die Edge

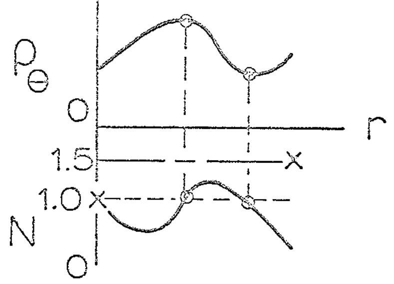

(vi) Minimum & Maximum ρ_θ

Mathematically Possible For Only Two Crossings Of N With The N = 1 Line

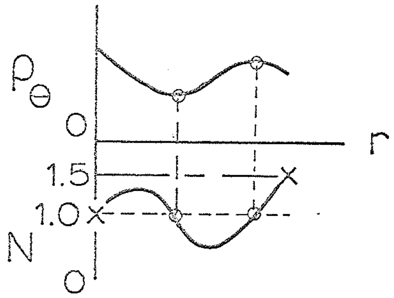

(vii) Spherical Bulge

Impossible - Violates Constraint Of $2>N>1$ At The Die Edge

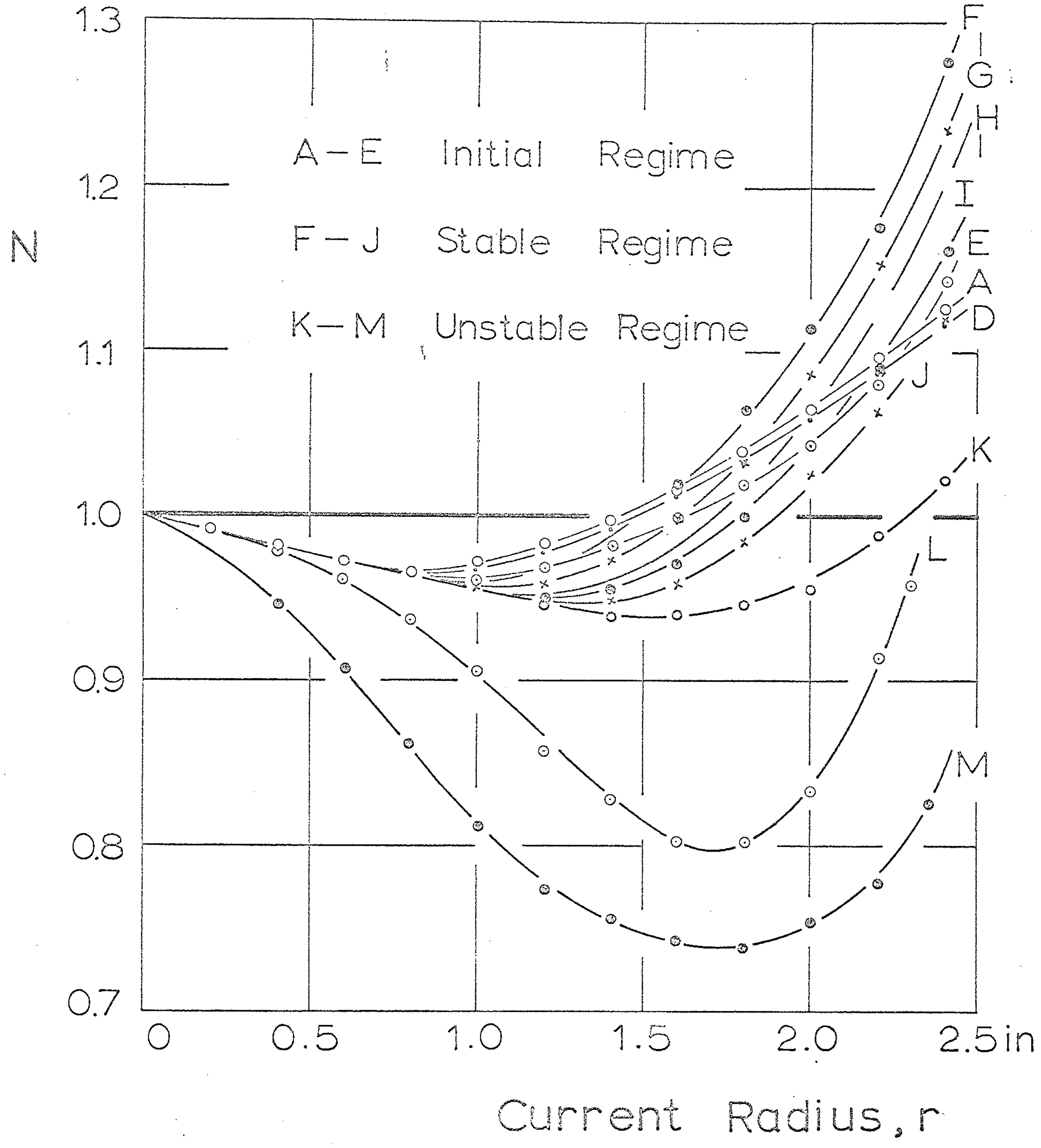
A–E Initial Regime
F – J Stable Regime
K–M Unstable Regime
N
1.3
1.2
1.1
1.0
0.9
0.8
0.7
0
0.5
1.0
1.5
2.0
2.5 in
Current Radius, r
F
G
H
I
E
A
D
J
K
L
M

Fig.(8.9)

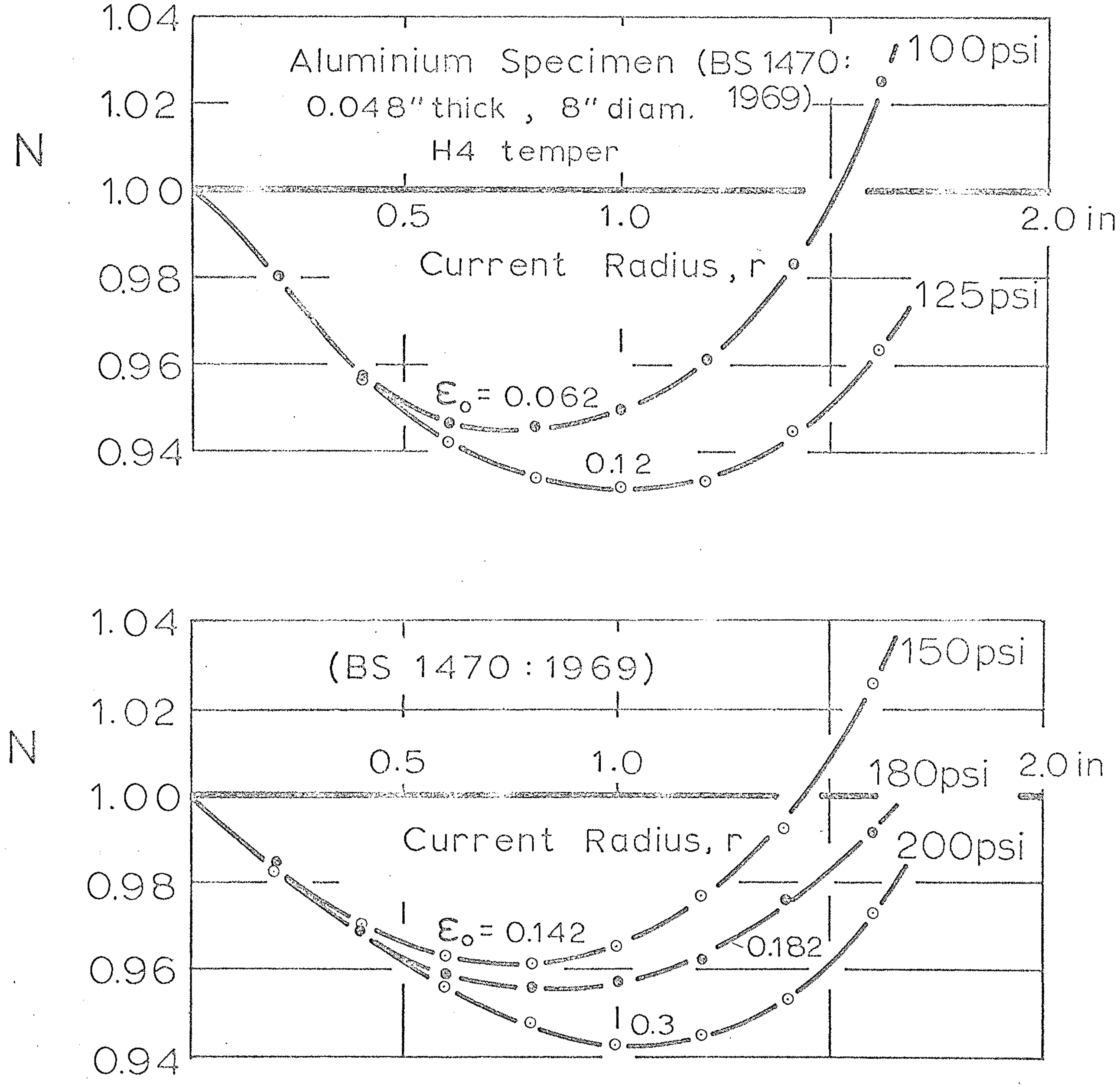
1.04
1.02
1.00
0.98
0.96
0.94
N
Aluminium Specimen (BS 1470: 1969)
0.048" thick , 8" diam.
H4 temper
0.5
1.0
2.0 in
Current Radius, r
100psi
125psi
$\varepsilon_o = 0.062$
0.12
1.04
1.02
1.00
0.98
0.96
0.94
N
(BS 1470 : 1969)
0.5
1.0
2.0 in
Current Radius, r
150psi
180psi
200psi
$\varepsilon_o = 0.142$
0.182
0.3

Fig.(8.10)

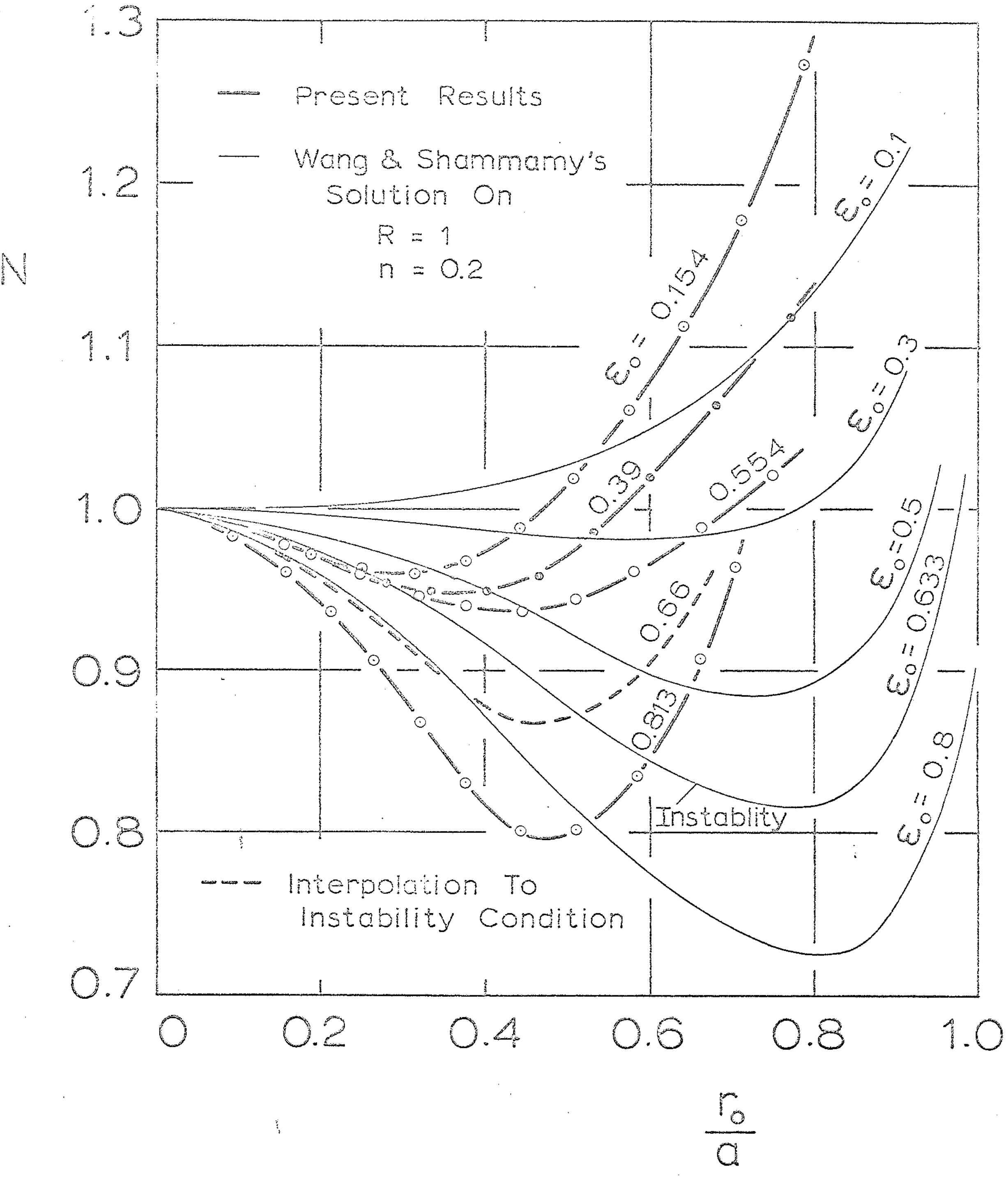

1.3
1.2
1.1
1.0
0.9
0.8
0.7
N
0
0.2
0.4
0.6
0.8
1.0
$\frac{r_o}{a}$
Present Results
Wang & Shammamy's Solution On
R = 1
n = 0.2
Interpolation To Instability Condition
ε_o = 0.154
ε_o = 0.1
ε_o = 0.3
0.39
0.554
0.66
0.813
ε_o = 0.5
ε_o = 0.633
ε_o = 0.8
Instablity

Fig.(8.11)

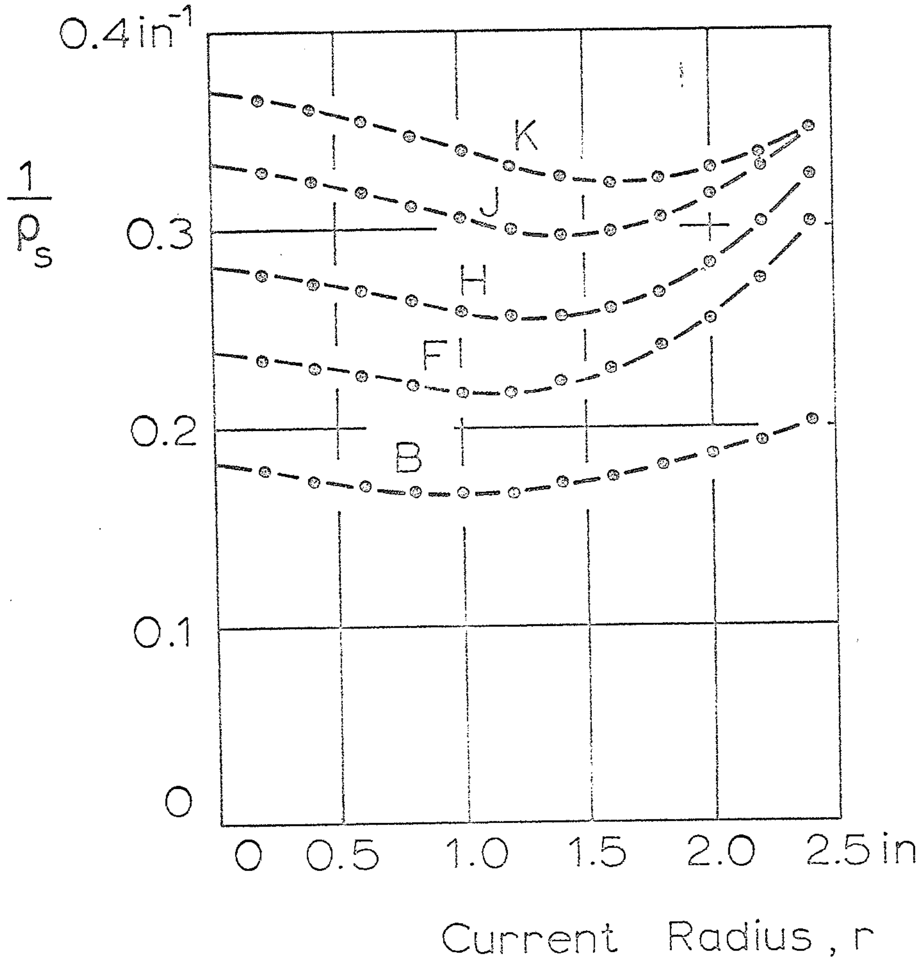

Fig.(8.12)

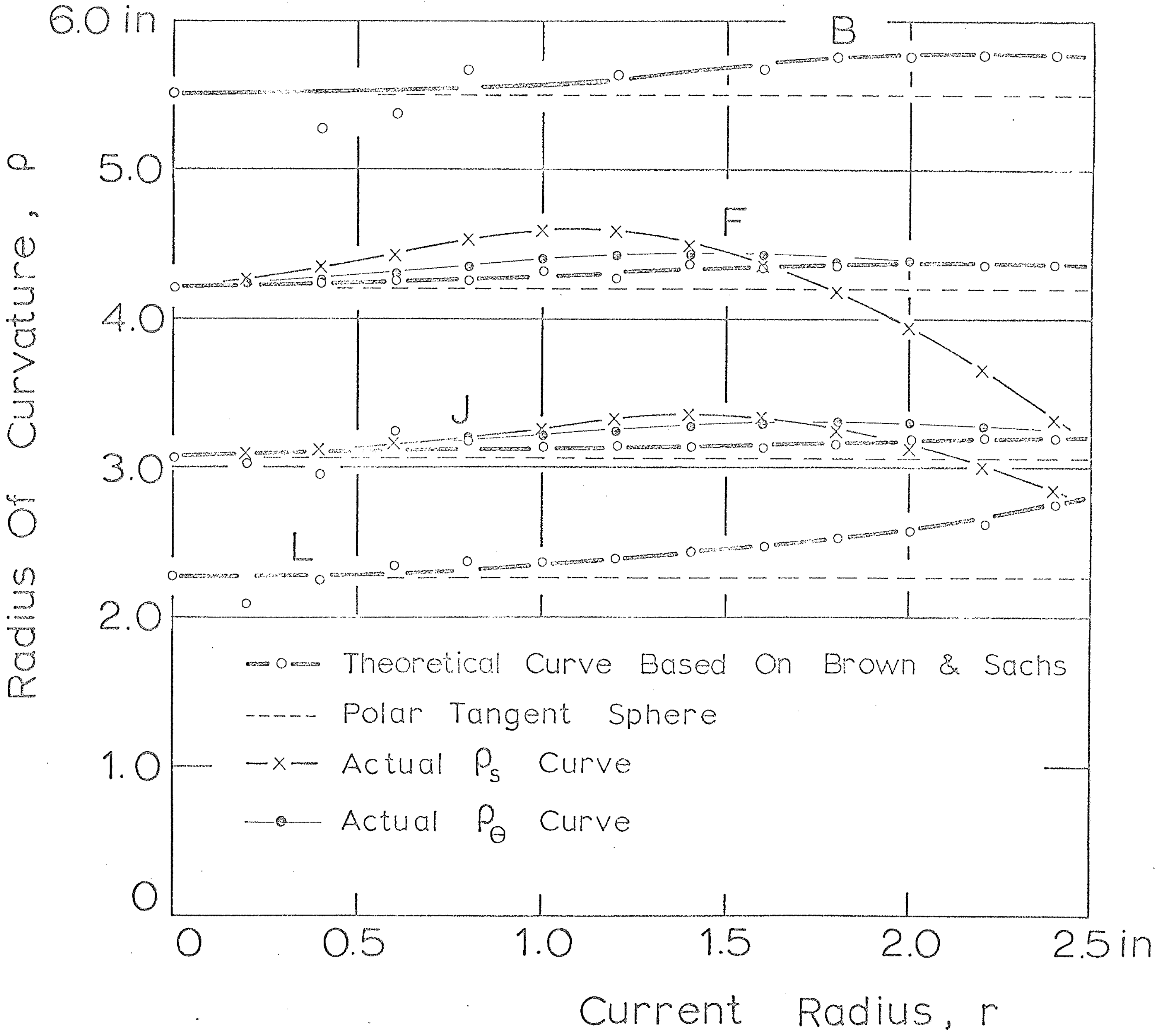
6.0 in
5.0
4.0
3.0
2.0
1.0
0
Radius Of Curvature, ρ
B
F
J
L
0
0.5
1.0
1.5
2.0
2.5 in
Current Radius, r
Theoretical Curve Based On Brown & Sachs
Polar Tangent Sphere
Actual ρ_s Curve
Actual ρ_θ Curve

Fig.(8.13)

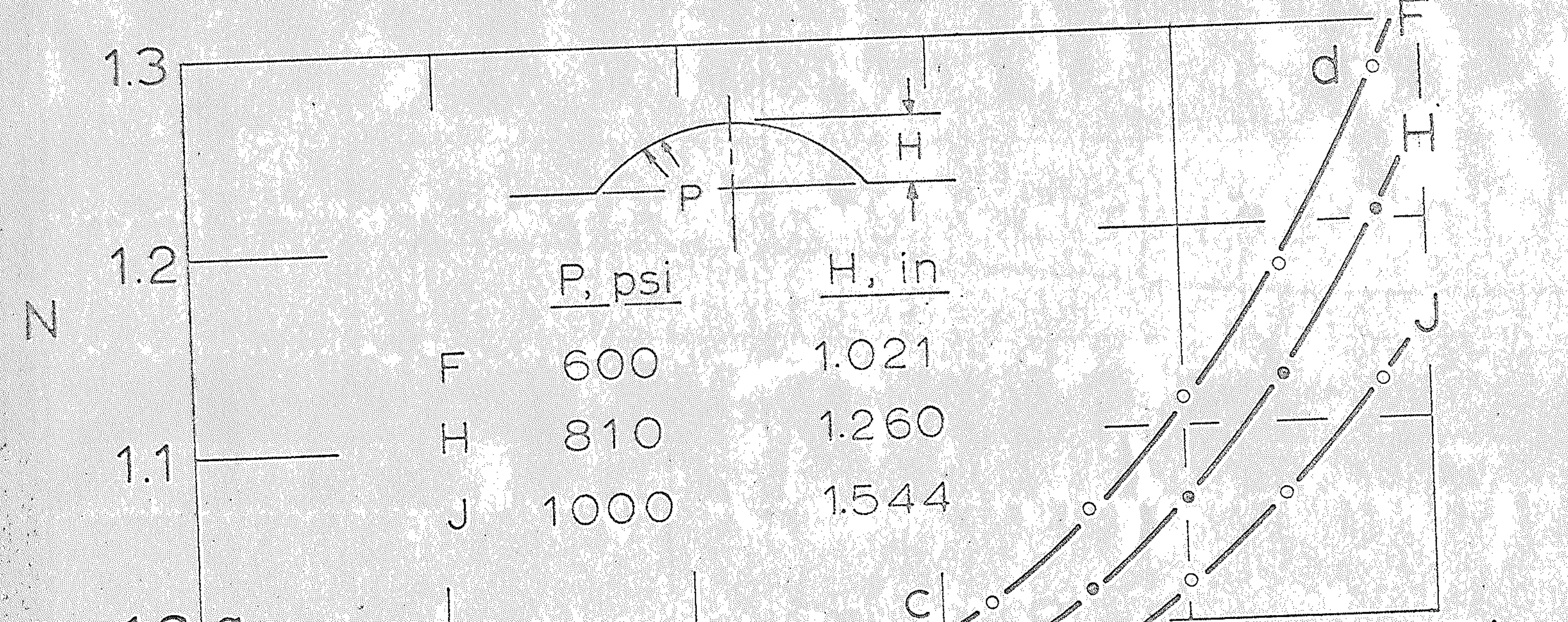
1.3
1.2
1.1
1.0
N
a
b
c
d
F
H
J
P
H
P, psi
H, in
F 600 1.021
H 810 1.260
J 1000 1.544
2.0
2.5 in
r
1.6 k/in
1.4
1.2
1.0
$\sigma_s t$
$\frac{dN}{dr} < 0$
$\frac{dN}{dr} > 0$
$\frac{dN}{dr} > 0$
Minimum N Locus
Maximum Force Locus
0
0.5
1.0
1.5
2.0
2.5 in
Current Radius, r

Fig.(9.1)

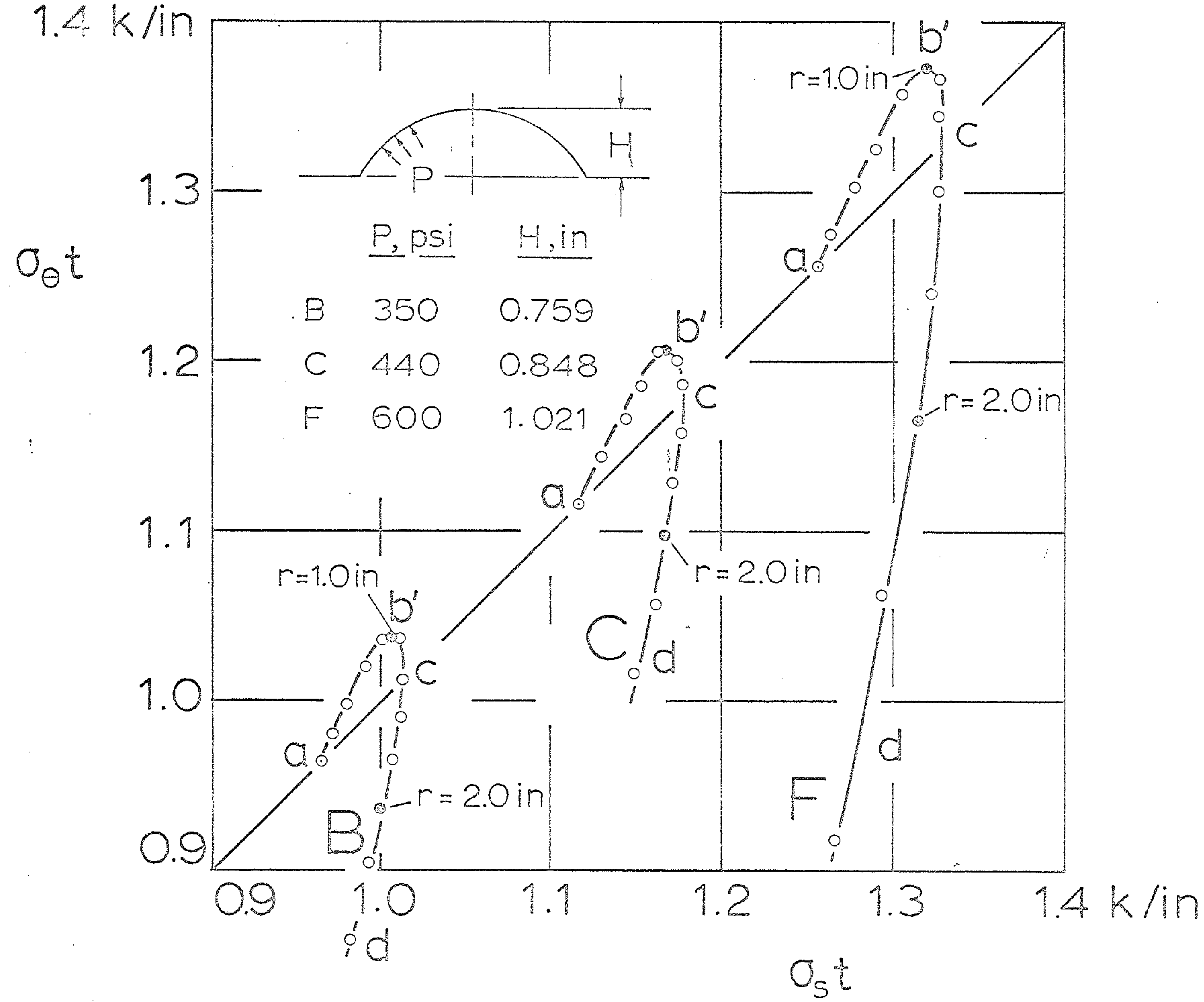
1.4 k/in
1.3
1.2
1.1
1.0
0.9
σθt
0.9
1.0
1.1
1.2
1.3
1.4 k/in
σst
P
H
P, psi
H, in
B 350 0.759
C 440 0.848
F 600 1.021
a
b'
c
d
r=1.0in
r=2.0in
B
C
F

Fig.(9.2)

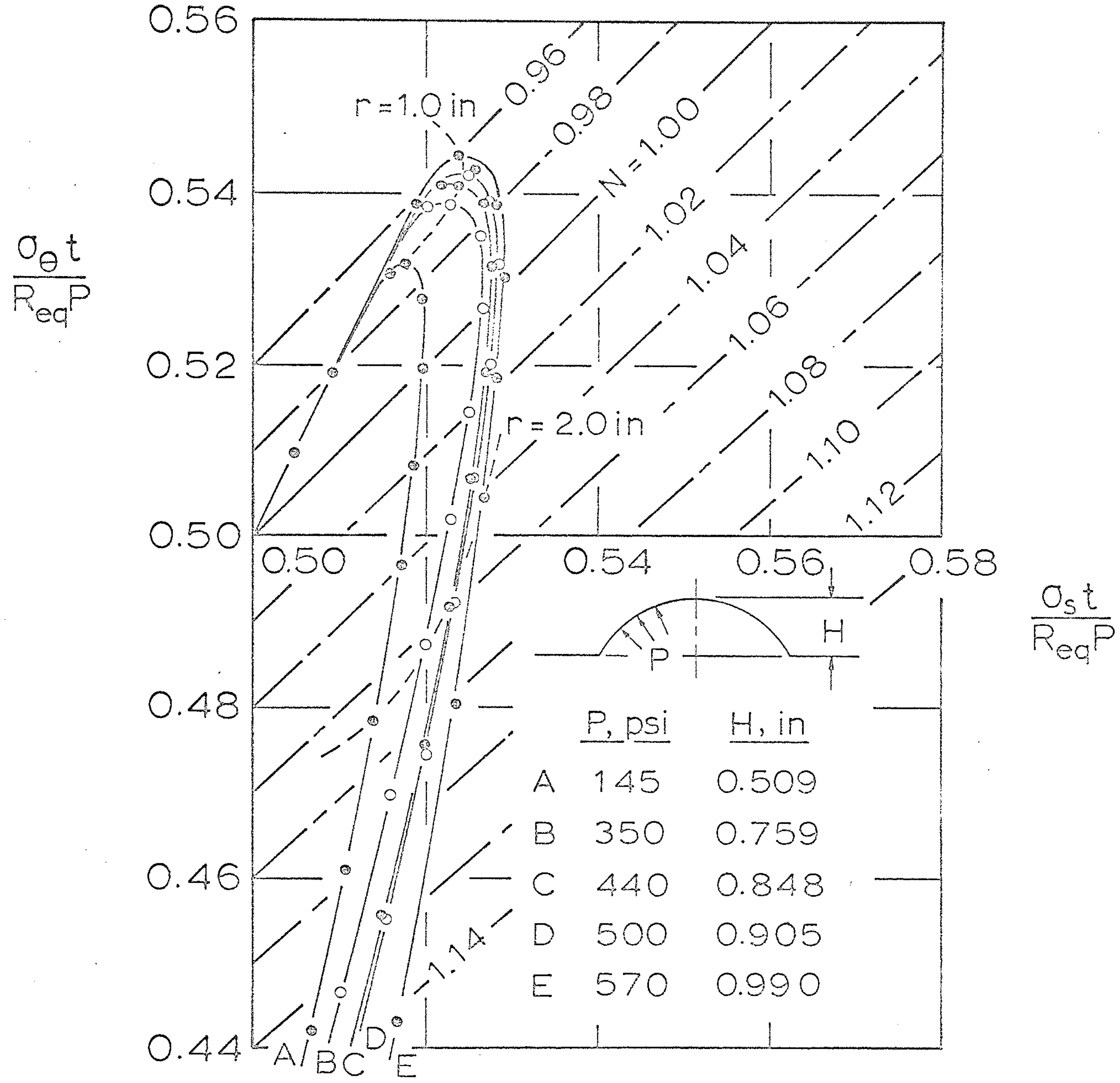
$\frac{\sigma_\theta t}{R_{eq}P}$
0.56
0.54
0.52
0.50
0.48
0.46
0.44
0.50
0.54
0.56
0.58
$\frac{\sigma_s t}{R_{eq}P}$
r = 1.0 in
r = 2.0 in
0.96
0.98
N = 1.00
1.02
1.04
1.06
1.08
1.10
1.12
1.14
A
B
C
D
E
P
H
P, psi
H, in
A 145 0.509
B 350 0.759
C 440 0.848
D 500 0.905
E 570 0.990

Fig.(9.3)

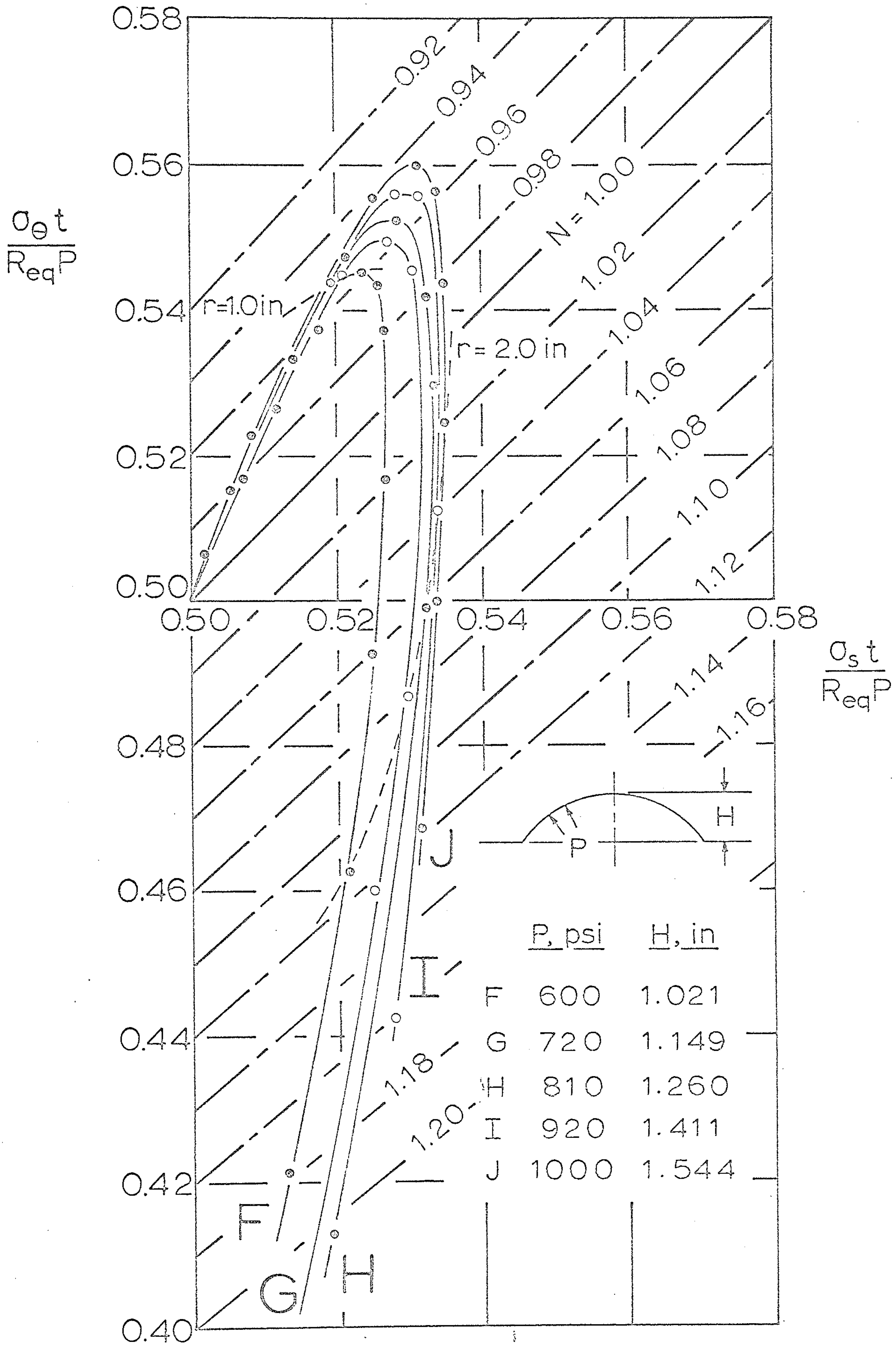
$\frac{\sigma_\theta t}{R_{eq} P}$
$\frac{\sigma_s t}{R_{eq} P}$
0.58
0.56
0.54
0.52
0.50
0.48
0.46
0.44
0.42
0.40
0.50
0.52
0.54
0.56
0.58
0.92
0.94
0.96
0.98
N = 1.00
1.02
1.04
1.06
1.08
1.10
1.12
1.14
1.16
1.18
1.20
r=1.0in
r = 2.0 in
F
G
H
I
J
H
P
P, psi
H, in
F 600 1.021
G 720 1.149
H 810 1.260
I 920 1.411
J 1000 1.544

Fig.(9.4)

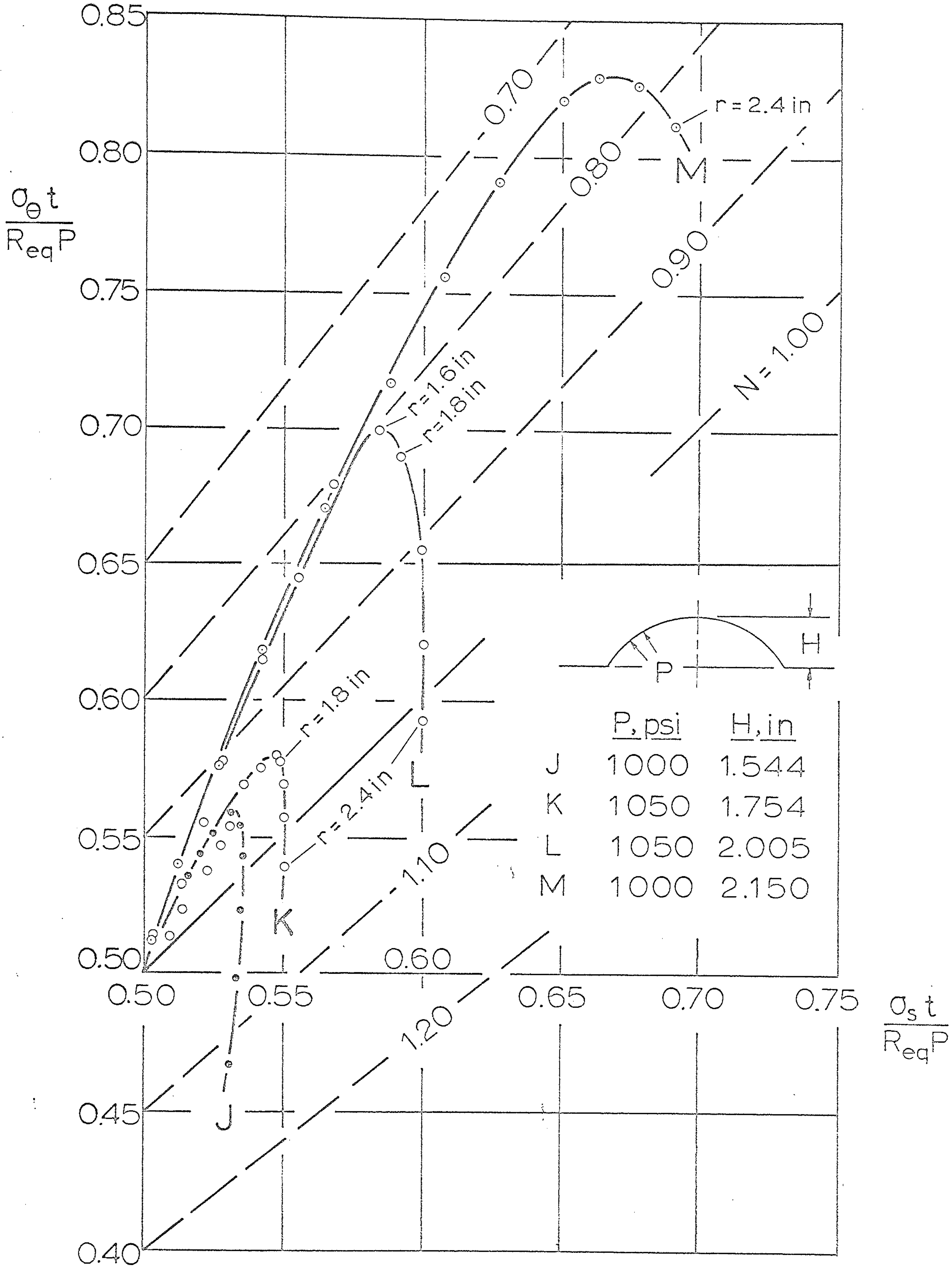

$\frac{\sigma_\theta t}{R_{eq} P}$
$\frac{\sigma_s t}{R_{eq} P}$
0.85
0.80
0.75
0.70
0.65
0.60
0.55
0.50
0.45
0.40
0.50
0.55
0.60
0.65
0.70
0.75
0.70
0.80
0.90
N = 1.00
1.10
1.20
r = 2.4 in
r = 1.6 in
r = 1.8 in
r = 1.8 in
r = 2.4 in
J
K
L
M
H
P
P, psi
H, in
J 1000 1.544
K 1050 1.754
L 1050 2.005
M 1000 2.150

Fig.(9.5)

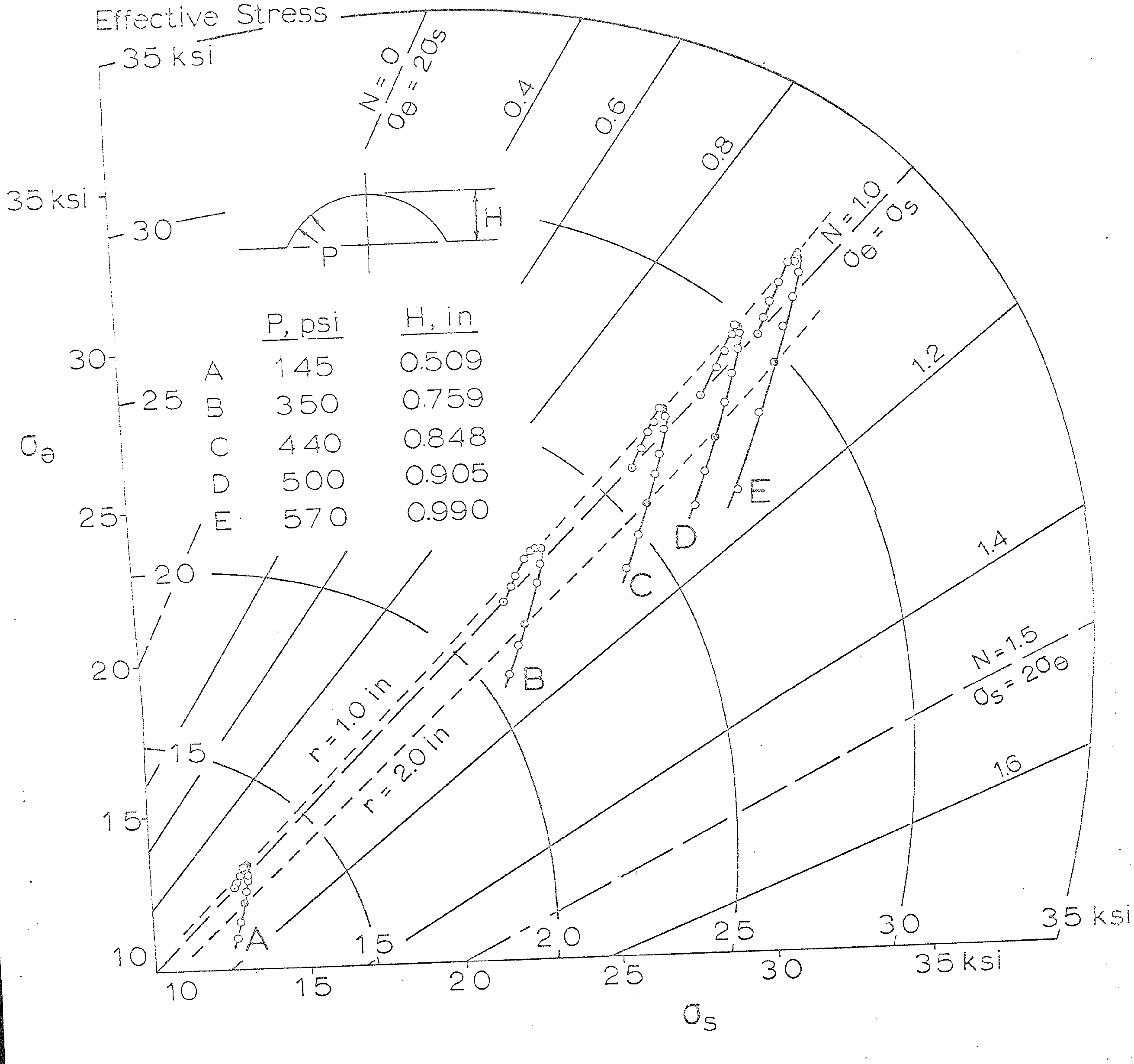

Effective Stress
35 ksi
30
25
20
15
10
35 ksi
30
25
20
15
10
σθ
σs
N = 0
σθ = 2σs
0.4
0.6
0.8
N = 1.0
σθ = σs
1.2
1.4
N = 1.5
σs = 2σθ
1.6
r = 1.0 in
r = 2.0 in
P
H
P, psi
H, in
A 145 0.509
B 350 0.759
C 440 0.848
D 500 0.905
E 570 0.990
A
B
C
D
E

Fig.(9.6)

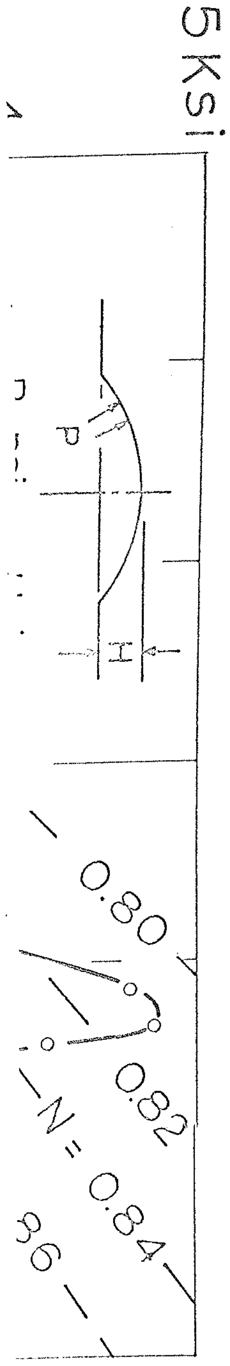

5 Ksi
P
H
0.80
0.82
N = 0.84
86

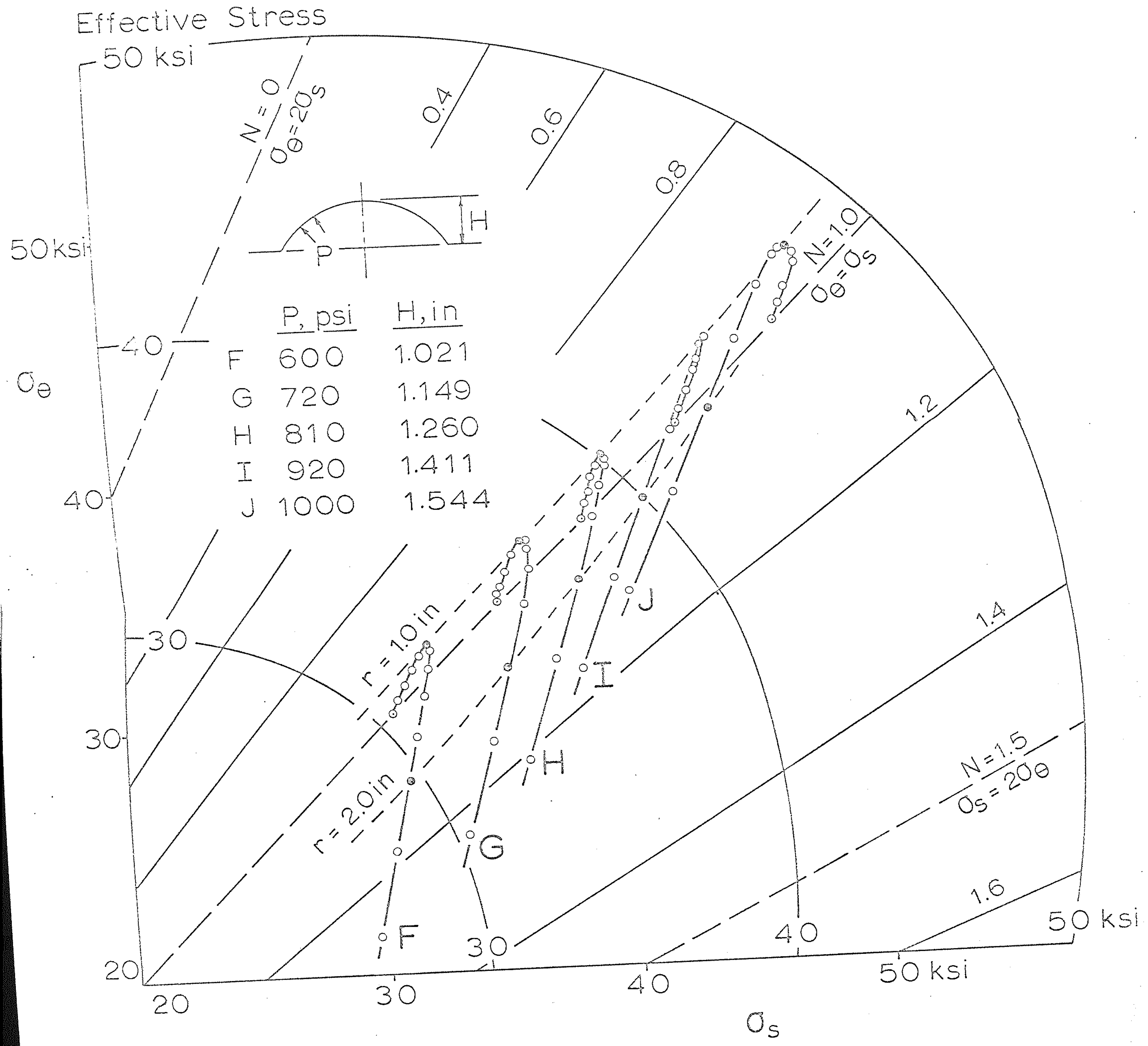

	P, psi	H, in
F	600	1.021
G	720	1.149
H	810	1.260
I	920	1.411
J	1000	1.544

Fig.(9.7)

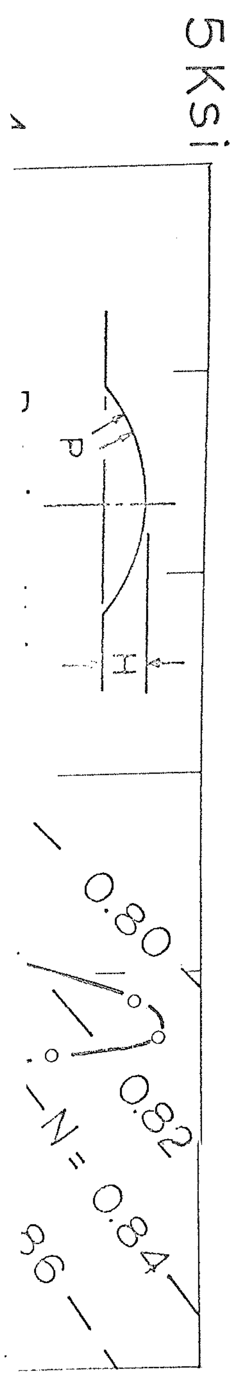

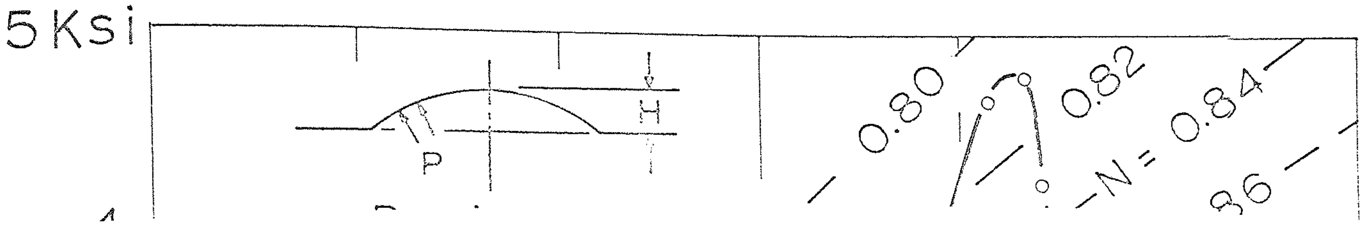
5 Ksi
H
P
0.80
0.82
N = 0.84
.86

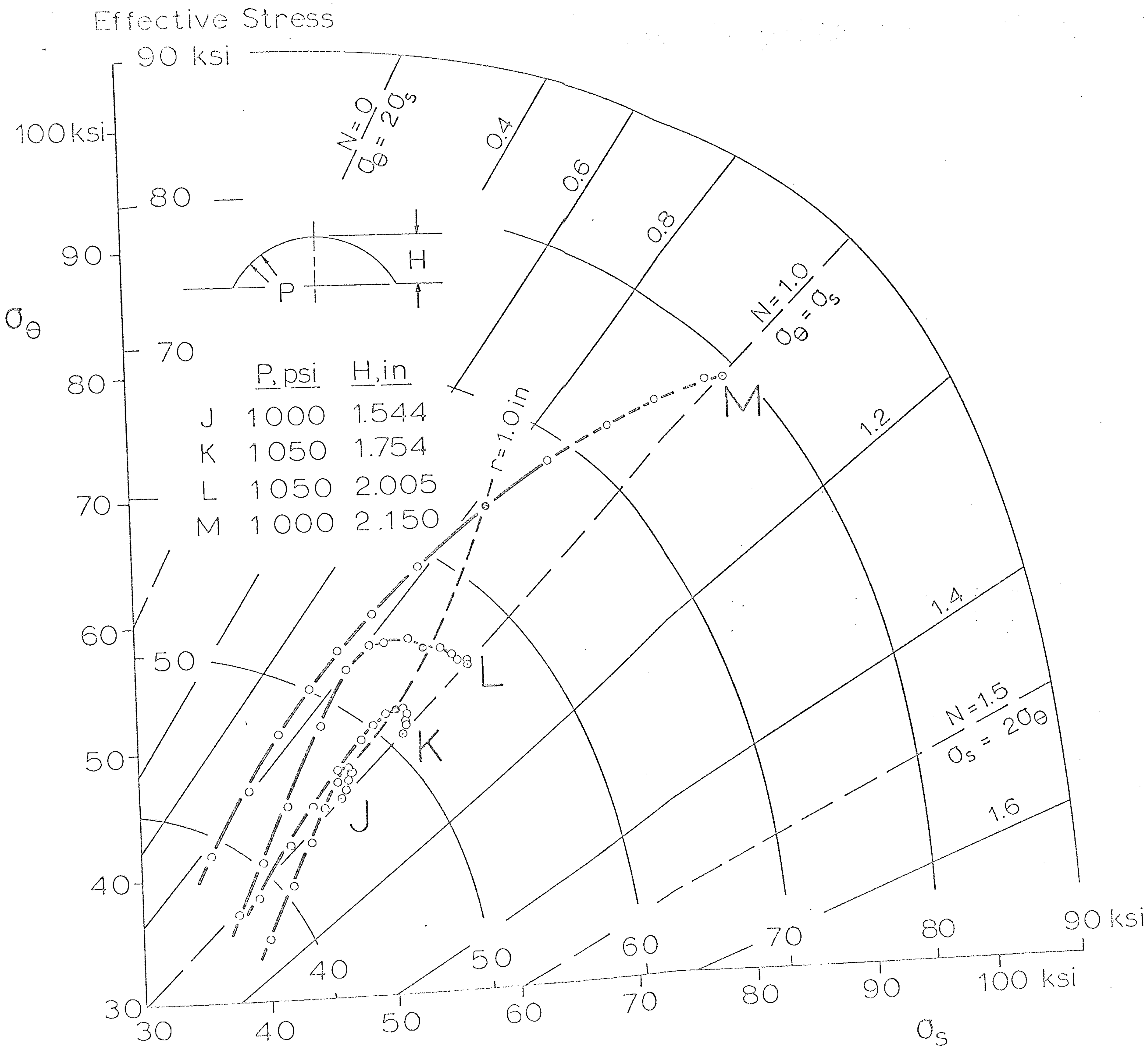
Effective Stress
90 ksi
100 ksi
80
90
70
80
60
70
50
60
50
40
30
30
40
50
60
70
80
90
100 ksi
40
50
60
70
80
90 ksi
σθ
σs
N=0
σθ = 2σs
0.4
0.6
0.8
N=1.0
σθ = σs
1.2
1.4
N=1.5
σs = 2σθ
1.6
r=1.0 in
H
P
P, psi H, in
J 1000 1.544
K 1050 1.754
L 1050 2.005
M 1000 2.150
J
K
L
M

Fig.(9.8)

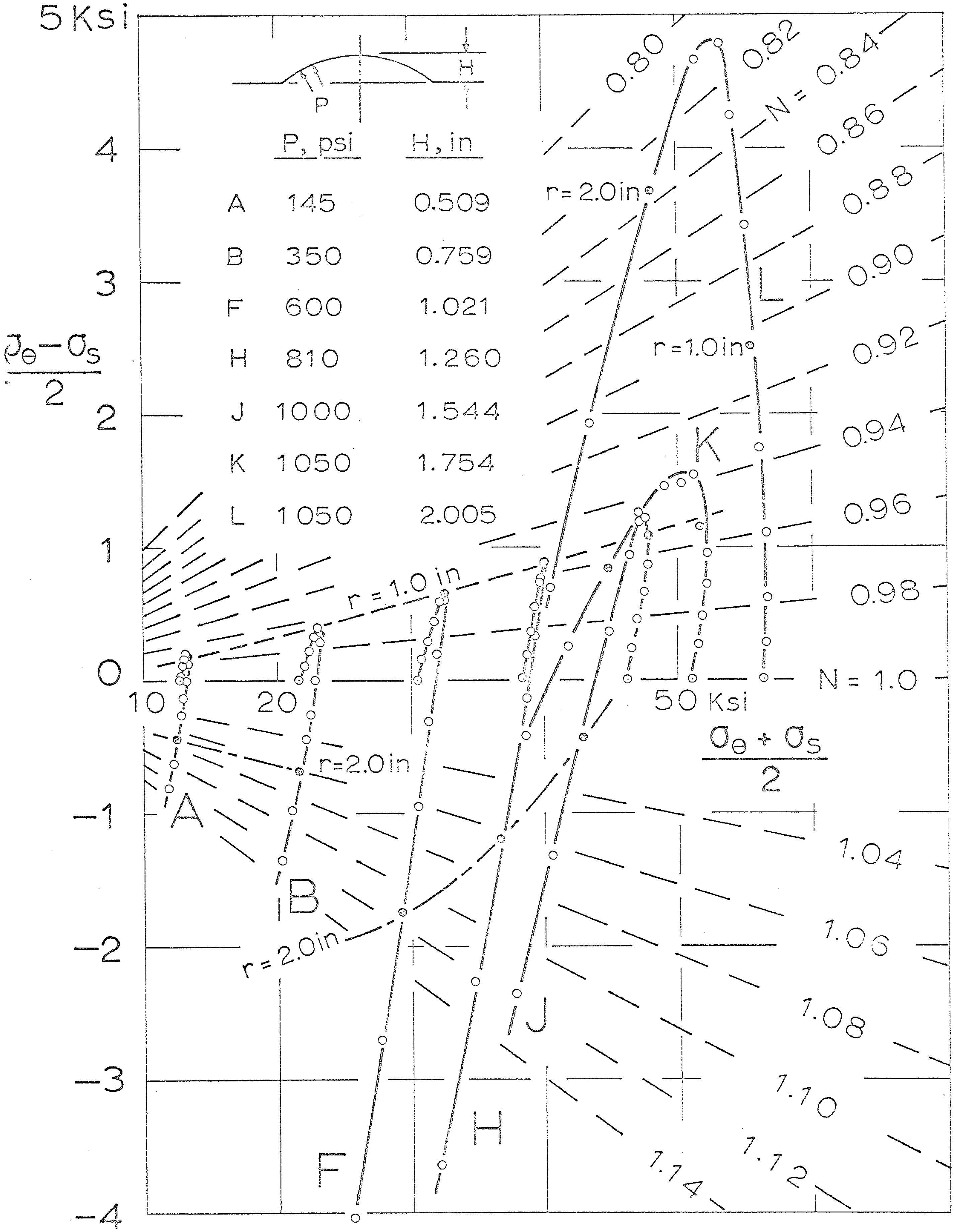
5 Ksi
4
3
2
1
0
−1
−2
−3
−4
$\frac{\sigma_\theta - \sigma_s}{2}$
10
20
50 Ksi
$\frac{\sigma_\theta + \sigma_s}{2}$
P
H
P, psi
H, in
A 145 0.509
B 350 0.759
F 600 1.021
H 810 1.260
J 1000 1.544
K 1050 1.754
L 1050 2.005
0.80
0.82
N = 0.84
0.86
0.88
0.90
0.92
0.94
0.96
0.98
N = 1.0
1.04
1.06
1.08
1.10
1.12
1.14
r = 2.0in
r = 1.0in
r = 1.0 in
r=2.0in
r = 2.0in
A
B
F
H
J
K
L

Fig.(9.9)

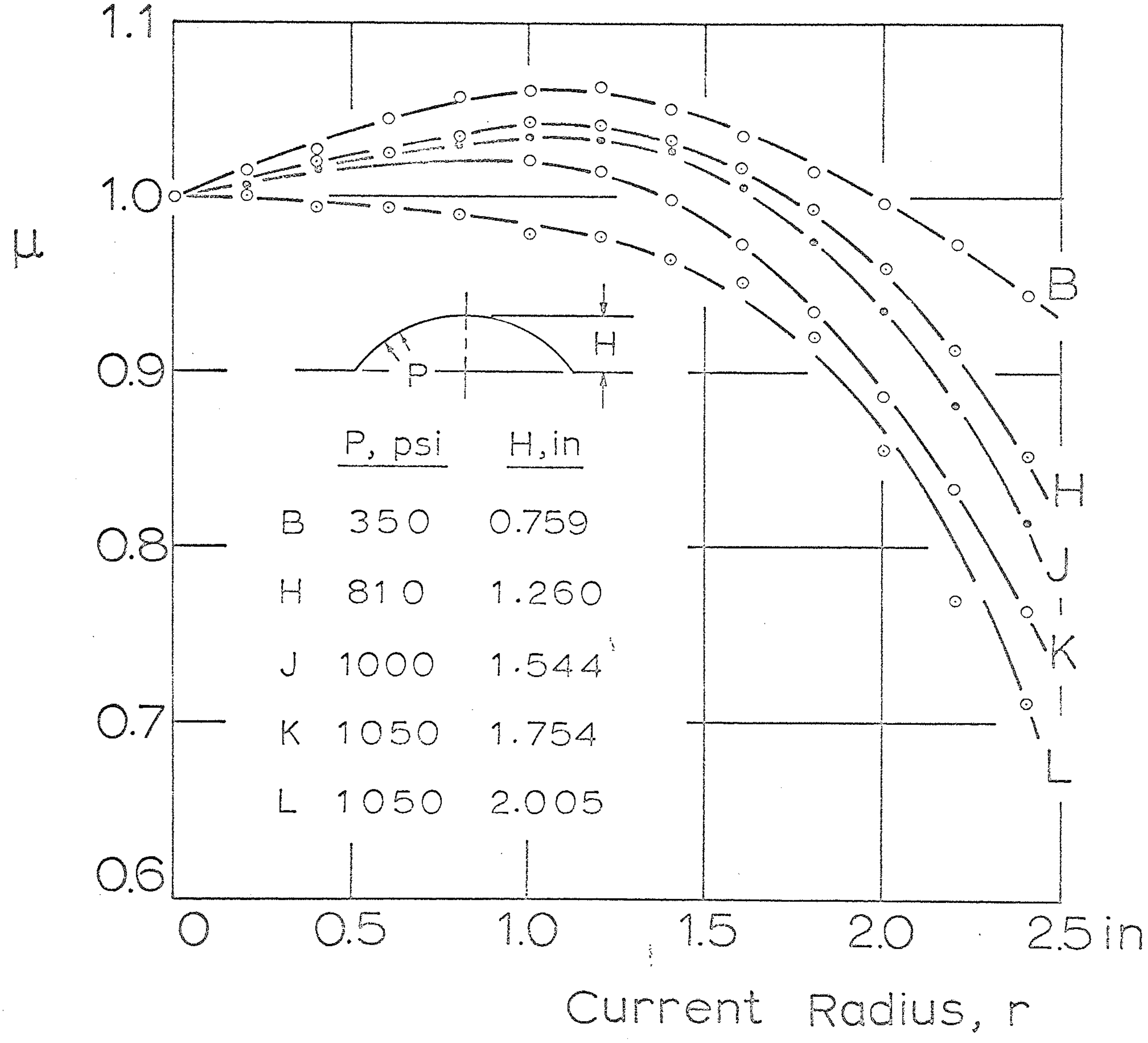
1.1
1.0
0.9
0.8
0.7
0.6
μ
0
0.5
1.0
1.5
2.0
2.5 in
Current Radius, r
B
H
J
K
L
P
H
P, psi
H, in
B 350 0.759
H 810 1.260
J 1000 1.544
K 1050 1.754
L 1050 2.005

Fig.(9.10)

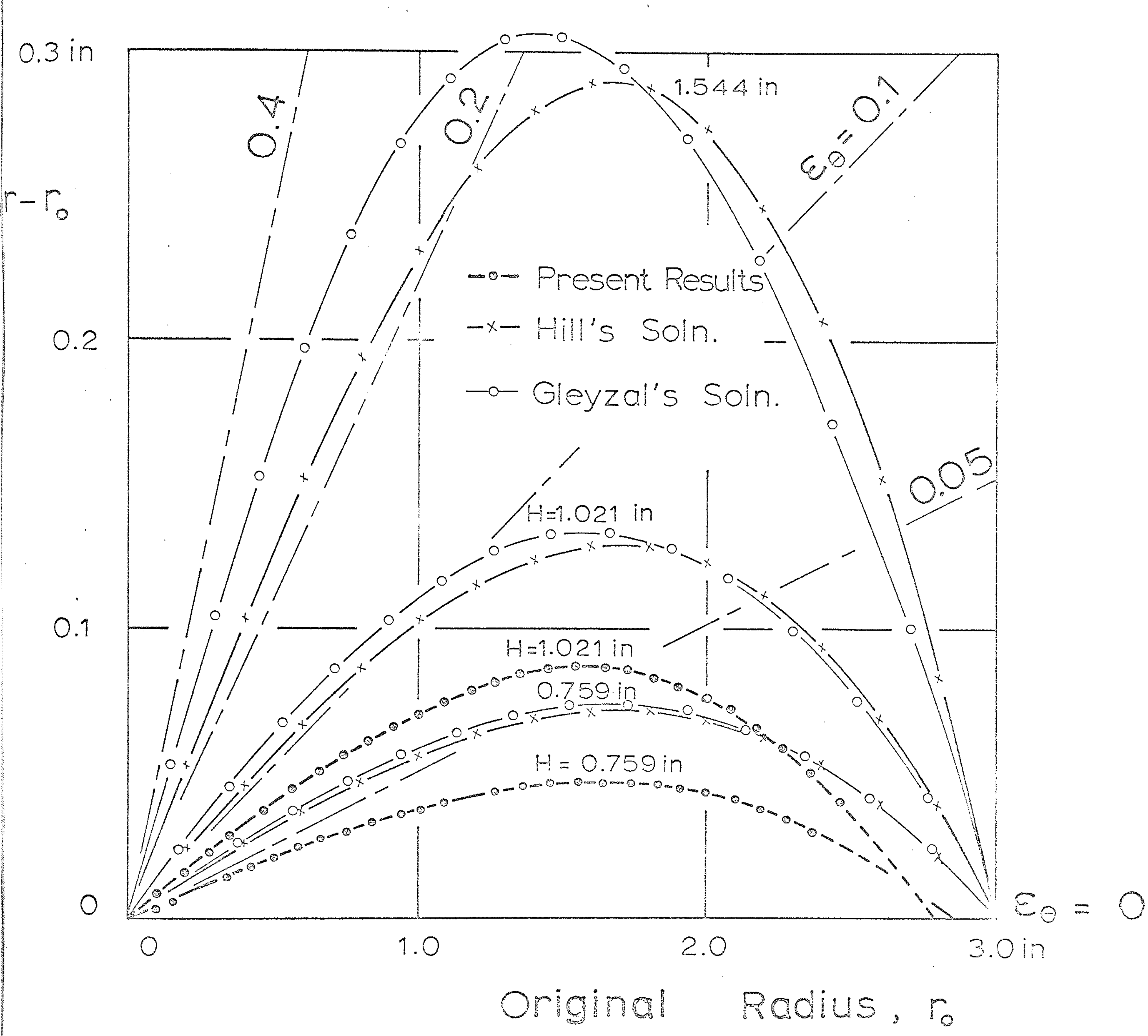
0.3 in
0.2
0.1
0
r − r₀
0.4
0.2
1.544 in
ε_θ = 0.1
Present Results
Hill's Soln.
Gleyzal's Soln.
0.05
H=1.021 in
H=1.021 in
0.759 in
H = 0.759 in
ε_θ = 0
0
1.0
2.0
3.0 in
Original Radius, r₀

Fig.(10.1)

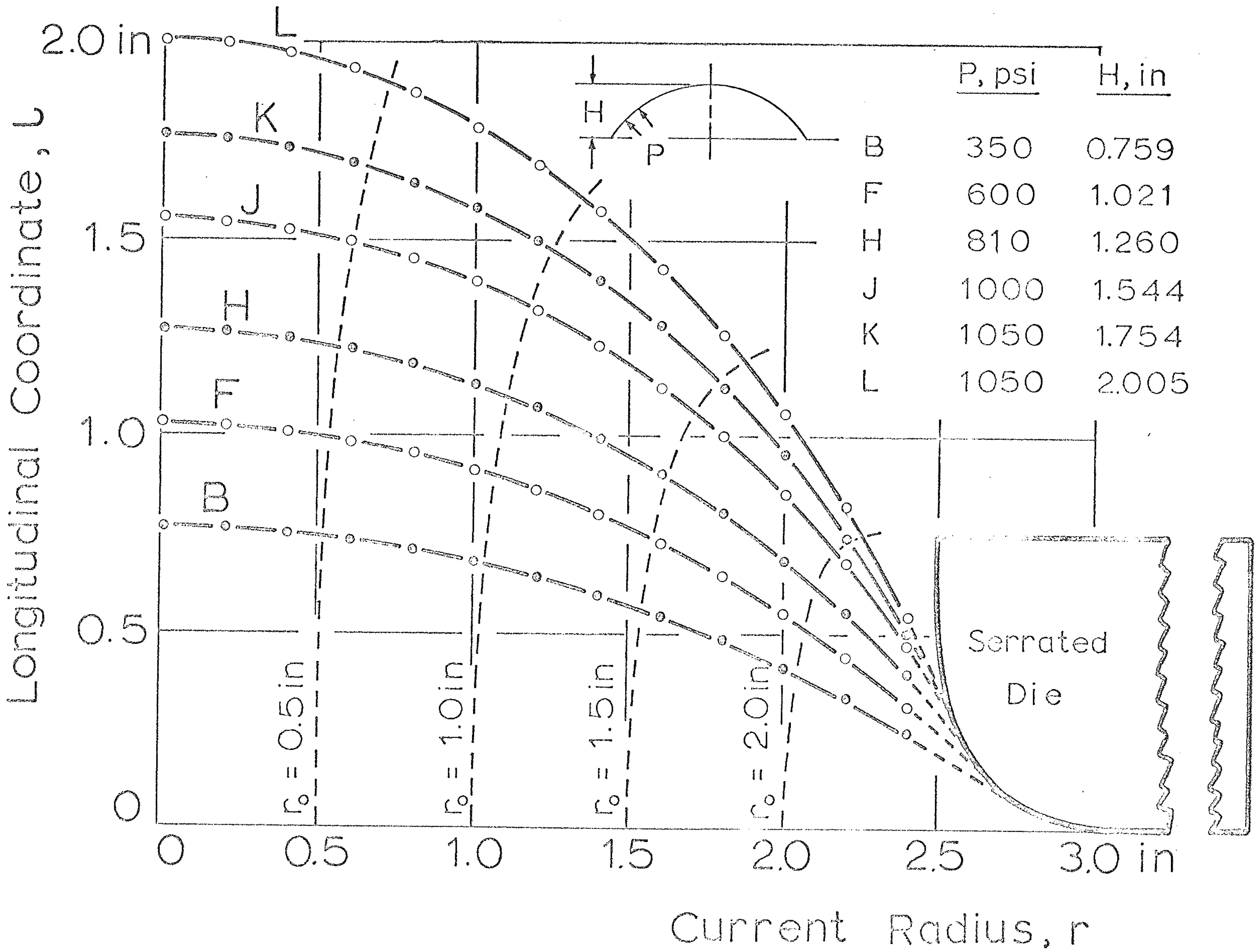
Longitudinal Coordinate, L
2.0 in
1.5
1.0
0.5
0
L
K
J
H
F
B
H
P
P, psi
H, in
B 350 0.759
F 600 1.021
H 810 1.260
J 1000 1.544
K 1050 1.754
L 1050 2.005
r₀ = 0.5 in
r₀ = 1.0 in
r₀ = 1.5 in
r₀ = 2.0 in
Serrated Die
0
0.5
1.0
1.5
2.0
2.5
3.0 in
Current Radius, r

Fig.(10.2)

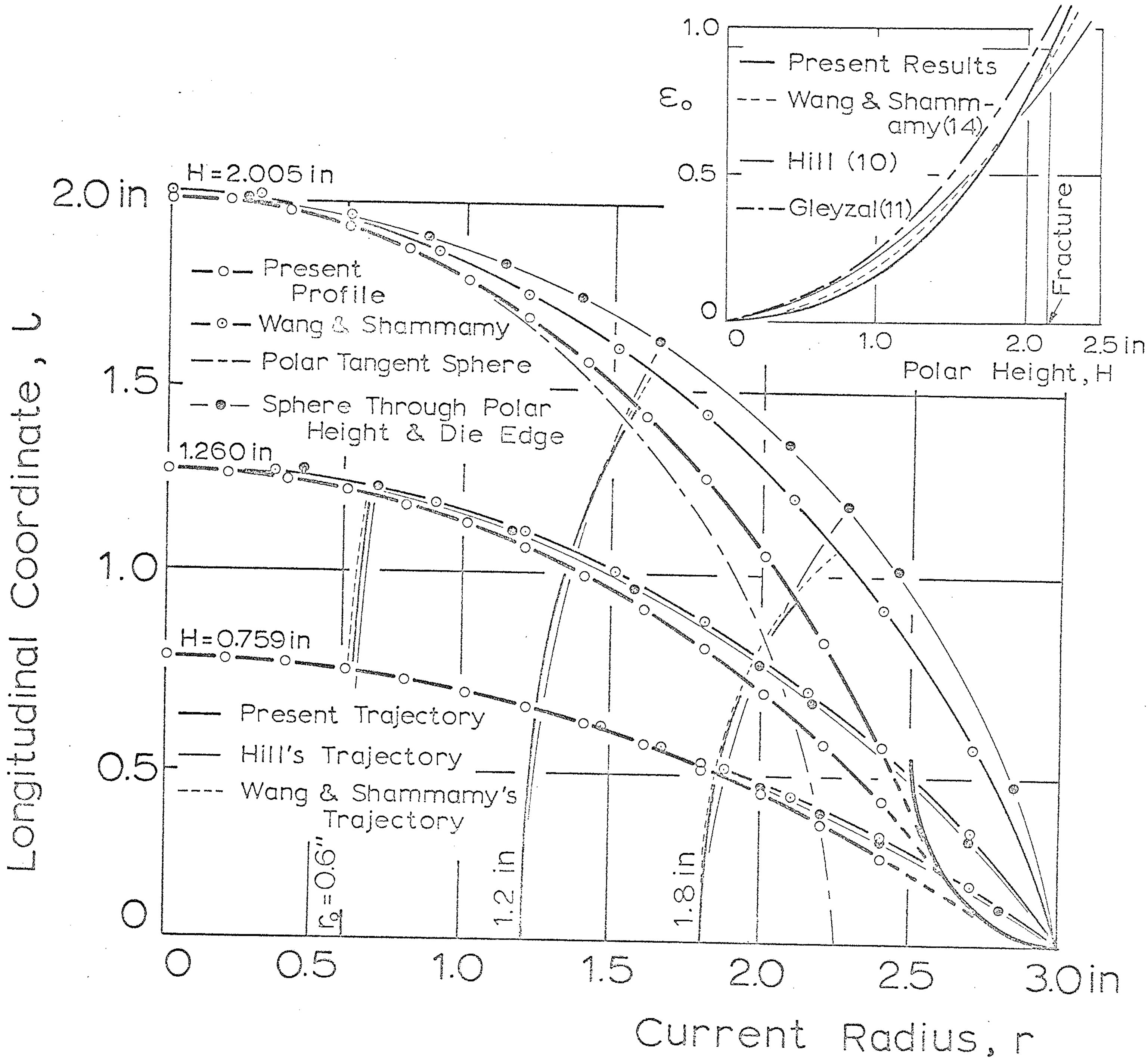
H=2.005 in
2.0 in
1.5
1.0
0.5
0
Longitudinal Coordinate, L
Present Profile
Wang & Shammamy
Polar Tangent Sphere
Sphere Through Polar Height & Die Edge
1.260 in
H=0.759 in
Present Trajectory
Hill's Trajectory
Wang & Shammamy's Trajectory
r_o=0.6"
1.2 in
1.8 in
0
0.5
1.0
1.5
2.0
2.5
3.0 in
Current Radius, r
1.0
ε_o
0.5
0
Present Results
Wang & Shammamy(14)
Hill (10)
Gleyzal(11)
Fracture
0
1.0
2.0
2.5 in
Polar Height, H

Fig.(10.3)

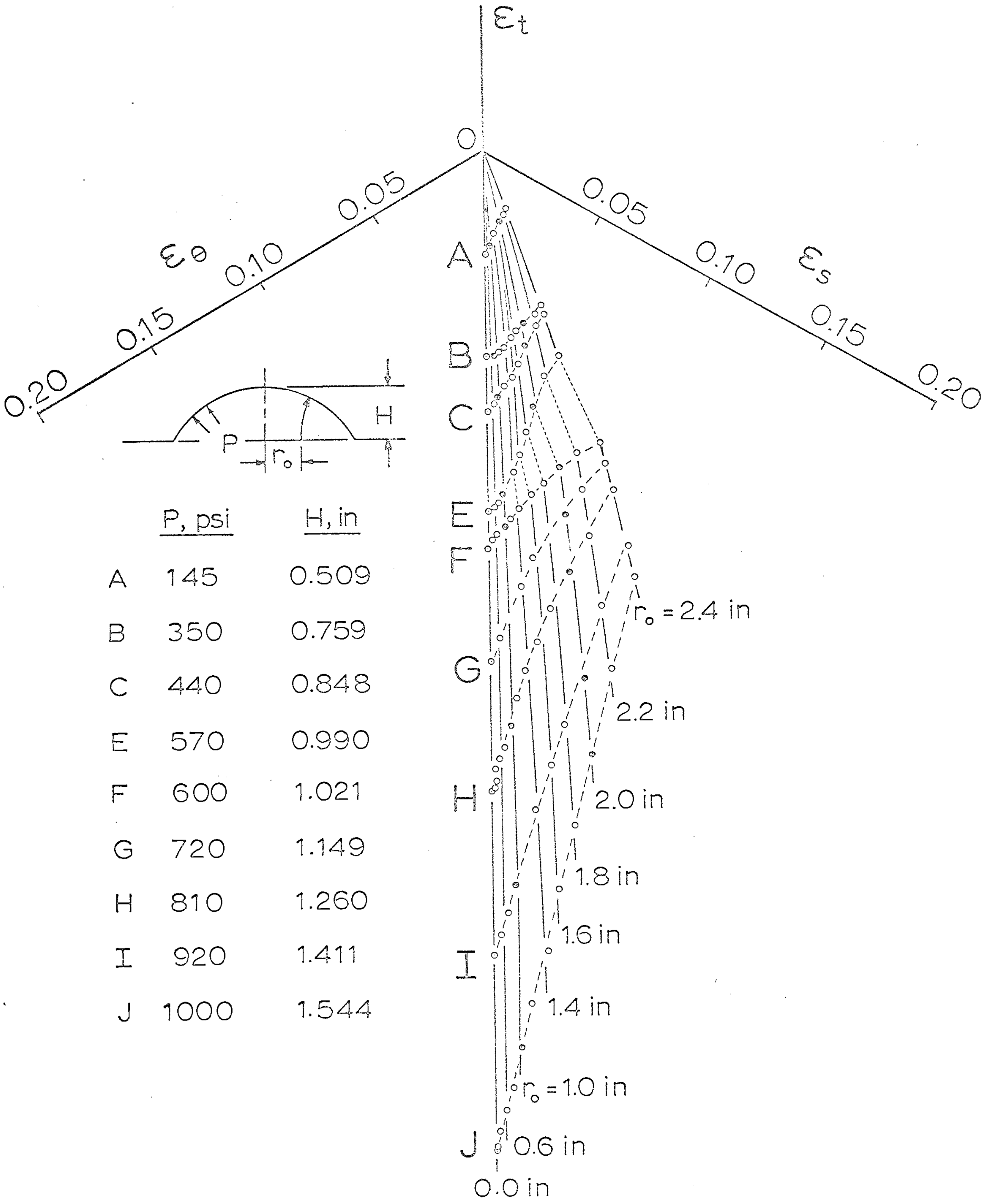

	P, psi	H, in
A	145	0.509
B	350	0.759
C	440	0.848
E	570	0.990
F	600	1.021
G	720	1.149
H	810	1.260
I	920	1.411
J	1000	1.544

Fig.(10.4)

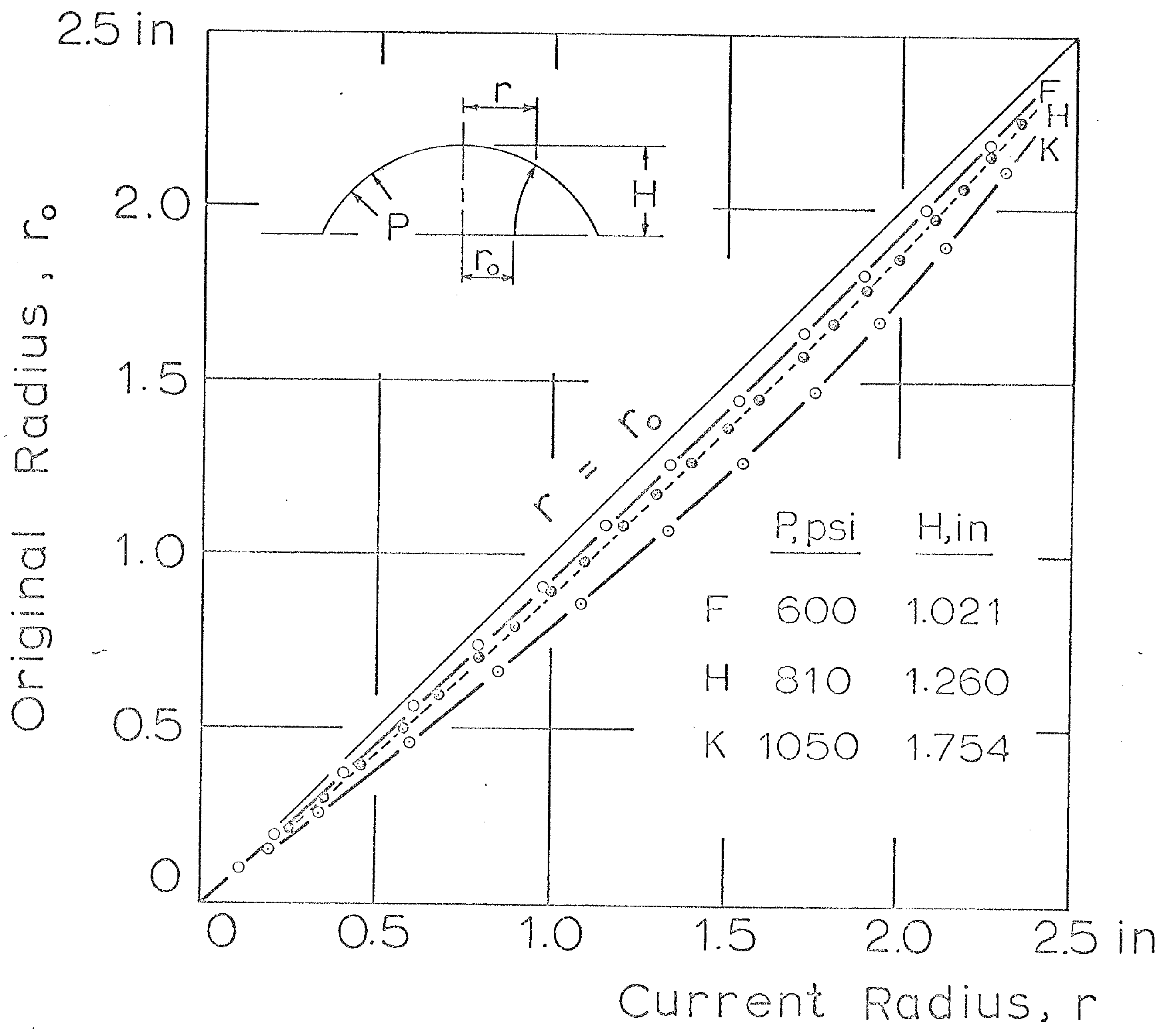
2.5 in
2.0
1.5
1.0
0.5
0
0
0.5
1.0
1.5
2.0
2.5 in
Original Radius, r_o
Current Radius, r
r
H
P
r_o
$r = r_o$
F
H
K
P, psi
H, in
F 600 1.021
H 810 1.260
K 1050 1.754

Fig.(10.5)

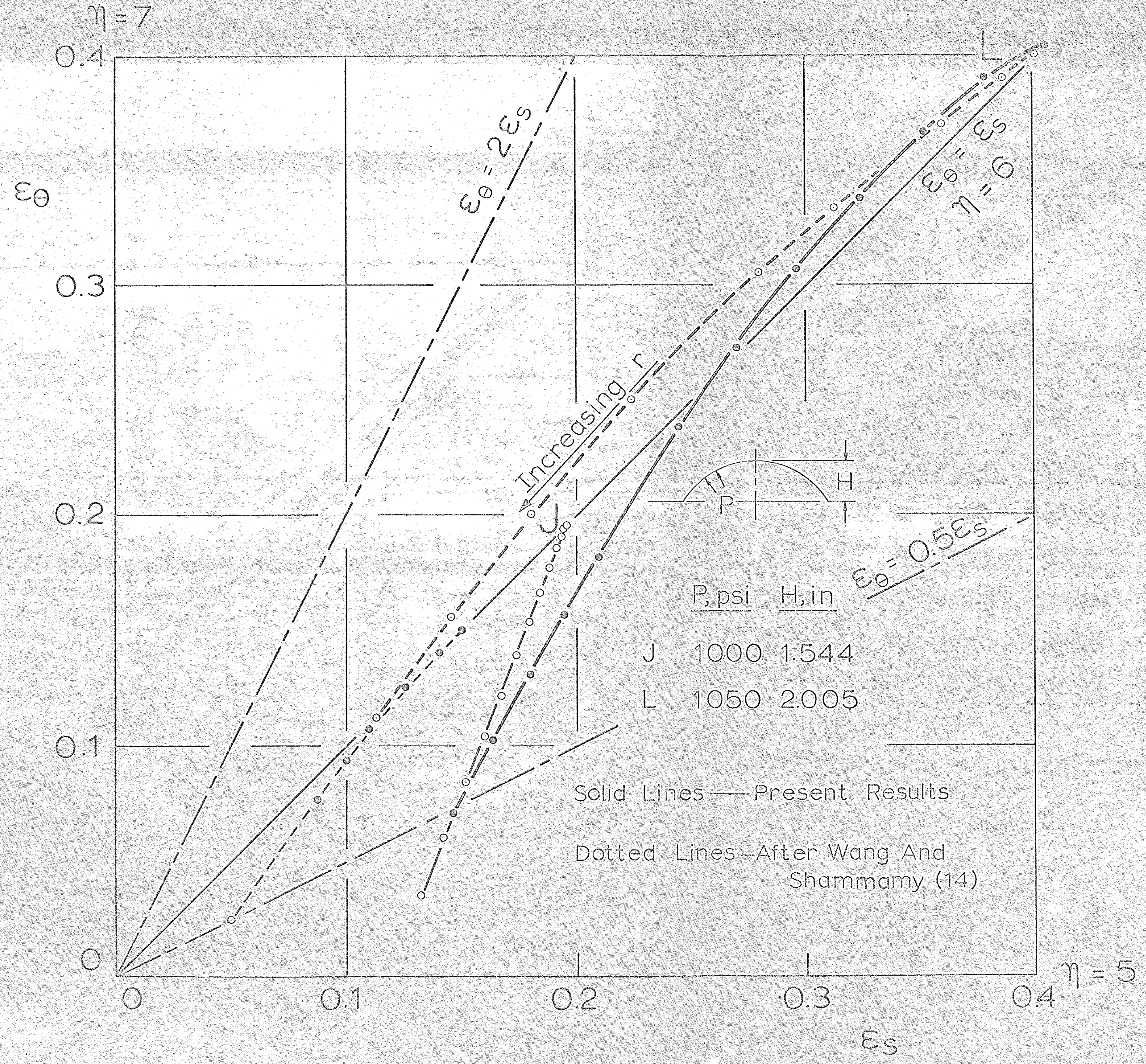
η = 7
0.4
0.3
0.2
0.1
0
εθ
εθ = 2εs
εθ = εs
η = 6
L
J
Increasing r
H
P
εθ = 0.5εs
P, psi
H, in
J
1000
1.544
L
1050
2.005
Solid Lines — Present Results
Dotted Lines — After Wang And Shammamy (14)
0
0.1
0.2
0.3
0.4
η = 5
εs

Fig.(10.6)

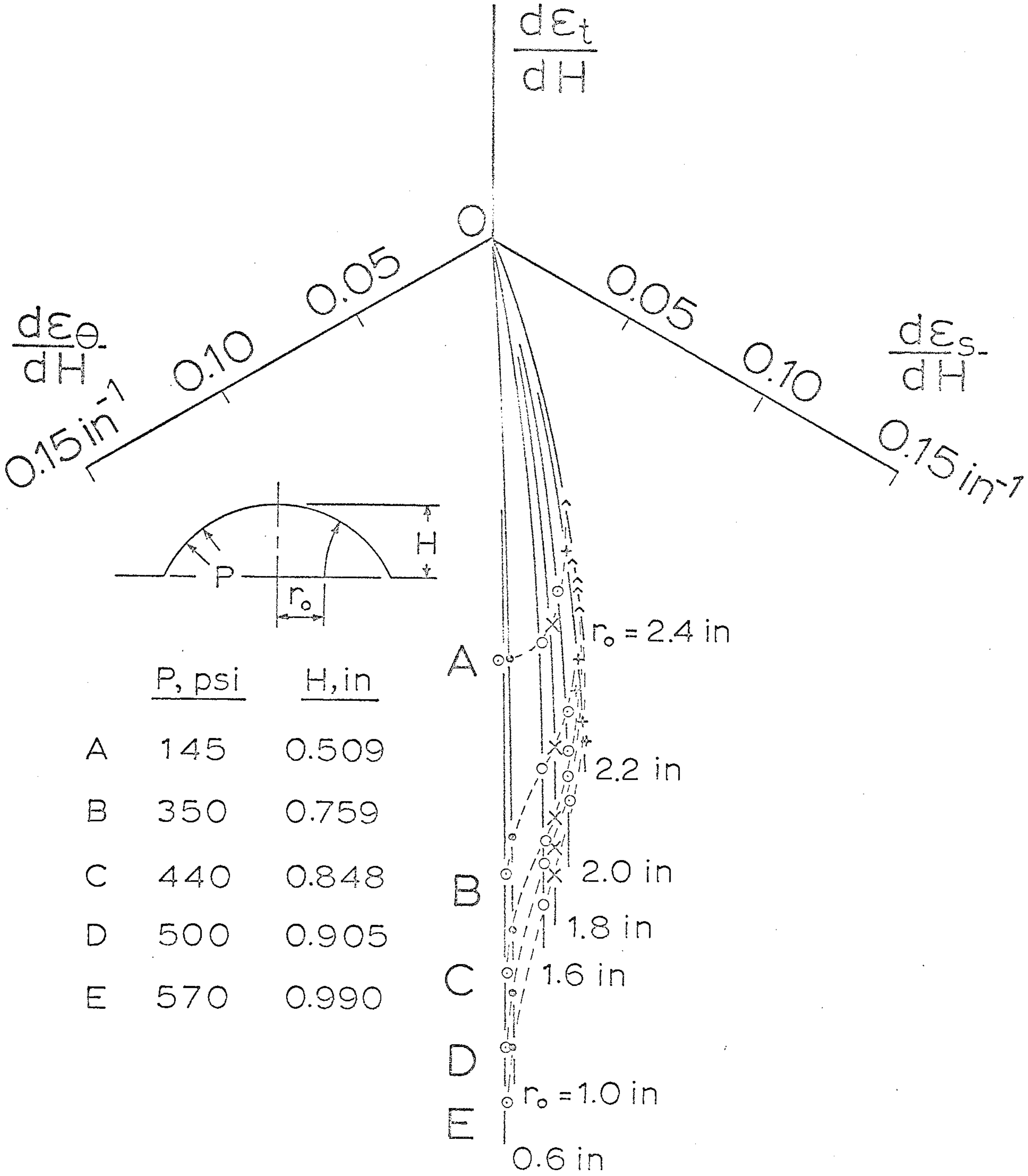

	P, psi	H, in
A	145	0.509
B	350	0.759
C	440	0.848
D	500	0.905
E	570	0.990

Fig.(10.7)

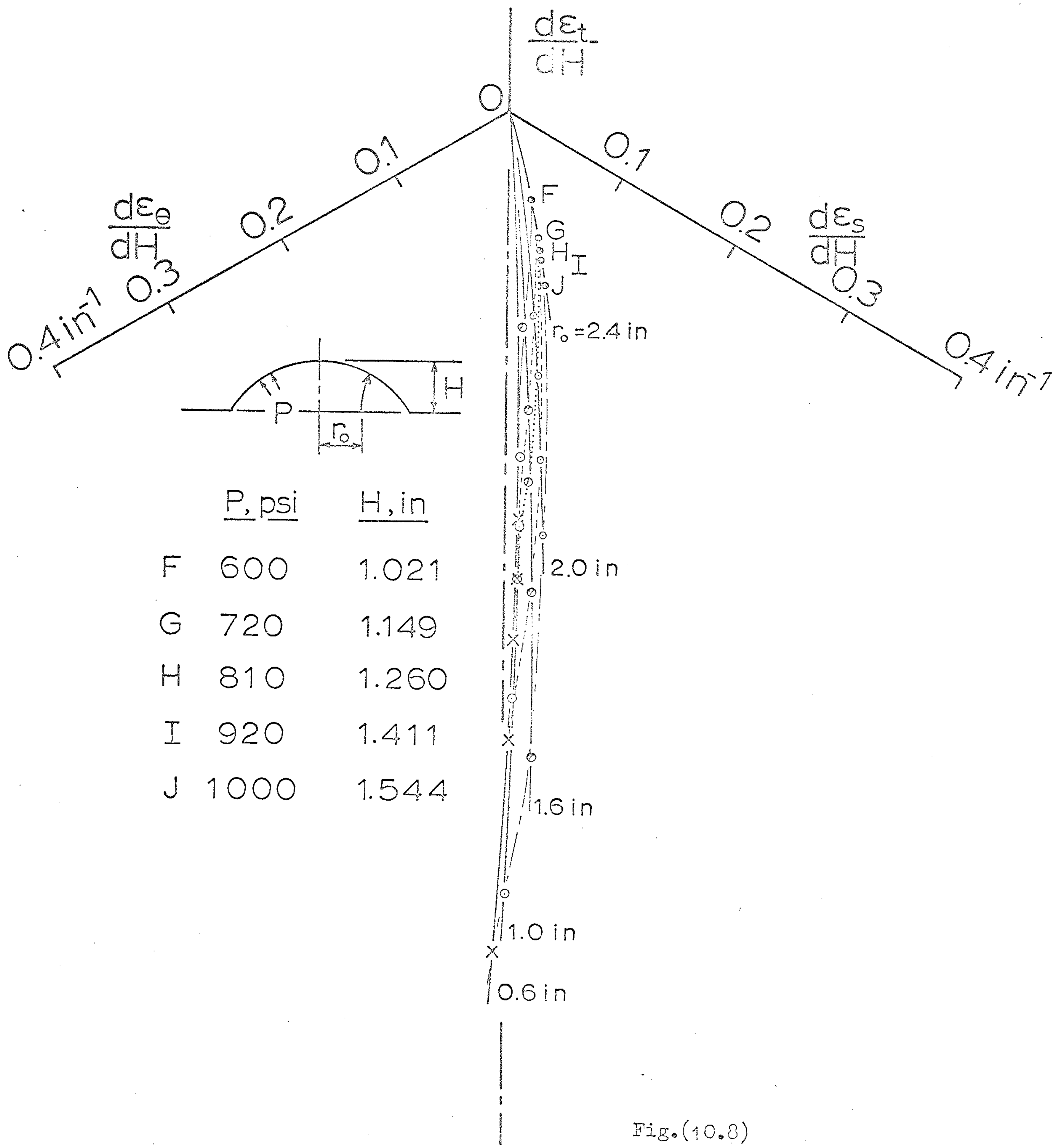

	P, psi	H, in
F	600	1.021
G	720	1.149
H	810	1.260
I	920	1.411
J	1000	1.544

Fig.(10.8)

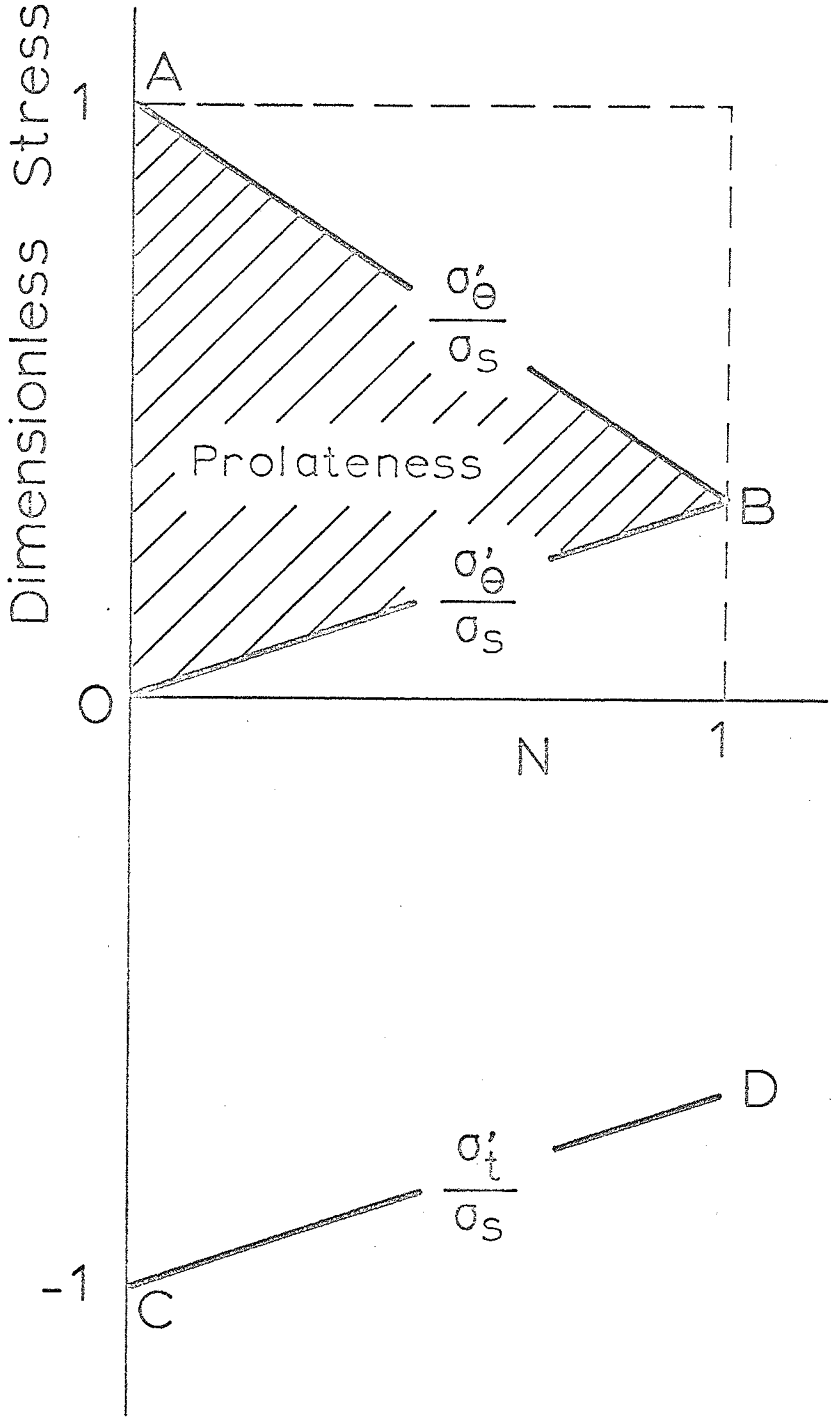
Dimensionless Stress
A
1
$\frac{\sigma'_\theta}{\sigma_s}$
Prolateness
B
$\frac{\sigma'_\theta}{\sigma_s}$
O
N
1
D
$\frac{\sigma'_t}{\sigma_s}$
-1
C

Fig.(11.1)

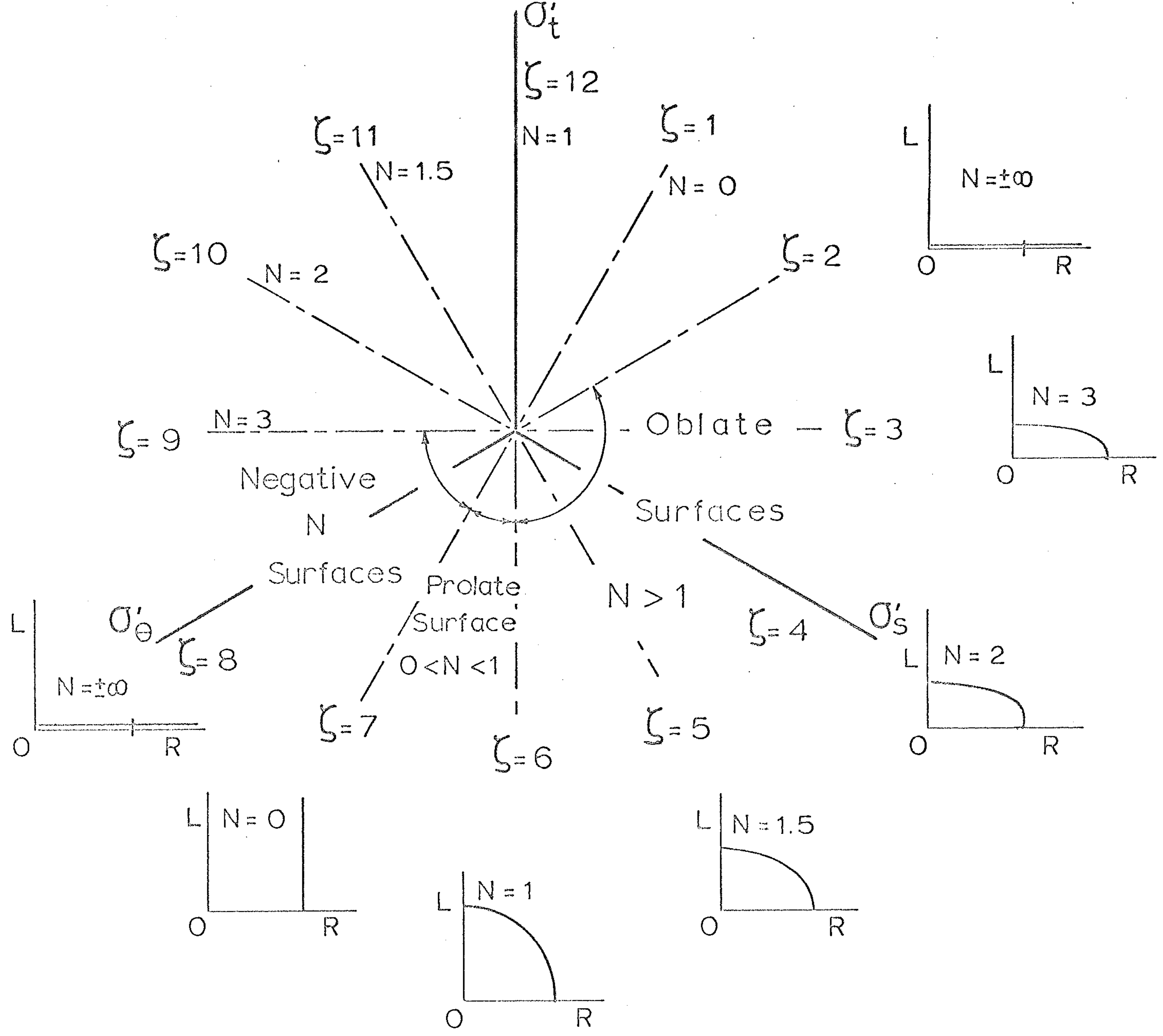
σ'_t
$\zeta=12$
N = 1
$\zeta=1$
N = 0
$\zeta=2$
Oblate
$\zeta=3$
Surfaces
N > 1
$\zeta=4$
σ'_s
$\zeta=5$
$\zeta=6$
Prolate
Surface
0 < N < 1
$\zeta=7$
$\zeta=8$
σ'_θ
Negative
N
Surfaces
$\zeta=9$
N = 3
$\zeta=10$
N = 2
$\zeta=11$
N = 1.5
L
O
R
N = ±∞
N = 3
N = 2
N = 1.5
N = 1
N = 0

Fig.(11.2)

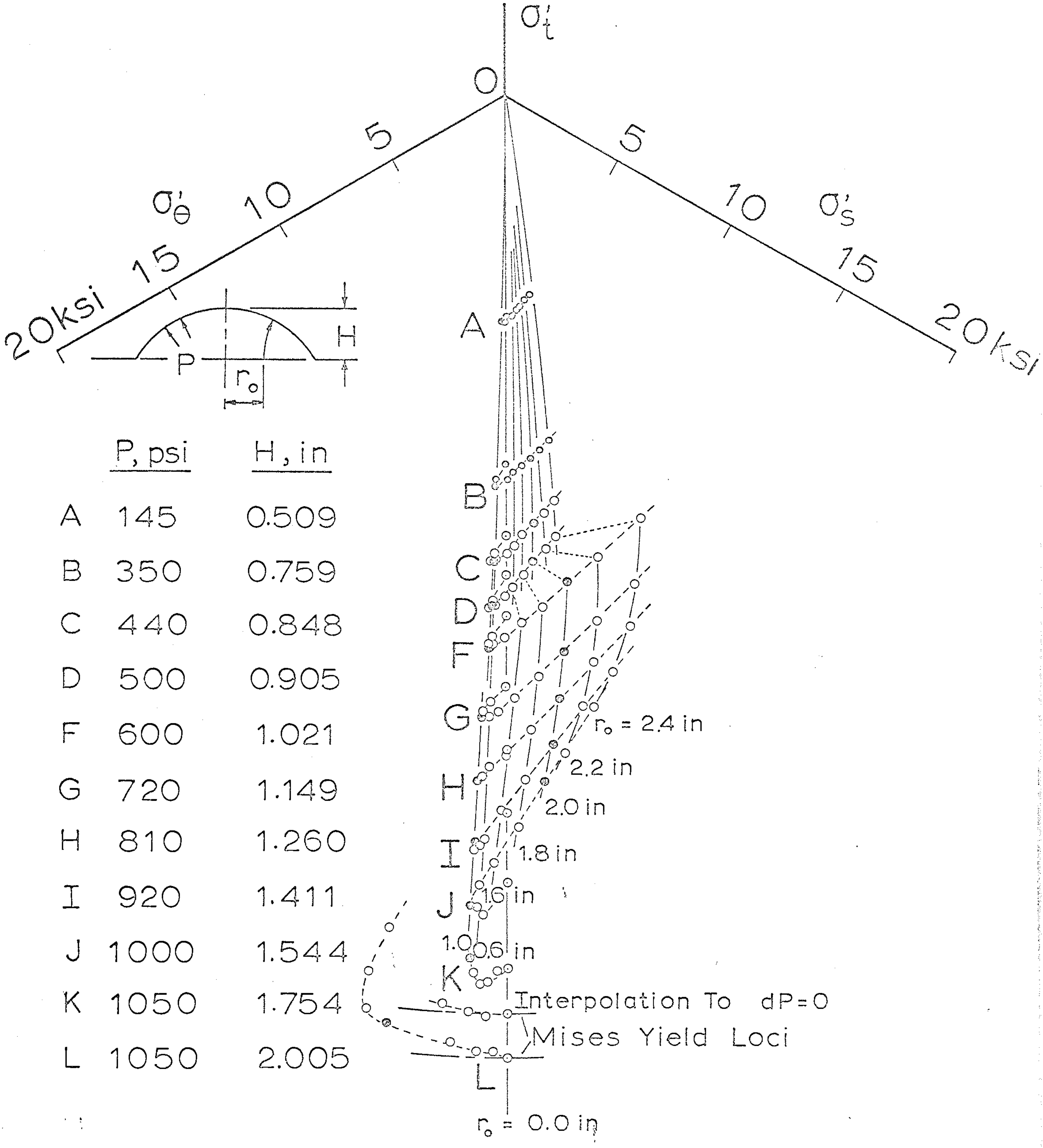

	P, psi	H, in
A	145	0.509
B	350	0.759
C	440	0.848
D	500	0.905
F	600	1.021
G	720	1.149
H	810	1.260
I	920	1.411
J	1000	1.544
K	1050	1.754
L	1050	2.005

Fig.(11.3)

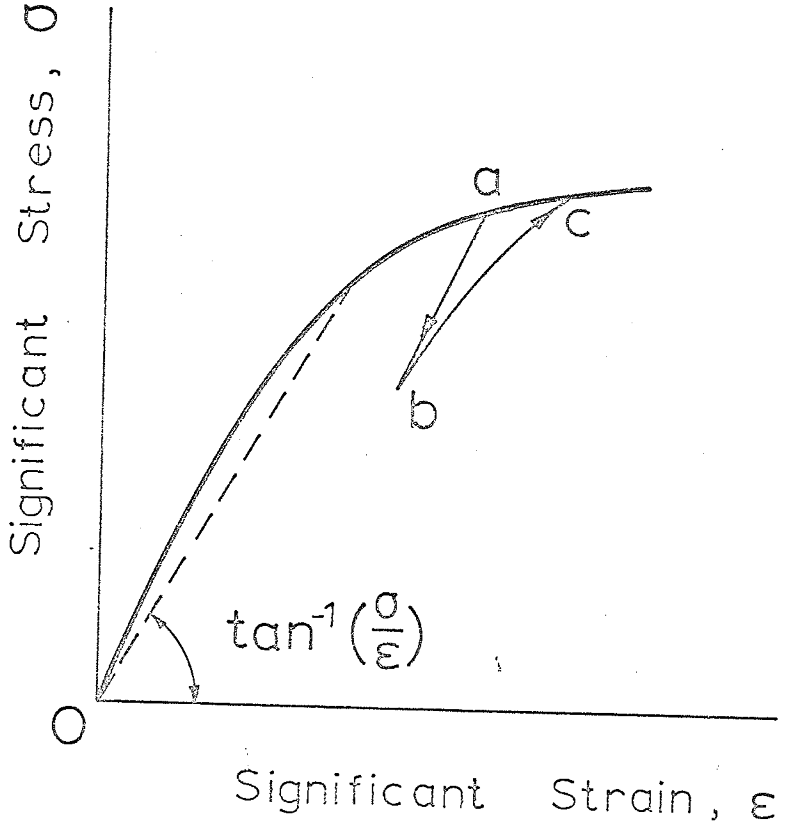
Significant Stress, σ
a
c
b
$\tan^{-1}\left(\frac{\sigma}{\varepsilon}\right)$
O
Significant Strain, ε

Fig.(11.4)

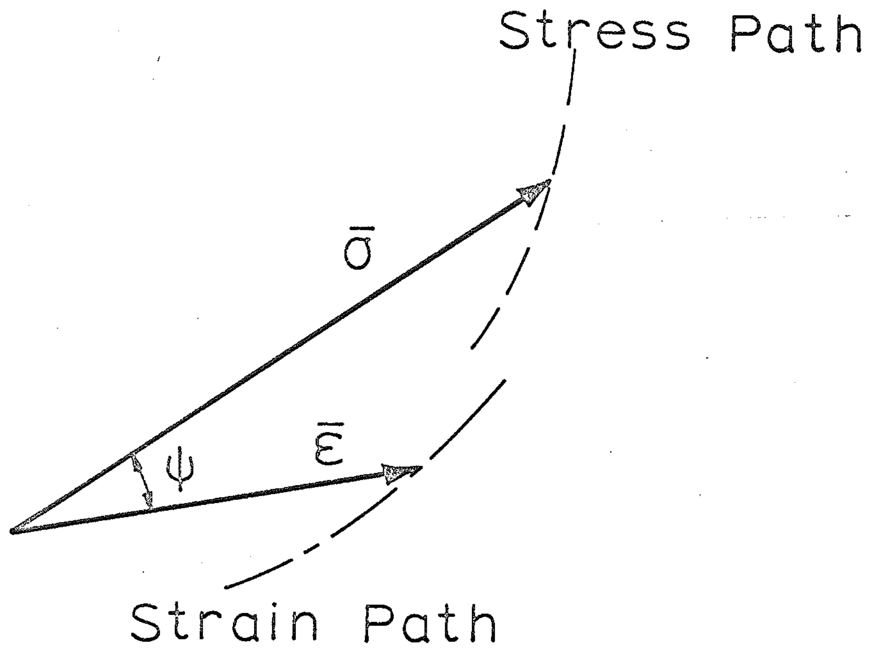

Fig.(11.5)

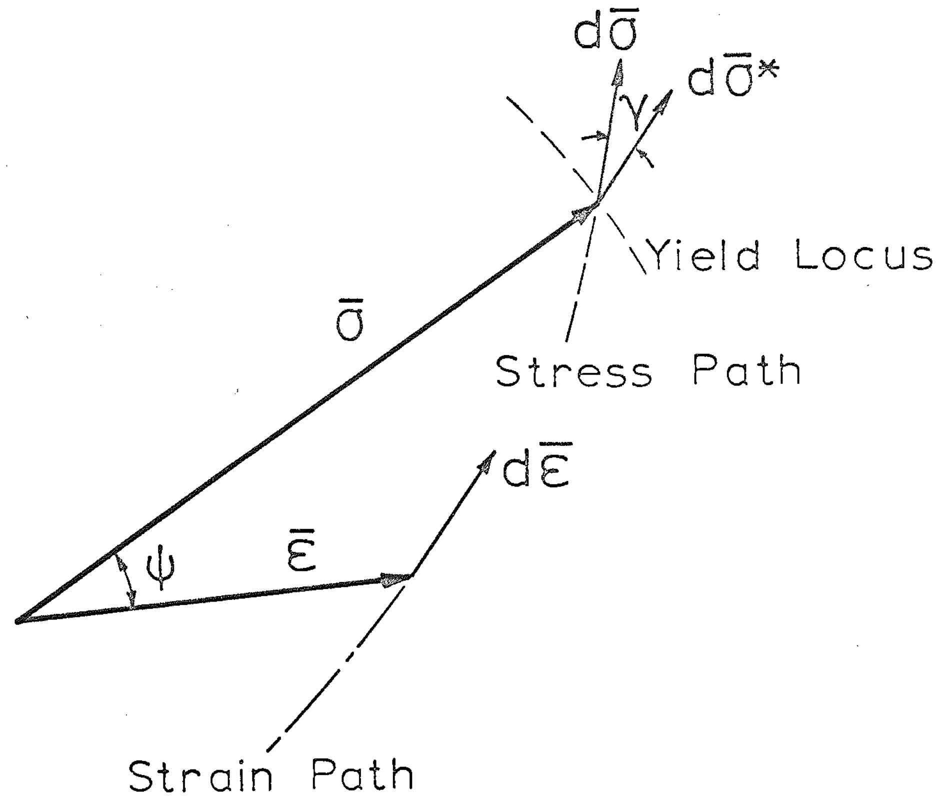
$d\bar{\sigma}$
$d\bar{\sigma}^*$
γ
Yield Locus
$\bar{\sigma}$
Stress Path
$d\bar{\varepsilon}$
ψ
$\bar{\varepsilon}$
Strain Path

Fig.(11.6)

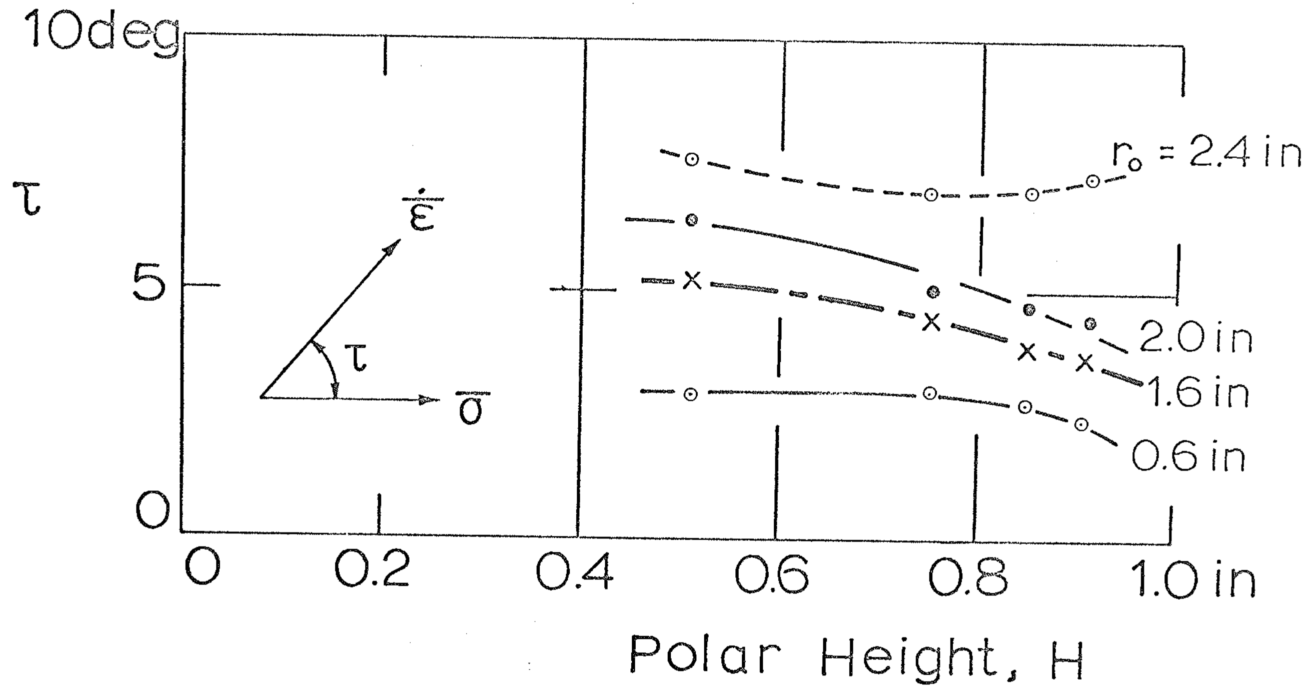
10deg
τ
5
0
$\dot{\bar{\varepsilon}}$
τ
$\bar{\sigma}$
r_o = 2.4 in
2.0 in
1.6 in
0.6 in
0
0.2
0.4
0.6
0.8
1.0 in
Polar Height, H

Fig.(11.7)

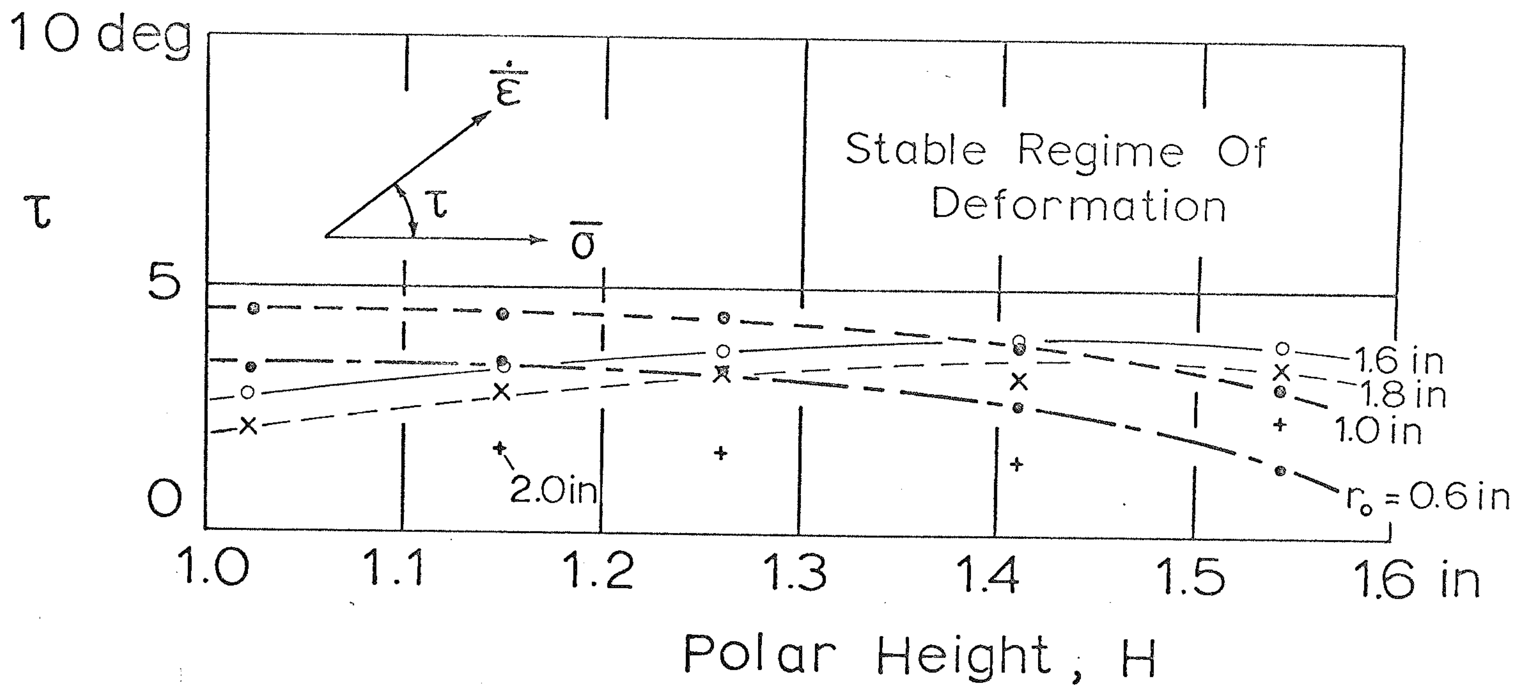
10 deg
τ
5
0
$\dot{\bar{\varepsilon}}$
τ
$\bar{\sigma}$
Stable Regime Of Deformation
1.6 in
1.8 in
1.0 in
r_o = 0.6 in
2.0in
1.0
1.1
1.2
1.3
1.4
1.5
1.6 in
Polar Height , H

Fig.(11.8)

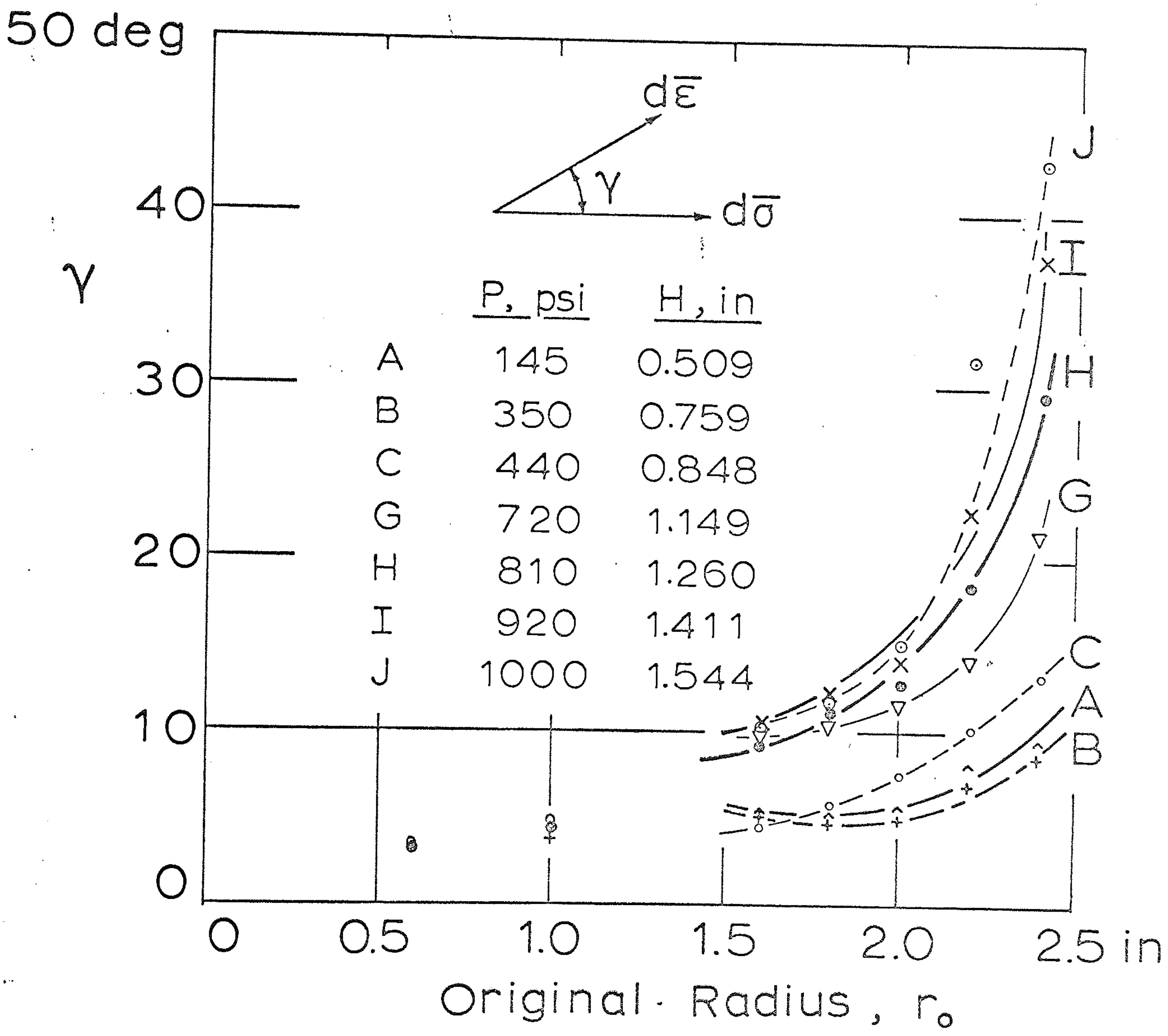
50 deg
40
30
20
10
0
γ
dε̄
dσ̄
γ
P, psi
H, in
A 145 0.509
B 350 0.759
C 440 0.848
G 720 1.149
H 810 1.260
I 920 1.411
J 1000 1.544
J
I
H
G
C
A
B
0
0.5
1.0
1.5
2.0
2.5 in
Original Radius, r₀

Fig.(11.9)

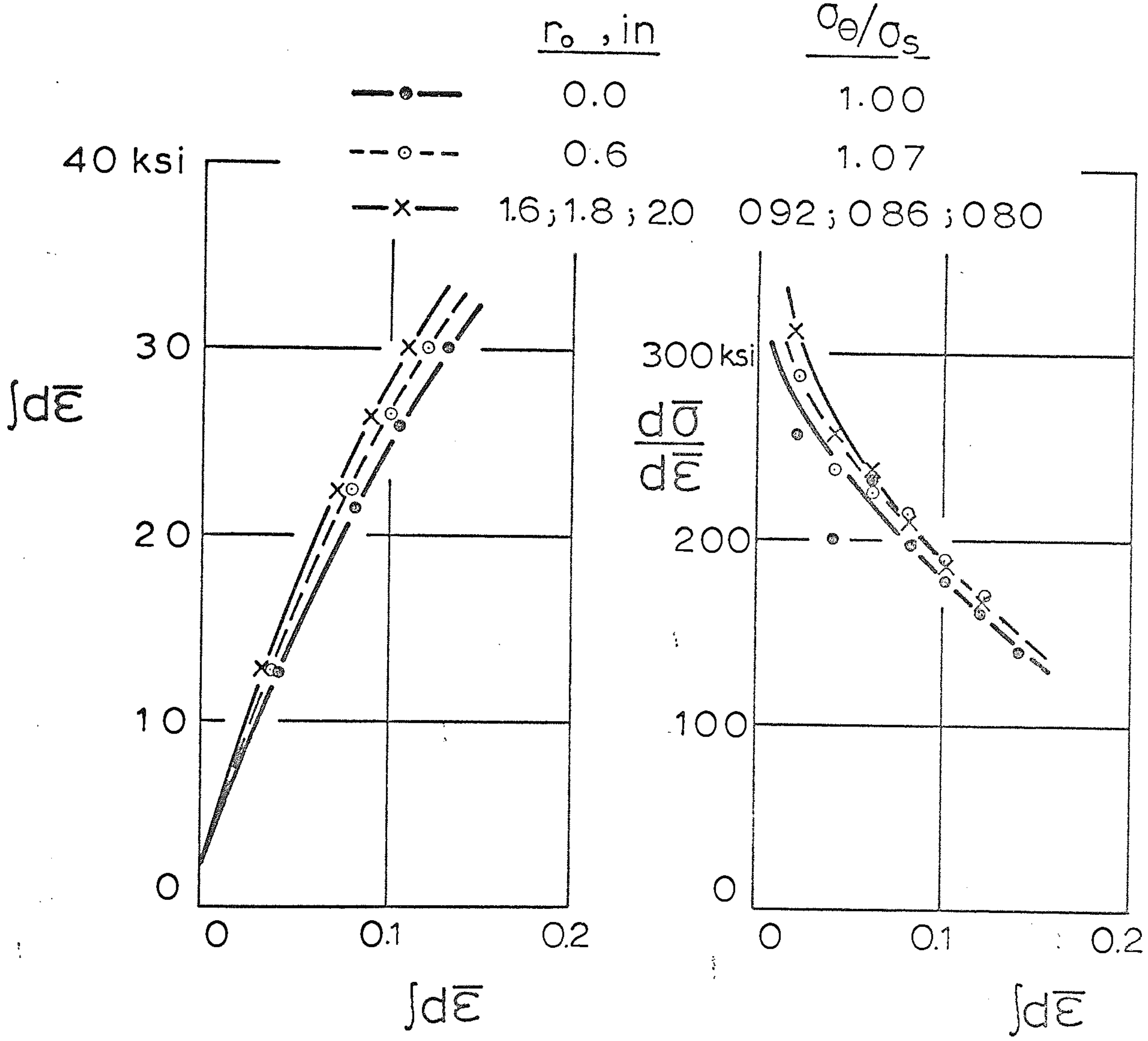
r₀ , in
σθ/σs
0.0
1.00
0.6
1.07
1.6 ; 1.8 ; 2.0
092 ; 086 ; 080
40 ksi
30
20
10
0
∫dε̄
0
0.1
0.2
∫dε̄
300 ksi
dσ̄/dε̄
200
100
0
0
0.1
0.2
∫dε̄

Fig.(11.10)

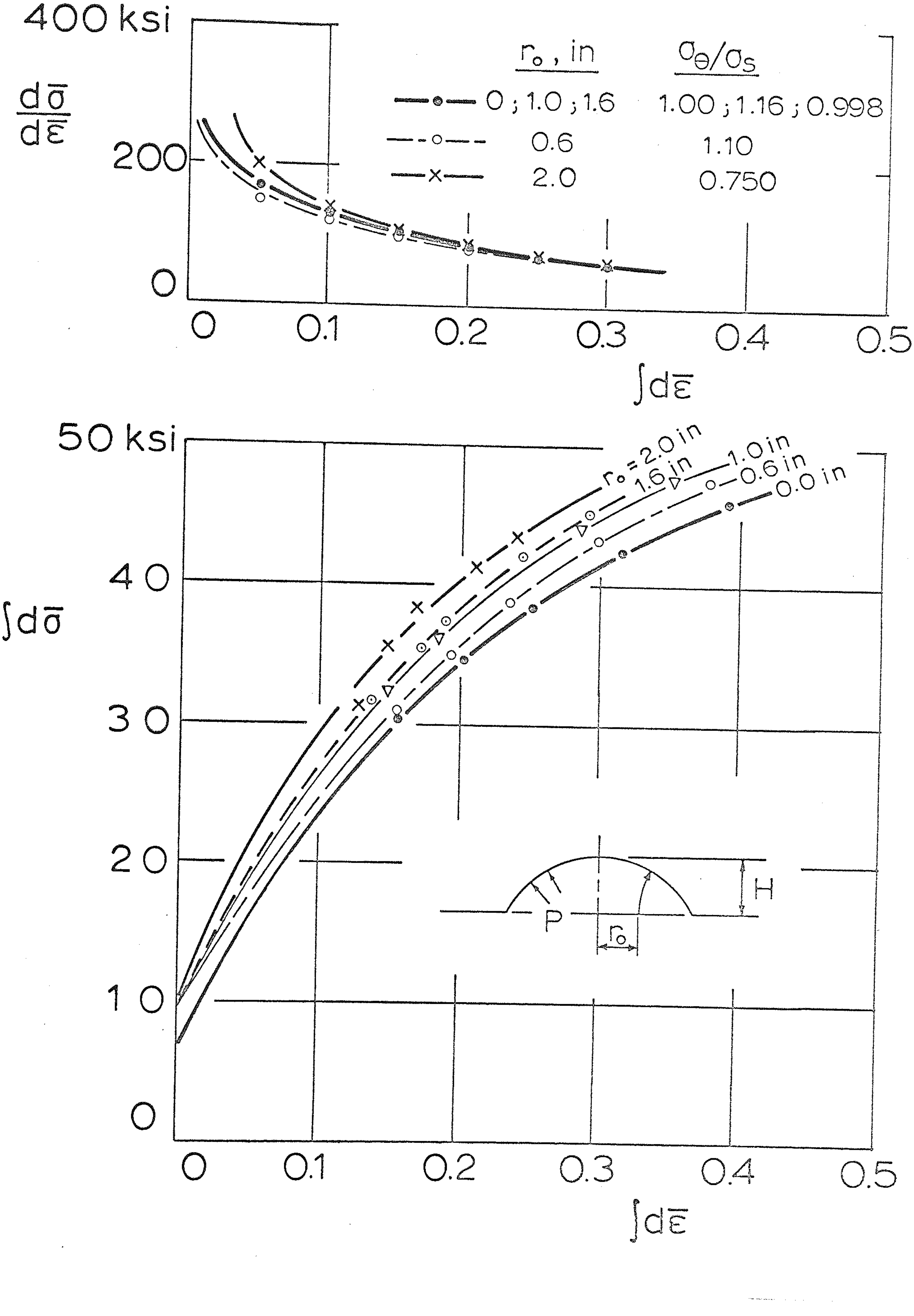
400 ksi
$\frac{d\bar{\sigma}}{d\bar{\varepsilon}}$
200
0
r_o, in
σ_θ/σ_s
0 ; 1.0 ; 1.6
1.00 ; 1.16 ; 0.998
0.6
1.10
2.0
0.750
0
0.1
0.2
0.3
0.4
0.5
$\int d\bar{\varepsilon}$
50 ksi
40
30
20
10
0
$\int d\bar{\sigma}$
r_o=2.0 in
1.6 in
1.0 in
0.6 in
0.0 in
H
P
r_o
0
0.1
0.2
0.3
0.4
0.5
$\int d\bar{\varepsilon}$

Fig.(11.11)

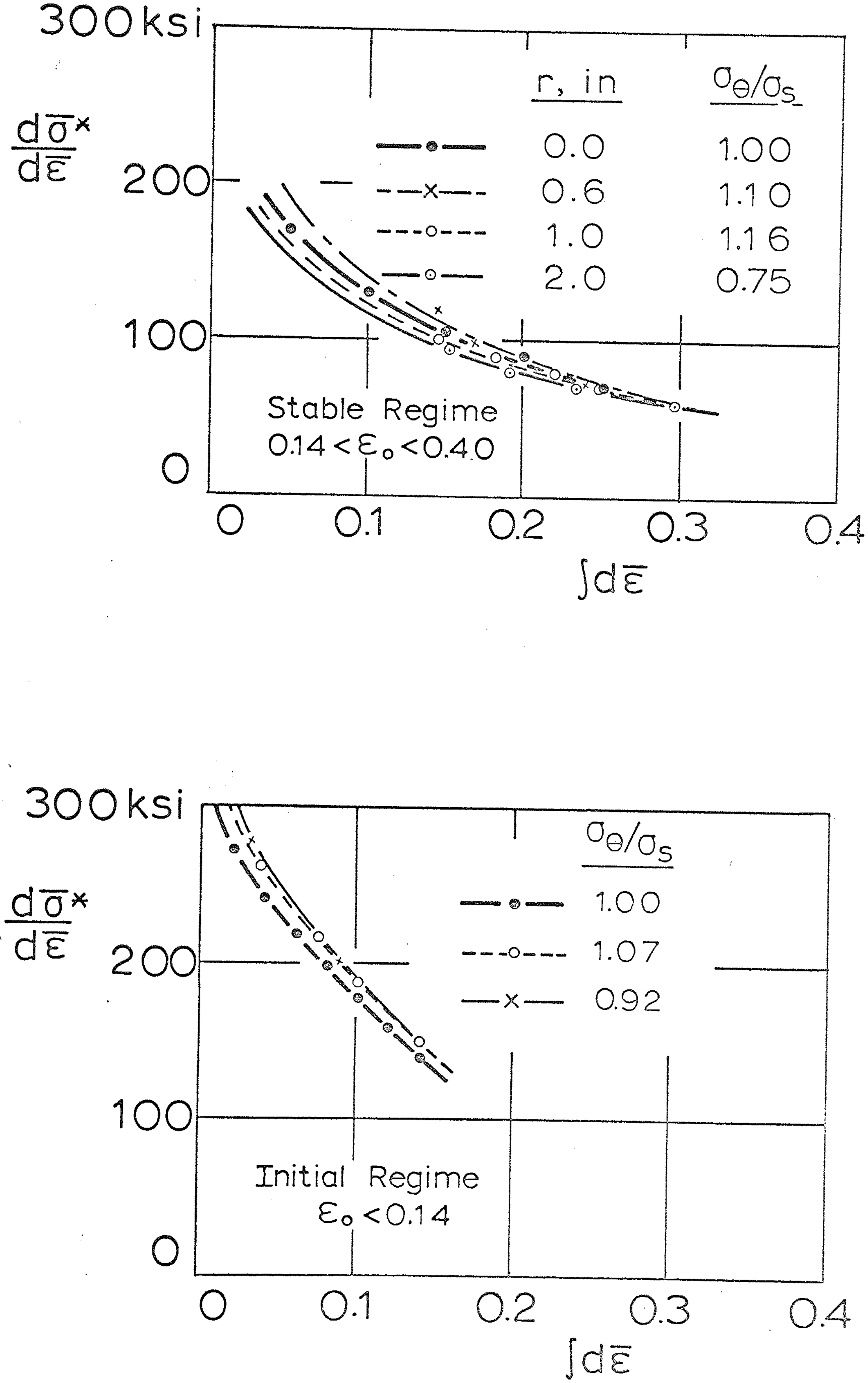
300 ksi
$\frac{d\bar{\sigma}^*}{d\bar{\varepsilon}}$
200
100
0
r, in
σ_θ/σ_s
0.0
1.00
0.6
1.10
1.0
1.16
2.0
0.75
Stable Regime
$0.14 < \varepsilon_o < 0.40$
0
0.1
0.2
0.3
0.4
$\int d\bar{\varepsilon}$
300 ksi
$\frac{d\bar{\sigma}^*}{d\bar{\varepsilon}}$
200
100
0
σ_θ/σ_s
1.00
1.07
0.92
Initial Regime
$\varepsilon_o < 0.14$
0
0.1
0.2
0.3
0.4
$\int d\bar{\varepsilon}$

Fig. (11.12)

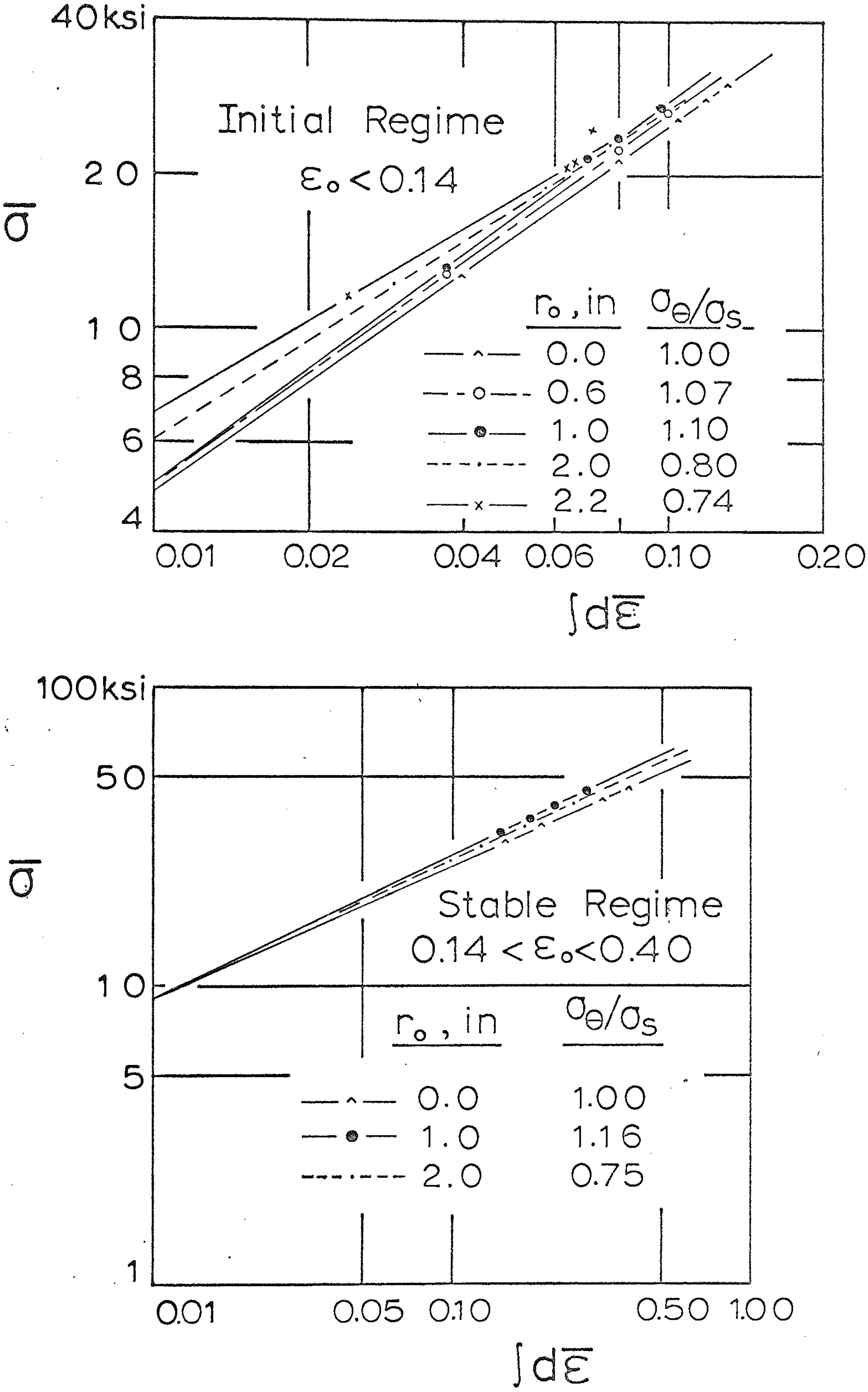
40ksi
20
10
8
6
4
$\overline{\sigma}$
Initial Regime
$\varepsilon_o < 0.14$
r_o, in
σ_θ/σ_s
0.0 1.00
0.6 1.07
1.0 1.10
2.0 0.80
2.2 0.74
0.01
0.02
0.04
0.06
0.10
0.20
$\int d\overline{\varepsilon}$
100ksi
50
10
5
1
$\overline{\sigma}$
Stable Regime
$0.14 < \varepsilon_o < 0.40$
r_o, in
σ_θ/σ_s
0.0 1.00
1.0 1.16
2.0 0.75
0.01
0.05
0.10
0.50
1.00
$\int d\overline{\varepsilon}$

Fig.(11.13)

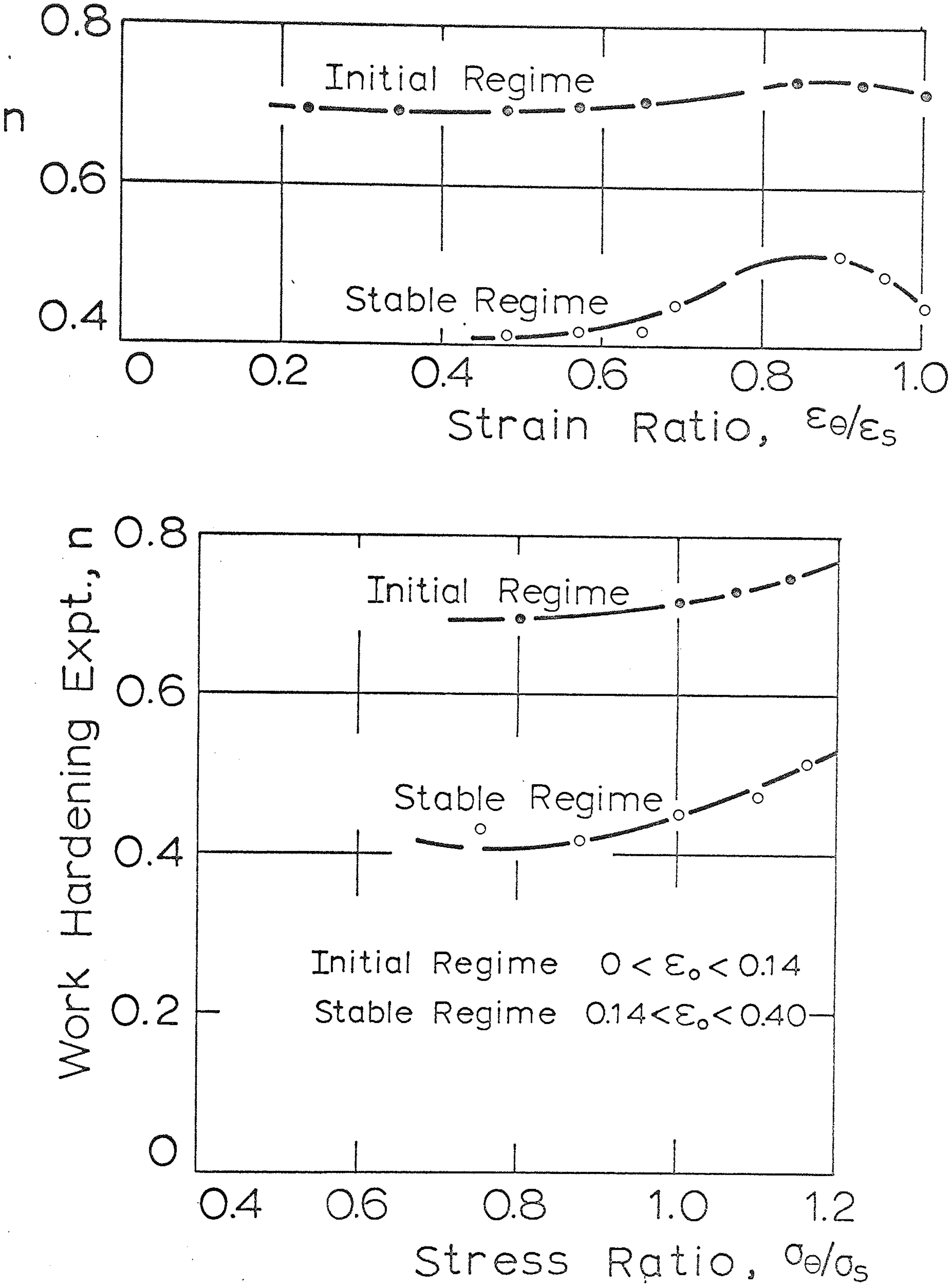
0.8
0.6
0.4
n
Initial Regime
Stable Regime
0
0.2
0.4
0.6
0.8
1.0
Strain Ratio, $\varepsilon_\theta/\varepsilon_s$
Work Hardening Expt., n
0.8
0.6
0.4
0.2
0
Initial Regime
Stable Regime
Initial Regime $0 < \varepsilon_o < 0.14$
Stable Regime $0.14 < \varepsilon_o < 0.40$
0.4
0.6
0.8
1.0
1.2
Stress Ratio, σ_θ/σ_s

Fig.(11.14)

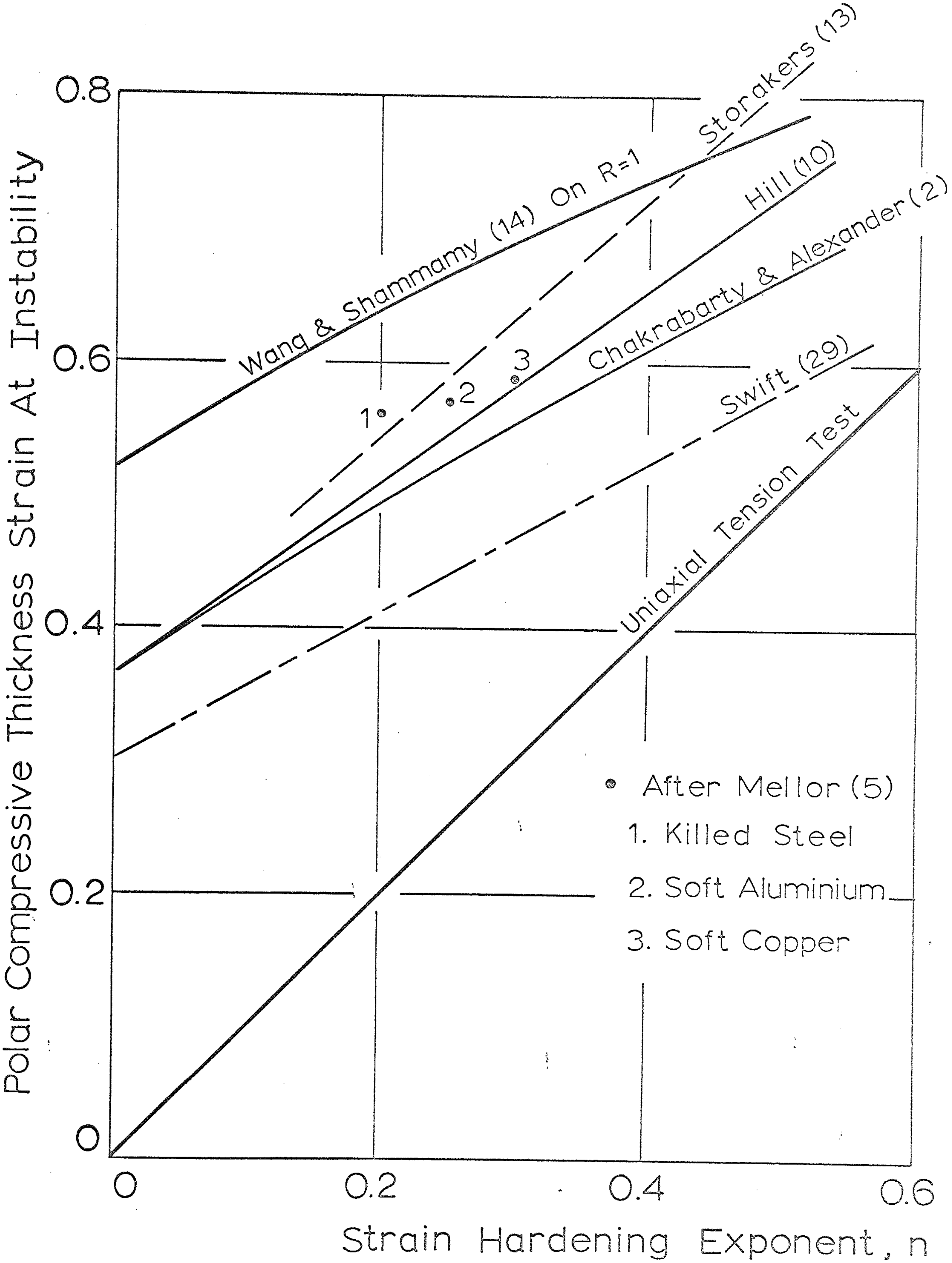
Storakers (13)
Wang & Shammamy (14) On R=1
Hill (10)
Chakrabarty & Alexander (2)
Swift (29)
Uniaxial Tension Test
1
2
3
• After Mellor (5)
1. Killed Steel
2. Soft Aluminium
3. Soft Copper
0.8
0.6
0.4
0.2
0
0
0.2
0.4
0.6
Polar Compressive Thickness Strain At Instability
Strain Hardening Exponent, n

Fig.(12.1)

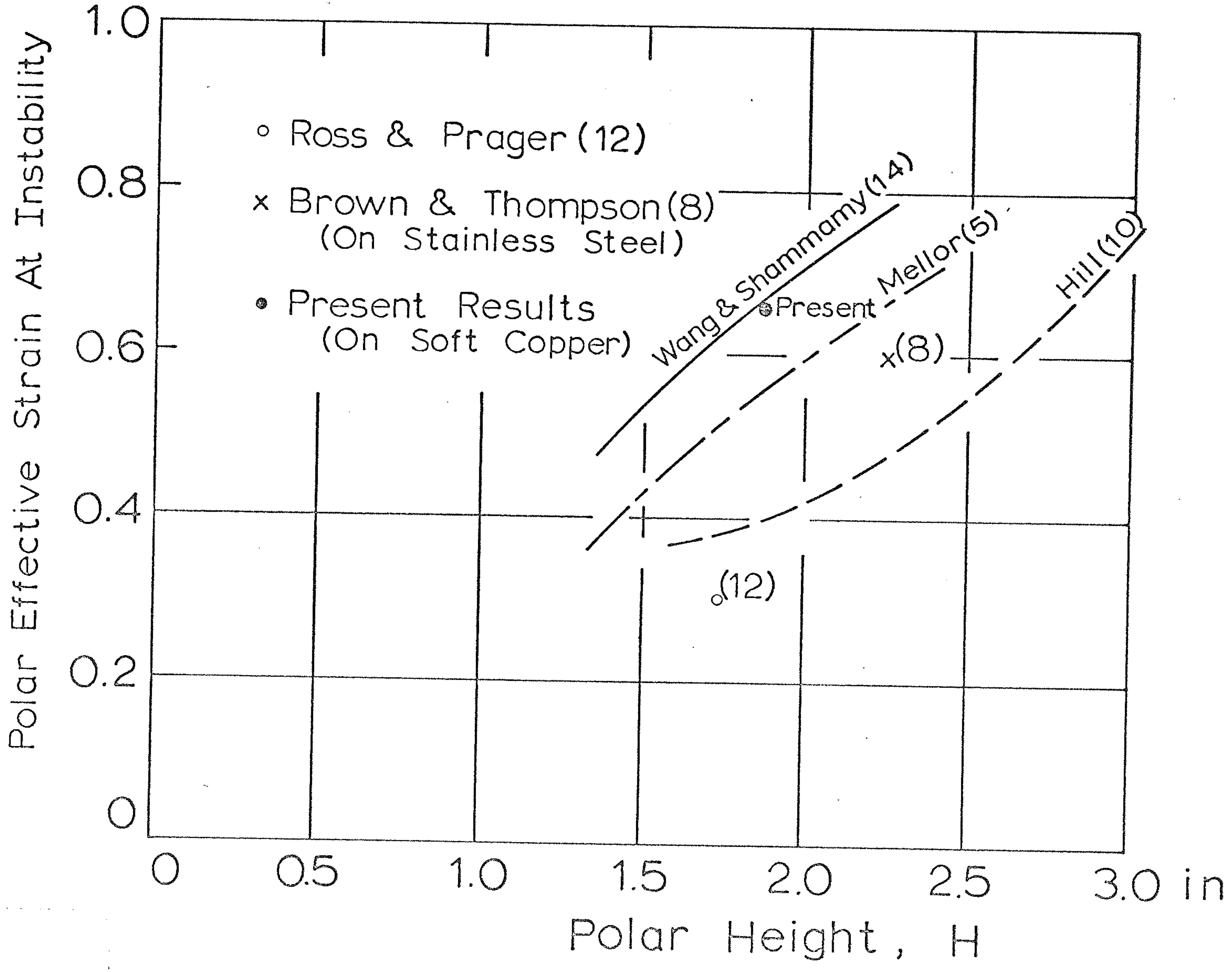

1.0
0.8
0.6
0.4
0.2
0
Polar Effective Strain At Instability
○ Ross & Prager (12)
× Brown & Thompson (8)
(On Stainless Steel)
● Present Results
(On Soft Copper)
Wang & Shammamy (14)
Present
Mellor (5)
Hill (10)
×(8)
○(12)
0
0.5
1.0
1.5
2.0
2.5
3.0 in
Polar Height , H

Fig.(12.2)

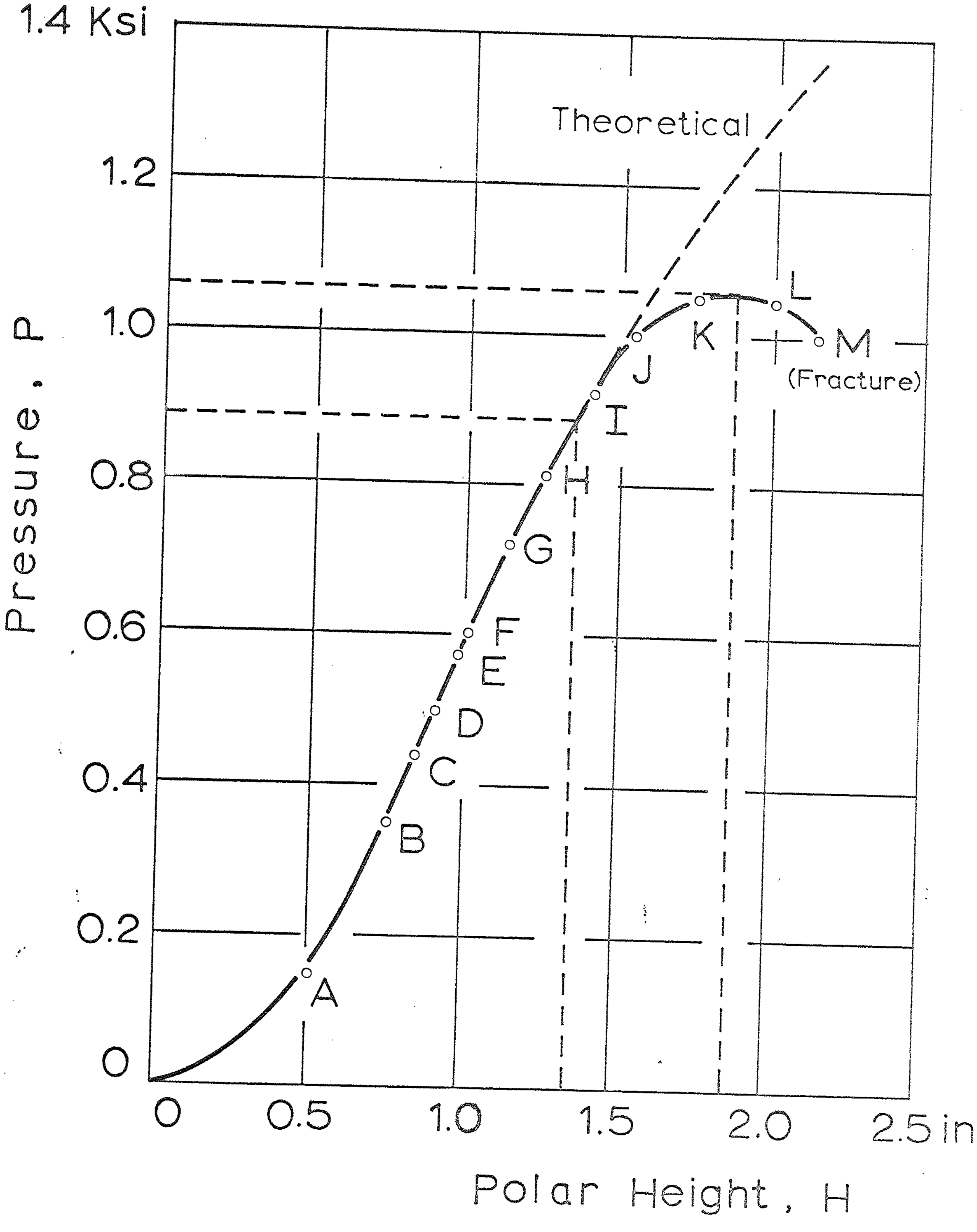

1.4 Ksi
1.2
1.0
0.8
0.6
0.4
0.2
0
Pressure, P
Theoretical
A
B
C
D
E
F
G
H
I
J
K
L
M
(Fracture)
0
0.5
1.0
1.5
2.0
2.5 in
Polar Height, H

Fig.(12.3)

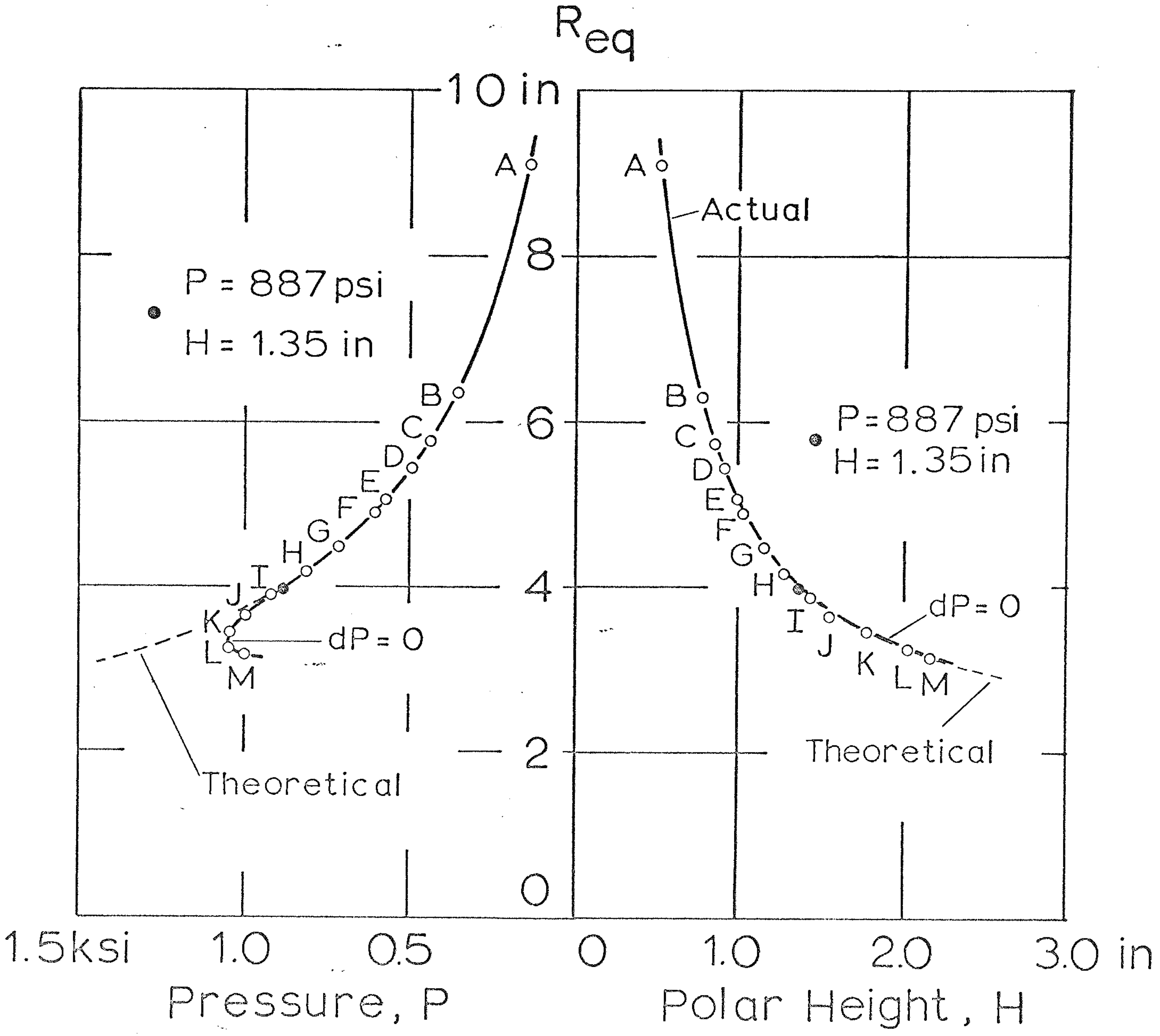
R_{eq}
10 in
8
6
4
2
0
1.5ksi
1.0
0.5
0
1.0
2.0
3.0 in
Pressure, P
Polar Height, H
P = 887 psi
H = 1.35 in
P = 887 psi
H = 1.35 in
A
B
C
D
E
F
G
H
I
J
K
L
M
Actual
dP = 0
dP = 0
Theoretical
Theoretical

Fig.(12.4)

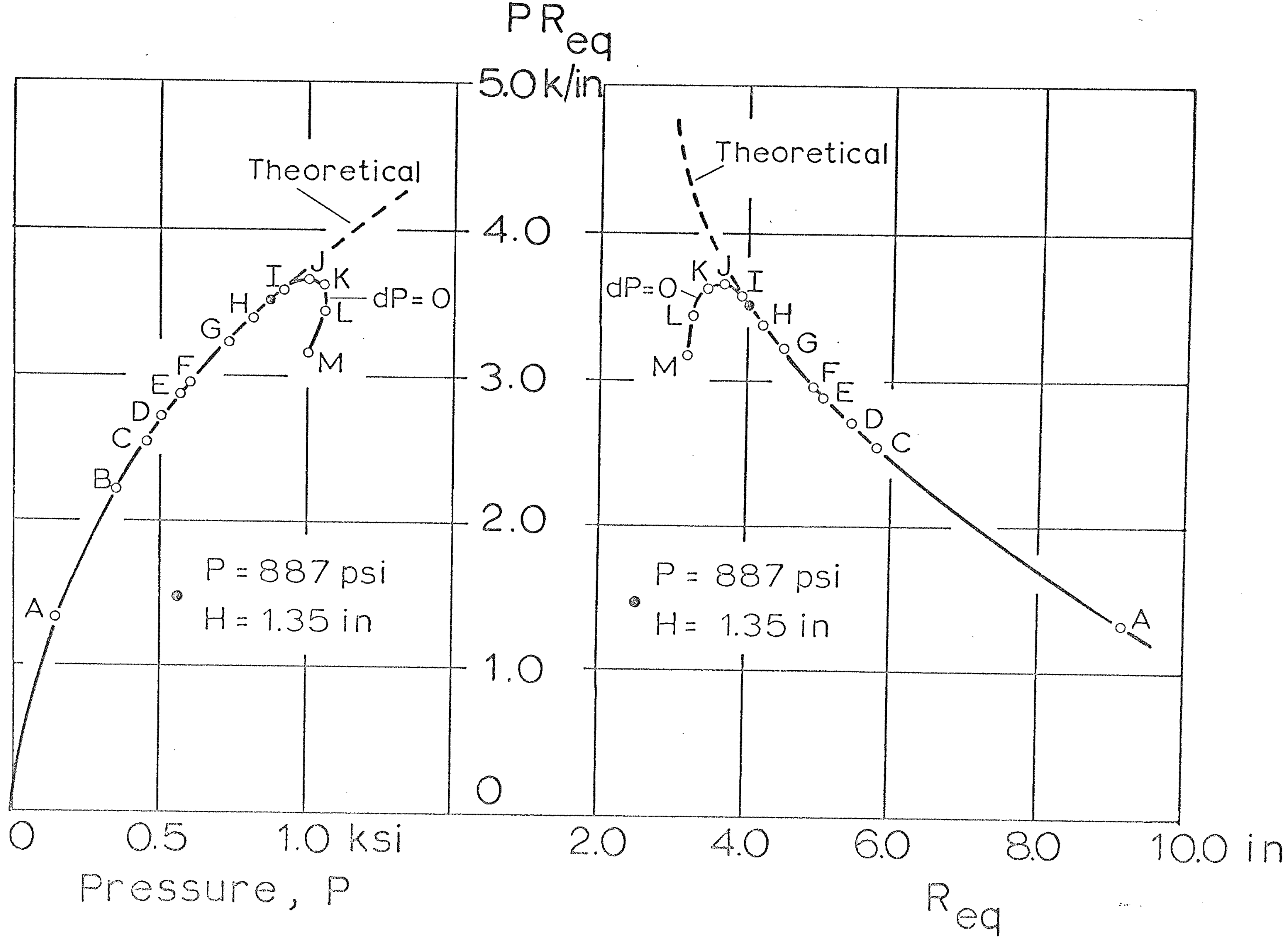
P R_eq
5.0 k/in
4.0
3.0
2.0
1.0
0
0
0.5
1.0 ksi
Pressure, P
2.0
4.0
6.0
8.0
10.0 in
R_eq
Theoretical
Theoretical
A
B
C
D
E
F
G
H
I
J
K
L
M
dP = 0
P = 887 psi
H = 1.35 in
A
C
D
E
F
G
H
I
J
K
L
M
dP = 0
P = 887 psi
H = 1.35 in

Fig.(12.5)